

# Room acoustic modeling with the time-domain discontinuous Galerkin method

## ***Citation for published version (APA):***

Wang, H. (2021). *Room acoustic modeling with the time-domain discontinuous Galerkin method*. [Phd Thesis 1 (Research TU/e / Graduation TU/e), Built Environment]. Eindhoven University of Technology.

## ***Document status and date:***

Published: 06/10/2021

## ***Document Version:***

Publisher's PDF, also known as Version of Record (includes final page, issue and volume numbers)

## ***Please check the document version of this publication:***

- A submitted manuscript is the version of the article upon submission and before peer-review. There can be important differences between the submitted version and the official published version of record. People interested in the research are advised to contact the author for the final version of the publication, or visit the DOI to the publisher's website.
- The final author version and the galley proof are versions of the publication after peer review.
- The final published version features the final layout of the paper including the volume, issue and page numbers.

[Link to publication](#)

## ***General rights***

Copyright and moral rights for the publications made accessible in the public portal are retained by the authors and/or other copyright owners and it is a condition of accessing publications that users recognise and abide by the legal requirements associated with these rights.

- Users may download and print one copy of any publication from the public portal for the purpose of private study or research.
- You may not further distribute the material or use it for any profit-making activity or commercial gain
- You may freely distribute the URL identifying the publication in the public portal.

If the publication is distributed under the terms of Article 25fa of the Dutch Copyright Act, indicated by the "Taverne" license above, please follow below link for the End User Agreement:

[www.tue.nl/taverne](http://www.tue.nl/taverne)

## ***Take down policy***

If you believe that this document breaches copyright please contact us at:

[openaccess@tue.nl](mailto:openaccess@tue.nl)

providing details and we will investigate your claim.



# Room acoustic modeling with the time-domain discontinuous Galerkin method

Huiqing Wang

---

---

# Room acoustic modeling with the time-domain discontinuous Galerkin method

PROEFSCHRIFT

ter verkrijging van de graad van doctor aan de Technische Universiteit  
Eindhoven, op gezag van de rector magnificus prof.dr.ir. F.P.T. Baaijens,  
voor een commissie aangewezen door het College voor Promoties, in het  
openbaar te verdedigen  
op woensdag 06 oktober 2021 om 16:00 uur

door

Huiqing Wang

geboren te Yantai, China

Dit proefschrift is goedgekeurd door de promotoren en de samenstelling van de promotiecommissie is als volgt:

voorzitter:	prof.dr.ir. T.A.M. Salet
1 <sup>e</sup> promotor:	prof.dr.ir. M.C.J. Hornikx
co-promotor:	dr. M. Cosnefroy
leden:	prof.dr.ir. E.H. van Brummelen prof.dr. S. Bilbao (The University of Edinburgh) dr. C-H. Jeong (Technical University of Denmark) dr.ir. H. Hofmeyer

Het onderzoek dat in dit proefschrift wordt beschreven is uitgevoerd in overeenstemming met de TU/e Gedragscode Wetenschapsbeoefening.

# ROOM ACOUSTIC MODELING WITH THE TIME-DOMAIN DISCONTINUOUS GALERKIN METHOD

HUIQING WANG

Department of the Built Environment  
Eindhoven University of Technology  
July 2021

The work in this dissertation was performed within the unit of Building Physics and Services (BPS) at the Department of the Built Environment of the Eindhoven University of Technology (the Netherlands), and was financially supported by the European Commission within the ITN Marie Skłodowska-Curie Action project ACOUTECT under the 7<sup>th</sup> Framework Programme (EC grant agreement Nr. 721536).

Project website: <http://www.acoutect.eu/>

Copyright © 2021, *Huiqing Wang*

All rights are reserved. No part of this publication may be reproduced, stored in a retrieval system, or transmitted, in any form or by any means, including electronic, mechanical, photocopying, recording or otherwise, without the prior permission of the author.

A catalogue record is available from the Eindhoven University of Technology Library.

ISBN: 978-90-386-5357-0

Bouwstenen: 321

NUR: 955

Cover design: Huiqing Wang

Printed by: ADC-Nederland

*Dedicated to my parents and grandparents*

献给我的父母, 姥姥和姥爷



---

## Abstract

The acoustic properties of indoor spaces significantly impact our comfort, well-being and productivity. Room acoustic simulations have been a practical tool for acoustic consultants in the design phase of buildings to ensure pleasant and functional acoustic environments. More recently, advancements of modern computing hardware make room acoustic modeling applicable to more computationally intensive real-time systems such as virtual reality applications.

Over the past 50 years, numerous room acoustic modeling techniques have been developed, which are typically classified as geometrical acoustics methods or wave-based methods. Compared to geometrical acoustics methods, which treat sound waves as rays and thus suffer from the loss of accuracy in the low-frequency range, wave-based methods simulate wave propagation by directly solving its governing equations based on advanced numerical modeling techniques, and are able to more accurately predict complex wave phenomena, such as scattering, diffraction and interference effects, at the cost of more computational efforts.

This PhD project aims at contributing to the room acoustic modeling community via the development and validation of an efficient, robust and accurate wave-based method. Reflecting on the state of the art numerical modeling techniques, the time-domain discontinuous Galerkin (DG) method is chosen as the focus of this thesis, due to its inherent favorable properties of high-order accuracy, geometric flexibility, and potential for massive parallel computing. The DG method derives discrete representations of the spatial derivatives of the governing equations based on elementwise approximations of unknown solutions using a local polynomial basis, and uses the so-called numerical flux to communicate across element interfaces and to impose boundary conditions. The resulting semi-discrete formulation is integrated in time by an explicit scheme.

Although the DG method has been widely used for numerical simulations of varieties of physical processes, its application to room acous-

---

tic modeling has not been explored. Therefore, the positioning of the method is addressed first, which involves a presentation of its mathematical formulation for solving the linear wave equations, a formulation of real-valued impedance boundary conditions, a semi-discrete stability analysis and numerical verifications. Numerical tests quantify the propagation error and demonstrate the convergence of the scheme. To simulate the locally reacting behavior of sound wave reflection and transmission in the vicinity of boundaries, a time-domain frequency-dependent boundary condition formulation, which is based on multi-pole model representations of the plane wave reflection and transmission coefficients, is proposed, and is incorporated into the framework of the DG method by reformulating the upwind numerical fluxes near acoustic boundaries. It is shown that the boundary formulation can maintain the high-order accuracy of the scheme. Numerical examples of practical boundary scenarios are presented as evidence of its applicability. To enhance the computational efficiency in the presence of constraints that limit time step sizes, a local time-stepping strategy based on the arbitrary high-order derivatives methodology is proposed and numerically verified. A preliminary application to the acoustic field analysis of an open plan office examines the reliability and limitations of the developed scheme for real-world problems.

---

## Publications

### Thesis publications

The thesis is based on the research work contained in the following publications, which are appended to the thesis. The contributions of individual author for each publication, which are based on CRediT ([Contributor Roles Taxonomy](#)), are described below.

- **Paper I**

**H. Wang**, I. Sihar, R. Pagán Muñoz, M. Hornikx. (2019). *Room acoustics modelling in the time-domain with the nodal discontinuous Galerkin method. The Journal of the Acoustical Society of America*, 145(4), 2650-2663.

**H. Wang**: Conceptualization, Methodology, Software, Validation, Visualization, Formal analysis, Writing (whole paper except for Section I, IV.D and IV.C). **I. Sihar**: Software, Validation, Writing (Section IV.C). **R. Pagán Muñoz**: Software, Validation, Investigation, Writing (Section I and IV.D). **M. Hornikx**: Supervision, Writing-Reviewing and Editing.

- **Paper II**

**H. Wang**, M. Hornikx. (2020). *Time-domain impedance boundary condition modeling with the discontinuous Galerkin method for room acoustics simulations. The Journal of the Acoustical Society of America*, 147 (4), 2534-2546.

**H. Wang**: Conceptualization, Methodology, Software, Validation, Visualization, Formal analysis, Writing. **M. Hornikx**: Supervision, Writing-Reviewing and Editing.

- **Paper III**

**H. Wang**, J. Yang, M. Hornikx. (2020). *Frequency-dependent transmission boundary condition in the acoustic time-domain nodal discontinuous Galerkin model. Applied Acoustics* 164, 107280.

**H. Wang**: Conceptualization, Methodology, Software, Validation, Visualization, Formal analysis, Writing. **J. Yang**: Software, Visualization, Writing-Reviewing and Editing. **M. Hornikx**: Supervision, Writing-Reviewing and Editing.

---

- **Paper IV**

**H. Wang**, M. Cosnefroy, M. Hornikx. (2021). *An arbitrary high-order discontinuous Galerkin method with local time-stepping for linear acoustic wave propagation. The Journal of the Acoustical Society of America*, 147 (4), 2534-2546.

**H. Wang**: Conceptualization, Methodology, Software, Validation, Visualization, Formal analysis, Writing. **M. Cosnefroy**: Formal analysis, Writing-Reviewing and Editing. **M. Hornikx**: Supervision, Writing-Reviewing and Editing.

- **Paper V**

**H. Wang**, W. Wittebol, M. Cosnefroy, M. Hornikx, R. Wenmaekers (2021). *Wave-based room acoustic simulations of an open plan office. In Proceedings of Euronoise 2021(Madeira, Portugal, 2021).*

**H. Wang**: Conceptualization, Methodology, Software, Validation, Visualization, Writing. **W. Wittebol**: Software, Validation, Writing-Reviewing and Editing. **M. Cosnefroy**: Software, Writing-Reviewing and Editing. **M. Hornikx**: Conceptualization, Writing-Reviewing and Editing. **R. Wenmaekers**: Investigation.

## Other publications

The following academic publications were produced during this PhD project, some of which are collaborative work. Due to the less relevance or overlapping contents, these publications are not appended to this thesis.

### Proceedings and conference contributions

- **H. Wang**, M. Hornikx (2019). *Broadband time-domain impedance boundary modeling with the discontinuous Galerkin method for room acoustics simulations. In Proceedings of the 23rd International Congress on Acoustics (Aachen, Germany, 2019).*
- B. Briere de la Hosserraye, **H. Wang**, F. Georgiou, M. Hornikx, P. W. Robinson (2019). *Derivation of time-domain impedance boundary conditions based on in-situ surface measurement and model fitting. In Proceedings of the 23rd International Congress on Acoustics (Aachen, Germany, 2019).*
- B. Briere de la Hosserraye, F. Egner, G. Diapoulis, **H. Wang** (2020). *A case study on workstation-dependent acoustic characterization of open-plan offices. Poster in Forum Acusticum 2020 (Lyon, France, 2020).*

### Booklet chapter

- B. Briere de la Hosserraye, G. Diapoulis, F. Egner, **H. Wang** (2020). *A case study on workstation-dependent acoustic characterization of open-plan offices. ACOUTECT project. ([Link to download](#))*

---

# Table of contents

<b>Abstract</b>	<b>i</b>
<b>Publications</b>	<b>iii</b>
<b>Table of contents</b>	<b>v</b>
<b>List of acronyms and abbreviations</b>	<b>vii</b>
<b>1 General introduction</b>	<b>1</b>
1.1 Background on room acoustic modeling . . . . .	1
1.2 State-of-the-art room acoustic modeling techniques . . . . .	9
1.3 Thesis objective and main contributions . . . . .	20
1.4 Thesis structure and related publications . . . . .	21
<b>2 Room acoustic modeling with the time-domain nodal discontinuous Galerkin method</b>	<b>23</b>
2.1 A conceptual introduction of the DG method . . . . .	23
2.2 Overview of Paper I . . . . .	25
<b>3 Time-domain locally reacting impedance boundary conditions</b>	<b>29</b>
3.1 Extendedly and locally reacting sound absorption modeling . . . . .	29
3.2 Overview of Paper II . . . . .	33
<b>4 Time-domain locally reacting transmission boundary conditions</b>	<b>35</b>
4.1 Sound transmission modeling . . . . .	35
4.2 Overview of Paper III . . . . .	36
4.3 Application to modeling limp permeable membranes . . . . .	37

---

<b>5</b>	<b>ADER-DG with local time-stepping</b>	<b>41</b>
5.1	Context . . . . .	41
5.2	Overview of Paper IV . . . . .	42
<b>6</b>	<b>Application study: wave-based simulations of an open plan office</b>	<b>45</b>
6.1	Reference measurements . . . . .	45
6.2	Boundary characterization . . . . .	46
6.3	Mesh generation . . . . .	50
6.4	Summary of findings . . . . .	51
<b>7</b>	<b>Conclusions and prospects</b>	<b>55</b>
7.1	Concluding remarks . . . . .	55
7.2	Future work . . . . .	56
	<b>Bibliography</b>	<b>59</b>
	<b>Paper I</b>	<b>91</b>
	<b>Paper II</b>	<b>107</b>
	<b>Paper III</b>	<b>123</b>
	<b>Paper IV</b>	<b>139</b>
	<b>Paper V</b>	<b>153</b>
	<b>Acknowledgements</b>	<b>165</b>
	<b>Curriculum Vitae</b>	<b>167</b>

---

## List of acronyms and abbreviations

<b>ADE</b>	Auxiliary Differential Equation
<b>ADER</b>	Arbitrary high-order DERivatives
<b>ARD</b>	Adaptive Rectangular Decomposition
<b>BEM</b>	Boundary Element Method
<b>CFL</b>	Courant-Friedrichs-Lewy
<b>DG</b>	Discontinuous Galerkin
<b>DOF</b>	Degree Of Freedom
<b>EDC</b>	Energy Decay Curve
<b>EDT</b>	Early Decay Time
<b>EFM</b>	Equivalent Fluid Model
<b>FDTD</b>	Finite Difference Time-Domain
<b>FEM</b>	Finite Element Method
<b>FVM</b>	Finite Volume Method
<b>GA</b>	Geometrical Acoustics
<b>GPU</b>	Graphics Processing Pnit
<b>LPM</b>	Limp Permeable Membrane
<b>LTS</b>	Local Time-Stepping
<b>MDS</b>	Mass-Damper-Spring
<b>ODE</b>	Ordinary Differential Equation
<b>PDE</b>	Partial Differential Equation
<b>PPW</b>	Points Per Wavelength
<b>PSTD</b>	PseudoSpectral Time-Domain

<b>RIR</b>	Room Impulse Response
<b>RT</b>	Reverberation Time
<b>SPL</b>	Sound Pressure Level
<b>TDIBC</b>	Time-Domain Impedance Boundary Condition
<b>VF</b>	Vector Fitting

---

# 1 | General introduction

## 1.1 Background on room acoustic modeling

People of modern days spend the main part of their lives in offices, homes, factories, cars, lecture rooms and many other kinds of closed spaces. Meanwhile, sound is all around us, which can be in the form of speech, music and noise. With such daily exposure to indoor sounds <sup>1</sup>, satisfactory acoustical environment is of vital importance to our comfort [1], health and well-being [2, 3, 4], work productivity [5, 6, 7, 8] and study performance [9, 10]. The need for a pleasant, functional and healthy acoustic environment calls for appropriate guidelines and designs from acoustical scientists and engineers.

### 1.1.1 Room acoustics fundamentals

Room acoustics deals with the study of the behavior of sound waves in indoor spaces. From a scientific point of view, it aims to understand influencing factors on the sound experienced in rooms and thereby to improve the acoustical environment of indoor spaces. Generally speaking, a room acoustician needs to take two aspects into account: the physical process of sound generation and propagation in closed spaces, and the psychological factors related with humans' perception of sounds [11]. As standardized by the international standard ISO 3382 [12, 13, 14], these two aspects are connected through a set of objective and perceptually relevant room acoustic parameters, such as the source-independent reverberation time and the speech transmission index. These acoustical parameters can serve as guidelines for design purposes to fulfill certain functions of the space, and as a reference frame for the comparison and evaluation of room acoustic qualities. They will be discussed in section 1.1.3.

---

<sup>1</sup>The sources of sound can potentially originate from external locations, *e.g.*, neighbor noise and outdoor traffic noise.

The fundamental quantities associated with room acoustics include the acoustic pressure  $p$ , the particle velocity vector  $\mathbf{v} = [u, v, w]^T$ , the static density of air  $\rho_0$  and the adiabatic sound speed  $c_0$ ; these acoustical quantities are connected through the mass, momentum and energy conservation laws [15], from which we can derive a linearized set of governing partial differential equations (PDEs), to describe sound propagation in free space. For typical room acoustic problems, it is further assumed that the propagation medium has zero mean velocity. Under these assumptions, the following homogeneous (without source term) coupled system of linear equations can be derived

$$\begin{aligned}\frac{\partial \mathbf{v}}{\partial t} + \frac{1}{\rho_0} \nabla p &= \mathbf{0}, \\ \frac{\partial p}{\partial t} + \rho_0 c_0^2 \nabla \cdot \mathbf{v} &= 0,\end{aligned}\tag{1.1}$$

which is equivalent to second-order wave equation,

$$c_0^2 \nabla^2 p = \frac{\partial^2 p}{\partial t^2}.\tag{1.2}$$

These equations describe the variations in time and space of the acoustic variables  $p$  and  $\mathbf{v}$ . The speed of sound can be calculated from the formula  $c_0 = (331 + 0.6T_r)$  [m/s], where  $T_r$  is the room temperature in Celsius [12]. In this work,  $T_r$  is set to 20°C and  $c_0$  is 343 m/s. Assuming that the convention  $e^{i\omega t}$  is used for the harmonic time variation and inserting the following single frequency ansatz of the form

$$p(t) = P(\omega)e^{i\omega t}\tag{1.3}$$

into the wave equation, we obtain the Helmholtz equation

$$\nabla^2 P + k^2 P = 0,\tag{1.4}$$

where  $k$  is the wavenumber as  $k = \omega/c_0$ .

Besides the governing equations describing sound wave propagation, a complete quantification of a sound field inside a closed space mathematically requires a geometrical model of the interested space, boundary conditions that characterize acoustic properties of surface materials by relating the acoustic pressure  $p$  to the normal component of the particle velocity on the boundaries (treated in Chapter 3 and 4) and sound sources. In this work, sound sources are introduced via the initial conditions (see, *e.g.*, Eq. (29) in the appended **Paper I**); it is thus sufficient to

consider homogeneous propagation equations. Even though the physics of sound generation and free field propagation is well understood fundamentally, solutions in analytical forms only exists for certain cases with simple boundary conditions and geometries. For real problems of interest, accurate predictions call for advanced numerical techniques.

### 1.1.2 Room impulse response

Room acoustic modeling aims to describe sound fields in complex enclosures by numerically calculating impulse responses of the space of interest. A room impulse response (RIR) is a (pressure) signal as a function of time at a discrete point in space in response to an acoustic excitation. When a room is acoustically considered as a linear time-invariant (LTI) system, the RIR is mathematically defined as the point-to-point time-domain transfer function  $h(t)$  between a point source  $q(t)$  and a specific receiver. The impulse response fully characterizes the propagation between the source and the receiver, in terms of both phase and magnitude, as the acoustic pressure recorded at the receiver for an arbitrary monopole source signal can be obtained from the convolution theorem

$$p(t) = \int_{-\infty}^t h(t - \tau)q(\tau)d\tau, \quad (1.5)$$

under the assumption of linearity, time-invariance, and limited spatial support of the source. This is also the principle behind auralization, which will be elaborated upon in Sec. 1.1.4. Practical measurements of the RIR follow the guidelines and procedures documented in ISO 3382 [12, 13, 14], which also specify detailed requirements on the equipment and the source signal. However, the measured RIR is fundamentally inexact since it is hard to obtain point sources and receivers in practice.

Generally, an RIR consists of three separate parts as shown in Fig. 1.1: direct sound, early reflections, and late reverberation. If there is a line of sight between the source and receiver, the direct sound is the sound that arrives at the receiver along the shortest path from the source without any reflections and is usually perceived as the loudest. The early reflections are the sounds that arrive at the receiver undergoing at least one reflection from the walls, ceiling, floor and other potential indoor objects. The direct sound and the early reflections together are mainly responsible for sound localization by the human brain [16]. The late reverberation is the sound that reaches the receiver after the early reflections; as a result of the large amount of repetitive reflections, the

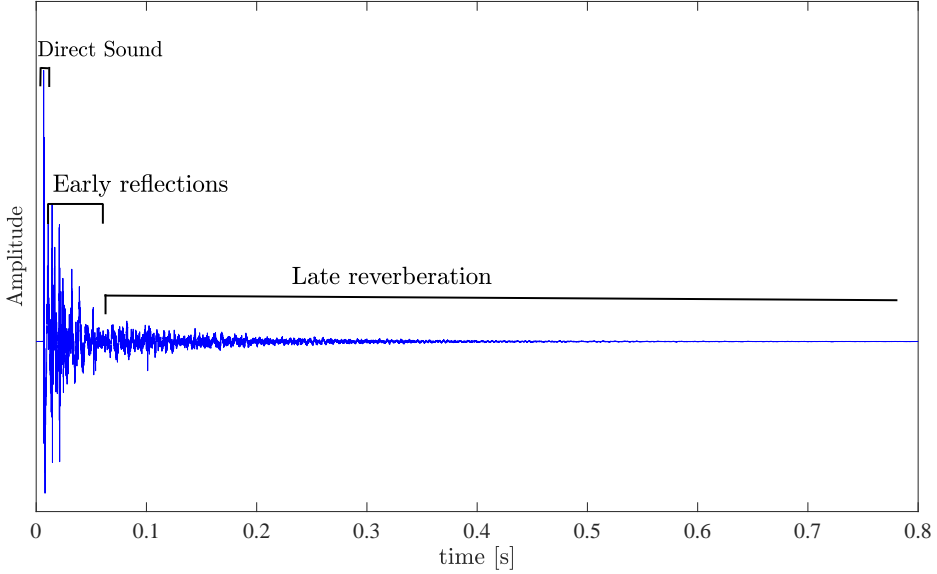


Figure 1.1: An example of RIR from a measurement.

sound field is typically quite diffuse, which means that the direction of propagating sounds is random and the sound energy distribution is more or less isotropic. The reverberation is closely related to the size and boundary properties of the room.

### 1.1.3 Room acoustic parameters

Upon collection of RIRs, various room acoustic parameters that objectively characterize the acoustic conditions of the space of interest can be evaluated as documented in ISO 3382 [12, 13, 14], depending on the function and usage of the room, *e.g.*, theater, lecture room or open plan office. In the following, a list of parameters that are typically considered in practice for performance spaces and for open plan offices are briefly introduced.

#### Reverberation time

The reverberation time (RT, in [s]), which is a predominant room acoustic indicator, measures the time taken for the sound energy to drop by 60 dB of its initial strength. ISO 3382-2 [13] describes a rigorous approach termed as the integrated impulse response method [17] to calculate the RT. It is based on creating an energy decay curve (*EDC*), which is calculated as follows

$$EDC(t) = \int_t^{\infty} h^2(\tau) d\tau, \quad (1.6)$$

where  $\infty$  denotes the time when the sound field reaches the equilibrium state. If the background noise level is known,  $\infty$  is calculated as the intersection between a horizontal line through the background noise and a sloping line through a representative part of the squared impulse response displayed using a logarithmic scale [13]. Actually,  $EDC(t)$  measures the amount of sound energy that has yet to arrive at the receiver.

The reverberation time is calculated by fitting a linear regression line to the  $EDC(t)$ , which is first normalized by the maximum energy level and plotted in the logarithmic scale, starting from -5 dB. Based on the slope of the fitting line, which specifies the decay rate  $d_r$  [dB·/s], the reverberation time is the time it takes to reach a 60 dB drop of the sound energy and amounts to  $60/d_r$ . To overcome the issue associated with the background noise and the power of the source, the regression range that is used to calculate the slope can be shortened, for example between -5 dB and -25 (or -35) dB. The reverberation time is then labelled as  $T_{20}$  (or  $T_{30}$ ) accordingly.

It should be noted that reverberation time and every other parameter described in the following are normally evaluated in either octave or one-third octave bands, which require the band-pass filtering of RIRs. A single number also can be retrieved by averaging the RT values in the 500 Hz and 1000 Hz octave bands. In figure 1.2, the energy decay curve evaluated for the 500 Hz octave band of the RIR in Fig. 1.1 is shown, along with the linear regression obtained using the evaluation range [-5,-35] dB.

### Early decay time

The early decay time (in [s]), denoted as  $EDT$ , measures the initial part of the sound energy decay. Its calculation is similar to the reverberation time, which involves a linear regression based on the fixed range of 0 dB to -10 dB and an extrapolation to a decay time of 60 dB. Since both the direct sound and the early reflection components are covered in the [-10,0] dB range of  $EDC(t)$ ,  $EDT$  is more important subjectively and more related to perceived reverberance than  $T_{20}$  or  $T_{30}$  [18]. For an ideally diffuse sound field with an exponential decay in energy,  $EDT$  equals the reverberation time.

### Early-to-late index

The early-to-late index ( $C_{te}$ , in [dB]), represents the logarithmic ratio between the early arriving and late arriving sound energy.  $C_{te}$  is formally

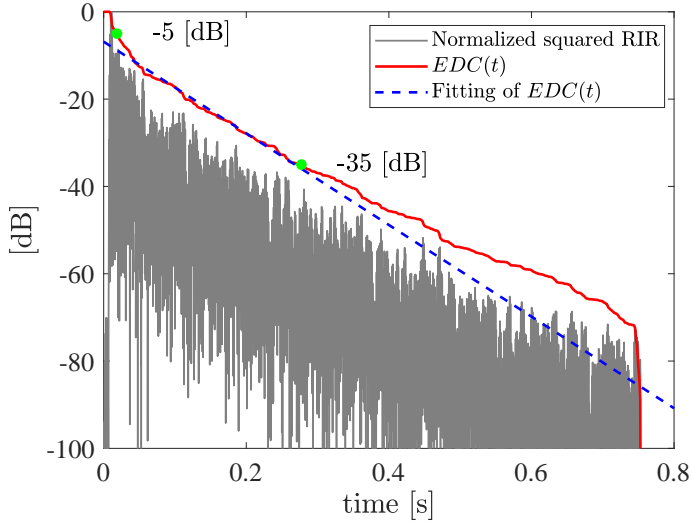


Figure 1.2: Energy decay curve example and fitting to calculate  $T_{30}$ .

calculated as:

$$C_{t_e} = 10 \log_{10} \left( \frac{\int_0^{t_e} h^2(t) dt}{\int_{t_e}^{\infty} h^2(t) dt} \right), \quad (1.7)$$

where  $t_e$  is the early time limit of either 50 ms (suitable for speech conditions) or 80 ms (suitable for music conditions). A high value of  $C_{t_e}$  indicates that the perceived sound is clear and distinguishable whereas a low value of  $C_{t_e}$  implies that the audio information is perceptually fuzzy and unclear at the listening position. For this reason,  $C_{t_e}$  is also referred to as ‘clarity’. Typical values of  $C_{t_e}$  fall into the range of  $[-5, 5]$  dB. For an intelligible speech,  $C_{50}$  should be higher than -2 dB [12].

### Center time

The center time ( $T_S$ , in [ms]), is the time of the center of gravity of the squared impulse response:

$$T_S = 10 \log_{10} \left( \frac{\int_0^{\infty} t h^2(t) dt}{\int_0^{\infty} h^2(t) dt} \right). \quad (1.8)$$

The subscript  $S$  of  $T_S$  stands for “Schwerpunktzeit” in German.  $T_S$  specifies the balance between clarity and reverberance [12]. To be specific, low values of  $T_S$  allude to a clear sound whereas high values indicate a reverberant sound environment. Similar to the clarity,  $T_S$  is valuable in acoustic evaluations of the speech and music conditions.

### A-weighted sound pressure level of speech and its spatial decay rate

The A-weighted sound pressure level (SPL) of speech ( $L_{p,A,S}$ ) and its spatial decay rate ( $D_{2,S}$ ), as specified in ISO 3382-3 [14], are single number acoustic parameters indicating the acoustic performances of open plan offices with furnishing, the principal aims of which being to ensure good speech privacy and to weaken distractions between workstations. These quantities are measured or simulated by placing a single omnidirectional loudspeaker at one selected working position and by recording the sound pressure signal in other working positions, mimicking the situation where a single person is talking and others are silent.

The following steps need to be conducted to obtain these parameters. First of all, the SPL at measurement point  $n$  (with a distance  $r_n$  from the source) in  $i$ -th octave band (from 125 Hz to 8000 Hz), which is denoted as  $L_{p,Ls,n,i}$  (index  $Ls$  refers to loudspeaker), is calculated by processing measured or simulated impulse responses. Then, the corresponding attenuation  $D_{n,i}$  in decibels compared to the SPL at a distance of 1 m in the free field condition ( $L_{p,Ls,1m,i}$ ) is determined by

$$D_{n,i} = L_{p,Ls,1m,i} - L_{p,Ls,n,i}. \quad (1.9)$$

Given the sound power level of the loudspeaker in octave bands  $L_{W,Ls,i}$ ,  $L_{p,Ls,1m,i}$  is approximately equal to  $L_{W,Ls,i} - 11$  dB. Upon collections of  $D_{n,i}$ , the SPL of normal speech  $L_{p,S,n,i}$  are calculated as

$$L_{p,S,n,i} = L_{p,S,1m,i} - D_{n,i}, \quad (1.10)$$

where  $L_{p,S,1m,i}$  is the SPL of normal speech standardized for normal voice effort [14]. Finally, the A-weighted SPL of speech  $L_{p,A,S,n}$  is obtained by adding the A-weighting values  $A_i$  in each octave band and the logarithmic summation:

$$L_{p,A,S,n} = 10 \lg \left( \sum_{i=1}^7 10^{\frac{L_{p,S,n,i} + A_i}{10}} \right). \quad (1.11)$$

The spatial decay rate  $D_{2,S}$  is calculated by performing a linear regression of  $L_{p,A,S,n}$  with respect to the receiver distances  $r_n$  within the range 2 m to 16 m in a logarithmic scale to base 2. Therefore, it indicates the SPL reduction when the distance is doubled. Furthermore, the A-weighted SPL of speech at 4 m ( $L_{p,A,S,4m}$ ), which is evaluated in practice as a single number target quantity, is determined based on the linear regression. For better clarification, an example taken from ISO 3382-3 [14] is shown in Fig. 1.3.

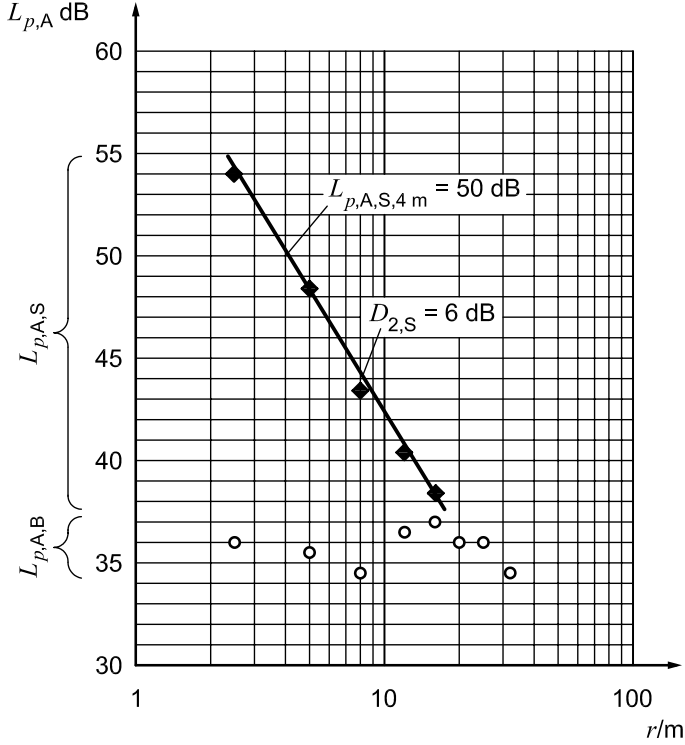


Figure 1.3: Example of the determination of  $D_{2,S}$  and  $L_{p,A,S,4m}$  from Ref. [14]. The white dots denote the A-weighted SPL of the background noise while the black dots stand for the A-weighted SPL of speech.

### 1.1.4 Applications

With its ability to accurately reproduce indoor sound behavior, room acoustic modeling plays an important role in the following applications:

- One application is associated with the realization and improvement of certain acoustic conditions, which are prevalent in many fields, such as architecture design [19, 11, 20]; the acoustic properties of various design or renovation options can be evaluated and further optimized. In such applications, the physical accuracy of the simulated sound field is of primary concern. Such modeling procedures become a key step in the early design phase and act as an economical substitute to the traditional acoustic research method using the scaled physical models of spaces.
- The second application category is more inclined to synthesizing a certain spatial immersion or to conveying an aesthetically pleasing

auditory feeling, while preserving a desired level of realism. Typical examples are observed in the areas of computer games [21], where artificial reverberation effects [22] are added to mimic realistic environments. Here, real-time interaction, which involves dynamic model attributes such as time-dependent geometry and moving source/receiver locations, is a priority whereas the accuracy of the detailed physical model is of less concern.

- The last category of application is concerned with the concept of *auralization*, which by definition is *the process of rendering audible, by physical or mathematical modeling, the sound field of a source in a space, in such a way as to simulate the binaural listening experience at a given position in the modeled space*. [23]. In other words, it focuses on creating a virtual auditory environment where the aural experience can be as close to reality as possible [24, 25, 26]. In a technical sense, auralization requires an (binaural) RIR as accurate as possible with limited computational resources, and therefore is more challenging compared to the previous two types of applications. Driven by the vast potential of application needs, recent years have witnessed great advancements of auralization in various scenarios, for example building design [27, 28] and cognitive training [29].

## 1.2 State-of-the-art room acoustic modeling techniques

The concept of room acoustic simulation was conceived by Schroeder [30] in the early 1960s. Since then, numerous modeling techniques have been developed along with the advancement of ever-increasing computing power. Depending on their fundamental assumptions, room acoustic modeling approaches fall in general into two categories: geometrical acoustics (GA) methods and wave-based methods.

It should be mentioned that in literature there exists another type of energy-based method called the diffusion equation method, which is efficient in modeling the reverberation tail of impulse responses. Compared to traditional statistical models of a perfectly diffuse sound field with limited applicability and accuracy [11], it allows for local variations of energy densities [31] and is considered more accurate for practical room scenarios. One influencing factor on the accuracy in practice is related to the difficulty to obtain the controlling parameters of the diffusion process

for complex geometries. Further details of the diffusion equation method can be found in Refs. [32, 33, 34].

Besides, data driven techniques and machine learning have spurred rejuvenated interest in the field of acoustics [35]. Recent related developments include machine learning methods for the simulating wave propagation [36], artificial/convolutional neural network techniques for fast auralization [37, 38] and estimation of sound scattering [39], unsupervised machine learning algorithm for reduced-order modeling of traveling waves [40]. More kinds of techniques for room acoustic modeling, which are not established enough yet, could be expected in the future.

### 1.2.1 Geometrical acoustics

Geometrical room acoustic modeling techniques treat sound waves as rays without fully considering the wave nature of sound. Generally, this fundamental assumption is valid at high frequencies, where the largest wavelength of interest is supposed to be at least one order of magnitude smaller than the relevant geometry details [41]. The main approaches are the image source method and the ray tracing method.

#### Image source methods

The concept of image source was applied to room acoustics by Eyring in 1930 [42] to predict the reverberation time. In 1972, Gibbs and Jones applied the image source method for calculating the variation in sound pressure level in a rectangular room with various absorption configurations [43]. The first open source code of the algorithm was published by Allen and Berkeley in 1979 [44]. Extension of the image source method to arbitrary polyhedra was described by Borish [45], where the first extensive attempt to check the validity and visibility of reflection paths was made.

In the image source method, a sound propagation path originates from the source and then reflects on the boundary surface specularly. Each reflection is represented using a secondary source, the intensity of which depends on the traveling distance and absorption properties of the surface. One deterministically considers all specular reflection paths from a source to a receiver by mirroring the image sources at each reflection surface recursively. During this process, the sound field is collected. The recursion process continues until a given reflection order is achieved or the reflected component has lost a certain percentage of its initial energy level.

The computational cost of the image source method increases dramatically with the order of reflections. Furthermore, it is generally able

to obtain an accurate approximation of the early reflections in an RIR. However, only specular reflections are taken into account naturally and sound diffusion is neglected. Also, handling non-trivial geometries requires significant implementation efforts.

### Ray tracing methods

One of the earliest application of ray tracing method in room acoustic modeling was proposed by Krokstad *et al.* [46] in 1968. In ray tracing, a given number of rays carrying a finite amount of energy is emitted from the source location in directions that follow the desired source directivity. For each ray, the energy remains constant during the free propagation [47] and its reflection on the boundary surfaces follows the geometric law of specular reflection. After each reflection, a certain amount of energy is deducted from the previous energy level. A ray terminates its path upon hitting the volume surrounding the receiver or experiencing a sufficient energy decay. The elapsed time since the source excitation is recorded. Main drawbacks of ray tracing include the accuracy degradation in modeling diffraction, negligence of important early reflection paths and inclusion of duplicated or invalid recorded ray paths [48].

When sound rays hit surfaces in a room, a portion of the sound energy is absorbed as characterized by the absorption coefficient  $\alpha$ , while the remaining parts are reflected either specularly or non-specularly (scattered). The ratio of the non-specularly reflected sound energy to the total reflected energy defines the scattering coefficient  $s$  [49] as illustrated in Fig. 1.4. It is found that the inclusion of scattering effects generated by edges and surface roughness is effective in improving the accuracy of room acoustic parameters that hinge on early reflections, such as early decay time and clarity [50, 51, 52]. The scattering coefficient alone is inadequate at describing the complex acoustic behavior of scattering surfaces. In order to describe the spatial distribution of the scattered sound, the diffusion coefficient is defined to quantify the degree of uniformity of the polar response of a surface. If the energy is scattered uniformly in all directions, then the diffusion coefficient<sup>2</sup> is equal to one. If all the energy is scattered in one direction, then the diffusion coefficient is equal to zero [11]. It was demonstrated that the incorporation of the diffuse surface reflections into the ray tracing model leads to better prediction accuracy[53].

Frequency dependency can be added by splitting the energy spectrum into frequency bands and making the absorption coefficients dependent

<sup>2</sup>Here, diffusion refers to the diffuse reflection, not volume diffusion.

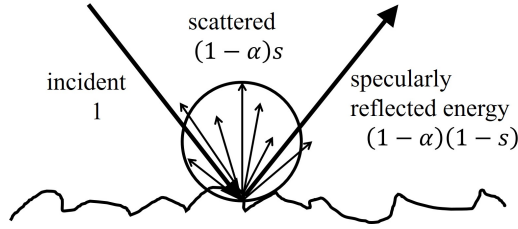


Figure 1.4: Illustration of the separation of reflected energy into scattered and specular components (after Vorländer and Mommertz [54]).

on the frequency. The energy associated with each ray pertains to some frequency band of a given width (e.g., an octave). As a result, multiple simulations required, one for each frequency band of interest. The individual responses obtained can then be recombined using a bank of digital filters.

### Summary of geometrical acoustic methods

Over the past decades, various improvements and extensions of applicabilities of GA methods have been proposed, such as incorporating the phase information [55, 56] and edge diffraction [57, 58, 59]. Geometrical room acoustic modeling techniques mainly require geometric computations, which are relatively cheap for modern computer power. Therefore, they have been adopted in commercial room acoustic simulation software such as Odeon [60], CATT-Acoustic [61] and EASE [62] and are favored among room acoustic consultants. A comprehensive literature overview of state-of-the-art GA methods can be found in Ref. [41].

However, apart from the constraint of the applicable frequency range, geometrical acoustic methods generally require multiple simulations, each of which pertains to a certain frequency band of a given width, to incorporate the frequency-dependent acoustic properties of boundaries and to obtain a broadband response. Other drawbacks of geometrical acoustic methods involve inaccurate locally reacting reflection modeling, negligence of detailed geometric treatments, and simplified use of random incidence absorption and scattering coefficients, which render the difference between the simulated and measured impulse responses audible [50, 51].

### 1.2.2 Wave-based methods

In contrast to geometrical acoustics methods, wave-based methods simulate sound propagation from a fundamental point of view by directly solving the governing linear acoustic equations Eq. (1.1) or Eq. (1.2),

based on numerical approximation techniques. Therefore, wave-based methods are able to capture wave phenomena such as scattering, diffraction and interference effects with no/fewer inherent constraints on the frequency range.

Wave-based methods can be classified into two types: time-domain methods and frequency-domain methods. Particularly, time-domain approaches, which are in line with the physical nature of sound propagation, have the benefits of calculating the solution over a broad frequency range. Furthermore, they are capable of handling room acoustic scenarios involving moving sources. However, frequency-domain approaches are preferred by certain methods due to their nature of numerical formulations. Time-domain methods generally follow the methodology of the method of lines, where spatial derivatives are treated first and then time integration is performed at each time step. In the following, an abstract and not-exhaustive overview of a variety of wave-based methods is presented as they are the main focus of this thesis, including the finite difference time-domain method, the spectral method, the finite volume method, the finite element method and the boundary element method.

### Finite Difference Time-Domain methods

Among the wave-based methods, the finite difference time-domain (FDTD) methods, which originated from the computational electromagnetics community [63, 64] in the middle of 1960s, are so far the most established and popular numerical techniques for room acoustic simulation purposes. Due to their simplicity and relative ease of implementation, finite difference methods have been widely used in many engineering applications, including computational acoustics [65, 66, 67, 68, 69]. Their applicability to time-domain room acoustic modeling were firstly and independently investigated by Chiba *et al.* [70], Savioja *et al.* [71] and Botteldooren [72, 73] in the 1990's.

As a class of numerical techniques for solving PDEs, the finite difference methods discretize both the spatial domain and time interval into discrete points. The PDEs are converted into algebraic equations by approximating derivatives with finite differences from nearby points based on polynomial interpolants. The solution values at these discrete points are calculated approximately by solving the resulting algebraic equations. To date, considerable research efforts have been devoted to improve FDTD methods for room acoustic simulations in various aspects, including high-order accuracy schemes [74, 75, 76, 77, 78, 79, 80, 81], sound source modeling [82, 83, 84, 85, 86], high-performance-computing implementations with the graphics processing unit (GPU) and parallelization

[87, 88, 89, 90], real-time applications [91] and impedance boundary modeling [92, 93, 94, 95, 96, 97].

However, despite their remarkable features, FDTD methods are plagued with its inherent lack of geometric flexibility due to their use of structured meshes. Consequently, their application is mostly restricted to problems with simple geometries. If the Cartesian grid discretization is employed, curved geometries have to be represented with a staircase approximation, which is only accurate for cases where the shape variations are relatively large compared to the smallest wavelength of interest [98]; otherwise, significant errors arise in estimating sound scattering and reflection [98, 99]. Another strategy to deal with practical geometries is to use a multi-block approach or curvilinear meshes [100, 101], where the physical domain is mapped onto several Cartesian grid blocks through (non-)linear geometric transformations.

It is worth mentioning that there is another class of closely-related techniques referred to as the digital waveguide mesh methods [102, 103, 104, 105, 84] that share similar formulations with FDTD methods. A systematic elaboration of the functional equivalence of these two approaches and the conditions for building mixed models are presented in Ref. [106]. Since FDTD methods are not the main focus of this thesis, interested readers can refer to the PhD thesis of Hamilton [98] and van Mourik [107] for an in-depth discussion of uses and developments of FDTD methods in room acoustic simulations; their applications within the context of auralization can be found in the PhD thesis of Saarelma [108].

### Spectral methods

Another broad class of methods that rely on structured grids for the approximation of spatial derivatives are the (pseudo) spectral methods [109, 110, 111, 112]. In contrast to finite difference methods, which approximate the solutions at any given point with a local polynomial interpolant based on information at neighboring points, spectral methods expand the unknown solutions with a global orthogonal polynomial basis. Depending on the type of global basis employed, spectral methods can be further classified, *e.g.*, Fourier spectral methods (for periodic problems) and Chebyshev spectral methods (for non-periodic cases). Further distinguishment arises from the different ways to calculate the expansion coefficients of the global basis, *e.g.*, the Tau approach, the Galerkin approach and the collocation approach [113, 114].

In the general context of solving time-dependent PDEs, spectral meth-

ods exhibit several appealing properties. First of all, as a result of the spectral expansion, evaluations of the spatial derivative are transformed from the physical space to the space of the polynomial basis (wavenumber space in the case of Fourier basis), and hence can be performed pseudo-analytically. It implies that for periodic problems, there is no dispersion error from the spatial discretization and exponential convergence rate is achieved [114]. The efficient implementations of pseudospectral methods benefit greatly from the fast Fourier transform (FFT) algorithm developed by Cooley and Tukey [115]. Theoretically, Fourier spectral methods need only two points per wavelength (PPW) while Chebyshev methods need  $\pi$  PPW on condition that the approximated solutions are sufficiently smooth and periodic. However, periodic boundary conditions are hardly met in practice and a larger number of PPW is needed to capture the geometrical details of the physical space. Furthermore, compared to FDTD, the advantage of higher convergence rate comes at a cost of the more stringent Courant-Friedrichs-Lewy (CFL) condition [116].

In the specific field of room acoustics modeling, adaptive rectangular decomposition (ARD) methods [117, 118] and pseudospectral time-domain methods (PSTD) [119, 120, 121] have been applied based on the Fourier basis. Combined with domain decomposition techniques, they demonstrate attractive computational efficiency for problems with relatively simple geometries and boundary conditions. However, like FDTD methods, several factors result in difficulties or inefficiencies for room acoustics when using spectral methods. For example, an extra error arises from communication across the interface between sub-domains. Another challenging issue that remains to be addressed is the accurate and efficient modeling of frequency-dependent impedance boundary conditions.

### Finite Volume methods

Finite volume methods (FVM) overcome the geometric flexibility issues of methods based on structured grids by utilizing an unstructured tessellation of the computational domain in the form of polygonal or polyhedral elements (cells in the nomenclature of FVM). In contrast to finite difference and spectral methods, FVM operates on the integral form of the governing PDEs, where the divergence term is converted to a surface integral using the divergence theorem. Specifically, the integral of unknown solutions over each grid cell at one time instant, also known as the cell average, is approximated and tracked. In each time step, these cell averages are updated using approximations to the fluxes through the cell edges. A high-order accuracy is achieved by using local polynomial

reconstructions with nearby cell averages in the construction of numerical flux functions. A popular choice is the upwind flux [122] and it relies on the solutions to the Riemann problem, which is simply the governing equation with piecewise constant initial data that has a single jump discontinuity [123].

FVM has undergone decades of developments in various fields of engineering, especially for computational fluid dynamics. Its application in room acoustic simulation started from the work of Botteldooren [72]. Recent developments include locally reacting frequency dependent boundaries [124, 125] and air absorption [126]. However, the main limitation of FVM lies in its difficulty to achieve high-order accuracy (beyond second-order) on general multi-dimensional unstructured meshes in an efficient way.

### Finite Element methods

The continuous finite element methods (FEM), which first appeared in wave-based analysis of room acoustic modes in 1965 [127], constitute another class of methods that operate on unstructured meshes, and therefore are suitable for problems with complex geometries. The discretization strategy is characterized by the variational (weak) formulation. Usually, the Bubnov-Galerkin approach is followed, which means that the function space for both test functions and solution functions are the same.

In contrast to FVM, FEM uses piecewise polynomial interpolations inside each element, ensuring high-order approximations locally without the need of large stencils across neighboring elements. Since the nodes along the faces of neighboring elements are shared, the basis functions are continuous across elements and essentially globally defined. As a result, the discretized system is implicitly coupled between the elements, implying that a large sparse linear system is needed to be solved using a direct or an iterative approach. This poses computational challenges for large scale 3D problems. Generally speaking, FEM is a natural choice for elliptic boundary value problems, such as the Helmholtz equation (1.4) and therefore it is mainly used for modeling room acoustic problems in the frequency domain [128, 129, 130, 131, 132, 133].

Applications of FEM to time-domain room acoustic modeling have been investigated by Okuzono *et al.*, using the implicit Newmark time integration scheme with preconditioned iterative solver [134, 135, 136] or the explicit time integration scheme with the mass lumping technique [137]. Recently, a high-order variant of FEM, the so-called spec-

tral element method (SEM) [138, 139] was applied to time-domain room acoustic modeling by Pind *et al.* [140], where the mass lumping technique [141] is adopted to increase the efficiency and a formulation of frequency-dependent impedance boundary condition is presented.

### Boundary Element methods

Boundary element methods (BEM) are established numerical techniques to solve boundary-value problems based on a discretization of the boundaries of the space of interest, different from the aforementioned methods that employ a spatial (volumetric) discretization. In the field of acoustics, pioneering work began in 1960s [142], which predicted sound radiation from an arbitrary vibrating body immersed in an infinite fluid medium. The governing equation to be numerically solved in the time domain is the integral form of the wave equation known as the Kirchhoff integral equation, whereas in the frequency domain, it is the integral form of the Helmholtz equation, *i.e.*, the Kirchhoff-Helmholtz integral equation, both of which are derived based on the divergence theorem. These integral equations fundamentally state that the acoustic pressure at an arbitrary location is determined by the distribution of the acoustic pressure and its normal derivative (normal velocity) on the boundary surface [143].

Depending on the way to solve the unknown pressure along the boundaries and to fulfill the integral equation, BEM can be classified into the collocation approach [144, 145] and the variational approach [146]. To address the inherent non-uniqueness problem of the frequency domain formulation at certain frequencies, the Burton-Miller formulation [147] and the combined Helmholtz integral equation formulation (CHIEF) [148] were proposed. To predict the extended reaction in a cavity containing sound absorbing materials, a multi-domain method, which enforces the continuity condition of the normal velocity and acoustic pressure at the interface, can be employed [149]. To overcome the difficulty of modeling thin objects for conventional BEM, indirect BEM using degenerate boundary formulation is introduced [150, 151].

Since only the boundaries need to be discretized in the form of unstructured elements, the number of degrees of freedom (DOFs) is significantly reduced compared to volumetric discretization methods discussed so far. In general, BEM is considered efficient for exterior problems involving sound radiation and scattering phenomena in homogeneous media [152]. However, the benefit of dimension reduction comes at a cost of solving dense discretization matrices, making it difficult to apply the BEM to large-scale problems. Remedies using the fast-multipole

methods [153, 154] are used to speed up the analysis of sound fields [155, 156, 157]. Applications of time-domain BEM to room acoustic analysis are presented in Refs. [158, 159].

### 1.2.3 Hybrid methods

Each of the above mentioned room acoustic modeling methods has its own merits and limitations. It can therefore be beneficial to adopt a hybrid methodology, thus exploiting the advantage of each contributing method and achieving a decent balance in terms of the accuracy, computational cost and applicable frequency range. There are various kinds of hybridizations. For example, hybrid GA models tend to utilize the image source method to simulate the early specular reflection paths and ray tracing or radiosity-based techniques for the late reverberation part of the impulse response [160].

Hybridizing of GA and wave-based methods can be a feasible solution to addressing the issue of the wide audible frequency range. Wave-based methods are used for the low frequencies, where the wavelengths are close to the characteristic dimensions of rooms (and objects) and wave phenomena dominate the acoustics, while GA methods are employed for high frequencies [161, 162, 163, 164, 165, 166, 167]. The crossover frequency is generally case-dependent based on acoustic characteristics of rooms. The Schroeder frequency [11], which approximately indicates the boundary between overlapping and distinguishable resonant room modes, is usually used as a rough estimate of the upper limit of the low-frequency range.

Hybrid methods that spatially couple different wave-based methods also exist, the fundamental principle behind which is the spatial domain decomposition. A popular strategy is to utilize more efficient methods to treat the interior domain with relatively simple geometries and large volumes, and to use more accurate but time-consuming methods near the boundaries. Examples include the hybrid of the ARD method with FDTD [117, 118], the hybrid of the PSTD method with FEM [168], and the hybrid of the FVM with FDTD [124, 126].

### 1.2.4 Summary and discussion

To the best of the author’s knowledge, the properties and capabilities of each wave-based method discussed so far is summarized in terms of entries listed in Table 1.1. The entry of “explicit semi-discrete form” is relevant for time-domain approaches, and the explicit formulation saves the trouble of using an iterative solver to solve large linear systems of

equations. It should be noted that some of the issues and restrictions could be addressed and overcome with on-going active research efforts. Nevertheless, this comparison does highlight the most obvious shortcomings of each method that need to be resolved for room acoustic modeling.

Table 1.1: A summary of generic properties of the state-of-the-art wave-based methods for room acoustic modeling. The numbers represent to what extent the properties are addressed in the respective method. 1 means it can be well handled; 2 indicates efforts are needed to resolve the issue; 3 implies even more efforts are needed.

	FDTD	Spectral M.	FVM	FEM	BEM
Geometric flexibility	3	3	1	1	2
High-order accuracy	1	1	3	1	1
Impedance boundary conditions	1	3	1	1	1
Explicit semi-discrete form	1	1	1	2	3
Parallel computing	1	1	1	2	2

Generally speaking, wave-based methods, which are built upon numerically solving the fundamental physical laws governing sound propagation, have relatively higher accuracy compared to geometrical room acoustic modeling techniques and energy-based methods for both the free propagation and the interaction with boundaries, especially in the low-frequency range. Furthermore, compared to other approaches, it is more natural and straightforward to integrate wave-based sound propagation modeling with other fields of modeling that are relevant to room acoustics. For example, direct modeling of (multiple) directional source by coupling sound emitting physical objects with the propagation media [169, 170, 171] can be realized more easily with wave-based methods. On this account, the framework of sound synthesis can be connected with room acoustic modeling. More than that, binaural sound localisation can be realized naturally by incorporating head and torso models into the simulated space [172, 173].

However, a general criticism of wave-based methods is that the computational cost can become prohibitive. As a general rule of thumb, state-of-the-art wave-based methods typically require spatial discretization resolution of 6 up to 10 PPW for the sake of the dispersion and dissipation error [174] arising from the numerical approximation. In 3D, the degrees of freedoms for volumetric discretization techniques scale with the maximum frequency of interest  $f_{max}$  as  $\mathcal{O}(f_{max}^3)$ . Therefore, it is generally acknowledged that acoustic simulations of large rooms at high frequencies remain a challenging issue for the foreseen future. However,

low- and mid-frequency calculations are becoming more and more feasible, and the upper limit of the applicable frequency range is expanded thanks to the ever-growing computing power with parallel architectures [87, 88, 89, 90].

### 1.3 Thesis objective and main contributions

This PhD project is motivated towards an efficient, robust and accurate wave-based room acoustic modeling technique. Following the discussions presented in the previous section and reflecting on the state-of-the-art numerical modeling techniques, the time-domain discontinuous Galerkin (DG) method is chosen as the focus of this thesis, since it possesses each of the attractive properties listed in Table 1.1. As will be discussed in Chapter 2, the DG method is a well-established numerical approximation technique for solving partial differential equations that govern various physical processes. However, its applications to room acoustic modeling was far less developed at the outset of this PhD project. Therefore, it is the goal of this work to develop the necessary formulations of the DG method for room acoustic modeling purposes, and to perform validations against analytical, numerical and measurement results.

The main contributions of this thesis are as follows:

- For room acoustic modeling purposes, the performance of the time-domain nodal DG method is evaluated. A comprehensive derivation of the nodal DG scheme for solving the linear acoustic equations is presented. A formulation of real-valued impedance boundary condition is proposed as a preliminary attempt to simulate the sound absorption phenomena along the boundaries. The semi-discrete stability of the scheme is analyzed using the energy method. Verifications are performed against analytical solutions, demonstrating the convergence of the scheme. As a collaborative work, simulation results for a real empty room are compared with measured results and a good match is observed in 1/3 octave bands.
- A high-order accurate and generic time-domain impedance boundary condition formulation for locally reacting materials is developed and validated, aiming at a further step towards a fully-fledged time-domain DG solver for realistic room acoustic simulations. The benefits of using a high-order basis in terms of cost-efficiency and memory-efficiency is demonstrated with numerical experiments. The applicability of the proposed formulation for modeling real-world

materials is demonstrated through an example of a rigidly-backed glass-wool baffle.

- Following the impedance boundary formulation, a formulation of broadband time-domain transmission boundary conditions for locally reacting surfaces is proposed and validated. A few examples of sound transmissive boundaries are presented to illustrate the applicability of the scheme to handle practical scenarios.
- A numerical scheme of arbitrary order of accuracy in both space and time, based on the arbitrary high-order derivatives (ADER) methodology, for linear acoustic wave propagation is developed and validated. The scheme combines the nodal DG method for the spatial discretization and Taylor series integrator for the time integration. A novel local time-stepping approach is proposed to increase the simulation efficiency for realistic problems containing geometric or parametric constraints without losing high-order accuracy.
- A preliminary application to the room acoustic simulations of a real open plan office in the low-frequency range is explored, with the purpose of assessing the accuracy and applicability of the developed time-domain nodal DG method for a realistic sound field analysis by comparing simulation results with the results from measurements.

## 1.4 Thesis structure and related publications

The thesis is mainly based on work presented in the appended Journal Papers. Each of the following chapter summarizes the main findings and contributions of each paper respectively. Additional comments are presented where necessary. The rest of the thesis is structured as follows.

- **Chapter 2** is mainly based on the appended **Paper I**.  
This chapter lays the foundation of this thesis, where the positioning of time-domain DG method as a wave-based method for room acoustic modeling purposes has been addressed. It introduces the main ingredients of the DG method and reviews its development in the general context of the computational physics community. Then, a brief overview of the content of **Paper I** follows.
- **Chapter 3** is mainly based on the appended **Paper II**.  
This chapter is devoted to the accurate modeling of sound reflection and absorption along locally reacting impedance boundaries within the time-domain DG framework. An introduction of acoustic

boundary conditions under the extendedly and locally reacting assumption is presented first, followed by the discussion on the porous sound absorber. A brief review of time-domain impedance boundary condition formulation is presented. Lastly, the main content of **Paper II** are summarized.

- **Chapter 4** is mainly based on the appended **Paper III**.  
This chapter presents a formulation of broadband time-domain transmission boundary conditions for locally reacting surfaces in the framework of the time-domain DG method. It begins with a short literature review on sound transmission modeling in the context of room acoustics. Then, a summary of the main contributions of **Paper III** is given. Additionally, the formulation of simulating an acoustic boundary modeled by a limp permeable membrane is presented.
- **Chapter 5** is mainly based on the appended **Paper IV**.  
This chapter aiming at accelerating realistic room acoustic simulations with the time-domain DG method. To achieve this goal, we first explore the challenges associated with time integration schemes and identify the need for a more efficient scheme, in the presence of geometric or parametric constraints that limit time step sizes. A short review of publications produced in this context is summarized. Then, the main contributions of **Paper IV** are presented.
- **Chapter 6** is mainly based on the appended **Paper V**.  
This chapter is related to validating the developed time-domain DG wave-based solver by means of a realistic case study. The simulation results are compared against measurements for a real open-plan office. As complements to the content of **Paper V**, a discussion on retrieving accurate acoustical boundary conditions from measured absorption coefficients data is introduced first, followed by more details on the mesh generation.
- **Chapter 7** contains concluding remarks and insights for future work.

---

## 2 | Room acoustic modeling with the time-domain nodal discontinuous Galerkin method

The purpose of this chapter is to introduce the time-domain discontinuous Galerkin (DG) method for room acoustics modeling purposes. It begins with a brief discussion and with the development of the DG method in the general context of the computational physics community. Then, a brief overview of the content of **Paper I** and a summary of its main contributions are presented.

### 2.1 A conceptual introduction of the DG method

The discontinuous Galerkin (DG) method, as a subtype of the finite element method (FEM), is based on locally piecewise polynomial approximations to represent the unknown solutions. It supports both structured and unstructured mesh elements of various shapes as the generic FEM. Different from the (classical) FEM that utilizes continuous basis functions, DG method uses basis functions that can be completely discontinuous across the interface of neighboring mesh elements to approximate the unknown variables, where duplicated solutions exist at all nodes, as shown in Fig. 2.1. As a result of this discontinuity, the weak formulation can be obtained by performing the Galerkin projection locally, *i.e.*, by setting the local residual of the approximated governing equation orthogonal to all test functions. Following the same idea as FVM, the divergence term inside the weak formulation is converted into a surface flux using Gauss' theorem. The surface flux, which is referred to as the numerical flux, is a single valued function that depends on the solution values at the element surfaces from both sides of the interface. The numerical flux serves not only to couple the elements, but also to enforce boundary conditions, which is also illustrated in Fig. 2.1.

The construction of local polynomial approximations and subsequent

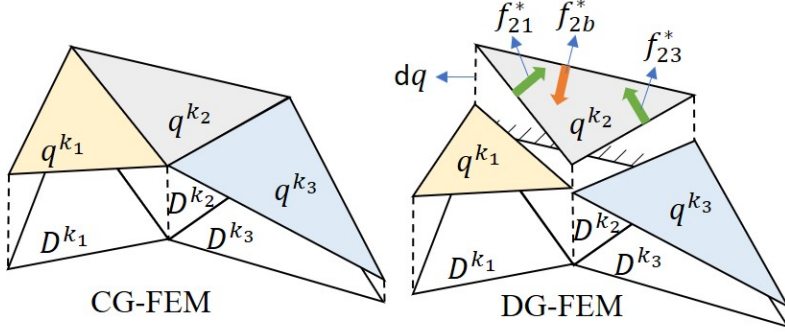


Figure 2.1: Illustration of the difference between the continuous Galerkin (CG) and the discontinuous Galerkin (DG) FEM in a 2D domain.  $D^k$  denotes the space elements and  $q^k$  is the corresponding local approximation. The height of the vertical dotted line denotes the solution values. For the DG-FEM, there are steps, denoted as  $dq$ , between the approximations of neighboring elements, which introduce the need for the numerical fluxes  $f^*$ , *e.g.*,  $f_{21}^*$  and  $f_{23}^*$  for the element  $D^{k_2}$ . The boundary conditions are imposed weakly through the numerical flux  $f_{2b}^*$  as well.

evaluations of volume and surface integrals can be conducted in various ways, which further classify different approaches, *e.g.*, the modal and nodal approaches. The calculation of the numerical flux, which is the only non-local operation involving different elements, involves only the solution nodes on the element surfaces, whereas the volume integration depends on all interior nodes inside the element.

Following the method of lines, the semi-discrete formulation obtained from the spatial discretization of the DG method can be marched in time with general ordinary differential equation (ODE) solvers, *e.g.*, the Runge-Kutta method [81]. It should be noted that the semi-discrete formulation can be easily rewritten in ODE form due to the fact that the spatial matrices can be easily inverted.

Similar to FVM, the DG method exhibits strong stability and robustness when dealing with sharp gradients or even jumps in material properties that are aligned with the mesh, making it suitable for numerically solving time-dependent hyperbolic PDEs, such as the linear acoustic equations under consideration here. However, the high-order representation of the solutions in each cell of FVM, which involves the polynomial reconstruction procedure using a large stencil of cells on general multi-dimensional unstructured grids, is not necessary for the DG method, since the solutions within each element are approximated locally using high-order polynomials. Therefore, the DG method may be considered as a favorable combination of FVM and FEM. Furthermore,

the DG method offers great flexibility in local mesh and order adaptivity. Because most operations are performed elementwise, it allows for easy parallelization with a significant acceleration potential [175, 176].

Historically, the DG method was firstly introduced in 1973 by Reed and Hill [177] in the framework of neutron transport problems and was later analyzed by Lesaint and Raviart [178]. The stability and error estimates for the DG method applied to a linear hyperbolic equation were first proved by Johnson and Pitkäranta [179] in 1986. Eigensolution analysis to the linear wave equations can be found in Refs. [180, 181, 182, 183]. Developments of the DG method for non-linear hyperbolic conservation laws were carried out by Cockburn *et al.* in a series of papers [184, 185, 186, 187]. In related work, Atkins and Shu [188] proposed a quadrature-free implementation that achieves a significant reduction in computational cost and storage requirements. Interested readers can refer to more extensive literature [189, 190, 191], which contains more detailed discussions and references concerning the development of DG in all aspects including algorithm design, implementations, analysis and applications.

The DG method has enjoyed substantial development in recent years in diverse fields such as electromagnetics [192, 193], seismology [194], poroelastic wave modeling [195], elastic-acoustic wave propagation [196, 197, 171], aeroacoustics [198, 199, 200, 201, 202], shallow water modeling [203], coastal ocean modeling [204], computational fluid dynamics [139]. However, it has never been used for room acoustic modeling by the time **Paper I** was published.

## 2.2 Overview of Paper I

**Paper I** aims to address the positioning of time-domain DG as a wave-based method for room acoustics. This paper begins with a brief review of the state-of-the-art room acoustic modeling techniques, highlighting the necessity of using wave-based methods for low-frequency problems. Then, general features of the DG method are introduced, demonstrating its strong potential for room acoustic problems. Meanwhile, developments needed to achieve a fully-fledged DG method for room acoustic modeling, such as a proper formulation of impedance boundary conditions, are identified.

The equations governing wave propagation in the context of room acoustics are the linear acoustic equations introduced in Eq. (1.1), which are derived from the general conservation laws [15]. To numerically solve

the governing equations, the nodal DG method is used for the evaluation of the spatial derivatives, and for the time-integration an explicit multi-stage Runge-Kutta method [200] is adopted. The main ingredients for the spatial discretization are adopted directly from the nodal formulation presented by Hesthaven and Warburton [190], including the construction of local approximations using a multi-dimensional Lagrange polynomial basis with an  $\alpha$ -optimized node distribution [205], and efficient calculations of mass, stiffness, and surface integral matrices. The derivation of the upwind numerical flux associated with the linear acoustic equations is presented, which completes the semi-discrete formulation for free-field propagation. To provide insight into the numerical dissipation and dispersion properties of the DG scheme, relevant literature is referred to and major findings are summarized.

To deal with sound absorption on the boundaries, a frequency-independent real-valued impedance boundary formulation is proposed, and is incorporated into the scheme via the upwind flux along the boundaries. The principle behind the formulation is that the characteristic waves [206, 207] of the linear acoustic equations, which appear in the definition of the upwind numerical flux and are thus evaluated nodally, act as plane waves locally along the normal direction to the boundary surfaces. Therefore, incoming (reflected) characteristic waves can be calculated as a product of the plane wave reflection coefficient and the outgoing (incident) characteristic waves. The semi-discrete stability of the spatial DG operator together with the proposed impedance boundary conditions is analyzed using the energy method. It is proven that the semi-discrete system resulting from the DG discretization is unconditionally stable for passive boundary conditions with a real-valued impedance. It is worth mentioning that the reflection coefficient also enables the use of all real-valued impedance boundary conditions regardless of the imposed impedance values, sparing the need for exceptional treatments even for singular cases such as an infinitely hard wall and soft wall. A discussion on the discrete stability of the scheme is presented and a criterion for choosing the time step is presented.

To evaluate the performance of the time-domain DG method for room acoustics problems, various 3D numerical tests are presented.

- The first test is a free field propagation of a single frequency plane wave with periodic boundary conditions. In this case, the dissipation errors and the dispersion errors are quantified with respect to

the number of PPW and the propagation distance.

- The second configuration is a sound source over an impedance plane. The convergence of the spherical wave reflection coefficient under two different angles of incidence is verified for frequency-independent impedance boundary conditions. It is also found that the accuracy is rather independent from the incidence angle.
- As a third scenario, a cuboid room with rigid boundaries is used, for which a long-time (10 seconds) simulation is run. By comparing the numerical results against the analytical solution, it can be concluded again that with increasing spatial resolution, the dispersion and dissipation errors become monotonously small, *i.e.*, convergence is achieved.
- Finally, the comparison in terms of the narrow and 1/3 octave bands sound pressure level between numerical and experimental solutions shows that DG is a suitable tool for acoustic predictions in rooms. Taking into account that only one uniform real-valued impedance has been used for the whole frequency range of interest, the comparison against the measurement is quite satisfactory. In this case, the incorporation of frequency dependent boundary conditions would definitely help to produce a better match with the real measurements. This topic will be addressed in the following chapter.



---

## 3 | Time-domain locally reacting impedance boundary conditions

While the fundamental recipe of the nodal DG method to solve the linear acoustic equations has been described, the efficacy of the introduced real-valued impedance boundary condition is quite limited in terms of bandwidth, since most of realistic materials absorb sound waves in a frequency-dependent way. The purpose of this chapter is to introduce the time-domain frequency-dependent impedance boundary condition formulation, which is an indispensable part of a fully-fledged room acoustic modeling solver. This chapter begins with a discussion and literature review of the extendedly and locally reacting assumption for impedance boundary modeling. Then, a brief overview that outlines the content of Paper **P2** and a summary of its main contributions are presented.

### 3.1 Extendedly and locally reacting sound absorption modeling

Sound absorption along surfaces of various objects inside a room has a major influence on the acoustics of the room. Therefore, accurate modeling of the behaviour of sound waves in the immediate vicinity of boundaries is of primary concern. In various room acoustic modeling techniques, the boundary conditions that represent the sound absorption properties of materials can be characterized in terms of either the acoustic surface impedance, the sound absorption coefficient or the plane-wave reflection coefficient. These quantities in general vary with the frequency and the angle of incidence. The absorption coefficient is usually used in geometrical acoustics models, while the acoustic surface impedance comes into play in wave-based methods (*e.g.*, FEM, BEM, FDTD, DG, *etc.*) through the imposition of boundary conditions.

Suppose the outward normal vector to the boundary surface is denoted

as  $\mathbf{n}$ . At a given angular frequency  $\omega$ , the normalized surface impedance  $Z_s$ , is defined as the ratio of the complex sound pressure  $P(\omega)$  and the particle velocity component normal to the surface  $V_n(\omega) = \mathbf{V}(\omega) \cdot \mathbf{n}$ , divided by the characteristic impedance of air, *i.e.*,

$$Z_s(\omega) = \frac{1}{\rho_0 c_0} \frac{P(\omega)}{V_n(\omega)}. \quad (3.1)$$

In the time domain, relation (3.1) can be expressed as:

$$p(t) = \rho_0 c_0 \int_{-\infty}^{\infty} z_s(t - \tau) v_n(\tau) d\tau, \quad (3.2)$$

where  $z_s(t)$  is the inverse Fourier transform of  $Z_s(\omega)$ , and the same holds for  $p(t)$  and  $v_n(t)$ .

The impedance model has to satisfy three necessary conditions in the frequency domain in order to be physically admissible, as proposed by Rienstra [208]:

- Causality condition: the present states must be time-updated based on the past and present states. In other words, the response of the system is supposed to be zero before it is simulated. Mathematically, it indicates that  $Z_s(\omega)$  is analytic and non-zero in  $\text{Im}(\omega) < 0$ ;
- Reality condition:  $p(t)$ ,  $v_n(t)$  and  $z(t)$  must be real-valued quantities. In other words,  $Z_s^*(\omega) = Z_s(-\omega)$ , where the superscript  $*$  denotes the complex conjugate;
- Passivity condition: the reflecting surfaces absorb energy rather than generate it. Consequently,  $\text{Re}(Z_s(\omega)) \geq 0$  must hold for all frequencies.

The physical admissibility of some popular semi-empirical impedance models are discussed in [209, 210].

The physics behind the reflection of sound waves is well described by Snell's law. However, the fact that surface impedance values vary with the incidence angle of the impinging sound wave, which is referred to as extendedly reacting behavior, poses great challenges to numerical modeling. To deal with this issue, a general approach based on a wave-splitting technique [211] was proposed to extract the incidence angle, which makes it feasible to adapt the impedance value to the incident acoustic field on the run [212]. However, this method can only detect

the incidence angle accurately on the condition that a sparse sound field is present, which is not typical for room acoustics. Another approach to cope with the extendedly reacting behavior is to couple the sound propagation between the boundary materials and the air, by explicitly solving the governing equations inside the materials. However, this coupling approach, which requires problem-dependent treatments, suffers from the extra computational cost of modeling the boundary materials.

### 3.1.1 Porous sound absorber

The porous material, which might exhibit a strong extended reaction, is the most widely used type of acoustic treatments in architectural design. Acoustic wave propagation inside porous materials with elastic solid frames is most systematically described by the Biot poroelastic theory [213, 214, 215, 216], which accounts for structure-born waves as well. However, the high complexity of the Biot model necessitates a number of material parameters that are difficult to measure, such as the frame shear modulus, thus limiting its practical applicability.

For cases where the frame is motionless or the structural waves are highly damped, simplified (semi-) empirical equivalent fluid models (EFM) prove to be realistically adequate for porous absorbers. In its most general formulation, EFM can involve up to six material parameters, *i.e.*, flow resistivity  $\sigma_0$  [ $\text{Pa}\cdot\text{s}\cdot\text{m}^{-2}$ ], material porosity  $\phi_0$ , material tortuosity  $\alpha_\infty$ , viscous characteristic length  $\Lambda$  [m], thermal characteristic length  $\Lambda'$  [m], static thermal permeability  $k'_0$  [ $\text{m}^2$ ]. Based on these parameters, the frequency-dependent complex quantities describing wave propagation inside the materials, *i.e.* the propagation constant and the characteristic impedance, or the effective density and the effective bulk modulus, can be obtained. Examples of well-known empirical EFMs are the Zwikker and Kosten model [217], Delany and Bazley model [218], and Miki model [219].

Sound propagation based on EFM has been studied quite extensively, including theoretical analysis [220, 221, 222, 223, 224], time-domain formulations [225, 226, 227, 228] and numerical modeling in the frequency domain using FEM [229, 133] and BEM [230]. The time-domain numerical modeling of acoustic wave propagation based on EFM have been performed in various wave-based frameworks, including the PSTD framework [231], the FDTD framework [232, 233] and the DG framework [234], to name a few recent developments.

It should be noted that other common materials used for room acoustic treatments also exhibit extendedly reacting behavior, such as thin

solid panels [235, 236], permeable membranes [237], suspended ceilings [238, 239], especially when they are backed by a large air cavity [240, 241].

### 3.1.2 Local reaction modeling

In the literature, most of the wave-based room acoustic modeling techniques employ the locally reacting assumption due to its simplicity. It indicates that responses (velocity, displacement, acceleration, *etc.*) at a certain point on the surface are related to the sound pressure and acoustic velocity of that specific point alone. In other words, the surface impedance is constant with respect to the incidence angle, and is set to be the same as for normal incidence [242]. The locally reacting assumption is appropriate for: (1) single layer isotropic porous absorptive materials with a high flow resistivity or large losses, especially when the speed of longitudinal waves in such materials is much lower than the speed of sound [240]; (2) anisotropic solids, such as plates with low stiffness, perforated structures or honeycomb core structures, where the lateral wave is rapidly attenuated or blocked.

Various formulations of locally reacting time-domain impedance boundary conditions (TDIBC) that have been developed in computational acoustics communities differ mainly in terms of the following three aspects:

- The acoustic quantities that characterize the acoustic properties of reflecting surfaces or materials. Besides the acoustic surface impedance, TDIBCs based on the acoustic admittance [243, 124, 125, 244] and the plane-wave reflection coefficient [245, 246, 247, 248, 249, 250] have been developed. Compared to others, the formulation using the plane-wave reflection coefficient has more ease dealing with (asymptotically) singular boundaries of both the hard-wall and pressure-release boundaries.
- The broadband approximations (including the parameter fitting approach) in the numerical impedance (admittance/reflection coefficient) models to the measurement data or specific (semi-) empirical impedance models in the frequency-domain. One early attempt to incorporate the frequency-dependency was to model the impedance boundary as a mass-damper-spring (MDS) system, which is analogous to the resistance-inductance-capacitance (RLC) system in an electrical circuit. Tam and Auriault [251] first used it for aeroacoustic applications and at the same time, Botteldooren [73] applied it

for FDTD room acoustic modeling. Other examples that use series of MDS can be found in Refs. [245, 246, 93, 124, 125, 97]. Later on, as a generalization of the MDS model, the multi-pole model, which approximates the frequency response of the impedance (admittance/reflection coefficient) using a sum of first order (real poles) and second order (complex conjugate poles) rational functions, gained popularity [252, 253, 254, 250, 255, 136], due to its extended range of representation of generic impedance models and more flexibility in the parameter fitting. Therefore, the multi-pole model is considered in this thesis.

- The time-domain implementations. The follow-up time-domain implementations, which are usually tailored to the specific spatial discretization method, are quite diverse. Here, it is not intended to present an exhaustive overview of all the developed TDIBCs, which are discussed more systematically in Ref. [256]. Among the approaches to the computation of the convolution integral of Eq. (3.2), the auxiliary differential equation (ADE) method [257, 258, 231, 136] is widely used because of its high-order accuracy and low-storage benefit.

## 3.2 Overview of Paper II

**Paper II** aims to develop a robust and efficient time-domain implementation of a generic broadband impedance boundary condition for locally reacting boundary materials, as a further step towards a time-domain DG solver for realistic room acoustic simulations. The formulation of the numerical flux along the impedance boundary is derived straightforwardly based on the plane wave reflection coefficient and the characteristic acoustic waves, and its detailed implementation in the DG method is presented. The extension of the previous frequency-independent impedance boundary formulation presented in **Paper I** to account for a frequency dependence is achieved through the multi-pole representation of the reflection coefficient in the frequency domain. Combined with the ADE method [258, 231], the whole computation can be performed in a low-storage and high-order accuracy manner.

The multi-pole model is essentially a linear summation of rational functions plus a constant term. Properties of rational functions are discussed, and requirements for the parameters to satisfy the above-mentioned physical admissibility conditions are presented. The fitting of the multi-pole model to a given empirical impedance model or measurement data is of concern from the following three aspects. Firstly,

computational costs associated with the boundary modeling alone are linearly proportional to the number of poles/rational functions resulting from the fitting procedure. Secondly, the maximum value of the parameters determines the stiffness of the auxiliary differential equations, which might affect the maximum allowable time step size of the explicit time-integration scheme. Last, the accuracy of the complex-valued fitting procedure has a direct impact on the accuracy of the boundary absorption modeling.

In this study, the optimization technique firstly presented by Cotté et al. [252] is chosen to fit the parameters in the multi-pole model for the following reasons. Firstly, the optimization technique is capable of ensuring causality and reality conditions by enforcing the positivity of the fitting parameters values. Secondly, the number of poles can be predefined and the maximum values of parameters can be confined such that the stiffness of auxiliary differential equations falls below the threshold as determined by the discrete stability condition. It should be noted that the fitting solution is not unique, and there exist other methods to fit the parameters such as the well-known vector fitting (VF) method with pole relocations [259, 260]. Both the optimization technique and the VF method are based on an iterative procedure and the resulting approximation depends heavily on the choice of the starting poles. In practice, some degree of expertise is needed to obtain an accurate fitting, especially when multiple local extrema of the reflection coefficients that correspond to resonances are present within the frequency range of interest. The optimization-based method is chosen because of its control over the range of the fitting parameters and the number of poles.

In **Paper II**, a typical room acoustic treatment using a glass-wool baffle mounted on a rigid backing is considered, the acoustic property of which can be represented by the Johnson-Champoux-Allard-Lafarge (JCAL) model [223, 224]. To validate this formulation, numerical simulations of a single reflection scenario are performed. Both the amplitude and the phase error from the reflection, which are important for room acoustics modeling featuring successive multiple reflections, are investigated and quantified for both the plane wave reflection in a 1D setting and the spherical wave reflection in 3D. The convergence rates of different spatial orders are verified. Cost-efficiency and memory-efficiency of high-order basis functions are demonstrated. To sum up, the proposed TDIBC formulation further strengthens the potential of the time-domain discontinuous Galerkin method as a wave-based method for room acoustics modeling.

---

## 4 | Time-domain locally reacting transmission boundary conditions

This chapter is based on **Paper III**, which presents a framework to model the sound transmission behavior across boundaries for room acoustic modeling purposes. Sound transmission is an acoustic phenomenon relating how a sound wave travels from one medium into another. As before, this chapter begins with a short literature review. Then, a summary of the main contributions of **Paper III** is presented. Last, the possibility of simulating a limp permeable membrane is discussed.

### 4.1 Sound transmission modeling

As reviewed in Sec. 3.1, many efforts in the field of room acoustic modeling have been devoted to model the reflection and absorption behavior of sound impinging on boundary materials, which are generally backed by acoustically rigid walls, by imposing an acoustic boundary condition. However, in certain practical scenarios with sound transmissive boundaries, *e.g.*, a suspended ceiling or a sound barrier made of permeable materials, the acoustics of the space hinges on not only the boundary material, but also the space or cavity behind, which boils down to an acoustic problem involving three propagation media.

There are mainly two types of approaches to simulate sound transmission phenomena. One type is to simulate the sound propagation inside the boundary material explicitly, such as in porous materials as previously discussed in Sec. 3.1.1, by coupling it with the neighboring propagation media. The other type of approaches is to formulate ad hoc internally locally reacting boundary conditions at both sides of the boundary materials that fit their acoustic properties.

For modeling permeable panels/plates, formulations of boundary conditions within the framework of FDTD can be found in Refs. [235, 236],

whereas the formulations using FEM are presented in Refs. [261, 262, 237]. Aiming for a more general formulation, Toyoda and Ishikawa [97] have proposed a locally reacting boundary condition within the FDTD framework using the mass-damper-spring (MDS) system inserted between propagation media to simulate the frequency-dependent absorption and transmission characteristics. The MDS boundary has in total seven parameters to fit the frequency characteristics of materials in terms of the impedance, including three masses, two damping and two spring constants. To the best of authors' knowledge, no formulation regarding the sound transmission boundary condition has been presented so far for the time-domain DG method in the context of room acoustics. Therefore, it would be desirable to develop a general acoustic boundary condition that could take both the sound reflection and transmission phenomena into account.

## 4.2 Overview of Paper III

The purpose of **Paper III** is to present a general formulation of the transmission boundary condition within the time-domain DG framework for locally reacting materials. Similar to the TDIBC presented in **Paper II**, the formulation is derived based on the plane wave theory. The plane wave reflection and transmission coefficients at normal incidence conforming to the frequency-dependent reflection and transmission characteristics of the considered materials are represented with the multi-pole model and then incorporated into the upwind numerical flux of DG. Following the same steps as for the impedance boundary condition, the fitting of parameters in this representation for a target transmission characteristic is achieved by the optimization technique and the time-domain implementations based on the auxiliary differential equations (ADE) method [258, 231] are presented. It should be noted that the formulation also applies to cases where the simulated boundary material has anisotropic physical attributes and consequent asymmetrical reflection and transmission properties, under the local reaction assumption.

As a demonstration of its applicability, three scenarios, *i.e.*, the limp wall, the MDS partition (*e.g.*, fiberglass) and the single layer of porous material based on the equivalent fluid model (EFM), are discussed and numerically tested. Numerical verifications of the proposed boundary formulation in 1D against analytical solutions are presented, and 2D verifications are performed against the frequency-domain FEM solver of COMSOL Multiphysics® [263]. A good match in terms of the magnitude and the phase of the reflected/transmitted sound pressure is observed.

### 4.3 Application to modeling limp permeable membranes

**Paper III** considers the sound transmission across three different boundary materials. The purpose of this section is to demonstrate that the transmission boundary formulation is also applicable to materials that can be categorized as a limp permeable membrane (LPM), *e.g.*, curtains made of woven fabric and suspended ceilings.

The acoustic properties of acoustic treatments made of LPM have been investigated by analytical approaches for a single-leaf structure [264, 265] and a double-leaf structure [266, 267, 268]. It is found that the acoustic characteristics of a LPM absorber are mainly governed by two properties, namely the inertia due to its mass and the flow resistance from its air permeability.

Suppose the surface mass density of the LPM is given by  $m$  ( $\text{kg}\cdot\text{m}^{-2}$ ). Then, from Newton's second law, the equation of motion for the LPM is

$$m \frac{\partial v_m}{\partial t} = p_a - p_b, \quad (4.1)$$

where  $v_m$  denotes the vibration velocity of the membrane,  $p_a$  and  $p_b$  denote the acoustic pressure on both sides of LPM, as illustrated in Fig. 4.1. When the membrane is not permeable, the local average of acoustic particle velocity on the membrane, denoted as  $v_f$ , is equal to  $v_m$  following the velocity continuity condition. The transfer impedance, also referred to as wall impedance or partition impedance, is defined as the ratio of the pressure difference on the two sides of the limp material and the acoustic particle velocity, and is identified as  $i\omega m$  according to Eq. (4.1).

For the case of a permeable membrane,  $v_f$  is not equal to  $v_m$  anymore since there is a net flow of air through the LPM. However, it is still reasonable to assume the local average velocities on both sides of the LPM are equal on the condition that the pore volume per unit surface area of LPM is substantially less than a quarter of a wavelength [242]. The effect of air permeability of materials is described by the flow resistance  $r_f$  [ $\text{Pa}\cdot\text{s}\cdot\text{m}^{-1}$ ] as

$$r_f = \frac{p_a - p_b}{v_f - v_m}, \quad (4.2)$$

which is usually assumed independent of frequency.  $r_f$  is linearly proportional to the thickness of the membrane and its value per unit thickness is the flow resistivity  $\sigma_0$ . By considering Eq. (4.1) and Eq. (4.2), the

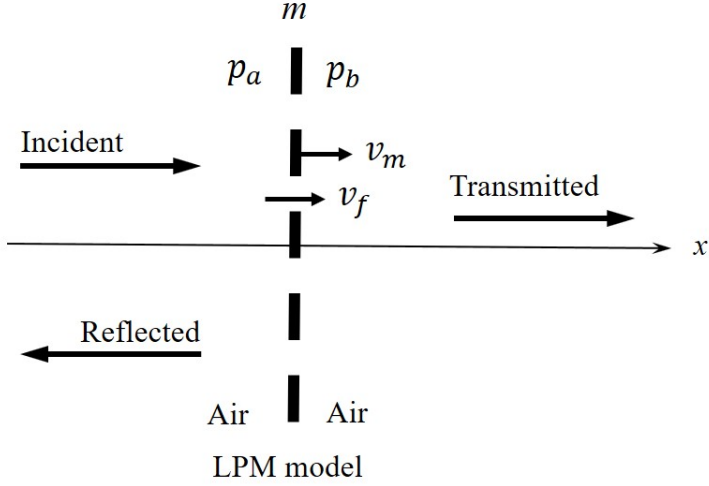


Figure 4.1: Schematic diagram of a LPM absorber under a normal incidence of a plane wave.

transfer impedance of a LPM is obtained as

$$Z_{LPM}(\omega) = \left( \frac{1}{r_f} + \frac{1}{i\omega m} \right)^{-1} \quad (4.3)$$

which is analogous to the electric impedance of two circuit elements in parallel, namely the inertia  $i\omega m$  and the flow resistance  $r_f$ . When the LPM is surrounded by air, its surface acoustic impedance is  $Z_{sur}(\omega) = Z_{LPM}(\omega) + Z_c$ , where  $Z_c = \rho_0 c_0$  is the characteristic impedance of air. Again, in terms of an electric-circuit analogy, the surface impedance consists of  $Z_{LPM}$  and  $Z_c$  in series.

With the surface impedance  $Z_{sur}(\omega)$ , both the reflection coefficient  $R(\omega)$  and the transmission coefficient  $T(\omega)$  can be derived in the follow-

ing multi-pole model form

$$\begin{aligned}
 R(\omega) &= \frac{Z_{sur}(\omega) - Z_c}{Z_{sur}(\omega) + Z_c} \\
 &= \frac{Z_{LPM}(\omega)}{Z_{LPM}(\omega) + 2Z_c} \\
 &= A_{LPM} - \frac{A_{LPM}\zeta}{i\omega + \zeta} \quad (4.4)
 \end{aligned}$$

$$\begin{aligned}
 T(\omega) &= 1 - R \\
 &= 1 - A_{LPM} + \frac{A_{LPM}\zeta}{i\omega + \zeta}, \quad (4.5)
 \end{aligned}$$

with a constant  $A_{LPM} = r_f/(r_f + 2Z_c)$  and a single real pole  $\zeta = 2r_fZ_c/(r_fm + 2Z_cm)$ . Fig. 4.2 shows an example of the magnitude and phase information of  $R(\omega)$  and  $T(\omega)$  for a LPM with  $r_f = 196 \text{ Pa}\cdot\text{s}\cdot\text{m}^{-1}$  and  $m = 0.065 \text{ kg}\cdot\text{m}^{-2}$ , which is representative of air-permeable thin (woven) fabrics [237].

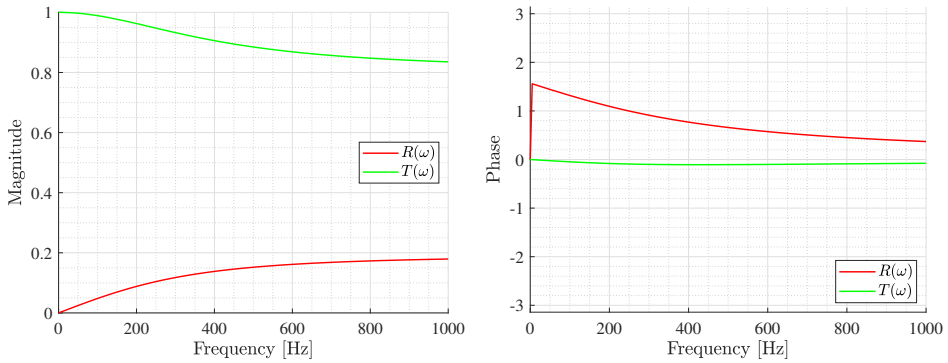


Figure 4.2: Example of the plane wave reflection coefficient  $R(\omega)$  and transmission coefficient  $T(\omega)$  of a LPM.

Since the numerical formulation of the transmission boundary condition has been verified, repetitive numerical verifications are not performed here. In the future, it would be interesting to apply this formulation to model the extended reaction inside the air cavity behind the LPM.



---

## 5 | ADER-DG with local time-stepping

The chapter is based on **Paper IV**, which presents an efficient numerical scheme of arbitrary order of accuracy in both space and time based on the arbitrary high-order derivatives (ADER) methodology, and a novel local time-stepping (LTS) strategy for transient acoustic simulations, including room acoustic modeling. In this chapter, we explore the challenges associated with time integration schemes that are combined with the DG method, with the aim of boosting simulation efficiency. This chapter begins with a short review of publications produced in this context. Then, a summary of the main contributions of **Paper IV** is presented.

### 5.1 Context

As mentioned in Sec. 2.1, following the method of lines, the semi-discrete formulation obtained from the spatial discretization of the DG method can be integrated in time with computationally efficient ODE solvers. Explicit low-storage Runge-Kutta methods [269, 270, 271, 200], which involve only a linear combination of the evaluations of the semi-discrete formulation, were used in **Paper I**, **Paper II** and **Paper III**, because they are easy to implement, and each unknown solution only needs one extra memory unit to store its intermediate stage values. Furthermore, their accuracy and stability properties [189, 272, 81, 273] have been well understood from the scientific computing community. However, the inefficiency issue due to a restrictive maximum allowable time step accompanying explicit time integration schemes, which is imposed by the well-known Courant-Friedrichs-Lewy (CFL) conditional stability condition, makes industrial applications of the wave-based solver infeasible for long-time simulations. In the context of room acoustic modeling, the uniformly defined time step might be mainly constrained by two factors. One is the geometric constraint resulting from some elements in the mesh that are considerably smaller than the rest. The other is the so-called

parametric constraint. For example, the wave speed inside the coupling medium (*e.g.* vibrating plate) might be larger than the speed of sound. Besides, as mentioned in Sec. 3.2, the pole values of the multi-pole model are another potential parametric constraint.

The existing methods devoted to addressing the issue of restrictive time step sizes can be generally classified into three kinds: implicit-explicit schemes [274, 275, 276], exponential-based time integrators [277, 278] and explicit LTS methods. LTS methods, also called multiple or multi-rate time-stepping, are preferred in practice due to their high compatibility with modern parallel computing techniques. The essential idea is to advance elements locally in time with their maximum allowable time steps. Various LTS methods have been developed in the scientific computing community targeting either general ODEs containing coupling components of various time scales [279, 280, 281] or specific spatially discretized governing equations of physical systems, *e.g.*, the shallow-water equations [203, 204], the linearized Euler equations [202], the second-order wave equation [282, 283, 284, 285, 286], the Maxwell equations [287, 288, 289, 290, 193], the linear elastic wave equations [291, 194, 292] and the non-linear conservation laws [293].

Among the above mentioned methods, the modal form of the ADER-DG method [291, 194] has exhibited strong potential for accelerating the solutions of linear first-order wave equations containing geometric or parametric constraints. However, it has the drawback that the high-order spatial derivatives of the polynomial basis are rather tedious to derive and to implement. The purpose of this study is to develop the nodal formulation of the ADER-DG method with LTS capability, in order to enhance the simulation efficiency of the wave-based solver for realistic problems containing geometric or parametric constraints without losing high-order accuracy.

## 5.2 Overview of Paper IV

**Paper IV** first present a nodal form of the ADER-DG approach with an arbitrary order of accuracy in time and space. Following the same methodology used in paper **P1**, the governing acoustic equations are first spatially discretized with the nodal DG method by projection onto the space-dependent polynomial basis functions, and the semi-discrete formulation in terms of time-dependent expansion coefficients are obtained. Then, these coefficients are integrated in time by the Taylor series integrator. The needed time derivatives are replaced with the numerically

approximated spatial derivatives by recursively using the semi-discrete formulation. The whole procedure can be seen as a discrete version of the conventional Cauchy-Kovalewski procedure [294] or the Lax–Wendroff scheme [295].

Secondly, this paper presents a novel LTS algorithm accompanying the ADER-DG scheme to overcome the inefficiency issue occurring in stiff systems. Without involving any overlapping subdomains or extrapolation of neighboring spatial points across the interface, the proposed coupling procedure between domains with different time steps maintains the same high-order accuracy as that of the usual global time-stepping scheme, and is valid for arbitrary ratios of time steps. The CFL stability condition is investigated numerically, with the aim of providing guidance on the choice of time step sizes in practical simulations. Numerical tests demonstrate that the LTS scheme maintains the same order of accuracy as that of the global time-stepping scheme, and the stability is ensured locally without a huge compromise on the time steps. An application to the sound propagation across a transmissive noise barrier exhibits the computational benefits of the proposed LTS strategy.



---

## 6 | Application study: wave-based simulations of an open plan office

This chapter is concerned with a preliminary application study of a real open plan office, as presented in the appended conference proceeding **Paper V**. The purpose of this work is to assess the accuracy and applicability of the developed wave-based time-domain DG method for realistic sound field analysis in the low-frequency range (up to 500 Hz octave band). The reference data to be compared against are measurement results, which were previously published in a study on how room acoustic parameters are affected by varying configurations of furniture and sound absorbing barriers [296]. In this chapter, the measurement setups are recapitulated first. Then, additional results on top of the content of **Paper V** are presented to give more details about the following topics: boundary characterization and mesh generation. Lastly, the comparison findings are summarized.

### 6.1 Reference measurements

As shown in Fig. 6.1, the open plan office under study has a long and narrow floor plan with windows along the walls. Small closed rooms indicated by the blue areas are present to subdivide the long space. The office has a volume of 962 m<sup>3</sup>. The 2.9 m tall sound absorbing suspended ceiling is made of 20 mm thick Rockfon panels with an air cavity of at least 200 mm. The floor is covered with a carpet. During the measurements, the room was completely empty except for the 5 workstation islands. Within each group of 4 workstations, two variations of the setup are considered:

- V1: only tables in the room,
- V2: tables with dividing panels and side panels.

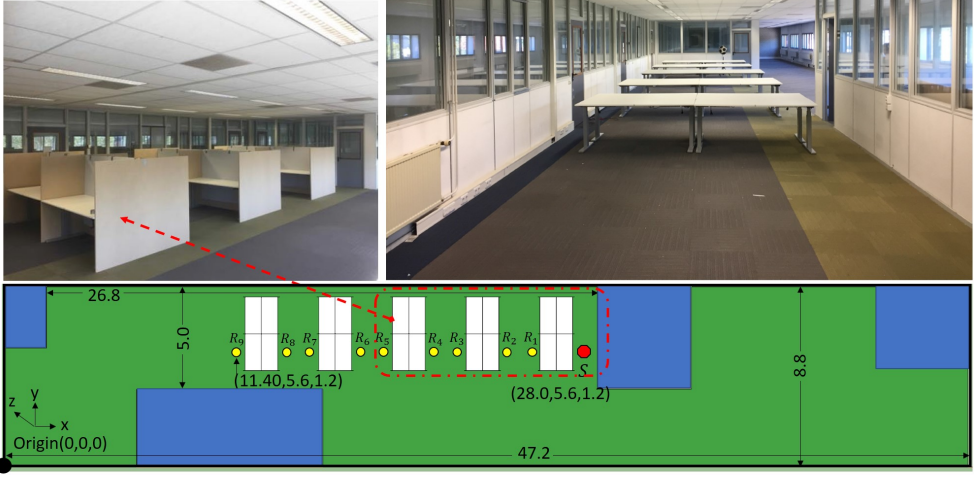


Figure 6.1: Picture of the measured open plan office and its floor plan in top view.

Dividing and side panels, which are made of 25 mm chipboard, stand on the floor and have a height of 1.5 m. To increase sound absorption, 30 mm thick melamine foam is applied to both sides of the upper 1.3 m part of the table dividing panels that are along the y-direction.

The source location and the 9 receiver locations are denoted by the red and yellow circles respectively, with the exact position of the source and of one receiver ( $R_9$ ) provided. The table depth for each sitting position is 0.8 m and the source and microphones are positioned 0.3 m away from the tables. More geometrical details can be found in Ref. [296]. The measurements have been performed following ISO 3382-3 [14]. An omnidirectional sound source (B&K 4292) and omnidirectional microphones were connected to a laptop with measurement software Dirac 6 (B&K 7841) via a triton USB device (AE) and an amplifier (B&K 2734).

## 6.2 Boundary characterization

Acoustic properties of the room surface materials in the considered office, which are represented with Sabine absorption coefficients, were measured in a reverberation chamber according to ISO 354, which *specifies a method of measuring the sound absorption coefficient of acoustical materials used as wall or ceiling treatments, or the equivalent sound absorption area of objects, such as furniture, persons or space absorbers, in a reverberation room* [297]. The Sabine absorption coefficient measured by the

reverberation chamber method is defined as follows:

$$\alpha_{Sab} = \frac{55.3V}{Sc_0} \left( \frac{1}{T_2} - \frac{1}{T_1} \right), \quad (6.1)$$

where  $V$  is the volume of the reverberation chamber,  $S$  is the area of the material sample,  $T_1$  is the reverberation time for an empty condition, and  $T_2$  is the reverberation time with the test sample.

However, it is debatable to directly use the Sabine absorption coefficients measured in a specific chamber as boundary conditions in room acoustic simulations for the following reasons. First of all, any reverberation chamber is non-diffuse in different ways, resulting in a poor reproducibility of the Sabine absorption coefficients from laboratory to laboratory [298, 299]. Moreover, test samples have finite sizes, which incurs a size effect due to the diffraction from edges of the test samples. As a consequence, overestimated measured absorption coefficients, which in some cases exceed unity, are observed. Other reasons include the finite volume of a reverberation chamber, the locations of the sample/source/microphones and the mounting methods [300].

In practice, the measured Sabine absorption coefficients should not be confused with the theoretical random incidence absorption coefficient, which is calculated using Paris' law [301]:

$$\alpha_{rand} = \int_0^{\pi/2} \alpha_{inf}(\theta) \sin(2\theta) d\theta, \quad (6.2)$$

where  $\alpha_{inf}(\theta)$  is the oblique incidence absorption coefficient for plane waves at an incidence angle  $\theta$  on an infinitely large surface. It is defined as

$$\alpha_{inf}(\theta) = \frac{4\text{Re}(Z_s(\theta)) \cos(\theta)}{(Z_s(\theta) \cos \theta)^2 + 2\text{Re}(Z_s(\theta)) \cos \theta + 1}, \quad (6.3)$$

with  $Z_s$  being the normalized surface impedance. The theoretical random incidence absorption coefficient is defined based on the assumption of a perfectly diffuse field, where the intensity of the incident sound is uniformly distributed over all possible directions and the phases of incident waves are randomly distributed. It has been found that using the theoretical random incidence absorption coefficient as boundary conditions for a phased beam tracing model achieves reasonably accurate results [302].

Large discrepancies between the measured Sabine absorption coefficients  $\alpha_{Sab}$  and the theoretical random incidence absorption coefficients

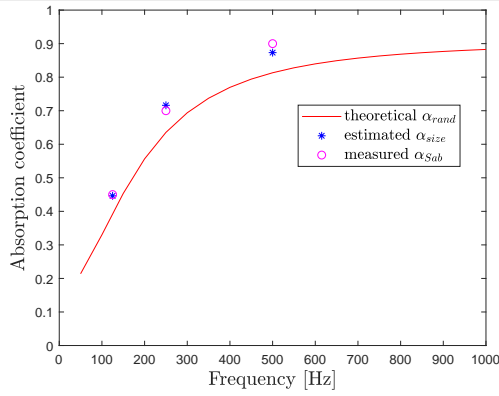
$\alpha_{rand}$  have already been reported in the literature. Corrections to the measured Sabine absorption coefficients are needed in order to provide reliable input data for room acoustic simulations. Thomasson [303] originally suggested corrections of measured absorption coefficients under the locally reacting assumption, with respect to the two main factors, *i.e.*, the non-uniform sound intensity distributions in terms of incidence angles and the size effect associated with the radiation impedance of a finite-sized absorber. To obtain correction (angular weighting) functions concerning the first factor, Jeong [304, 305] investigated sound intensity distributions on an absorber under measurement conditions using phased beam tracing simulations. It was found that the frequency-dependent sound intensity distributions on absorbers depend on the geometry and dimensions of reverberation chambers, the absorption capability of the test sample, and the placement of the test sample. Furthermore, at high frequencies above 1 kHz for all studied cases, intensity distributions exhibit similar patterns of downturn with respect to increasing incidence angles, and better agreements between measured and corrected absorption coefficients are observed when the angular weighting is incorporated. By contrast, at low frequencies, intensity distributions are rather uniform across the range of incidence angle.

Subsequent study [300] on converting  $\alpha_{Sab}$  to  $\alpha_{rand}$  based on Miki's model has emphasized the fact that the size correction should be taken into account for frequencies below 1 kHz [303], while the non-uniform intensity distributions are of primary importance at frequencies higher than 1 kHz. Therefore, given the low frequency range of interest in the current work, only the size correction is considered and the size corrected absorption coefficient is calculated as

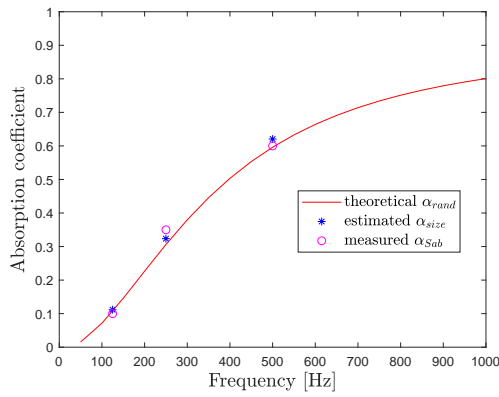
$$\alpha_{size}(\theta) = 8 \int_0^{\pi/2} \frac{\text{Re}(Z_s(\theta)) \sin \theta}{|Z_s(\theta) + \bar{Z}_r(\theta)|^2} d\theta. \quad (6.4)$$

$\bar{Z}_r$  is the averaged radiation impedance over azimuthal angles  $\phi$  expressed as  $\bar{Z}_r = \int_0^{2\pi} Z_r d\phi / 2\pi$ . For the case of an infinitely large plate, the radiation impedance is known to be a constant equal to  $1/\cos(\theta)$ , and the size corrected absorption coefficient Eq. (6.4) becomes equivalent to the oblique incidence absorption coefficient as in Eq. (6.3). The averaged radiation impedance of a finite absorber can be calculated with numerical integrations in an accurate way, based on tabulated values provided in Ref. [306, 300].

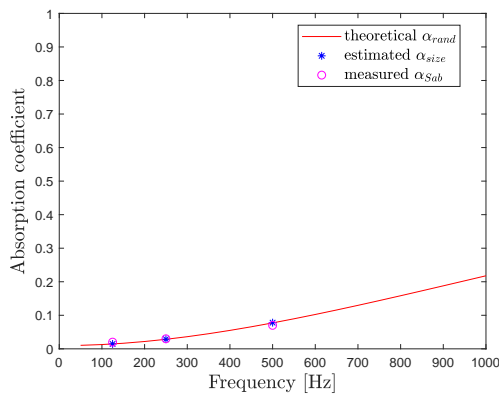
The assumptions and details of the parameter fitting needed for the



(a) ceiling



(b) foam



(c) carpet

Figure 6.2: Measured and estimated absorption coefficients.

TDIBC are presented in Sec. 3.3 of **Paper V**. It should be noted that the

strategies on converting absorption coefficients into surface impedances as proposed in Refs. [307] are considered but not followed exactly. In this work, the pressure reflection coefficient at normal incidence in the multi-pole form, which uniquely defines the surface impedance as in Eq. (6.4), is used directly in the optimization procedure of the parameter fitting, whereas Ref. [307] considers the surface impedance expressed in terms of fractional integrals and derivative. In addition to the measured Sabine absorption coefficients, Fig. 6.2 displays both the theoretical random incidence absorption coefficients and the size-corrected absorption coefficients that are based on the multi-pole approximation of the reflection coefficients; the size-corrected ones are used as input for the DG simulations.

Sound absorption measurement is an on-going research topic. Besides the reverberation chamber method, there are other options such as the impedance tube method [308, 309] and the *in situ* acoustic impedance measurement technique [310, 311, 312]. However, large discrepancies of measured absorption properties are observed with different measurement techniques [162]. Such uncertainties pertaining to the input parameters can have an influential impact on the correctness of room acoustic simulations [313, 160].

### 6.3 Mesh generation

One key step in a simulation with the time-domain DG method is the generation of an unstructured mesh. In this work, the tetrahedral meshes generated by the widely used open access meshing software Gmsh [314] is considered. Although Gmsh proposes several automatic meshing algorithms for 3D applications, the 3D Delaunay algorithm is the only one that supports generating conformal meshes with 2D infinitely thin surfaces embedded in a 3D volume. Therefore, it is used in this study in order to mesh these “floating” surfaces such as the tables and panels.

It is well known that the element size and the mesh quality have a pivotal influence on the maximum allowable time step size and the simulation accuracy. In Gmsh, mesh element sizes are usually prescribed by adjusting the so-called characteristic lengths (denoted as  $L_c$ ), which are more or less equal to the length of the element edges. There are varieties of measures proposed to characterize the size of an unstructured mesh to fulfill the CFL stability condition. Here, for tetrahedral elements, a typical size measure, which is the radius of the largest inscribed sphere  $r_{in}$  within each element, is used. As for the mesh quality (denoted as

$r_q$ ), various measures that characterize distortion of mesh elements have been tested in Ref. [315]. Based on the comparison, the triple of the ratio between  $r_{in}$  and the radius of the smallest circumscribed sphere  $r_{cir}$ , i.e.  $r_q = 3r_{in}/r_{cir}$ , is chosen as the mesh quality measure. As a reference, a regular tetrahedron has  $r_q = 1$  (optimal mesh quality), and a degenerate tetrahedron (zero volume) has  $r_q = 0$ .

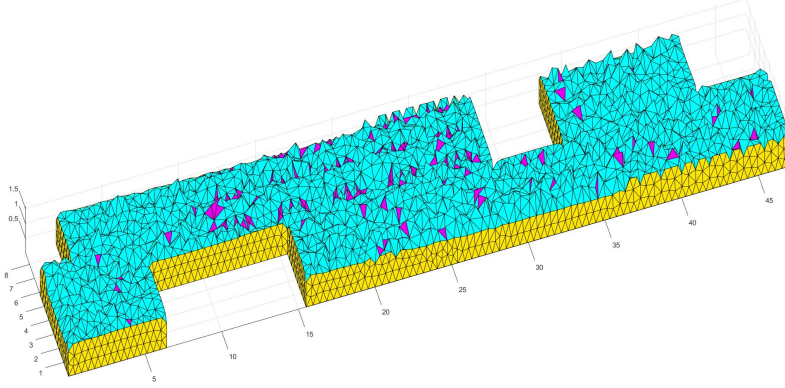


Figure 6.3: Interior view of the mesh around the height of the desks. Coarse and fine elements have cyan and purple face color respectively.

To gain insights into the effects of the characteristic length  $L_c$  on the mesh quality and the element sizes, meshes with five different  $L_c = [0.3, 0.35, 0.4, 0.45, 0.5]$  m values are generated for the two furniture setups. The distributions of the mesh quality measure  $r_q$  and the element size measure  $r_{in}$  are shown in Figure 6.4 and 6.5 for the V1 and V2 setups, respectively.  $K_{\#}$  denotes the total number of tetrahedral elements. It can be seen that decreasing the characteristic lengths of the mesh elements (increasing the number of elements) does not necessarily yield larger values of  $r_q$  (better mesh quality). For both setups, the meshes with  $L_c = 0.45$  m, which have an optimal balance between  $K_{\#}$  and  $r_{in}$ , are adopted in the simulations.

To accelerate the simulations, all elements are divided into two groups. All elements with  $r_{in} \leq 3 \min(r_{in})$  are marked as fine elements, and the rest are considered as coarse elements, as shown in Fig. 6.3. The local time-stepping scheme presented in **Paper IV** is used to integrate the fine and coarse elements in time with their corresponding time step sizes.

## 6.4 Summary of findings

This study first compares four room acoustic parameters in three octave bands defined in ISO 3382-1 [12], including reverberation time ( $T_{30}$ ),

early decay time ( $EDT$ ), clarity ( $C_{50}$ ) and center of gravity ( $T_S$ ). Then, the spatial decay rate of speech  $D_{2,S}$  (level reduction when doubling the distance) and A-weighted sound pressure level of speech at a distance of 4m from the sound source ( $L_{p,A,S,4m}$ ) as described in ISO 3382-3 [14] are investigated. It is found there are discrepancies between the simulation and measurement results for all considered parameters. The mismatch could result from three aspects, namely, the inherent uncertainties in the real measurements, imprecise input of acoustic boundary properties and the incapability of modeling extended reaction of boundaries.

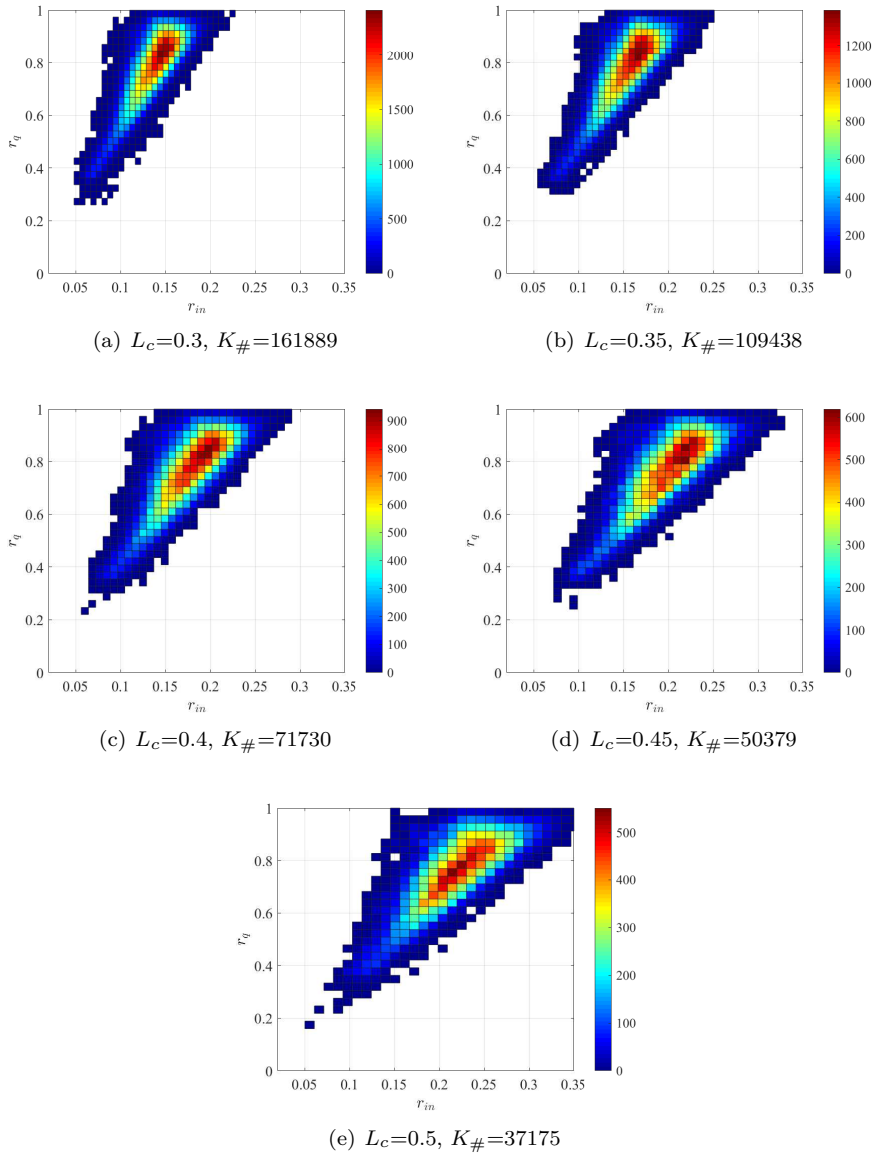


Figure 6.4: Distribution of the mesh quality measure  $r_q$  and the mesh size measure  $r_{in}$  for the V1 setup. The color indicates the number of elements in each bin.

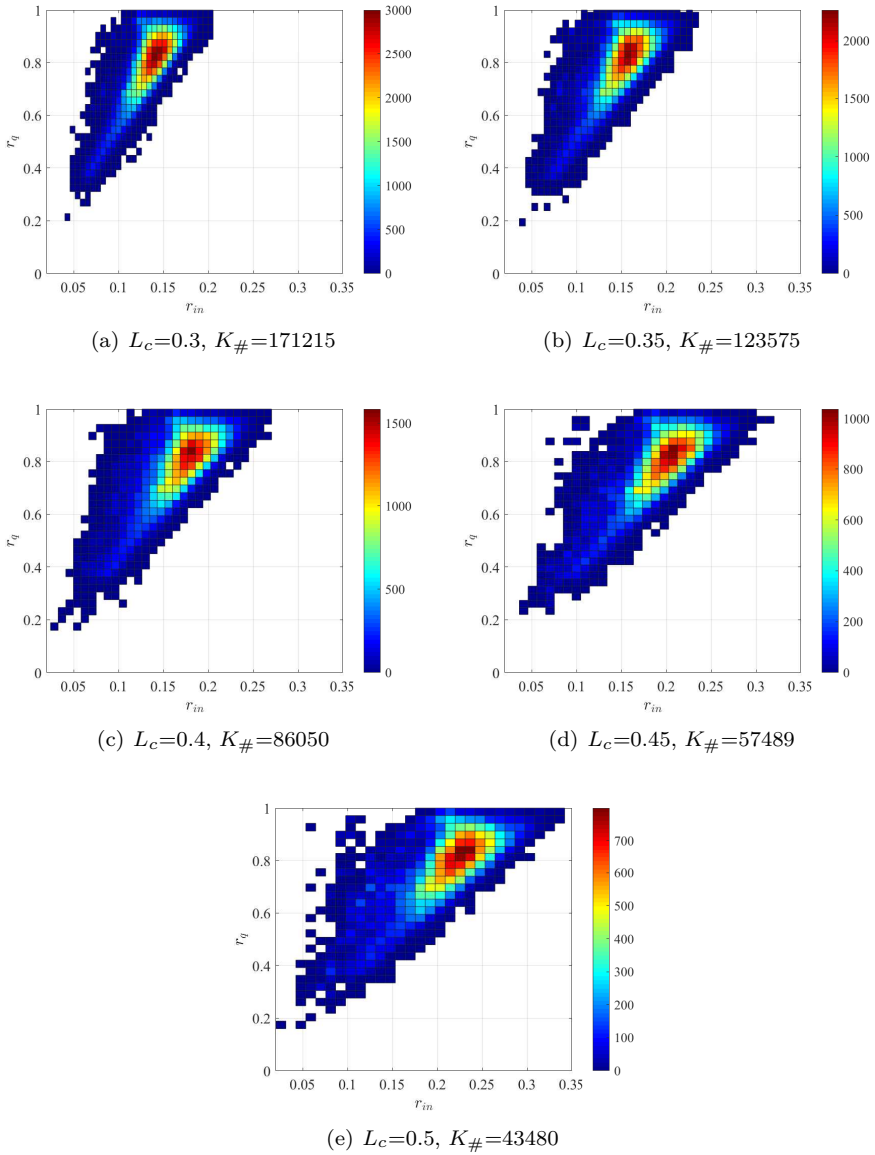


Figure 6.5: Distribution of the mesh quality measure  $r_q$  and the mesh size measure  $r_{in}$  for the V2 setup. The color indicates the number of elements in each bin.

---

## 7 | Conclusions and prospects

### 7.1 Concluding remarks

The past decades have witnessed fruitful advancements in room acoustic modeling techniques and ever expanding applications. This PhD project aims to further contribute to the room acoustic simulation community by developing an efficient, robust and accurate wave-based modeling technique. In Chapter 1, state-of-the-art room acoustic modeling techniques are reviewed, pros and cons of each numerical methodology are discussed. As a well-established numerical approximation technique, the discontinuous Galerkin method combines favorable properties of high-order accuracy, geometric flexibility, and potential for massive parallel computing. It is the goal of this work to develop and validate the necessary formulations of the time-domain discontinuous Galerkin method for room acoustic modeling purposes.

Chapter 2 (**Paper I**) addresses the positioning of time-domain DG method as a wave-based for room acoustic modeling purposes. Numerical verifications demonstrate its appealing properties such as high-order accuracy, long-time simulation stability and capability of handling complex-shaped rooms.

Chapter 3 (**Paper II**) and Chapter 4 (**Paper III**) present the time-domain boundary formulations that simulate the local reaction of sound reflection and sound transmission, respectively. Albeit fundamentally imprecise, locally reacting assumptions have prevailed in the room acoustic modeling community due to their simplicity and ease of implementation. For boundary materials that do not exhibit significant discrepancies between extended and local reactions, the proposed time-domain boundary condition formulations are efficient and general.

Chapter 5 (**Paper IV**) focuses on improving simulation efficiency for realistic problems that contain geometric and parametric constraints,

which can compromise stability in the case of explicit time integration. It has been demonstrated that the proposed local time-stepping approach maintains the original high-order precision of the scheme.

Finally, Chapter 6 (**Paper V**) applies the developed time-domain DG method to the room acoustic modeling of a real open office. Measurement results serve as the reference solution. In order to further reduce the computational cost, only the low-to-middle frequency range (125 Hz to 500 Hz octave bands) is considered. The available information on the acoustic properties of the materials in the room are in the form of Sabine absorption coefficients measured in full octave bands. Therefore, the required impedance values for the boundary modeling are retrieved by solving a constrained optimization problem. During this process, the acoustic properties of the materials are respected. However, partly due to the lack of high-resolution and to the inaccuracy of the sound absorption characterization, large discrepancies in terms of the considered room acoustic parameters between the simulation and measurement results are observed. The lack of extended reaction in the simulations also contributes to the deviation with the measurements

## 7.2 Future work

The work presented in this thesis highlights the strong potential of the time-domain DG method for room acoustic modeling applications. However, there are still some challenging issues to be tackled and interesting topics worth investigating in the future, which include:

- Further developments of time-domain boundary conditions for simulating extendedly-reacting behavior are needed to further extend the applicability of the time-domain DG method to more practical problems. A general formulation may be difficult to achieve, but *ad hoc* formulations for certain realistic examples, such as porous sound absorbers backed by an air cavity and permeable vibrating thin panels, could yield more accurate results.
- A quantitative accuracy analysis of the time-domain DG method for the determination of room acoustics parameters, such the reverberation time and clarity, is still missing. As is common with time-domain methods, both dissipation and dispersion errors increase gradually with the simulation duration. Therefore, a rigorous error analysis is needed, in order to provide a more detailed guideline on the efficient combination of meshing resolution, polynomial order

and time step sizes, that guarantees room acoustics parameters in accordance with the just noticeable differences.

- The sound sources in this work are omni-directional. To be able to simulate more realistic sound sources, sound source directivity [316, 86, 317] can be incorporated into the current time-domain DG framework.
- Only specular reflection is considered in the current model, which works well for the low frequency range. However, as the simulation moves towards higher frequency ranges, surface roughness and air absorption comes into play. It is necessary to develop a computationally efficient model that takes those effects into account.
- Advancements in terms of computational performance are needed at the implementation level. It would be beneficial to incorporate the present developments into an existing open source toolkit [176, 318, 319] that involves outstanding parallelization executed on Graphics Processing Units.
- Further comparisons with regards to measurements with increasing levels of complexity should be performed in order to appraise the effects of input data, particularly boundary properties, on the overall accuracy.



---

## Bibliography

- [1] T. Lokki, “Tasting music like wine: Sensory evaluation of concert halls,” *Physics Today*, vol. 67, no. 1, p. 27, 2014.
- [2] G. Tiesler, R. Machner, and H. Brokmann, “Classroom acoustics and impact on health and social behaviour,” *Energy Procedia*, vol. 78, pp. 3108–3113, 2015.
- [3] K. Persson Waye, E. Ryherd, B. Lindahl, and I. Bergbom, “Relating the hospital sound environment to occupant psychological and physiological response,” *The Journal of the Acoustical Society of America*, vol. 123, no. 5, pp. 3193–3193, 2008.
- [4] M. Basner, W. Babisch, A. Davis, M. Brink, C. Clark, S. Janssen, and S. Stansfeld, “Auditory and non-auditory effects of noise on health,” *The lancet*, vol. 383, no. 9925, pp. 1325–1332, 2014.
- [5] A. Haapakangas, V. Hongisto, J. Hyönä, J. Kokko, and J. Keränen, “Effects of unattended speech on performance and subjective distraction: The role of acoustic design in open-plan offices,” *Applied Acoustics*, vol. 86, pp. 1–16, 2014.
- [6] L. Brocolini, E. Parizet, and P. Chevret, “Effect of masking noise on cognitive performance and annoyance in open plan offices,” *Applied Acoustics*, vol. 114, pp. 44–55, 2016.
- [7] V. Hongisto, J. Varjo, H. Leppämäki, D. Oliva, and J. Hyönä, “Work performance in private office rooms: The effects of sound insulation and sound masking,” *Building and Environment*, vol. 104, pp. 263–274, 2016.
- [8] J. Reinten, P. E. Braat-Eggen, M. Hornikx, H. S. Kort, and A. Kohlrausch, “The indoor sound environment and human task performance: A literature review on the role of room acoustics,” *Building and Environment*, vol. 123, pp. 315–332, 2017.

- 
- [9] E. Braat-Eggen, M. K. vd Poll, M. Hornikx, and A. Kohlrausch, "Auditory distraction in open-plan study environments: Effects of background speech and reverberation time on a collaboration task," *Applied Acoustics*, vol. 154, pp. 148–160, 2019.
  - [10] E. Braat-Eggen, J. Reinten, M. Hornikx, and A. Kohlrausch, "The influence of background speech on a writing task in an open-plan study environment," *Building and Environment*, vol. 169, p. 106586, 2020.
  - [11] H. Kuttruff, *Room acoustics*. New York: CRC Press, 2019.
  - [12] ISO 3382-1, "Acoustics - Measurement of room acoustic parameters - Part 1: Performance spaces," standard, International Organization for Standardization, Geneva, CH, Mar. 2015.
  - [13] ISO 3382-2, "Acoustics - Measurement of room acoustic parameters - Part 2: Reverberation time in ordinary rooms," standard, International Organization for Standardization, Geneva, CH, Mar. 2016.
  - [14] ISO 3382-3, "Acoustics - Measurement of room acoustic parameters - Part 3: Open plan offices," standard, International Organization for Standardization, Geneva, CH, 2017.
  - [15] V. E. Ostashev, D. K. Wilson, L. Liu, D. F. Aldridge, N. P. Symons, and D. Marlin, "Equations for finite-difference, time-domain simulation of sound propagation in moving inhomogeneous media and numerical implementation," *The Journal of the Acoustical Society of America*, vol. 117, no. 2, pp. 503–517, 2005.
  - [16] W. M. Hartmann, "Localization of sound in rooms," *The Journal of the Acoustical Society of America*, vol. 74, no. 5, pp. 1380–1391, 1983.
  - [17] M. R. Schroeder, "New method of measuring reverberation time," *The Journal of the Acoustical Society of America*, vol. 37, no. 6, pp. 1187–1188, 1965.
  - [18] D. Howard and J. Angus, *Acoustics and psychoacoustics*. New York: Taylor & Francis Group, 2009.
  - [19] S. Pelzer, L. Aspöck, D. Schröder, and M. Vorländer, "Integrating real-time room acoustics simulation into a CAD modeling software to enhance the architectural design process," *Buildings*, vol. 4, no. 2, pp. 113–138, 2014.
-

- 
- [20] T. Sakuma, S. Sakamoto, and T. Otsuru, *Computational simulation in architectural and environmental acoustics*. Springer, 2014.
- [21] N. Moustakas, A. Floros, and N. Kanellopoulos, “Eidola: An interactive augmented reality audio-game prototype,” in *Audio Engineering Society Convention 127*, Audio Engineering Society, 2009.
- [22] V. Valimaki, J. D. Parker, L. Savioja, J. O. Smith, and J. S. Abel, “Fifty years of artificial reverberation,” *IEEE Transactions on Audio, Speech, and Language Processing*, vol. 20, no. 5, pp. 1421–1448, 2012.
- [23] M. Kleiner, B.-I. Dalenbäck, and P. Svensson, “Auralization-an overview,” *Journal of the Audio Engineering Society*, vol. 41, no. 11, pp. 861–875, 1993.
- [24] M. Vorländer, *Auralization: fundamentals of acoustics, modelling, simulation, algorithms and acoustic virtual reality*. Springer Science & Business Media, 2007.
- [25] L. Savioja, J. Huopaniemi, T. Lokki, and R. Väänänen, “Creating interactive virtual acoustic environments,” *Journal of the Audio Engineering Society*, vol. 47, no. 9, pp. 675–705, 1999.
- [26] R. Mehra, A. Rungta, A. Golas, M. Lin, and D. Manocha, “Wave: Interactive wave-based sound propagation for virtual environments,” *IEEE transactions on visualization and computer graphics*, vol. 21, no. 4, pp. 434–442, 2015.
- [27] M. Vorländer, D. Schröder, S. Pelzer, and F. Wefers, “Virtual reality for architectural acoustics,” *Journal of Building Performance Simulation*, vol. 8, no. 1, pp. 15–25, 2015.
- [28] H. S. Llopis, F. Pind, and C.-H. Jeong, “Development of an auditory virtual reality system based on pre-computed B-format impulse responses for building design evaluation,” *Building and Environment*, vol. 169, p. 106553, 2020.
- [29] K. Allain, B. Dado, M. Van Gelderen, O. Hokke, M. Oliveira, R. Bidarra, N. D. Gaubitch, R. C. Hendriks, and B. Kybartas, “An audio game for training navigation skills of blind children,” in *2015 IEEE 2nd VR workshop on sonic interactions for virtual environments (SIVE)*, pp. 1–4, IEEE, 2015.
-

- 
- [30] M. R. Schroeder, “Novel uses of digital computers in room acoustics,” *The Journal of the Acoustical Society of America*, vol. 33, p. 1669, nov 1961.
- [31] J. Picaut, L. Simon, and J.-D. Polack, “A mathematical model of diffuse sound field based on a diffusion equation,” *ACTA Acustica united with Acustica*, vol. 83, no. 4, pp. 614–621, 1997.
- [32] V. Valeau, J. Picaut, and M. Hodgson, “On the use of a diffusion equation for room-acoustic prediction,” *The Journal of the Acoustical Society of America*, vol. 119, pp. 1504–1513, mar 2006.
- [33] J. M. Navarro, J. Escolano, and J. J. López, “Implementation and evaluation of a diffusion equation model based on finite difference schemes for sound field prediction in rooms,” *Applied Acoustics*, vol. 73, pp. 659–665, jun 2012.
- [34] Y. Jing and N. Xiang, “A modified diffusion equation for room-acoustic prediction,” *The Journal of the Acoustical Society of America*, vol. 121, no. 6, pp. 3284–3287, 2007.
- [35] M. J. Bianco, P. Gerstoft, J. Traer, E. Ozanich, M. A. Roch, S. Gannot, and C.-A. Deledalle, “Machine learning in acoustics: Theory and applications,” *The Journal of the Acoustical Society of America*, vol. 146, no. 5, pp. 3590–3628, 2019.
- [36] B. Moseley, T. Nissen-Meyer, and A. Markham, “Deep learning for fast simulation of seismic waves in complex media,” *Solid Earth*, vol. 11, no. 4, pp. 1527–1549, 2020.
- [37] R. A. Tenenbaum, F. O. Taminato, and V. S. Melo, “Fast auralization using radial basis functions type of artificial neural network techniques,” *Applied Acoustics*, vol. 157, p. 106993, 2020.
- [38] Z. Fan, V. Vineet, H. Gamper, and N. Raghuvanshi, “Fast acoustic scattering using convolutional neural networks,” in *ICASSP 2020-2020 IEEE International Conference on Acoustics, Speech and Signal Processing (ICASSP)*, pp. 171–175, IEEE, 2020.
- [39] V. Pulkki and U. P. Svensson, “Machine-learning-based estimation and rendering of scattering in virtual reality,” *The Journal of the Acoustical Society of America*, vol. 145, no. 4, pp. 2664–2676, 2019.
- [40] A. Mendible, S. L. Brunton, A. Y. Aravkin, W. Lowrie, and J. N. Kutz, “Dimensionality reduction and reduced-order modeling for
-

- 
- traveling wave physics,” *Theoretical and Computational Fluid Dynamics*, vol. 34, no. 4, pp. 385–400, 2020.
- [41] L. Savioja and U. P. Svensson, “Overview of geometrical room acoustic modeling techniques,” *The Journal of the Acoustical Society of America*, vol. 138, pp. 708–730, aug 2015.
- [42] C. F. Eyring, “Reverberation time in “dead” rooms,” *The Journal of the Acoustical Society of America*, vol. 1, no. 2A, pp. 217–241, 1930.
- [43] B. M. Gibbs and D. Jones, “A simple image method for calculating the distribution of sound pressure levels within an enclosure,” *Acta Acustica united with Acustica*, vol. 26, no. 1, pp. 24–32, 1972.
- [44] J. B. Allen and D. A. Berkley, “Image method for efficiently simulating small-room acoustics,” *The Journal of the Acoustical Society of America*, vol. 65, no. 4, pp. 943–950, 1979.
- [45] J. Borish, “Extension of the image model to arbitrary polyhedra,” *The Journal of the Acoustical Society of America*, vol. 75, no. 6, pp. 1827–1836, 1984.
- [46] A. Krokstad, S. Strøm, and S. Sørsdal, “Calculating the acoustical room response by the use of a ray tracing technique,” *Journal of Sound and Vibration*, vol. 8, no. 1, pp. 118–125, 1968.
- [47] A. Kulowski, “Algorithmic representation of the ray tracing technique,” *Applied Acoustics*, vol. 18, no. 6, pp. 449–469, 1985.
- [48] H. Lehnert, “Systematic errors of the ray-tracing algorithm,” *Applied Acoustics*, vol. 38, no. 2-4, pp. 207–221, 1993.
- [49] T. J. Cox, B.-I. Dalenback, P. D’Antonio, J.-J. Embrechts, J. Y. Jeon, E. Mommertz, and M. Vorländer, “A tutorial on scattering and diffusion coefficients for room acoustic surfaces,” *Acta Acustica united with ACUSTICA*, vol. 92, no. 1, pp. 1–15, 2006.
- [50] I. Bork, “Report on the 3rd round robin on room acoustical computer simulation—part i: Measurements,” *Acta Acustica united with Acustica*, vol. 91, no. 4, pp. 740–752, 2005.
- [51] I. Bork, “Report on the 3rd round robin on room acoustical computer simulation—part ii: Calculations,” *Acta Acustica united with Acustica*, vol. 91, no. 4, pp. 753–763, 2005.
-

- 
- [52] F. Brinkmann, L. Aspöck, D. Ackermann, S. Lepa, M. Vorländer, and S. Weinzierl, “A round robin on room acoustical simulation and auralization,” *The Journal of the Acoustical Society of America*, vol. 145, no. 4, pp. 2746–2760, 2019.
- [53] M. Hodgson, “Evidence of diffuse surface reflections in rooms,” *The Journal of the Acoustical Society of America*, vol. 89, no. 2, pp. 765–771, 1991.
- [54] M. Vorländer and E. Mommertz, “Definition and measurement of random-incidence scattering coefficients,” *Applied acoustics*, vol. 60, no. 2, pp. 187–199, 2000.
- [55] G. Marbjerg, J. Brunskog, C.-H. Jeong, and E. Nilsson, “Development and validation of a combined phased acoustical radiosity and image source model for predicting sound fields in rooms,” *The Journal of the Acoustical Society of America*, vol. 138, no. 3, pp. 1457–1468, 2015.
- [56] C.-H. Jeong, J.-G. Ih, and J. H. Rindel, “An approximate treatment of reflection coefficient in the phased beam tracing method for the simulation of enclosed sound fields at medium frequencies,” *Applied Acoustics*, vol. 69, no. 7, pp. 601–613, 2008.
- [57] L. Antani, A. Chandak, M. Taylor, and D. Manocha, “Efficient finite-edge diffraction using conservative from-region visibility,” *Applied Acoustics*, vol. 73, no. 3, pp. 218–233, 2012.
- [58] P. T. Calamia, *Advances in edge-diffraction modeling for virtual-acoustic simulations*. Ph.D. dissertation, The University of Edinburgh, 2009.
- [59] R. R. Torres, U. P. Svensson, and M. Kleiner, “Computation of edge diffraction for more accurate room acoustics auralization,” *The Journal of the Acoustical Society of America*, vol. 109, no. 2, pp. 600–610, 2001.
- [60] G. M. Naylor, “ODEON—Another hybrid room acoustical model,” *Applied Acoustics*, vol. 38, no. 2-4, pp. 131–143, 1993.
- [61] B.-I. Dalenbäck, *A new model for room acoustic prediction and auralization*. PhD thesis, Chalmers University of Technology, 1995.
- [62] W. Ahnert and R. Feistel, “EARS auralization software,” *Journal of the Audio Engineering Society*, vol. 41, no. 11, pp. 894–904, 1993.
-

- 
- [63] K. Yee, "Numerical solution of initial boundary value problems involving maxwell's equations in isotropic media," *IEEE Transactions on antennas and propagation*, vol. 14, no. 3, pp. 302–307, 1966.
  - [64] K. S. Kunz and R. J. Luebbers, *The finite difference time domain method for electromagnetics*. CRC press, 1993.
  - [65] R. Alford, K. Kelly, and D. M. Boore, "Accuracy of finite-difference modeling of the acoustic wave equation," *Geophysics*, vol. 39, no. 6, pp. 834–842, 1974.
  - [66] S. K. Lele, "Compact finite difference schemes with spectral-like resolution," *Journal of Computational Physics*, vol. 103, no. 1, pp. 16–42, 1992.
  - [67] C. K. Tam, "Computational aeroacoustics-issues and methods," *AIAA journal*, vol. 33, no. 10, pp. 1788–1796, 1995.
  - [68] D. W. Zingg, "Comparison of high-accuracy finite-difference methods for linear wave propagation," *SIAM Journal on Scientific Computing*, vol. 22, no. 2, pp. 476–502, 2000.
  - [69] V. Thomée, "From finite differences to finite elements: A short history of numerical analysis of partial differential equations," *Journal of Computational and Applied Mathematics*, vol. 128, no. 1, pp. 1 – 54, 2001. Numerical Analysis 2000. Vol. VII: Partial Differential Equations.
  - [70] O. Chiba, "Analysis of sound field in three-dimensional space by the time-dependent finite-difference method based on the leap-frog algorithm," *JJAP*, vol. 49, pp. 551–562, 1993.
  - [71] L. Savioja, T. Rinne, and T. Takala, "Simulation of Room Acoustics with a 3-D Finite Difference Mesh," in *Proc. Int. Comp. Music Conf. (ICMC)*, pp. 463–466, 1994.
  - [72] D. Botteldooren, "Acoustical finite-difference time-domain simulation in a quasi-cartesian grid," *The Journal of the Acoustical Society of America*, vol. 95, no. 5, pp. 2313–2319, 1994.
  - [73] D. Botteldooren, "Finite-difference time-domain simulation of low-frequency room acoustic problems," *The Journal of the Acoustical Society of America*, vol. 98, no. 6, pp. 3302–3308, 1995.
-

- 
- [74] C. K. Tam and J. C. Webb, "Dispersion-relation-preserving finite difference schemes for computational acoustics," *Journal of Computational Physics*, vol. 107, no. 2, pp. 262–281, 1993.
- [75] S. Sakamoto, "Phase-error analysis of high-order finite difference time domain scheme and its influence on calculation results of impulse response in closed sound field," *Acoustical science and technology*, vol. 28, no. 5, pp. 295–309, 2007.
- [76] S. Sakamoto, H. Nagatomo, A. Ushiyama, and H. Tachibana, "Calculation of impulse responses and acoustic parameters in a hall by the finite-difference time-domain method," *Acoustical science and technology*, vol. 29, no. 4, pp. 256–265, 2008.
- [77] K. Kowalczyk and M. Van Walstijn, "Room acoustics simulation using 3-D compact explicit FDTD schemes," *IEEE Transactions on Audio, Speech, and Language Processing*, vol. 19, no. 1, pp. 34–46, 2010.
- [78] S. Bilbao and B. Hamilton, "Higher-order accurate two-step finite difference schemes for the many-dimensional wave equation," *Journal of Computational Physics*, vol. 367, pp. 134–165, 2018.
- [79] B. Hamilton and S. Bilbao, "FDTD Methods for 3-D Room Acoustics Simulation With High-Order Accuracy in Space and Time," *IEEE/ACM Transactions on Audio, Speech, and Language Processing*, vol. 25, pp. 2112–2124, nov 2017.
- [80] J. Van Mourik and D. Murphy, "Explicit higher-order FDTD schemes for 3D room acoustic simulation," *IEEE/ACM Transactions on Audio, Speech, and Language Processing*, vol. 22, no. 12, pp. 2003–2011, 2014.
- [81] C. Bogey and C. Bailly, "A family of low dispersive and low dissipative explicit schemes for flow and noise computations," *Journal of Computational Physics*, vol. 194, no. 1, pp. 194–214, 2004.
- [82] J. Sheaffer, M. van Walstijn, and B. Fazenda, "Physical and numerical constraints in source modeling for finite difference simulation of room acoustics," *The Journal of the Acoustical Society of America*, vol. 135, pp. 251–261, jan 2014.
- [83] H. Jeong and Y. W. Lam, "Source implementation to eliminate low-frequency artifacts in finite difference time domain room acous-
-

- 
- tic simulation,” *The Journal of the Acoustical Society of America*, vol. 131, no. 1, pp. 258–268, 2012.
- [84] D. T. Murphy, A. Southern, and L. Savioja, “Source excitation strategies for obtaining impulse responses in finite difference time domain room acoustics simulation,” *Applied Acoustics*, vol. 82, pp. 6–14, 2014.
- [85] S. Bilbao, J. Ahrens, and B. Hamilton, “Incorporating source directivity in wave-based virtual acoustics: Time-domain models and fitting to measured data,” *The Journal of the Acoustical Society of America*, vol. 146, no. 4, pp. 2692–2703, 2019.
- [86] D. Takeuchi, K. Yatabe, and Y. Oikawa, “Source directivity approximation for finite-difference time-domain simulation by estimating initial value,” *The Journal of the Acoustical Society of America*, vol. 145, no. 4, pp. 2638–2649, 2019.
- [87] C. Spa, A. Rey, and E. Hernandez, “A GPU Implementation of an Explicit Compact FDTD Algorithm with a Digital Impedance Filter for Room Acoustics Applications,” *IEEE/ACM Transactions on Audio, Speech, and Language Processing*, vol. 23, pp. 1368–1380, aug 2015.
- [88] C. J. Webb, *Parallel computation techniques for virtual acoustics and physical modelling synthesis*. Ph.D. dissertation, The University of Edinburgh, 2014.
- [89] J. Sheaffer, B. Fazenda, *et al.*, “FDTD/K-DWM simulation of 3D room acoustics on general purpose graphics hardware using compute unified device architecture (CUDA),” *Proc. Institute of Acoustics*, vol. 32, no. 5, 2010.
- [90] J. Saarelma and L. Savioja, “An open source finite-difference time-domain solver for room acoustics using graphics processing units,” in *Forum Acusticum, Krakow, Poland*, p. SS11.8, 2014.
- [91] L. Savioja, “Real-time 3D finite-difference time-domain simulation of low-and mid-frequency room acoustics,” in *13th Int. Conf on Digital Audio Effects*, vol. 1, p. 75, 2010.
- [92] J. Escolano, F. Jacobsen, and J. J. López, “An efficient realization of frequency dependent boundary conditions in an acoustic finite-difference time-domain model,” *Journal of Sound and Vibration*, vol. 316, no. 1-5, pp. 234–247, 2008.
-

- 
- [93] K. Kowalczyk and M. van Walstijn, “Formulation of locally reacting surfaces in FDTD/K-DWM modelling of acoustic spaces,” *Acta Acustica united with Acustica*, vol. 94, no. 6, pp. 891–906, 2008.
- [94] K. Kowalczyk and M. v. Walstijn, “Modeling frequency-dependent boundaries as digital impedance filters in FDTD and K-DWM room acoustics simulations,” *Journal of the Audio Engineering Society*, vol. 56, no. 7/8, pp. 569–583, 2008.
- [95] J. Huopaniemi, L. Savioja, and M. Karjalainen, “Modeling of reflections and air absorption in acoustical spaces — a digital filter design approach,” in *Applications of Signal Processing to Audio and Acoustics, 1997. 1997 IEEE ASSP Workshop on*, pp. 4–pp, IEEE, 1997.
- [96] S. Oxnard, “Investigating the stability of frequency-dependent locally reacting surface boundary conditions in numerical acoustic models,” *The Journal of the Acoustical Society of America*, vol. 143, pp. EL266–EL270, apr 2018.
- [97] M. Toyoda and S. Ishikawa, “Frequency-dependent absorption and transmission boundary for the finite-difference time-domain method,” *Applied Acoustics*, vol. 145, pp. 159–166, 2019.
- [98] B. Hamilton, *Finite Difference and Finite Volume Methods for Wave-based Modelling of Room Acoustics*. PhD thesis, The University of Edinburgh, 2016.
- [99] J. De Poorter and D. Botteldooren, “Acoustical finite-difference time-domain simulations of subwavelength geometries,” *The Journal of the Acoustical Society of America*, vol. 104, no. 3, pp. 1171–1177, 1998.
- [100] J. Nordström and M. H. Carpenter, “High-order finite difference methods, multidimensional linear problems, and curvilinear coordinates,” *Journal of Computational Physics*, vol. 173, no. 1, pp. 149–174, 2001.
- [101] M. R. Visbal and D. V. Gaitonde, “On the use of higher-order finite-difference schemes on curvilinear and deforming meshes,” *Journal of Computational Physics*, vol. 181, no. 1, pp. 155–185, 2002.
- [102] J. O. Smith, “Physical modeling using digital waveguides,” *Computer music journal*, vol. 16, no. 4, pp. 74–91, 1992.
-

- 
- [103] S. A. van Duyne and J. O. Smith, “Physical modeling with the 2-D digital waveguide mesh,” in *Proceedings of the International Computer Music Conference*, pp. 40–40, INTERNATIONAL COMPUTER MUSIC ACCOCIATION, 1993.
  - [104] D. Murphy, A. Kelloniemi, J. Mullen, and S. Shelley, “Acoustic modeling using the digital waveguide mesh,” *IEEE Signal Processing Magazine*, vol. 24, no. 2, pp. 55–66, 2007.
  - [105] D. T. Murphy and M. Beeson, “The KW-boundary hybrid digital waveguide mesh for room acoustics applications,” *IEEE Transactions on Audio, Speech, and Language Processing*, vol. 15, no. 2, pp. 552–564, 2007.
  - [106] M. Karjalainen and C. Erkut, “Digital waveguides versus finite difference structures: Equivalence and mixed modeling,” *EURASIP Journal on Advances in Signal Processing*, vol. 2004, no. 7, p. 561060, 2004.
  - [107] J. van Mourik, *Higher-order Finite Difference Time Domain Algorithms for Room Acoustic Modelling*. PhD thesis, University of York, 2016.
  - [108] J. Saarelma, *Finite-difference time-domain method for room acoustic simulation-auralization and applications*. PhD thesis, Aalto University, 2019.
  - [109] B. Fornberg, “On a Fourier method for the integration of hyperbolic equations,” *SIAM Journal on Numerical Analysis*, vol. 12, no. 4, pp. 509–528, 1975.
  - [110] D. Gottlieb and S. A. Orszag, *Numerical analysis of spectral methods: theory and applications*. SIAM, 1977.
  - [111] Q. H. Liu, “The PSTD algorithm: A time-domain method requiring only two cells per wavelength,” *Microwave and optical technology letters*, vol. 15, no. 3, pp. 158–165, 1997.
  - [112] L. N. Trefethen, *Spectral methods in MATLAB*. SIAM, 2000.
  - [113] J. S. Hesthaven, S. Gottlieb, and D. Gottlieb, *Spectral methods for time-dependent problems*, vol. 21. Cambridge University Press, 2007.
  - [114] B. Fornberg, *A practical guide to pseudospectral methods*, vol. 1. Cambridge university press, 1998.
-

- 
- [115] J. W. Cooley and J. W. Tukey, “An algorithm for the machine calculation of complex Fourier series,” *Mathematics of computation*, vol. 19, no. 90, pp. 297–301, 1965.
  - [116] D. Gottlieb and E. Tadmor, “The CFL condition for spectral approximations to hyperbolic initial-boundary value problems,” *Mathematics of Computation*, vol. 56, no. 194, pp. 565–588, 1991.
  - [117] N. Raghuvanshi, R. Narain, and M. C. Lin, “Efficient and accurate sound propagation using adaptive rectangular decomposition,” *IEEE Transactions on Visualization and Computer Graphics*, vol. 15, no. 5, pp. 789–801, 2009.
  - [118] R. Mehra, N. Raghuvanshi, L. Savioja, M. C. Lin, and D. Manocha, “An efficient GPU-based time domain solver for the acoustic wave equation,” *Applied Acoustics*, vol. 73, no. 2, pp. 83–94, 2012.
  - [119] C. Spa, A. Garriga, and J. Escolano, “Impedance boundary conditions for pseudo-spectral time-domain methods in room acoustics,” *Applied Acoustics*, vol. 71, no. 5, pp. 402–410, 2010.
  - [120] M. Hornikx, T. Krijnen, and L. van Harten, “openPSTD: The open source pseudospectral time-domain method for acoustic propagation,” *Computer Physics Communications*, vol. 203, pp. 298–308, 2016.
  - [121] M. Hornikx, W. De Roeck, and W. Desmet, “A multi-domain Fourier pseudospectral time-domain method for the linearized Euler equations,” *Journal of Computational Physics*, vol. 231, no. 14, pp. 4759–4774, 2012.
  - [122] S. K. Godunov, “Finite difference method for numerical computation of discontinuous solutions of the equations of fluid dynamics,” *Matematičeskij sbornik*, vol. 47, no. 3, pp. 271–306, 1959.
  - [123] R. J. LeVeque, *Finite Volume Methods for Hyperbolic Problems*. Cambridge: Cambridge University Press, 2002.
  - [124] S. Bilbao, “Modeling of Complex Geometries and Boundary Conditions in Finite Difference/Finite Volume Time Domain Room Acoustics Simulation,” *IEEE Transactions on Audio, Speech, and Language Processing*, vol. 21, pp. 1524–1533, jul 2013.
  - [125] S. Bilbao, B. Hamilton, J. Botts, and L. Savioja, “Finite volume time domain room acoustics simulation under general impedance
-

- 
- boundary conditions,” *IEEE/ACM Transactions on Audio, Speech and Language Processing (TASLP)*, vol. 24, no. 1, pp. 161–173, 2016.
- [126] S. Bilbao and B. Hamilton, “Wave-based room acoustics simulation: Explicit/implicit finite volume modeling of viscothermal losses and frequency-dependent boundaries,” *Journal of the Audio Engineering Society*, vol. 65, no. 1/2, pp. 78–89, 2017.
  - [127] G. M. Gladwell, “A finite element method for acoustics,” in *5th International Congress on Acoustics*, pp. 2437–2444, 1965.
  - [128] M. Petyt, J. Lea, and G. Koopmann, “A finite element method for determining the acoustic modes of irregular shaped cavities,” *Journal of Sound and Vibration*, vol. 45, no. 4, pp. 495–502, 1976.
  - [129] A. Craggs, “A finite element method for the free vibration of air in ducts and rooms with absorbing walls,” *Journal of sound and vibration*, vol. 173, no. 4, pp. 568–576, 1994.
  - [130] V. Easwaran and A. Craggs, “An application of acoustic finite element models to finding the reverberation times of irregular rooms,” *Acta Acustica united with Acustica*, vol. 82, no. 1, pp. 54–64, 1996.
  - [131] L. L. Thompson, “A review of finite-element methods for time-harmonic acoustics,” *The Journal of the Acoustical Society of America*, vol. 119, no. 3, pp. 1315–1330, 2006.
  - [132] F. Ihlenburg, *Finite element analysis of acoustic scattering*, vol. 132. Springer Science & Business Media, 2006.
  - [133] M. Aretz and M. Vorländer, “Efficient modelling of absorbing boundaries in room acoustic FE simulations,” *Acta Acustica united with Acustica*, vol. 96, no. 6, pp. 1042–1050, 2010.
  - [134] T. Okuzono, T. Otsuru, R. Tomiku, and N. Okamoto, “Fundamental accuracy of time domain finite element method for sound-field analysis of rooms,” *Applied Acoustics*, vol. 71, no. 10, pp. 940–946, 2010.
  - [135] T. Okuzono, T. Otsuru, R. Tomiku, and N. Okamoto, “Application of modified integration rule to time-domain finite-element acoustic simulation of rooms,” *The Journal of the Acoustical Society of America*, vol. 132, no. 2, pp. 804–813, 2012.
-

- 
- [136] T. Okuzono, T. Yoshida, and K. Sakagami, “Efficiency of room acoustic simulations with time-domain FEM including frequency-dependent absorbing boundary conditions: Comparison with frequency-domain FEM,” *Applied Acoustics*, vol. 182, p. 108212, 2021.
- [137] T. Okuzono, T. Yoshida, K. Sakagami, and T. Otsuru, “An explicit time-domain finite element method for room acoustics simulations: Comparison of the performance with implicit methods,” *Applied Acoustics*, pp. 76–84, 2016.
- [138] A. T. Patera, “A spectral element method for fluid dynamics: laminar flow in a channel expansion,” *Journal of Computational Physics*, vol. 54, no. 3, pp. 468–488, 1984.
- [139] G. Karniadakis and S. Sherwin, *Spectral/hp Element Methods for Computational Fluid Dynamics*. Oxford University Press, 2nd ed., 2005.
- [140] F. Pind, A. P. Engsig-Karup, C.-H. Jeong, J. S. Hesthaven, M. S. Mejlum, and J. Strømmand-Andersen, “Time domain room acoustic simulations using the spectral element method,” *The Journal of the Acoustical Society of America*, vol. 145, no. 6, pp. 3299–3310, 2019.
- [141] G. Cohen, *Higher-Order Numerical Methods for Transient Wave Equations*. Springer-Verlag Berlin Heidelberg, 2002.
- [142] L. Chen and D. Schweikert, “Sound radiation from an arbitrary body,” *The Journal of the Acoustical society of America*, vol. 35, no. 10, pp. 1626–1632, 1963.
- [143] Y. Yasuda and T. Sakuma, “Boundary element method,” in *Computational Simulation in Architectural and Environmental Acoustics*, pp. 79–115, Springer, 2014.
- [144] S. Marburg and B. Nolte, *Computational acoustics of noise propagation in fluids: finite and boundary element methods*, vol. 578. Springer, 2008.
- [145] V. C. Henriquez and P. M. Juhl, “OpenBEM-An open source Boundary Element Method software in acoustics,” *Internoise 2010*, vol. 7, pp. 13–16, 2010.
-

- 
- [146] Z. Chen, G. Hofstetter, and H. Mang, "A symmetric Galerkin formulation of the boundary element method for acoustic radiation and scattering," *Journal of Computational Acoustics*, vol. 5, no. 02, pp. 219–241, 1997.
- [147] A. Burton and G. Miller, "The application of integral equation methods to the numerical solution of some exterior boundary-value problems," *Proceedings of the Royal Society of London. A. Mathematical and Physical Sciences*, vol. 323, no. 1553, pp. 201–210, 1971.
- [148] H. A. Schenck, "Improved integral formulation for acoustic radiation problems," *The journal of the acoustical society of America*, vol. 44, no. 1, pp. 41–58, 1968.
- [149] H. Utsuno, T. W. Wu, A. F. Seybert, and T. Tanaka, "Prediction of sound fields in cavities with sound absorbing materials," *AIAA journal*, vol. 28, no. 11, pp. 1870–1876, 1990.
- [150] T. Terai, "On calculation of sound fields around three dimensional objects by integral equation methods," *Journal of Sound and Vibration*, vol. 69, no. 1, pp. 71–100, 1980.
- [151] R. Martinez, "The thin-shape breakdown (TSB) of the Helmholtz integral equation," *The Journal of the Acoustical Society of America*, vol. 90, no. 5, pp. 2728–2738, 1991.
- [152] S. Kirkup, "The boundary element method in acoustics: A survey," *Applied Sciences*, vol. 9, no. 8, p. 1642, 2019.
- [153] V. Rokhlin, "Rapid solution of integral equations of classical potential theory," *Journal of Computational Physics*, vol. 60, no. 2, pp. 187–207, 1985.
- [154] V. Rokhlin, "Rapid solution of integral equations of scattering theory in two dimensions," *Journal of Computational Physics*, vol. 86, no. 2, pp. 414–439, 1990.
- [155] T. Sakuma and Y. Yasuda, "Fast multipole boundary element method for large-scale steady-state sound field analysis. Part I: setup and validation," *Acta Acustica united with Acustica*, vol. 88, no. 4, pp. 513–525, 2002.
- [156] Y. Yasuda and T. Sakuma, "Fast multipole boundary element method for large-scale steady-state sound field analysis. Part II:
-

- 
- Examination of numerical items,” *Acta Acustica united with Acustica*, vol. 89, no. 1, pp. 28–38, 2003.
- [157] Y. Yasuda, T. Oshima, T. Sakuma, A. Gunawan, and T. Masumoto, “Fast multipole boundary element method for low-frequency acoustic problems based on a variety of formulations,” *Journal of Computational Acoustics*, vol. 18, no. 04, pp. 363–395, 2010.
- [158] J. A. Hargreaves and T. J. Cox, “A transient boundary element method model of Schroeder diffuser scattering using well mouth impedance,” *The Journal of the Acoustical Society of America*, vol. 124, no. 5, pp. 2942–2951, 2008.
- [159] J. A. Hargreaves, L. R. Rendell, and Y. W. Lam, “A framework for auralization of boundary element method simulations including source and receiver directivity,” *The Journal of the Acoustical Society of America*, vol. 145, no. 4, pp. 2625–2637, 2019.
- [160] M. Vorländer, “Performance of computer simulations for architectural acoustics,” in *Proceedings of 20th International Congress on Acoustics*, 2010.
- [161] M. Aretz and M. Vorländer, “Combined wave and ray based room acoustic simulations of audio systems in car passenger compartments, Part I: Boundary and source data,” *Applied acoustics*, vol. 76, pp. 82–99, 2014.
- [162] M. Aretz, *Combined wave and ray based room acoustic simulations of small rooms*. PhD thesis, RWTH Aachen, 2012.
- [163] M. Aretz, R. Nöthen, M. Vorländer, and D. Schröder, “Combined broadband impulse responses using FEM and hybrid ray-based methods,” in *Proc. EAA Symp. Auralization*, pp. 201–206, 2009.
- [164] J. E. Summers, K. Takahashi, Y. Shimizu, and T. Yamakawa, “Assessing the accuracy of auralizations computed using a hybrid geometrical-acoustics and wave-acoustics method,” *The Journal of the Acoustical Society of America*, vol. 115, no. 5, pp. 2514–2515, 2004.
- [165] A. Southern, S. Siltanen, D. T. Murphy, and L. Savioja, “Room impulse response synthesis and validation using a hybrid acoustic model,” *IEEE transactions on audio, speech, and language processing*, vol. 21, no. 9, pp. 1940–1952, 2013.
-

- 
- [166] M. Vorländer, “Computer simulations in room acoustics: Concepts and uncertainties,” *The Journal of the Acoustical Society of America*, vol. 133, pp. 1203–1213, mar 2013.
- [167] S. Siltanen, T. Lokki, and L. Savioja, “Rays or waves? understanding the strengths and weaknesses of computational room acoustics modeling techniques,” in *Proc. Int. Symposium on Room Acoustics*, 2010.
- [168] R. P. Muñoz and M. Hornikx, “Hybrid Fourier pseudospectral/discontinuous Galerkin time-domain method for wave propagation,” *Journal of Computational Physics*, vol. 348, pp. 416–432, 2017.
- [169] L. Rhaouti, A. Chaigne, and P. Joly, “Time-domain modeling and numerical simulation of a kettledrum,” *The Journal of the Acoustical Society of America*, vol. 105, no. 6, pp. 3545–3562, 1999.
- [170] S. Bilbao, “Time domain simulation and sound synthesis for the snare drum,” *The Journal of the Acoustical Society of America*, vol. 131, no. 1, pp. 914–925, 2012.
- [171] S.-P. Simonaho, T. Lähivaara, and T. Huttunen, “Modeling of acoustic wave propagation in time-domain using the discontinuous Galerkin method—A comparison with measurements,” *Applied Acoustics*, vol. 73, no. 2, pp. 173–183, 2012.
- [172] T. Xiao and Q. Huo Liu, “Finite difference computation of head-related transfer function for human hearing,” *The Journal of the Acoustical Society of America*, vol. 113, no. 5, pp. 2434–2441, 2003.
- [173] C. J. Webb and S. Bilbao, “Binaural simulations using audio rate FDTD schemes and CUDA,” in *Proc. 15th Int. Conf. Digital Audio Effects (DAFx-12)*, 2012.
- [174] J. Saarelma, J. Botts, B. Hamilton, and L. Savioja, “Audibility of dispersion error in room acoustic finite-difference time-domain simulation as a function of simulation distance,” *The Journal of the Acoustical Society of America*, vol. 139, no. 4, pp. 1822–1832, 2016.
- [175] A. Modave, A. St-Cyr, and T. Warburton, “GPU performance analysis of a nodal discontinuous Galerkin method for acoustic and elastic models,” *Computers & Geosciences*, vol. 91, pp. 64–76, 2016.
-

- 
- [176] S. Schoeder, W. Wall, and M. Kronbichler, “ExWave: A high performance discontinuous Galerkin solver for the acoustic wave equation,” *SoftwareX*, vol. 9, pp. 49–54, 2019.
- [177] W. H. Reed and T. Hill, “Triangular mesh methods for the neutron transport equation,” tech. rep., Los Alamos Scientific Lab., N. Mex.(USA), 1973.
- [178] P. Lasaint and P.-A. Raviart, “On a finite element method for solving the neutron transport equation,” in *Mathematical aspects of finite elements in partial differential equations*, pp. 89–123, Elsevier, 1974.
- [179] C. Johnson and J. Pitkäranta, “An analysis of the discontinuous Galerkin method for a scalar hyperbolic equation,” *Mathematics of computation*, vol. 46, no. 173, pp. 1–26, 1986.
- [180] F. Q. Hu, M. Hussaini, and P. Rasetarinera, “An analysis of the discontinuous Galerkin method for wave propagation problems,” *Journal of Computational Physics*, vol. 151, no. 2, pp. 921–946, 1999.
- [181] F. Hu and H. Atkins, “Two-dimensional wave analysis of the discontinuous Galerkin method with non-uniform grids and boundary conditions,” in *8th AIAA/CEAS Aeroacoustics Conference & Exhibit*, p. 2514, 2002.
- [182] F. Q. Hu and H. Atkins, “Eigensolution analysis of the discontinuous Galerkin method with nonuniform grids: I. one space dimension,” *Journal of Computational Physics*, vol. 182, no. 2, pp. 516–545, 2002.
- [183] M. Ainsworth, “Dispersive and dissipative behaviour of high order discontinuous Galerkin finite element methods,” *Journal of Computational Physics*, vol. 198, no. 1, pp. 106–130, 2004.
- [184] B. Cockburn and C.-W. Shu, “TVB Runge-Kutta local projection discontinuous Galerkin finite element method for conservation laws. II. General framework,” *Mathematics of computation*, vol. 52, no. 186, pp. 411–435, 1989.
- [185] B. Cockburn, S.-Y. Lin, and C.-W. Shu, “TVB Runge-Kutta local projection discontinuous Galerkin finite element method for conservation laws III: one-dimensional systems,” *Journal of Computational Physics*, vol. 84, no. 1, pp. 90–113, 1989.
-

- 
- [186] B. Cockburn, S. Hou, and C.-W. Shu, “The Runge-Kutta local projection discontinuous Galerkin finite element method for conservation laws. IV. The multidimensional case,” *Mathematics of Computation*, vol. 54, no. 190, pp. 545–581, 1990.
- [187] B. Cockburn and C.-W. Shu, “The Runge-Kutta discontinuous Galerkin method for conservation laws V: multidimensional systems,” *Journal of Computational Physics*, vol. 141, no. 2, pp. 199–224, 1998.
- [188] H. L. Atkins and C.-W. Shu, “Quadrature-free implementation of discontinuous Galerkin method for hyperbolic equations,” *AIAA journal*, vol. 36, no. 5, pp. 775–782, 1998.
- [189] B. Cockburn and C.-W. Shu, “Runge-Kutta discontinuous Galerkin methods for convection-dominated problems,” *Journal of Scientific Computing*, vol. 16, no. 3, pp. 173–261, 2001.
- [190] J. S. Hesthaven and T. Warburton, *Nodal discontinuous Galerkin methods: Algorithms, Analysis and Applications*. New York: Springer-Verlag, 2007.
- [191] B. Cockburn, G. E. Karniadakis, and C.-W. Shu, *Discontinuous Galerkin methods: theory, computation and applications*, vol. 11. Berlin Heidelberg: Springer-Verlag, 2000.
- [192] J. S. Hesthaven and T. Warburton, “Nodal high-order methods on unstructured grids: I. Time-domain solution of Maxwell’s equations,” *Journal of Computational Physics*, vol. 181, no. 1, pp. 186–221, 2002.
- [193] H. Qi, X. Wang, J. Zhang, and J. Wang, “An ADER discontinuous Galerkin method with local time-stepping for transient electromagnetics,” *Computer Physics Communications*, vol. 229, pp. 106–115, 2018.
- [194] M. Dumbser, M. Käser, and E. F. Toro, “An arbitrary high-order Discontinuous Galerkin method for elastic waves on unstructured meshes-V. Local time stepping and p-adaptivity,” *Geophysical Journal International*, vol. 171, no. 2, pp. 695–717, 2007.
- [195] Q. Zhan, M. Zhuang, Y. Fang, Y. Hu, Y. Mao, W.-F. Huang, R. Zhang, D. Wang, and Q. H. Liu, “Full-anisotropic poroelastic
-

- 
- wave modeling: A discontinuous Galerkin algorithm with a generalized wave impedance,” *Computer Methods in Applied Mechanics and Engineering*, vol. 346, pp. 288–311, 2019.
- [196] T. Lähivaara and T. Huttunen, “A non-uniform basis order for the discontinuous Galerkin method of the 3D dissipative wave equation with perfectly matched layer,” *Journal of Computational Physics*, vol. 229, no. 13, pp. 5144–5160, 2010.
- [197] L. C. Wilcox, G. Stadler, C. Burstedde, and O. Ghattas, “A high-order discontinuous Galerkin method for wave propagation through coupled elastic–acoustic media,” *Journal of Computational Physics*, vol. 229, no. 24, pp. 9373–9396, 2010.
- [198] H. Atkins, “Continued development of the discontinuous Galerkin method for computational aeroacoustic applications,” in *3rd AIAA/CEAS Aeroacoustics Conference*, p. 1581, 1997.
- [199] I. Touloupoulos and J. A. Ekaterinaris, “High-order discontinuous Galerkin discretizations for computational aeroacoustics in complex domains,” *AIAA journal*, vol. 44, no. 3, pp. 502–511, 2006.
- [200] T. Toulorge and W. Desmet, “Optimal Runge-Kutta schemes for discontinuous Galerkin space discretizations applied to wave propagation problems,” *Journal of Computational Physics*, vol. 231, no. 4, pp. 2067–2091, 2012.
- [201] R. Della Ratta Rinaldi, A. Iob, and R. Arina, “An efficient discontinuous Galerkin method for aeroacoustic propagation,” *International Journal for Numerical Methods in Fluids*, vol. 69, pp. 1473–1495, jul 2012.
- [202] L. Liu, X. Li, and F. Q. Hu, “Nonuniform time-step Runge-Kutta discontinuous Galerkin method for computational aeroacoustics,” *Journal of Computational Physics*, vol. 229, no. 19, pp. 6874–6897, 2010.
- [203] C. J. Trahan and C. Dawson, “Local time-stepping in Runge-Kutta discontinuous Galerkin finite element methods applied to the shallow-water equations,” *Computer Methods in Applied Mechanics and Engineering*, vol. 217, pp. 139–152, 2012.
- [204] C. Dawson, C. J. Trahan, E. J. Kubatko, and J. J. Westerink, “A parallel local timestepping Runge-Kutta discontinuous Galerkin method with applications to coastal ocean modeling,” *Computer*
-

- 
- Methods in Applied Mechanics and Engineering*, vol. 259, pp. 154–165, 2013.
- [205] J. S. Hesthaven and C.-H. Teng, “Stable spectral methods on tetrahedral elements,” *SIAM Journal on Scientific Computing*, vol. 21, no. 6, pp. 2352–2380, 2000.
- [206] B.-T. Chu and L. S. Kovásznyai, “Non-linear interactions in a viscous heat-conducting compressible gas,” *Journal of Fluid Mechanics*, vol. 3, no. 5, pp. 494–514, 1958.
- [207] K. W. Thompson, “Time dependent boundary conditions for hyperbolic systems,” *Journal of Computational Physics*, vol. 68, no. 1, pp. 1–24, 1987.
- [208] S. Rienstra, “Impedance models in time domain, including the extended Helmholtz resonator model,” in *12th AIAA/CEAS Aeroacoustics Conference (27th AIAA Aeroacoustics Conference)*, p. 2686, 2006.
- [209] D. Dragna and P. Blanc-Benon, “Physically admissible impedance models for time-domain computations of outdoor sound propagation,” *Acta Acustica united with Acustica*, vol. 100, no. 3, pp. 401–410, 2014.
- [210] D. Dragna, K. Attenborough, and P. Blanc-Benon, “On the inadvisability of using single parameter impedance models for representing the acoustical properties of ground surfaces,” *The Journal of the Acoustical Society of America*, vol. 138, no. 4, pp. 2399–2413, 2015.
- [211] M. J. Grote, M. Kray, F. Nataf, and F. Assous, “Time-dependent wave splitting and source separation,” *Journal of Computational Physics*, vol. 330, pp. 981–996, 2017.
- [212] F. Pind, C.-H. Jeong, J. S. Hesthaven, A. P. Engsig-Karup, and J. Strømmand-Andersen, “A phenomenological extended-reaction boundary model for time-domain wave-based acoustic simulations under sparse reflection conditions using a wave splitting method,” *Applied Acoustics*, vol. 172, p. 107596, 2021.
- [213] M. A. Biot, “Theory of propagation of elastic waves in a fluid-saturated porous solid. i. low-frequency range,” *The Journal of the Acoustical Society of America*, vol. 28, no. 2, pp. 168–178, 1956.
-

- 
- [214] M. A. Biot, "Theory of propagation of elastic waves in a fluid-saturated porous solid. ii. higher frequency range," *The Journal of the Acoustical Society of America*, vol. 28, no. 2, pp. 179–191, 1956.
- [215] M. A. Biot, "Mechanics of deformation and acoustic propagation in porous media," *Journal of Applied Physics*, vol. 33, no. 4, pp. 1482–1498, 1962.
- [216] M. A. Biot, "Generalized theory of acoustic propagation in porous dissipative media," *The Journal of the Acoustical Society of America*, vol. 34, no. 9, pp. 1254–1264, 1962.
- [217] C. Zwikker and C. Kosten, *Sound absorbing materials*. New York: Elsevier, 1949.
- [218] M. Delany and E. Bazley, "Acoustical properties of fibrous absorbent materials," *Applied acoustics*, vol. 3, no. 2, pp. 105–116, 1970.
- [219] Y. Miki, "Acoustical properties of porous materials-modifications of delany-bazley models," *Journal of the Acoustical Society of Japan (E)*, vol. 11, no. 1, pp. 19–24, 1990.
- [220] D. L. Johnson, J. Koplik, and R. Dashen, "Theory of dynamic permeability and tortuosity in fluid-saturated porous media," *Journal of fluid mechanics*, vol. 176, pp. 379–402, 1987.
- [221] J. Allard and N. Atalla, *Propagation of sound in porous media: modelling sound absorbing materials*. John Wiley & Sons, 2009.
- [222] N. Atalla, R. Panneton, and P. Debergue, "A mixed displacement-pressure formulation for poroelastic materials," *The Journal of the Acoustical Society of America*, vol. 104, no. 3, pp. 1444–1452, 1998.
- [223] J.-F. Allard and Y. Champoux, "New empirical equations for sound propagation in rigid frame fibrous materials," *The Journal of the Acoustical Society of America*, vol. 91, no. 6, pp. 3346–3353, 1992.
- [224] D. Lafarge, P. Lemarinier, J. F. Allard, and V. Tarnow, "Dynamic compressibility of air in porous structures at audible frequencies," *The Journal of the Acoustical Society of America*, vol. 102, no. 4, pp. 1995–2006, 1997.
- [225] Z. Fella and C. Depollier, "Transient acoustic wave propagation in rigid porous media: A time-domain approach," *The Journal of the Acoustical Society of America*, vol. 107, no. 2, pp. 683–688, 2000.
-

- 
- [226] Z. E. A. Fellah, M. Fellah, W. Lauriks, and C. Depollier, “Direct and inverse scattering of transient acoustic waves by a slab of rigid porous material,” *The Journal of the Acoustical Society of America*, vol. 113, no. 1, pp. 61–72, 2003.
- [227] D. K. Wilson, V. E. Ostashev, and S. L. Collier, “Time-domain equations for sound propagation in rigid-frame porous media,” *The Journal of the Acoustical Society of America*, vol. 116, no. 4, pp. 1889–1892, 2004.
- [228] O. Umnova and D. Turo, “Time domain formulation of the equivalent fluid model for rigid porous media,” *The Journal of the Acoustical Society of America*, vol. 125, no. 4, pp. 1860–1863, 2009.
- [229] R. Panneton and N. Atalla, “An efficient finite element scheme for solving the three-dimensional poroelasticity problem in acoustics,” *The Journal of the Acoustical Society of America*, vol. 101, no. 6, pp. 3287–3298, 1997.
- [230] Y. Yasuda, S. Ueno, M. Kadota, and H. Sekine, “Applicability of locally reacting boundary conditions to porous material layer backed by rigid wall: Wave-based numerical study in non-diffuse sound field with unevenly distributed sound absorbing surfaces,” *Applied Acoustics*, vol. 113, pp. 45–57, 2016.
- [231] D. Dragna, P. Pineau, and P. Blanc-Benon, “A generalized recursive convolution method for time-domain propagation in porous media,” *The Journal of the Acoustical Society of America*, vol. 138, no. 2, pp. 1030–1042, 2015.
- [232] J. Zhao, M. Bao, X. Wang, H. Lee, and S. Sakamoto, “An equivalent fluid model based finite-difference time-domain algorithm for sound propagation in porous material with rigid frame,” *The Journal of the Acoustical Society of America*, vol. 143, no. 1, pp. 130–138, 2018.
- [233] J. Zhao, Z. Chen, M. Bao, H. Lee, and S. Sakamoto, “Two-dimensional finite-difference time-domain analysis of sound propagation in rigid-frame porous material based on equivalent fluid model,” *Applied Acoustics*, vol. 146, pp. 204–212, 2019.
- [234] F. Pind, C.-H. Jeong, A. P. Engsig-Karup, J. S. Hesthaven, and J. Strømmand-Andersen, “Time-domain room acoustic simulations with extended-reacting porous absorbers using the discontinuous
-

- 
- Galerkin method,” *The Journal of the Acoustical Society of America*, vol. 148, no. 5, pp. 2851–2863, 2020.
- [235] M. Toyoda and J. Motooka, “Prediction of permeable thin absorbers using the finite-difference time-domain method,” *The Journal of the Acoustical Society of America*, vol. 143, no. 5, pp. 2870–2877, 2018.
- [236] M. Toyoda and D. Eto, “Prediction of microperforated panel absorbers using the finite-difference time-domain method,” *Wave Motion*, vol. 86, pp. 110–124, 2019.
- [237] T. Okuzono, N. Shimizu, and K. Sakagami, “Predicting absorption characteristics of single-leaf permeable membrane absorbers using finite element method in a time domain,” *Applied Acoustics*, vol. 151, pp. 172–182, 2019.
- [238] K. Gunnarsdóttir, C.-H. Jeong, and G. Marbjerg, “Acoustic behavior of porous ceiling absorbers based on local and extended reaction,” *The Journal of the Acoustical Society of America*, vol. 137, no. 1, pp. 509–512, 2015.
- [239] E. Nilsson, “Decay processes in rooms with non-diffuse sound fields part i: ceiling treatment with absorbing material,” *Building Acoustics*, vol. 11, no. 1, pp. 39–60, 2004.
- [240] C.-H. Jeong, “Guideline for adopting the local reaction assumption for porous absorbers in terms of random incidence absorption coefficients,” *Acta Acustica united with Acustica*, vol. 97, no. 5, pp. 779–790, 2011.
- [241] B. Yousefzadeh and M. Hodgson, “Energy-and wave-based beam-tracing prediction of room-acoustical parameters using different boundary conditions,” *The Journal of the Acoustical Society of America*, vol. 132, no. 3, pp. 1450–1461, 2012.
- [242] A. D. Pierce, *Acoustics: An Introduction to Its Physical Principles and Applications*. Springer Nature Switzerland AG: Springer International Publishing, 2019.
- [243] Y. Reyman, M. Baelmans, and W. Desmet, “Efficient implementation of Tam and Auriault’s time-domain impedance boundary condition,” *AIAA journal*, vol. 46, no. 9, pp. 2368–2376, 2008.
-

- 
- [244] S. Zhong, X. Zhang, and X. Huang, “A controllable canonical form implementation of time domain impedance boundary conditions for broadband aeroacoustic computation,” *Journal of Computational Physics*, vol. 313, pp. 713–725, 2016.
- [245] K.-Y. Fung and H. Ju, “Broadband time-domain impedance models,” *AIAA journal*, vol. 39, no. 8, pp. 1449–1454, 2001.
- [246] H. Ju and K.-Y. Fung, “Time-domain simulation of acoustic sources over an impedance plane,” *Journal of Computational Acoustics*, vol. 10, no. 03, pp. 311–329, 2002.
- [247] K.-Y. Fung and H. Ju, “Time-domain impedance boundary conditions for computational acoustics and aeroacoustics,” *International Journal of Computational Fluid Dynamics*, vol. 18, no. 6, pp. 503–511, 2004.
- [248] S. Jaensch, C. Sovardi, and W. Polifke, “On the robust, flexible and consistent implementation of time domain impedance boundary conditions for compressible flow simulations,” *Journal of Computational Physics*, vol. 314, pp. 145–159, 2016.
- [249] J. Lin, C. Scalo, and L. Hesselink, “High-fidelity simulation of a standing-wave thermoacoustic-piezoelectric engine,” *Journal of Fluid Mechanics*, vol. 808, pp. 19–60, 2016.
- [250] Q. Douasbin, C. Scalo, L. Selle, and T. Poinso, “Delayed-time domain impedance boundary conditions (D-TDIBC),” *Journal of Computational Physics*, vol. 371, pp. 50–66, 2018.
- [251] C. K. Tam and L. Auriault, “Time-domain impedance boundary conditions for computational aeroacoustics,” *AIAA journal*, vol. 34, no. 5, pp. 917–923, 1996.
- [252] B. Cotté, P. Blanc-Benon, C. Bogey, and F. Poisson, “Time-domain impedance boundary conditions for simulations of outdoor sound propagation,” *AIAA journal*, vol. 47, no. 10, pp. 2391–2403, 2009.
- [253] X. Li, X. Li, and C. K. W. Tam, “Improved multipole broadband time-domain impedance boundary condition,” *AIAA journal*, vol. 50, no. 4, pp. 980–984, 2012.
- [254] D. Dragna, P. Blanc-Benon, and F. Poisson, “Time-domain solver in curvilinear coordinates for outdoor sound propagation over complex terrain,” *The Journal of the Acoustical Society of America*, vol. 133, no. 6, pp. 3751–3763, 2013.
-

- 
- [255] D. Dragna, B. Cotté, P. Blanc-Benon, and F. Poisson, “Time-domain simulations of outdoor sound propagation with suitable impedance boundary conditions,” *AIAA journal*, vol. 49, no. 7, pp. 1420–1428, 2011.
- [256] C. Richter, J. A. Hay, N. Schönwald, S. Busse, F. Thiele, *et al.*, “A review of time-domain impedance modelling and applications,” *Journal of Sound and Vibration*, vol. 330, no. 16, pp. 3859–3873, 2011.
- [257] R. Troian, D. Dragna, C. Bailly, and M.-A. Galland, “Broadband liner impedance eduction for multimodal acoustic propagation in the presence of a mean flow,” *Journal of Sound and Vibration*, vol. 392, pp. 200–216, 2017.
- [258] R. M. Joseph, S. C. Hagness, and A. Taflove, “Direct time integration of Maxwell’s equations in linear dispersive media with absorption for scattering and propagation of femtosecond electromagnetic pulses,” *Optics Letters*, vol. 16, no. 18, pp. 1412–1414, 1991.
- [259] B. Gustavsen and A. Semlyen, “Rational approximation of frequency domain responses by vector fitting,” *IEEE Transactions on power delivery*, vol. 14, no. 3, pp. 1052–1061, 1999.
- [260] B. Gustavsen, “Improving the pole relocating properties of vector fitting,” *IEEE Transactions on Power Delivery*, vol. 21, no. 3, pp. 1587–1592, 2006.
- [261] T. Okuzono and K. Sakagami, “A time-domain finite element model of permeable membrane absorbers,” *Acoustical Science and Technology*, vol. 37, no. 1, pp. 46–49, 2016.
- [262] T. Okuzono and K. Sakagami, “A frequency domain finite element solver for acoustic simulations of 3D rooms with microperforated panel absorbers,” *Applied Acoustics*, vol. 129, pp. 1–12, 2018.
- [263] COMSOL AB, Stockholm, Sweden, *COMSOL Multiphysics® v. 5.4*.
- [264] D. Takahashi, K. Sakagami, and M. Morimoto, “Acoustic properties of permeable membranes,” *The Journal of the Acoustical Society of America*, vol. 99, no. 5, pp. 3003–3009, 1996.
-

- 
- [265] K. Sakagami, M. Kiyama, M. Morimoto, and D. Takahashi, "Detailed analysis of the acoustic properties of a permeable membrane," *Applied Acoustics*, vol. 54, no. 2, pp. 93–111, 1998.
- [266] K. Sakagami, M. Kiyama, and M. Morimoto, "Acoustic properties of double-leaf membranes with a permeable leaf on sound incidence side," *Applied Acoustics*, vol. 63, no. 8, pp. 911–926, 2002.
- [267] R. Pieren, "Sound absorption modeling of thin woven fabrics backed by an air cavity," *Textile Research Journal*, vol. 82, no. 9, pp. 864–874, 2012.
- [268] K. Sakagami, Y. Fukutani, M. Yairi, and M. Morimoto, "Sound absorption characteristics of a double-leaf structure with an MPP and a permeable membrane," *Applied Acoustics*, vol. 76, pp. 28–34, 2014.
- [269] J. Williamson, "Low-storage Runge-Kutta schemes," *Journal of Computational Physics*, vol. 35, no. 1, pp. 48–56, 1980.
- [270] M. H. Carpenter and C. A. Kennedy, "Fourth-order 2N-storage Runge-Kutta schemes," in *NASA-TM-109112*, 1994.
- [271] F. Hu, M. Y. Hussaini, and J. Manthey, "Low-dissipation and low-dispersion Runge-Kutta schemes for computational acoustics," *Journal of Computational Physics*, vol. 124, no. 1, pp. 177–191, 1996.
- [272] D. Stanescu and W. Habashi, "2N-storage low dissipation and dispersion Runge-Kutta schemes for computational acoustics," *Journal of Computational Physics*, vol. 143, no. 2, pp. 674–681, 1998.
- [273] J. Berland, C. Bogey, and C. Bailly, "Low-dissipation and low-dispersion fourth-order Runge-Kutta algorithm," *Computers & Fluids*, vol. 35, no. 10, pp. 1459–1463, 2006.
- [274] A. Kanevsky, M. H. Carpenter, D. Gottlieb, and J. S. Hesthaven, "Application of implicit-explicit high order Runge-Kutta methods to discontinuous-Galerkin schemes," *Journal of Computational Physics*, vol. 225, no. 2, pp. 1753–1781, 2007.
- [275] V. Dolean, H. Fahs, L. Fezoui, and S. Lanteri, "Locally implicit discontinuous Galerkin method for time domain electromagnetics," *Journal of Computational Physics*, vol. 229, no. 2, pp. 512–526, 2010.
-

- 
- [276] S. Descombes, S. Lanteri, and L. Moya, “Locally implicit time integration strategies in a discontinuous Galerkin method for Maxwell’s equations,” *Journal of Scientific Computing*, vol. 56, no. 1, pp. 190–218, 2013.
- [277] M. Hochbruck and A. Ostermann, “Exponential multistep methods of Adams-type,” *BIT Numerical Mathematics*, vol. 51, no. 4, pp. 889–908, 2011.
- [278] H. Wang, L. Xu, B. Li, S. Descombes, and S. Lanteri, “A new family of exponential-based high-order DGTD methods for modeling 3-D transient multiscale electromagnetic problems,” *IEEE Transactions on Antennas and Propagation*, vol. 65, no. 11, pp. 5960–5974, 2017.
- [279] C. W. Gear and D. Wells, “Multirate linear multistep methods,” *BIT Numerical Mathematics*, vol. 24, no. 4, pp. 484–502, 1984.
- [280] M. Günther, A. Kvaernø, and P. Rentrop, “Multirate partitioned Runge-Kutta methods,” *BIT Numerical Mathematics*, vol. 41, no. 3, pp. 504–514, 2001.
- [281] V. Savcenco, W. Hundsdorfer, and J. Verwer, “A multirate time stepping strategy for stiff ordinary differential equations,” *BIT Numerical Mathematics*, vol. 47, no. 1, pp. 137–155, 2007.
- [282] J. Diaz and M. J. Grote, “Energy conserving explicit local time stepping for second-order wave equations,” *SIAM Journal on Scientific Computing*, vol. 31, no. 3, pp. 1985–2014, 2009.
- [283] J. Diaz and M. J. Grote, “Multi-level explicit local time-stepping methods for second-order wave equations,” *Computer Methods in Applied Mechanics and Engineering*, vol. 291, pp. 240–265, 2015.
- [284] M. Almquist and M. Mehlin, “MultiLevel Local Time-Stepping Methods of Runge-Kutta-type for Wave Equations,” *SIAM Journal on Scientific Computing*, vol. 39, no. 5, pp. A2020–A2048, 2017.
- [285] M. J. Grote, M. Mehlin, and T. Mitkova, “Runge-Kutta-based explicit local time-stepping methods for wave propagation,” *SIAM Journal on Scientific Computing*, vol. 37, no. 2, pp. A747–A775, 2015.
- [286] S. Schoeder, M. Kronbichler, and W. A. Wall, “Arbitrary high-order explicit hybridizable discontinuous Galerkin methods for the
-

- 
- acoustic wave equation,” *Journal of Scientific Computing*, vol. 76, no. 2, pp. 969–1006, 2018.
- [287] S. Piperno, “Symplectic local time-stepping in non-dissipative DGTD methods applied to wave propagation problems,” *ESAIM: Mathematical Modelling and Numerical Analysis-Modélisation Mathématique et Analyse Numérique*, vol. 40, no. 5, pp. 815–841, 2006.
- [288] E. Montseny, S. Pernet, X. Ferrières, and G. Cohen, “Dissipative terms and local time-stepping improvements in a spatial high order Discontinuous Galerkin scheme for the time-domain Maxwell’s equations,” *Journal of Computational Physics*, vol. 227, no. 14, pp. 6795–6820, 2008.
- [289] A. Taube, M. Dumbser, C.-D. Munz, and R. Schneider, “A high-order discontinuous Galerkin method with time-accurate local time stepping for the Maxwell equations,” *International Journal of Numerical Modelling: Electronic Networks, Devices and Fields*, vol. 22, no. 1, pp. 77–103, 2009.
- [290] S. Schomann, N. Godel, T. Warburton, and M. Clemens, “Local timestepping techniques using Taylor expansion for modeling electromagnetic wave propagation with discontinuous Galerkin-FEM,” *IEEE transactions on magnetics*, vol. 46, no. 8, pp. 3504–3507, 2010.
- [291] M. Käser and M. Dumbser, “An arbitrary high-order discontinuous Galerkin method for elastic waves on unstructured meshes-I. The two-dimensional isotropic case with external source terms,” *Geophysical Journal International*, vol. 166, no. 2, pp. 855–877, 2006.
- [292] M. Käser, M. Dumbser, J. De La Puente, and H. Igel, “An arbitrary high-order discontinuous Galerkin method for elastic waves on unstructured meshes-III. Viscoelastic attenuation,” *Geophysical Journal International*, vol. 168, no. 1, pp. 224–242, 2007.
- [293] L. Krivodonova, “An efficient local time-stepping scheme for solution of nonlinear conservation laws,” *Journal of Computational Physics*, vol. 229, no. 22, pp. 8537–8551, 2010.
- [294] M. Taylor, *Partial Differential Equations I: Basic Theory*. Springer-Verlag New York, 1996.
-

- 
- [295] P. Lax and B. Wendroff, "Systems of conservation laws," *Communications on Pure and Applied Mathematics*, vol. 13, no. 2, pp. 217–237, 1960.
- [296] R. Wenmaekers and N. van Hout, "How ISO 3382-3 acoustic parameter values are affected by furniture, barriers and sound absorption in a typical open plan office," in *23rd International Congress on Acoustics*, pp. 2437–2444, 2019.
- [297] ISO354: 2003, "Acoustics - Measurement of sound absorption in a reverberation room," standard, International Organization for Standardization, Geneva, CH, 2003.
- [298] M. Vercammen, "On the revision of ISO 354, measurement of the sound absorption in the reverberation room," in *23rd International Congress on Acoustics*, pp. 3991–3997, 2019.
- [299] C.-H. Jeong and J.-H. Chang, "Reproducibility of the random incidence absorption coefficient converted from the sabine absorption coefficient," *Acta Acustica united with Acustica*, vol. 101, no. 1, pp. 99–112, 2015.
- [300] C.-H. Jeong, "Converting sabine absorption coefficients to random incidence absorption coefficients," *The Journal of the Acoustical Society of America*, vol. 133, no. 6, pp. 3951–3962, 2013.
- [301] E. Paris, "L. on the coefficient of sound-absorption measured by the reverberation method," *The London, Edinburgh, and Dublin Philosophical Magazine and Journal of Science*, vol. 5, no. 29, pp. 489–497, 1928.
- [302] C.-H. Jeong, "Absorption and impedance boundary conditions for phased geometrical-acoustics methods," *The Journal of the Acoustical Society of America*, vol. 132, no. 4, pp. 2347–2358, 2012.
- [303] S.-I. Thomasson, "On the absorption coefficient," *Acta Acustica united with Acustica*, vol. 44, no. 4, pp. 265–273, 1980.
- [304] C.-H. Jeong, "A correction of random incidence absorption coefficients for the angular distribution of acoustic energy under measurement conditions," *The Journal of the Acoustical Society of America*, vol. 125, no. 4, pp. 2064–2071, 2009.
- [305] C.-H. Jeong, "Non-uniform sound intensity distributions when measuring absorption coefficients in reverberation chambers using
-

- 
- a phased beam tracing,” *The Journal of the Acoustical Society of America*, vol. 127, no. 6, pp. 3560–3568, 2010.
- [306] S.-I. Thomasson, “Theory and experiments on the sound absorption as a function of area,” *Royal Institute of Technology, Stockholm*, 1982.
- [307] B. Mondet, J. Brunskog, C.-H. Jeong, and J. H. Rindel, “From absorption to impedance: Enhancing boundary conditions in room acoustic simulations,” *Applied Acoustics*, vol. 157, p. 106884, 2020.
- [308] ISO 10534-1, “Acoustics-Determination of sound absorption coefficient and impedance in impedance tubes - Part 1: Method using standing wave ratio,” standard, International Organization for Standardization, Geneva, CH, 1996.
- [309] ISO 10534-2, “Acoustics-Determination of sound absorption coefficient and impedance in impedance tubes - Part 2: Transfer-function method,” standard, International Organization for Standardization, Geneva, CH, 1998.
- [310] E. Tijs, *Study and development of an in situ acoustic absorption measurement method*. PhD thesis, University of Twente, 2013.
- [311] E. Brandão, A. Lenzi, and S. Paul, “A review of the in situ impedance and sound absorption measurement techniques,” *Acta Acustica united with Acustica*, vol. 101, no. 3, pp. 443–463, 2015.
- [312] M. Ottink, J. Brunskog, C.-H. Jeong, E. Fernandez-Grande, P. Trojgaard, and E. Tiana-Roig, “In situ measurements of the oblique incidence sound absorption coefficient for finite sized absorbers,” *The Journal of the Acoustical Society of America*, vol. 139, no. 1, pp. 41–52, 2016.
- [313] T. Thydal, F. Pind, C.-H. Jeong, and A. P. Engsig-Karup, “Experimental validation and uncertainty quantification in wave-based computational room acoustics,” *Applied Acoustics*, vol. 178, p. 107939, 2021.
- [314] C. Geuzaine and J.-F. Remacle, “Gmsh: A 3-D finite element mesh generator with built-in pre-and post-processing facilities,” *International Journal for Numerical Methods in Engineering*, vol. 79, no. 11, pp. 1309–1331, 2009.
-

- 
- [315] V. Parthasarathy, C. Graichen, and A. Hathaway, "A comparison of tetrahedron quality measures," *Finite Elements in Analysis and Design*, vol. 15, no. 3, pp. 255–261, 1994.
- [316] S. Bilbao and B. Hamilton, "Directional sources in wave-based acoustic simulation," *IEEE/ACM Transactions on Audio, Speech, and Language Processing*, vol. 27, no. 2, pp. 415–428, 2018.
- [317] F. Georgiou and M. Hornikx, "Incorporating directivity in the fourier pseudospectral time-domain method using spherical harmonics," *The Journal of the Acoustical Society of America*, vol. 140, no. 2, pp. 855–865, 2016.
- [318] S. Balay, S. Abhyankar, M. F. Adams, J. Brown, P. Brune, K. Buschelman, L. Dalcin, A. Dener, V. Eijkhout, W. D. Gropp, D. Karpeyev, D. Kaushik, M. G. Knepley, D. A. May, L. C. McInnes, R. T. Mills, T. Munson, K. Rupp, P. Sanan, B. F. Smith, S. Zampini, H. Zhang, and H. Zhang, "PETSc Web page." <https://www.mcs.anl.gov/petsc>, 2021.
- [319] S. Balay, S. Abhyankar, M. F. Adams, J. Brown, P. Brune, K. Buschelman, L. Dalcin, A. Dener, V. Eijkhout, W. D. Gropp, D. Karpeyev, D. Kaushik, M. G. Knepley, D. A. May, L. C. McInnes, R. T. Mills, T. Munson, K. Rupp, P. Sanan, B. F. Smith, S. Zampini, H. Zhang, and H. Zhang, "PETSc users manual," Tech. Rep. ANL-95/11 - Revision 3.15, Argonne National Laboratory, 2021.

---

# Paper I

# Room acoustics modelling in the time-domain with the nodal discontinuous Galerkin method

Huiqing Wang,<sup>a)</sup> Indra Sihar, Raúl Pagán Muñoz, and Maarten Hornikx

*Department of the Built Environment, Eindhoven University of Technology, P.O. Box 513, 5600 MB Eindhoven, The Netherlands*

(Received 9 August 2018; revised 9 January 2019; accepted 10 January 2019; published online 30 April 2019)

To solve the linear acoustic equations for room acoustic purposes, the performance of the time-domain nodal discontinuous Galerkin (DG) method is evaluated. A nodal DG method is used for the evaluation of the spatial derivatives, and for the time-integration an explicit multi-stage Runge-Kutta method is adopted. The scheme supports a high order approximation on unstructured meshes. To model frequency-independent real-valued impedance boundary conditions, a formulation based on the plane wave reflection coefficient is proposed. Semi-discrete stability of the scheme is analyzed using the energy method. The performance of the DG method is evaluated for four three-dimensional configurations. The first two cases concern sound propagations in free field and over a flat impedance ground surface. Results show that the solution converges with increasing DG polynomial order and the accuracy of the impedance boundary condition is independent on the incidence angle. The third configuration is a cuboid room with rigid boundaries, for which an analytical solution serves as the reference solution. Finally, DG results for a real room scenario are compared with experimental results. For both room scenarios, results show good agreements.

© 2019 Acoustical Society of America. <https://doi.org/10.1121/1.5096154>

[LS]

Pages: 2650–2663

## I. INTRODUCTION

Computer simulation of the sound field in indoor environments has been investigated back in time since the publication of Manfred Robert Schroeder.<sup>1</sup> After all these years, prediction methods for room acoustic applications are still under development trying to improve efficiency of the calculations and accuracy and realism of the results, hand in hand with the advances in computer power. In acoustics, the computational techniques are mainly separated between wave-based, geometrical and diffuse field methods. Each of these methodologies has been amply presented in literature. Concepts, implementations and applications of room simulation methods are reviewed by Vorländer,<sup>2</sup> Savioja *et al.*,<sup>3</sup> and Hamilton<sup>4</sup> for geometrical and wave-based methods, while diffuse field methods are described for instance by Valeau<sup>5</sup> or Navarro *et al.*<sup>6</sup>

In contrast with the high-frequency simplifications assumed in the geometrical and diffuse field methods, wave-based methodologies solve the governing physical equations, implicitly including all wave effects such as diffraction and interference. Among these methods, time-domain approaches to model wave problems have attracted significant attention in the last few decades, since they are favoured for auralization purposes over frequency-domain methods. The main wave-based time-domain numerical techniques employed in room acoustics problems are the finite-differences time-domain method (FDTD),<sup>7–10</sup> finite-element (FEM)<sup>11</sup> and finite-volume (FVM) methods,<sup>12</sup> and Fourier spectral methods such

as the adaptive rectangular decomposition method (ARD)<sup>13</sup> and the pseudospectral time-domain method (PSTD).<sup>14–16</sup>

In the last few years, the discontinuous Galerkin time-domain method (DG)<sup>17</sup> is another approach gaining importance, mainly in the aero-acoustic community.<sup>18,19</sup> DG discretizes the spatial domain into non-overlapping mesh elements, in which the governing equations are solved elementwise, and uses the so-called numerical flux at adjacent elements interfaces to communicate the information between them. DG combines the favourable properties of existing wave-based time domain methods for room acoustics as it preserves high order accuracy, allows for local refinement by a variable polynomial order and element size, and therefore can deal with complex geometries. Also, because equations are solved elementwise, it allows for easy parallelization and massive calculation acceleration opportunities,<sup>20</sup> like other methods such as FDTD and FVM. DG can be seen as an extension to FV by using a polynomial basis for evaluating the spatial derivatives, leading to a higher order method. Also, DG can be seen as an extended FEM version by decoupling the elements without imposing continuity of the variables, thereby creating local matrices. Therefore, DG is a very suitable numerical method for acoustic propagation problems including, definitely, room acoustics. However, some developments towards room acoustic applications are still missing: although results for impedance boundary conditions with the DG method have been presented,<sup>21</sup> a proper formulation of these boundary conditions in the framework of DG have not been published. In contrast, frequency-dependent impedance conditions have been extensively developed in other methodologies (FDTD, FVTD).<sup>12</sup> In the present work, a frequency-independent

<sup>a)</sup>Electronic mail: h.wang6@tue.nl

real-valued impedance boundary formulation, based on the plane wave reflection coefficient is proposed, following the idea first presented by Fung and Ju.<sup>22</sup>

To the authors' best knowledge, no reference is found in the scientific literature about the application of DG to the room acoustics problems. The aim of this work is to address the positioning of DG as a wave-based method for room acoustics. The accuracy of the method for these type of applications is quantified and the developments needed to arrive at a fully fledged DG method for room acoustics are summarized as future work.

The paper is organized as follows. In Sec. II, the governing acoustic equations are introduced as well as the solution by the time-domain DG method. The formulations of impedance boundary conditions and its semi-discrete stability analysis are presented in Sec. III, and are in this work restricted to locally reacting frequency independent conditions. Section IV quantifies and discusses the accuracy of the implemented DG method for sound propagation in several scenarios: (1) free field propagation in a periodic domain; (2) a single reflective plane; (3) a cuboid room with acoustically rigid boundaries; (4) a real room. Finally, conclusions and outlook can be found in Sec. V.

## II. LINEAR ACOUSTIC EQUATIONS AND NODAL DG TIME-DOMAIN METHOD

### A. Linear acoustic equations

Acoustic wave propagation is governed by the linearized Euler equations (LEE), which are derived from the general conservation laws.<sup>23</sup> For room acoustics applications, we further assume that sound propagates in air that is completely at rest and constant in temperature. Under these assumptions, the LEE in primitive variables are simplified to the following homogeneous coupled system of linear acoustic equations:

$$\begin{aligned} \frac{\partial \mathbf{v}}{\partial t} + \frac{1}{\rho_0} \nabla p &= \mathbf{0}, \\ \frac{\partial p}{\partial t} + \rho_0 c_0^2 \nabla \cdot \mathbf{v} &= 0, \end{aligned} \quad (1)$$

where  $\mathbf{v} = [u, v, w]^T$  is the particle velocity vector,  $p$  is the sound pressure,  $\rho_0$  is the constant density of air, and  $c_0$  is the constant adiabatic sound speed. The linear acoustic equations can be combined into one equation, the wave equation. Equation (1), completed with initial values or a force formulation on the right side, as well as a formulation of boundary conditions at all room boundaries, complete the problem definition. In this study, the linear acoustic equations are solved instead of the wave equation because it is beneficial for implementing impedance boundary conditions.

### B. Spatial discretization with the nodal DG method

To numerically solve Eq. (1), the nodal discontinuous Galerkin method is used to discretize the spatial derivative operators. First of all, Eq. (1) is rewritten into the following linear hyperbolic system:

$$\frac{\partial \mathbf{q}}{\partial t} + \nabla \cdot \mathbf{F}(\mathbf{q}) = \frac{\partial \mathbf{q}}{\partial t} + \mathbf{A}_j \frac{\partial \mathbf{q}}{\partial x_j} = 0, \quad (2)$$

where  $\mathbf{q}(\mathbf{x}, t) = [u, v, w, p]^T$  is the acoustic variable vector and  $\mathbf{x} = [x, y, z]$  is the spatial coordinate vector with index  $j \in [x, y, z]$ . The flux is given as

$$\mathbf{F} = [\mathbf{f}_x, \mathbf{f}_y, \mathbf{f}_z] = [\mathbf{A}_x \mathbf{q}, \mathbf{A}_y \mathbf{q}, \mathbf{A}_z \mathbf{q}], \quad (3)$$

where the constant flux Jacobian matrix  $\mathbf{A}_j$

$$\mathbf{A}_j = \begin{bmatrix} 0 & 0 & 0 & \frac{\delta_{xj}}{\rho_0} \\ 0 & 0 & 0 & \frac{\delta_{yj}}{\rho_0} \\ 0 & 0 & 0 & \frac{\delta_{zj}}{\rho_0} \\ \rho_0 c_0^2 \delta_{xj} & \rho_0 c_0^2 \delta_{yj} & \rho_0 c_0^2 \delta_{zj} & 0 \end{bmatrix}, \quad (4)$$

and  $\delta_{ij}$  denotes the Kronecker delta function.

Similar to the finite element method, the physical domain  $\Omega$  is approximated by a computational domain  $\Omega_h$ , which is further divided into a set of  $K$  non-overlapping elements  $D^k$ , i.e.,  $\Omega_h = \cup_{k=1}^K D^k$ . In this work, the quadrature-free approach<sup>24</sup> is adopted and the nodal discontinuous Galerkin algorithm as presented in Ref. 25 is followed. The global solution is approximated by a direct sum of local piecewise polynomial solutions as

$$\mathbf{q}(\mathbf{x}, t) \approx \mathbf{q}_h(\mathbf{x}, t) = \bigoplus_{k=1}^K \mathbf{q}_h^k(\mathbf{x}, t). \quad (5)$$

The local solution  $\mathbf{q}_h^k(\mathbf{x}, t)$  in element  $D^k$  is expressed by

$$\mathbf{q}_h^k(\mathbf{x}, t) = \sum_{i=1}^{N_p} \mathbf{q}_h^k(\mathbf{x}_i^k, t) l_i^k(\mathbf{x}), \quad (6)$$

where  $\mathbf{q}_h^k(\mathbf{x}_i^k, t)$  are the unknown nodal values in element  $D^k$  and  $l_i^k(\mathbf{x}_i^k)$  is the multi-dimensional Lagrange polynomial basis of order  $N$  based on the nodes  $\mathbf{x} \in D^k$ , which satisfies  $l_i^k(\mathbf{x}_j^k) = \delta_{ij}$ . The number of local basis functions (or nodes)  $N_p$  is determined by both the dimensionality of the problem  $d$  and the order of the polynomial basis  $N$ , which can be computed as  $N_p = (N + d)!/N!d!$ . In this work, the  $\alpha$ -optimized nodes distribution<sup>26</sup> for tetrahedron elements are used over a wide range of polynomial order  $N$ . The locally defined basis functions constitute a function space as  $V_h^k = \text{span}\{l_i^k(\mathbf{x})\}_{i=1}^{N_p}$ . Then, the Galerkin projection is followed by choosing test functions equal to the basis functions. The solution is found by imposing an orthogonality condition: the local residual is orthogonal to all the test functions in  $V_h^k$ ,

$$\int_{D^k} \left( \frac{\partial \mathbf{q}_h^k}{\partial t} + \nabla \cdot \mathbf{F}^k(\mathbf{q}_h^k) \right) l_i^k d\mathbf{x} = 0. \quad (7)$$

Integration by parts and applying the divergence theorem results in the local weak formulation,

$$\int_{D^k} \left( \frac{\partial q_h^k}{\partial t} l_i^k - \mathbf{F}_h^k(\mathbf{q}_h^k) \cdot \nabla l_i^k \right) d\mathbf{x} = - \int_{\partial D^k} \mathbf{n} \cdot \mathbf{F}^* l_i^k d\mathbf{x}, \quad (8)$$

where  $\mathbf{n} = [n_x, n_y, n_z]$  is the outward normal vector of the element surface  $\partial D^k$  and  $\mathbf{F}^*(\mathbf{q}_h^-, \mathbf{q}_h^+)$  is the so-called numerical flux from element  $D^k$  to its neighboring elements through their intersection  $\partial D^k$ . In contrast to the classical continuous Galerkin method, the discontinuous Galerkin method uses local basis functions and test functions that are smooth within each element and discontinuous across the element intersections. As a result, the solutions are multiply defined on the intersections  $\partial D^k$ , where the numerical flux  $\mathbf{F}^*(\mathbf{q}_h^-, \mathbf{q}_h^+)$  should be defined properly as a function of both the interior and exterior (or neighboring) solution. In the remainder, the solution value from the interior side of the intersection is denoted by a superscript “−” and the exterior value by “+.” Applying integration by parts once again to the spatial derivative term in Eq. (8) yields the strong formulation

$$\begin{aligned} \int_{D^k} \left( \frac{\partial q_h^k}{\partial t} + \nabla \cdot \mathbf{F}_h^k(\mathbf{q}_h^k) \right) l_i^k d\mathbf{x} \\ = \int_{\partial D^k} \mathbf{n} \cdot (\mathbf{F}_h^k(\mathbf{q}_h^k) - \mathbf{F}^*) l_i^k d\mathbf{x}. \end{aligned} \quad (9)$$

In this study, the flux-splitting approach<sup>27</sup> is followed and the upwind numerical flux is derived as follows. Let us first consider the case where the element  $D^k$  lies in the interior of the computational domain. As is shown in Eq. (9), the formulation of a flux along the surface normal direction  $\mathbf{n}$ , i.e.,  $\mathbf{n} \cdot \mathbf{F} = (n_x f_x + n_y f_y + n_z f_z)$  is of interest. To derive the upwind flux, we utilize the hyperbolic property of the system and decompose the normal flux on the interface  $\partial D^k$  into outgoing and incoming waves. Mathematically, an eigendecomposition applied to the normally projected flux Jacobian yields

$$\begin{aligned} \mathbf{A}_n &= (n_x \mathbf{A}_x + n_y \mathbf{A}_y + n_z \mathbf{A}_z) \\ &= \begin{bmatrix} 0 & 0 & 0 & \frac{n_x}{\rho_0} \\ 0 & 0 & 0 & \frac{n_y}{\rho_0} \\ 0 & 0 & 0 & \frac{n_z}{\rho_0} \\ \rho_0 c_0^2 n_x & \rho_0 c_0^2 n_y & \rho_0 c_0^2 n_z & 0 \end{bmatrix} \\ &= \mathbf{L} \mathbf{\Lambda} \mathbf{L}^{-1}, \end{aligned} \quad (10)$$

where

$$\begin{aligned} \mathbf{L} &= \begin{bmatrix} -n_z & n_y & n_x/2 & -n_x/2 \\ n_z & -n_x & n_y/2 & -n_y/2 \\ -n_y & n_x & n_z/2 & -n_z/2 \\ 0 & 0 & \rho_0 c_0/2 & \rho_0 c_0/2 \end{bmatrix}, \\ \mathbf{\Lambda} &= \begin{bmatrix} 0 & 0 & 0 & 0 \\ 0 & 0 & 0 & 0 \\ 0 & 0 & c_0 & 0 \\ 0 & 0 & 0 & -c_0 \end{bmatrix}. \end{aligned} \quad (11)$$

The upwind numerical flux is defined by considering the direction of the characteristic speed, i.e.,

$$(\mathbf{n} \cdot \mathbf{F})^* = \mathbf{L}(\mathbf{\Lambda}^+ \mathbf{L}^{-1} \mathbf{q}_h^- + \mathbf{\Lambda}^- \mathbf{L}^{-1} \mathbf{q}_h^+), \quad (12)$$

where  $\mathbf{\Lambda}^+$  and  $\mathbf{\Lambda}^-$  contain the positive and negative entries of  $\mathbf{\Lambda}$ , respectively. Physically,  $\mathbf{\Lambda}^+$  ( $\mathbf{\Lambda}^-$ ) corresponds to the characteristic waves propagating along (opposite to) the normal direction  $\mathbf{n}$ , which are referred to as outgoing waves out of  $D_k$  (incoming waves into  $D_k$ ). Therefore, the outgoing waves are associated with the interior solution  $\mathbf{q}_h^-$  whereas the incoming waves are dependent on the exterior (neighboring) solution  $\mathbf{q}_h^+$ . The expression of the numerical flux on the impedance boundary will be discussed in Sec. III. Finally, the semi-discrete formulation is obtained by substituting the nodal basis expansion Eq. (6) and the upwind flux Eq. (12) into the strong formulation Eq. (9), which can be further recast into the following matrix form:

$$\mathbf{M}^k \frac{\partial \mathbf{u}_h^k}{\partial t} + \frac{1}{\rho} \mathbf{S}_x^k \mathbf{p}_h^k = \sum_{r=1}^f \mathbf{M}^{kr} \hat{\mathbf{F}}_u^{kr}, \quad (13a)$$

$$\mathbf{M}^k \frac{\partial \mathbf{v}_h^k}{\partial t} + \frac{1}{\rho} \mathbf{S}_y^k \mathbf{p}_h^k = \sum_{r=1}^f \mathbf{M}^{kr} \hat{\mathbf{F}}_v^{kr}, \quad (13b)$$

$$\mathbf{M}^k \frac{\partial \mathbf{w}_h^k}{\partial t} + \frac{1}{\rho} \mathbf{S}_z^k \mathbf{p}_h^k = \sum_{r=1}^f \mathbf{M}^{kr} \hat{\mathbf{F}}_w^{kr}, \quad (13c)$$

$$\mathbf{M}^k \frac{\partial \mathbf{p}_h^k}{\partial t} + \rho c^2 \mathbf{S}_x^k \mathbf{u}_h^k + \rho c^2 \mathbf{S}_y^k \mathbf{v}_h^k + \rho c^2 \mathbf{S}_z^k \mathbf{w}_h^k = \sum_{r=1}^f \mathbf{M}^{kr} \hat{\mathbf{F}}_p^{kr}, \quad (13d)$$

where the second superscript  $r$  denotes the  $r$ th faces  $\partial D^{kr}$  of the element  $D^k$  and  $f$  is the total number of faces of the element  $D^k$ , which is equal to 4 for tetrahedra elements. For brevity, the subscript 0 in  $\rho_0$  and  $c_0$  are omitted from here.  $\mathbf{u}_h^k$ ,  $\mathbf{v}_h^k$ ,  $\mathbf{w}_h^k$ , and  $\mathbf{p}_h^k$  are vectors representing all the unknown nodal values  $u_h^k(\mathbf{x}_i^k, t)$ ,  $v_h^k(\mathbf{x}_i^k, t)$ , and  $p_h^k(\mathbf{x}_i^k, t)$  respectively, e.g.,  $\mathbf{u}_h^k = [u_h^k(\mathbf{x}_1^k, t), u_h^k(\mathbf{x}_2^k, t), \dots, u_h^k(\mathbf{x}_{N_p}^k, t)]^T$ .  $\hat{\mathbf{F}}_u^{kr}$ ,  $\hat{\mathbf{F}}_v^{kr}$ ,  $\hat{\mathbf{F}}_w^{kr}$ , and  $\hat{\mathbf{F}}_p^{kr}$  are flux terms associated with the integrand  $\mathbf{n} \cdot (\mathbf{F}_h^k(\mathbf{q}_h^k) - \mathbf{F}^*)$  over the element surface  $\partial D^{kr}$  in the strong formulation Eq. (9). The element mass matrix  $\mathbf{M}^k$ , the element stiffness matrices  $\mathbf{S}_j^k$  and the element face matrices  $\mathbf{M}^{kr}$  are defined as

$$\mathbf{M}_{mn}^k = \int_{D^k} l_m^k(\mathbf{x}) l_n^k(\mathbf{x}) d\mathbf{x} \in \mathbb{R}^{N_p \times N_p}, \quad (14a)$$

$$(\mathbf{S}_j^k)_{mn} = \int_{D^k} l_m^k(\mathbf{x}) \frac{\partial l_n^k(\mathbf{x})}{\partial x_j} d\mathbf{x} \in \mathbb{R}^{N_p \times N_p}, \quad (14b)$$

$$\mathbf{M}_{mn}^{kr} = \int_{\partial D^{kr}} l_m^{kr}(\mathbf{x}) l_n^{kr}(\mathbf{x}) d\mathbf{x} \in \mathbb{R}^{N_p \times N_{fp}}, \quad (14c)$$

where  $j$  is the  $j$ th Cartesian coordinates and  $N_{fp}$  is the number of nodes along one element face. When the upwind flux is used, the flux terms for each acoustic variable read as

$$\begin{aligned}\hat{\mathbf{F}}_u^{kr} = & -\frac{cn_x^{kr^2}}{2}[\mathbf{u}_h^{kr}] - \frac{cn_x^{kr}n_y^{kr}}{2}[\mathbf{v}_h^{kr}] - \frac{cn_x^{kr}n_z^{kr}}{2}[\mathbf{w}_h^{kr}] \\ & + \frac{n_x^{kr}}{2\rho}[\mathbf{p}_h^{kr}],\end{aligned}\quad (15a)$$

$$\begin{aligned}\hat{\mathbf{F}}_v^{kr} = & -\frac{cn_y^{kr^2}}{2}[\mathbf{v}_h^{kr}] - \frac{cn_x^{kr}n_y^{kr}}{2}[\mathbf{u}_h^{kr}] - \frac{cn_y^{kr}n_z^{kr}}{2}[\mathbf{w}_h^{kr}] \\ & + \frac{n_y^{kr}}{2\rho}[\mathbf{p}_h^{kr}],\end{aligned}\quad (15b)$$

$$\begin{aligned}\hat{\mathbf{F}}_w^{kr} = & -\frac{cn_z^{kr^2}}{2}[\mathbf{w}_h^{kr}] - \frac{cn_x^{kr}n_z^{kr}}{2}[\mathbf{u}_h^{kr}] - \frac{cn_y^{kr}n_z^{kr}}{2}[\mathbf{v}_h^{kr}] \\ & + \frac{n_z^{kr}}{2\rho}[\mathbf{p}_h^{kr}],\end{aligned}\quad (15c)$$

$$\hat{\mathbf{F}}_p^{kr} = \frac{c^2\rho n_x^{kr}}{2}[\mathbf{u}_h^{kr}] + \frac{c^2\rho n_y^{kr}}{2}[\mathbf{v}_h^{kr}] + \frac{c^2\rho n_z^{kr}}{2}[\mathbf{w}_h^{kr}] - \frac{c}{2}[\mathbf{p}_h^{kr}],\quad (15d)$$

where  $[\mathbf{u}_h^{kr}] := \mathbf{u}_h^{kr} - \mathbf{u}_h^{ls}$ ,  $[\mathbf{v}_h^{kr}] := \mathbf{v}_h^{kr} - \mathbf{v}_h^{ls}$ ,  $[\mathbf{w}_h^{kr}] := \mathbf{w}_h^{kr} - \mathbf{w}_h^{ls}$ , and  $[\mathbf{p}_h^{kr}] := \mathbf{p}_h^{kr} - \mathbf{p}_h^{ls}$  are the jump differences across the shared intersection face  $\partial D^{kr}$  or, equivalently,  $\partial D^{ls}$ , between neighboring elements  $D^k$  and  $D^l$ ,  $\mathbf{u}_h^{kr}$ , etc., are the nodal value vectors, over the element surface  $\partial D^{kr}$ .

In this work, flat-faced tetrahedra elements are used so that each tetrahedron can be mapped into a reference tetrahedron by a linear transformation with a constant Jacobian matrix. As a consequence, the integrals in the above element matrices, i.e.,  $\mathbf{M}^k$ ,  $\mathbf{S}_f^k$ , and  $\mathbf{M}^{kr}$ , need to be evaluated only once. The reader is referred to Ref. 25 for more details on how to compute the matrices locally and efficiently.

### 1. Numerical dissipation and dispersion properties

For a discontinuous Galerkin scheme that uses polynomial basis up to order  $N$ , it is well known that generally the rate of convergence in terms of the global  $L^2$  error is  $h^{N+1/2}$  ( $h$  being the element size).<sup>28</sup> The dominant error comes from the representations of the initial conditions, while the additional dispersive and dissipative errors from the wave propagations are relatively small and only visible after a very long time integration.<sup>25</sup> The one-dimensional eigenvalue problem for the spatially propagating waves is studied in Ref. 29 and it is reported that the dispersion relation is accurate to  $(\kappa h)^{2N+2}$  locally, where  $\kappa$  is the wavenumber. Actually, when the upwind flux is used, the dissipation error has been proved to be of order  $(\kappa h)^{2N+2}$  while the dispersion error is of order  $(\kappa h)^{2N+3}$ .<sup>30</sup> When the centered numerical flux is used, the dissipation rate is exactly zero, but the discrete dispersion relation can only approximate the exact one for a smaller range of the wavenumber.<sup>31</sup> Extensions to the two-dimensional hyperbolic system on triangle and quadrilateral mesh are studied in Ref. 32 and the same numerical dispersion relation as the one-dimensional case are reported. In Ref. 30, a rigorous mathematical proof of the above numerical dispersion relation and error behavior is provided for a general multi-dimensional setting (including 3D).

### C. Time integration with the optimal Runge-Kutta method

After the spatial discretization by the nodal DG method, the semi-discrete system can be expressed in a general form of ordinary differential equations (ODE) as

$$\frac{d\mathbf{q}_h}{dt} = \mathcal{L}(\mathbf{q}_h(t), t),\quad (16)$$

where  $\mathbf{q}_h$  is the vector of all discrete nodal solutions and  $\mathcal{L}$  the spatial discretization operator of DG. Here, a low-storage explicit Runge-Kutta method is used to integrate Eq. (16), which reads

$$\begin{aligned}\mathbf{q}_h^{(0)} &= \mathbf{q}_h^n, \\ \begin{cases} \mathbf{k}^{(i)} = a_i \mathbf{k}^{(i-1)} + \Delta t \mathcal{L}(t^n + c_i \Delta t, \mathbf{q}_h^{(i-1)}), \\ \mathbf{q}_h^{(i)} = \mathbf{q}_h^{(i-1)} + b_i \mathbf{k}^{(i)}, \end{cases} & \text{for } i = 1, \dots, s, \\ \mathbf{q}_h^{n+1} &= \mathbf{q}_h^{(s)},\end{aligned}\quad (17)$$

where  $\Delta t = t^{n+1} - t^n$  is the time step,  $\mathbf{q}_h^{n+1}$  and  $\mathbf{q}_h^n$  are the solution vectors at time  $t^{n+1}$  and  $t^n$ , respectively,  $s$  is the number of stages of a particular scheme. In this work, the coefficients  $a_i$ ,  $b_i$ , and  $c_i$  are chosen from the optimal Runge-Kutta scheme reported in Ref. 33.

## III. IMPEDANCE BOUNDARY CONDITIONS AND NUMERICAL STABILITY

### A. Numerical flux for frequency-independent impedance boundary conditions

The numerical flux  $\mathbf{F}^*$  plays a key role in the DG scheme. Apart from linking neighboring interior elements, it serves to impose the boundary conditions and to guarantee stability of the formulation. Boundary conditions can be enforced weakly through the numerical flux either by reformulating the flux subject to specific boundary conditions or by providing the exterior solution  $\mathbf{q}_h^+$ .<sup>34</sup> In both cases, the solutions from the interior side of the element face (equivalent to boundary surface)  $\mathbf{q}_h^-$  are readily used, whereas, for the second case, the exterior solutions  $\mathbf{q}_h^+$  need to be suitably defined as a function of interior solution  $\mathbf{q}_h^-$  based on the imposed conditions. In the following, the impedance boundary condition is prescribed by reformulating the numerical flux. It should be noted that throughout this study, only plane-shaped reflecting boundary surfaces are considered. Furthermore, only locally reacting surfaces are considered, whose surface impedance is independent of the incident angle. This assumption is in accordance with the nodal DG scheme, since the unknown acoustic particle velocities on the boundary surface nodes depend on the pressure at exactly the same positions.

To reformulate the numerical flux at an impedance boundary, we take advantage of the characteristics of the underlying hyperbolic system and utilize the reflection coefficient  $R$  for plane waves at normal incidence. First, the same eigendecomposition procedure is performed for the projected flux Jacobian on the boundary as is shown in Eq. (10).

Second, by pre-multiplying the acoustic variables  $\mathbf{q}$  with the left eigenmatrix  $\mathbf{L}^{-1}$ , the characteristics corresponding to the acoustic waves<sup>35,36</sup> read

$$\begin{bmatrix} \omega_o \\ \omega_i \end{bmatrix} = \begin{bmatrix} p/\rho c + u n_x + v n_y + w n_z \\ p/\rho c - u n_x - v n_y - w n_z \end{bmatrix}, \quad (18)$$

where  $\omega_o$  corresponds to the outgoing characteristic variable that leaves the computational domain and  $\omega_i$  is the incoming characteristic variable.

The general principle for imposing boundary conditions of hyperbolic systems is that the outgoing characteristic variable should be computed with the upwind scheme using the interior values, while the incoming characteristic variable are specified conforming with the prescribed behaviour across the boundary. The proposed real-valued impedance boundary formulation is accomplished by setting the incoming characteristic variable as the product of the reflection coefficient and the outgoing characteristic variable, i.e.,  $\omega_i = R \omega_o$ . Finally, the numerical flux on the impedance boundary surface can be expressed in terms of the interior values  $\mathbf{q}_h^-$  as follows:

$$(\mathbf{n} \cdot \mathbf{F}^*) = \mathbf{L} \mathbf{A} \begin{bmatrix} 0 \\ 0 \\ p_h^- / \rho c + \mathbf{u}_h^- n_x + \mathbf{v}_h^- n_y + \mathbf{w}_h^- n_z \\ R \cdot (p_h^- / \rho c + \mathbf{u}_h^- n_x + \mathbf{v}_h^- n_y + \mathbf{w}_h^- n_z) \end{bmatrix}. \quad (19)$$

For given constant values of the normalized surface impedance  $Z_s$ , the reflection coefficient can be calculated from  $R = (Z_s - 1)/(Z_s + 1)$ , which is consistent with the fact that the numerical flux from the nodal DG scheme is always normal to the boundary surface. When the reflection coefficient is set to zero it can be easily verified that the proposed formulation reduces to the characteristic non-reflective boundary condition, which is equivalent to the first-order Engquist-Majda absorbing boundary condition.<sup>37</sup>

## B. Numerical stability of the DG scheme

In this section, the stability properties of the DG scheme are discussed. First, the semi-boundedness of the spatial DG operator together with the proposed impedance boundary conditions is analyzed using the energy method. Second, the fully discrete stability is discussed and the criterion for choosing the discrete time step is presented.

### 1. Stability of the semi-discrete formulation

Under a certain initial condition and impedance boundary condition, the governing linear acoustic equations (1) constitute a general initial-boundary value problem. For real-valued impedance boundary conditions, the classical von Neumann (or Fourier) stability analysis can no longer be applied, because the necessary periodic boundary conditions for the Fourier components do not exist. To analyze the stability or boundedness of the semi-discrete system, the energy method<sup>38</sup> is adopted here. The principle is to construct a

norm and to demonstrate it does not grow with increasing time. This technique has also been applied in other acoustic simulation methods,<sup>4,39</sup> even in the fully discrete case.

For the numerical solution of the acoustic variables, e.g.,  $u_h(\mathbf{x}, t)$ , the local inner product and its associated  $L^2$  norm in function space  $V_h^k$  are defined as

$$(u_h^k, u_h^k)_{D^k} = \int_{D^k} u_h^k(\mathbf{x}, t) u_h^k(\mathbf{x}, t) d\mathbf{x} = \|u_h^k\|_{D^k}^2. \quad (20)$$

Similarly, over the element surface  $\partial D^{kr}$ , define

$$(u_h^{kr}, u_h^{kr})_{\partial D^{kr}} = \int_{\partial D^{kr}} u_h^{kr}(\mathbf{x}, t) u_h^{kr}(\mathbf{x}, t) d\mathbf{x} = \|u_h^{kr}\|_{\partial D^{kr}}^2, \quad (21)$$

where  $u_h^{kr}$  is the numerical solution on the element surface  $\partial D^{kr}$ . Now, the discrete acoustic energy norm inside single element  $D^k$  can be defined

$$E_h^k = \frac{1}{2} \rho \|u_h^k\|_{D^k}^2 + \frac{1}{2} \rho \|v_h^k\|_{D^k}^2 + \frac{1}{2} \rho \|w_h^k\|_{D^k}^2 + \frac{1}{2 \rho c^2} \|p_h^k\|_{D^k}^2. \quad (22)$$

This definition is in complete analogy with the continuous acoustic energy, denoted as  $E$ , throughout the whole domain  $\Omega$ , i.e.,  $E = \int_{\Omega} (1/2 \rho c^2) p^2 + (\rho/2) |v|^2 d\mathbf{x}$ .

By summing all the local discrete acoustic energies over the volume and the boundaries, it can be proved in the Appendix that the total discrete acoustic energy, which is denoted as  $E_h = \sum_{k=1}^K E_h^k$ , is governed by

$$\begin{aligned} \frac{d}{dt} E_h = & - \sum_{\partial D^{mt} \in \mathcal{F}_B} \left( \frac{1 - R^{mt}}{2 \rho c} \|p_h^{mt}\|_{\partial D^{mt}}^2 \right. \\ & + \left. \frac{\rho c}{2} (1 + R^{mt}) \|v_h^{mt}\|_{\partial D^{mt}}^2 \right) \dots \\ & - \sum_{\partial D^{kr} \in \mathcal{F}_I} \left( \frac{1}{2 \rho c} \|p_h^{kr}\|_{\partial D^{kr}}^2 + \frac{\rho c}{2} \|n_h^{kr}\|_{\partial D^{kr}}^2 \right. \\ & + \left. n_y^{kr} [v_h^{kr}] + n_z^{kr} [w_h^{kr}] \|_{\partial D^{kr}}^2 \right), \end{aligned} \quad (23)$$

where  $\mathcal{F}_I$  and  $\mathcal{F}_B$  denote the union set of interior elements and elements with at least one surface collocated with a physical boundary.  $[\cdot]$  denotes the jump differences across the element surfaces.  $v_h^{mt} = n_x^{mt} u_h^{mt} + n_y^{mt} v_h^{mt} + n_z^{mt} w_h^{mt}$  denotes the outward velocity component normal to the impedance boundary.  $R^{mt}$  is the normal incidence plane-wave reflection coefficient along the  $t$ th boundary surface of element  $\partial D^{mt}$ .  $\partial D^{kr}$  and  $\partial D^{ls}$  refers to the same element intersection surface between neighboring elements  $D^k$  and  $D^l$ . Since each norm is non-negative and  $R \in [-1, 1]$  holds for a passive impedance boundary,<sup>40</sup> it is proved that the semi-discrete acoustic system resulting from the DG discretization is unconditionally stable for passive boundary conditions with a real-valued impedance.

It is worth mentioning that the second sum term of Eq. (23) is related to the energy dissipation inside the

computational domain due to the use of the upwind scheme. This dissipation will converge to zero when the jump differences across the shared element interfaces converge to zero at a rate corresponding to the approximation polynomial order. The first sum of Eq. (23) is associated with the energy flow through the impedance boundary. One advantage of using the reflection coefficient to impose the impedance boundary condition is that the following singular cases can be considered without the need for exceptional treatments.

- Hard wall case. As  $Z_s \rightarrow \infty$  or  $R \rightarrow 1$ ,  $v_{hn} \rightarrow 0$ , then the boundary energy term converges to 0, meaning that the energy is conserved.
- Pressure-release condition. As  $Z_s \rightarrow 0$  or  $R \rightarrow -1$ ,  $p_h \rightarrow 0$ , then the boundary energy term once again converges to 0, and the energy is conserved as well.

## 2. Stability of the fully discrete formulation and time step choices

The above analysis is devoted to the stability analysis of the semi-discrete formulation Eq. (16), which in matrix form reads

$$\frac{dq_h}{dt} = L_h q_h, \quad (24)$$

where  $L_h$  is the matrix representation of the spatial operator  $\mathcal{L}$ . Ideally, the fully discrete approximation should be stable, at least under a reasonable upper bound on the time step size. Unfortunately, the theoretical ground for stability of a discretized PDE system is not very complete,<sup>38</sup> particularly for high order time integration methods. A commonly used approach based on the von Neumann analysis is to choose the time step size  $\Delta t$  small enough so that the product of  $\Delta t$  with the full eigenvalue spectrum of  $L_h$  falls inside the stability region of the time integration scheme. It should be noted that this is only a necessary condition for a general initial-boundary value problem, with the sufficient condition being more restrictive and complex.<sup>41,42</sup> However, for real world problems, this necessary condition serves as a useful guideline.

It is computationally infeasible to compute the eigenvalue of  $L_h$  before the simulation is started for various unstructured mesh, polynomial order and boundary conditions. For the DG method, it is found that for the first order system Eq. (16), the gradients of the normalized  $N$ th order polynomial basis are of order  $\mathcal{O}(N^2/h)$  near the boundary part of the element,<sup>25</sup> consequently the magnitude of the maximum eigenvalue  $\lambda_N$  scales with the polynomial order  $N$  as:  $\max(\lambda_N) \propto N^2$ , indicating that  $\Delta t \propto N^{-2}$ . This severe time step size restriction limits the computational efficiency of high polynomial order approximations. In all the numerical experiments presented in this work, the temporal time steps are determined in the following way:<sup>33</sup>

$$\Delta t = C_{CFL} \min(r_D) \frac{1}{c}, \quad (25)$$

where  $r_D$  is the radius of the inscribed sphere of the tetrahedral elements. As a reference, the tabulated maximum allowable Courant number  $C_{CFL}$  of the current used *RKF84*

scheme for each polynomial order  $N$  can be found in Ref. 33. In each of the following numerical tests, the exact value of  $C_{CFL}$  are explicitly stated for completeness.

## IV. APPLICATIONS

To investigate the applicability of the nodal DG time-domain method as described in Sec. II and Sec. III for room acoustics problems, various 3-D numerical tests are designed and compared in this section. The first test is a free field propagation of a single frequency plane wave under periodic boundary conditions. In this case, the dissipation error in terms of the wave amplitude and the dispersion error are investigated. The second configuration is a sound source over an impedance plane. The accuracy of the proposed DG formulation to simulate frequency-independent impedance boundary conditions is verified. The third configuration is a sound source in a cuboid room with rigid boundary conditions, embodying an approximation to a real room including multiple reflections. The modal behaviour of the space is investigated for different polynomial order  $N$  of the basis functions when compared with the analytical solution, together with an analysis of the sound energy conservation inside the room to quantify the numerical dissipation. Finally, the fourth configuration is adopted to demonstrate the applicability of the method to a real room. The configuration is a room with complex geometry and a real-valued impedance boundary condition. In this configuration, the pressure response functions in the frequency domain are compared with the measured results at several receiver locations. For the acoustic speed and the air density,  $c = 343$  m/s and  $\rho = 1.2$  kg/m<sup>3</sup> are used in all calculations. Due to the fact that there are duplicated nodes along the element interfaces, in this work, the number of degrees of freedom per wavelength  $\lambda$  (DPW) is used to give a practical indication of the computational cost. It is computed as

$$DPW = \lambda^3 \sqrt{\frac{N_p \times K}{V}}, \quad (26)$$

where  $N_p \times K$  is the number of degrees of freedom for a single physical variable in the computational domain,  $V$  is the volume of the whole domain.

### A. Free field propagation in periodic domain

To verify the accuracy of the free field propagation, we consider a cubic computational domain of size  $[0, 1]^3$  in meters, which is discretized with six congruent tetrahedral elements.  $10 \times 10 \times 10$  receivers are evenly spaced in all directions throughout the domain. The domain is initialized with a single frequency plane wave propagating in the x-direction only,

$$p(x, t = 0) = \sin(-2\pi x), \quad (27a)$$

$$u(x, t = 0) = \frac{1}{\rho c} \sin(-2\pi x), \quad (27b)$$

$$v(x, t = 0) = 0, \quad w(x, t = 0) = 0. \quad (27c)$$

The wavelength  $\lambda$  is chosen to be equal to 1 m such that periodic boundary conditions can be applied in all directions. As mentioned in Sec. II B, when an initial value problem is

simulated, the approximation error associated with the representations of the initial conditions is a dominant component. In order to rule out this approximation error and to assess the dissipation and dispersion error accumulated from the wave propagation alone, the solution values at receiver locations recorded during the first wave period  $T$  of propagation are taken as the reference values. The solutions sampled during later time period interval  $t = [(n - 1)T, nT]$  are compared with these reference values, where  $n = 10, 20, 30, \dots, 100$ . The amplitude and phase values of the single frequency wave at each of the receiver locations are obtained from a Fourier transform of the recorded time signals without windowing. The dissipation error  $\epsilon_{amp}$  in dB and the phase error  $\epsilon_\phi$  in % are calculated as follows:

$$\epsilon_{amp} = \max \left( 20 \log_{10} \frac{|P_{ref}(x)|}{|P_{nT}(x)|} \right), \quad (28a)$$

$$\epsilon_\phi = \max \left( \frac{|\phi(P_{nT}(x)) - \phi(P_{ref}(x))|}{\pi} \times 100\% \right), \quad (28b)$$

where  $P_{ref}(x)$  and  $P_{nT}(x)$  are the Fourier transform of the recorded pressure values at different locations, during the first time period and the  $n$ th period, respectively.  $\phi(\cdot)$  extracts the phase angle of a complex number.

Simulations for  $N=5, 6, 7$  corresponding to  $DPW=6.9, 7.9, 8.9$  have been carried out and a single time step size  $\Delta t = T/100 = 1/(100 \times 343)$  is used for all simulations to make sure the time integration error is much smaller than the spatial error.

The dissipation and the phase error from the explicit Runge-Kutta time integration is calculated based on the descriptions presented in Ref. 43 and shown as dashed lines in Fig. 1. As can be seen, both the dissipation error and the phase error grow linearly with respect to the propagation distance. For the 5th order polynomial basis ( $DPW=6.9$ ), the averaged dissipation error is approximately 0.035 dB when the wave travels one wavelength distance while the phase error is 0.095%. Both error drop to 0.002 dB and 0.005%, respectively, when the  $DPW$  increases to 8. When the  $DPW$

is equal to 8.9, the dissipation error is  $1.1 \times 10^{-4}$  dB per wavelength of propagation and the phase error is less than  $3 \times 10^{-4}\%$ .

## B. Single reflective plane

To verify the performance of the proposed frequency-independent impedance boundary condition, a single reflection scenario is considered and the reflection coefficient obtained from the numerical tests is compared with the analytical one based on a locally reacting impedance. The experiment consists of two simulations. In the first simulation, we consider a cubic domain of size  $[-8, 8]^3$  in meters, where the source is located at the center  $[0, 0, 0]$  m, and two receivers are placed at  $x_{r1} = [0, 0, -1]$  m and  $x_{r2} = [0, 4, -1]$  m. In this case, the free field propagation of a sound source is simulated, and sound pressure signals are recorded at both receiver locations. In the second simulation, a plane reflecting surface is placed 2 m away from the source at  $z = -2$  m. The measured sound pressure signals not only contain the direct sound but also the sound reflected from the impedance surface. In both cases, initial pressure conditions are used to initiate the simulations:

$$p(x, t = 0) = e^{-\ln(2)/b^2((x-x_s)^2 + (y-y_s)^2 + (z-z_s)^2)}, \quad (29a)$$

$$v(x, t = 0) = 0, \quad (29b)$$

which is a Gaussian pulse centered at the source coordinates  $[x_s, y_s, z_s] = [0, 0, 0]$ . The half-bandwidth of this Gaussian pulse is chosen as  $b = 0.25$  m. Simulations are stopped at around 0.0321 s in order to avoid the waves reflected from the exterior boundaries of the whole domain. In order to eliminate the effects of the unstructured mesh quality on the accuracy, structured tetrahedra meshes are used for this study, which are generated with the meshing software GMSH.<sup>44</sup> The whole cuboid domain is made up of structured cubes of the same size, then each cube is split into six tetrahedra elements. The length of each cube is 0.5 m.

Let  $p_d$  denote the direct sound signal measured from the first simulation, then the reflected sound signal  $p_r(t)$  is

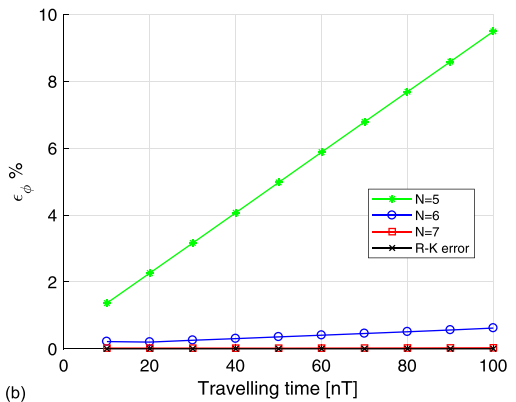
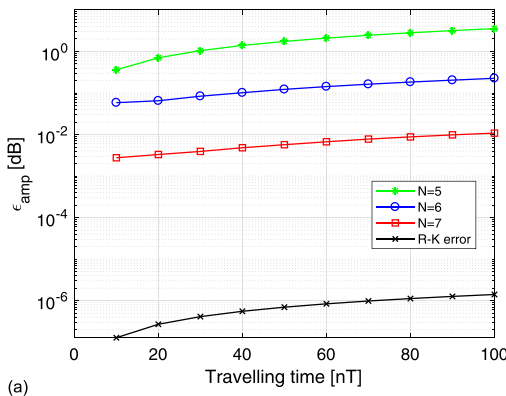


FIG. 1. (Color online) Amplitude error  $\epsilon_{amp}$  (a) and phase error  $\epsilon_\phi$  (b) for the periodic propagation of a single frequency plane wave Eq. (27).

obtained by eliminating  $p_d(t)$  from the solution of the second simulation. Let  $R_1$  denote the distance between the source and the receiver and  $R_2$  is the distance between the receiver and the image source (located at  $[0, 0, -4]$  m) mirrored by the reflecting impedance surface. The spectra of the direct sound and the reflected sound, denoted as  $P_d(f)$  and  $P_r(f)$  respectively, are obtained by Fourier transforming  $p_d$  and  $p_r$  without windowing. The numerical reflection coefficient  $Q_{num}$  is calculated as follows:

$$Q_{num}(f) = \frac{P_r(f) \cdot G(\kappa R_1)}{P_d(f) \cdot G(\kappa R_2)}, \quad (30)$$

where

$$G(\kappa R) = e^{i\kappa R} / R \quad (31)$$

is the Green function in 3D free space.  $\kappa$  is the wavenumber. The analytical spherical wave reflection coefficient  $Q$  reads<sup>45</sup>

$$Q = 1 - 2 \frac{\kappa R_2}{Z_s e^{i\kappa R_2}} \int_0^\infty e^{-q\kappa/Z_s} \frac{e^{i\kappa \sqrt{r_p^2 + (z+z_s+iq)^2}}}{\sqrt{r_p^2 + (z+z_s+iq)^2}} dq, \quad (32)$$

where  $Z_s$  is the normalized surface impedance,  $z=1$  is the distance between the receiver and the reflecting surface,  $z_s=2$  is the distance between the source and the surface,  $r_p$  is the distance between the source and the receiver projected on the reflecting surface.

Simulations with polynomial order  $N=5$  up to  $N=8$  are carried out with the corresponding  $C_{CFL}$  and time step  $\Delta t$  presented in Table I.

The results of the numerical tests for  $Z_s=3$  are illustrated in Fig. 2. The DPW is calculated based on the frequency of 500 Hz. The comparison of the magnitudes of the spherical wave reflection coefficient for both the normal incidence angle  $\theta=0^\circ$  and the oblique incidence ( $\theta=53^\circ$ ) are shown in Figs. 2(a) and 2(b), respectively. The phase angle comparison is presented in Figs. 2(c) and 2(d). It can be seen that with increasing polynomial order  $N$  (or DPW), the numerical reflection coefficient converges to the analytical one in terms of the magnitude and the phase angle. Also, the accuracy is rather independent on the two angles of incidence  $\theta$ . In order to achieve a satisfactory accuracy, at least 12 DPW are needed. Many tests are performed with different impedances ( $Z_s \in [1, \infty]$ ) and receiver locations ( $\theta \in [0^\circ, 90^\circ]$ ), the same conclusion can be reached.

TABLE I.  $C_{CFL}$  number and time step  $\Delta t$  for single reflection case ( $h=0.5$  m).

$N$	$C_{CFL}$	$\Delta t$ [s]
5	0.185	$9.721 \times 10^{-5}$
6	0.144	$7.550 \times 10^{-5}$
7	0.114	$5.993 \times 10^{-5}$
8	0.094	$4.908 \times 10^{-5}$

### C. Cuboid room with rigid boundaries

In this section, the nodal DG method is applied to sound propagation in a 3-D room with rigid boundaries ( $R=1$ ). In contrast to the previous applications, sound propagation inside the room is characterized by multiple reflections and sound energy is conserved. The domain of the room is  $[0, L_x] \times [0, L_y] \times [0, L_z]$  m, with  $L_x=1.8$ ,  $L_y=1.5$ ,  $L_z=2$ . Initial conditions are given as in Eqs. (29), with  $b=0.2$  m. The source is positioned at  $[0.9, 0.75, 1]$  m, and a receiver is positioned at  $[1.7, 1.45, 1.9]$  m. Similar as in the previous test case, the room is discretized using structured tetrahedral elements of size 0.4 m. The analytical pressure response in a cuboid domain can be obtained by the modal summation method, and can in the 3-D Cartesian coordinate system be written as<sup>46</sup>

$$p(\mathbf{x}, t) = \sum_{l=0}^{\infty} \sum_{m=0}^{\infty} \sum_{n=0}^{\infty} \hat{p}_{lmn}(t) \psi_{lmn}(\mathbf{x}) \cos(\omega_{lmn} t), \quad (33a)$$

$$\psi_{lmn}(\mathbf{x}) = \cos\left(\frac{l\pi x}{L_x}\right) \cos\left(\frac{m\pi y}{L_y}\right) \cos\left(\frac{n\pi z}{L_z}\right), \quad (33b)$$

$$\omega_{lmn} = c \sqrt{\left(\frac{l\pi}{L_x}\right)^2 + \left(\frac{m\pi}{L_y}\right)^2 + \left(\frac{n\pi}{L_z}\right)^2}, \quad (33c)$$

with  $\psi_{lmn}$  the modal shape function;  $\hat{p}_{lmn}$  the modal participation factor;  $\omega_{lmn}$  the natural angular frequency; and  $l, m, n$  the mode indices. Since reflections from the room boundaries occur without energy loss, the modal participation factors are constant over time. To obtain  $\hat{p}_{lmn}(0)$ , the initial pressure distribution is projected onto each modal shape as

$$\hat{p}_{lmn}(0) = \frac{1}{\Lambda_{lmn}} \int_{\Omega} p(\mathbf{x}, t=0) \psi_{lmn}(\mathbf{x}) d\mathbf{x}, \quad (34a)$$

$$\Lambda_{lmn} = \int_{\Omega} \psi_{lmn}^2(\mathbf{x}) d\mathbf{x}. \quad (34b)$$

The integration in Eq. (34a) can be calculated separately for each coordinate. For example, in the  $x$  coordinate, the indefinite integration can be expressed in terms of the error function as

$$\begin{aligned} & \int e^{(-a_0(x-x_0)^2)} \cos(b_0 x) dx \\ &= \frac{\sqrt{\pi}}{4\sqrt{a_0}} e^{(-b_0^2/4a_0) - ib_0 x_0} [\text{erf}(B) + e^{(i2b_0 x_0)} \text{erf}(B^*)] + C, \end{aligned} \quad (35)$$

with  $B = \sqrt{a_0}(x-x_0) + ib_0/2\sqrt{a_0}$ ,  $a_0 = \ln(2)/b^2$ ,  $b_0 = l\pi/L_x$ , and  $C$  is a constant. Equation (33a) is used as the reference solution with modal frequencies up to 8 kHz. Furthermore, to show the applicability of the nodal DG method for a long time simulation, 10 s is taken as the simulation duration.

To solve for this configuration, the  $C_{CFL}$  numbers and time steps for the approximating polynomial orders of  $N=3$  up to  $N=7$  are presented in Table II.

The sound pressure level is computed as

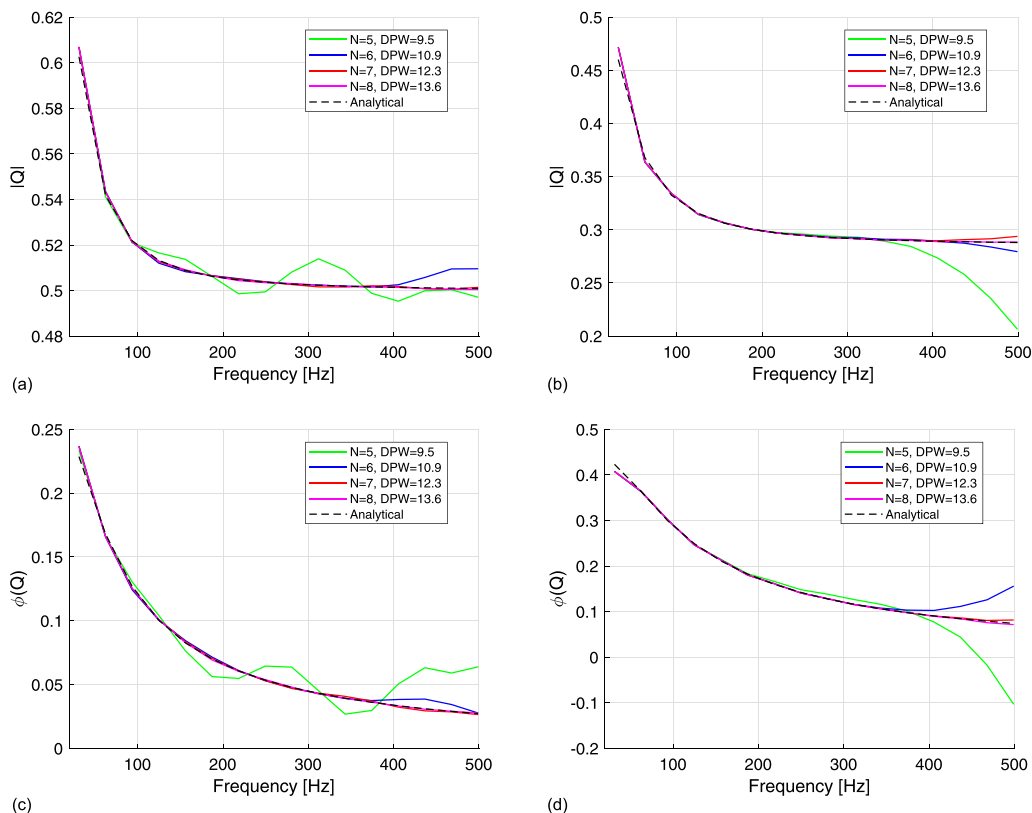


FIG. 2. (Color online) Numerical reflection coefficient calculated by Eq. (30) with different polynomial orders, compared with the theoretical result according to Eq. (32) (black dashed line): (a) magnitude for receiver 1,  $\theta = 0^\circ$ , (b) magnitude for receiver 2,  $\theta = 53^\circ$ , (c) phase angle for receiver 1,  $\theta = 0^\circ$ , (d) phase angle for receiver 2,  $\theta = 53^\circ$ .

$$L_p = 20 \log_{10} \left| \frac{P(f)}{\sqrt{2}P_0} \right|, \quad (36)$$

with  $P_0 = 2 \times 10^{-5}$  Pa, and  $P(f)$  the spectrum of recorded pressure time signal  $p(t)$  at the receiver location. The end of the time signal is tapered using a Gaussian window with a length of 3.5 s to avoid the Gibbs effect.

Figure 3 shows the sound pressure level at the receiver location. The numerical solutions show an excellent agreement with the reference solution, with the accuracy of the numerical solution increasing as the approximating polynomial order increases.

TABLE II.  $C_{CFL}$  number and time step  $\Delta t$  for a rigid cuboid room ( $h = 0.4$  m).

$N$	$C_{CFL}$	$\Delta t$ [s]
3	0.355	$1.400 \times 10^{-4}$
4	0.248	$9.810 \times 10^{-5}$
5	0.185	$7.322 \times 10^{-5}$
6	0.144	$5.687 \times 10^{-5}$
7	0.114	$4.514 \times 10^{-5}$

Figure 4 displays the results for  $f = 950$ – $1000$  Hz. From this figure, we can see that the resonance frequencies are not well represented for  $N \leq 5$ , for which DPW varies between 4.5 and 6.6 in this frequency range. On the other hand, the resonance frequencies are correctly represented for  $N \geq 6$ , where the minimum number of DPW is 7.2. The correct representation of the room resonance frequencies indicates that the numerical dispersion is low in the DG solution. The numerical dispersion aspect is essential with regards to auralization as shown by Saarela *et al.*,<sup>47</sup> where the audibility of the numerical dispersion error from the finite difference time domain simulation is investigated. Furthermore, Fig. 4 clearly shows that the DG results have reduced peak amplitudes when the approximating polynomial orders are low.

#### D. Real room with real-valued impedance boundary conditions

The final scenario is a comparison between experimental and numerical results of a real room. The room is located in the Acoustics Laboratory building (ECHO building) at the campus of the Eindhoven University of Technology. Geometrical data of the room, including the dimensions and

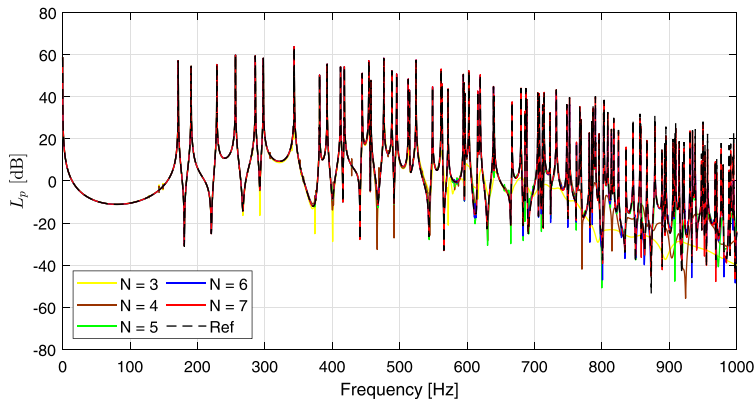


FIG. 3. (Color online) Sound pressure level at receiver position in the configuration of the 3-D rigid cuboid room.

the location of the source and microphone positions are presented in Fig. 5. The room has a volume of  $V=89.54 \text{ m}^3$  and a boundary surface area of  $S=125.08 \text{ m}^2$ .

The source is located at  $[1.7, 2.92, 1.77] \text{ m}$  and microphones (M) are located at  $[3.8, 1.82, 1.66] \text{ m}$  for M1 and  $[4.75, 3.87, 1.63] \text{ m}$  for M2. The height ( $z$ -coordinate) of the sound source location is measured at the opening (highest point) of the used sound source (B&K type 4295, OmniSource Sound Source). The measurements were performed using one free-field microphone B&K type 4189 connected to a Triton USB Audio Interface. The impulse responses were acquired with a sampling frequency of 48 KHz with a laptop using the room acoustics software DIRAC (B&K type 7841). The input channel is calibrated before starting the measurements using a calibrator (B&K type 4230). The sound signal used for the excitation of the room is the DIRAC built-in e-Sweep signal with a duration of 87.4 s connected to an Amphion measurement amplifier. At each microphone position, three measurement repetitions were performed. The results presented in this section for M1 and M2 represent the average of the three repetitions.

The room is discretized in 9524 tetrahedral elements by using GMSH and the largest element size is 0.5 m. A detail of the mesh is shown in Fig. 5(b). The same initial pressure

distribution as for the 3-D cuboid room of Sec. IV C is used. The polynomial order used in the calculations is  $N=4$  with a CFL number of  $C_{CFL}=0.25$ . The computed impulse responses have a duration of 15 s. The model uses a DPW of 13 for the frequency of 400 Hz. All the boundaries of the model are computed using a uniform real-valued reflection coefficient of  $R=0.991$ . The coefficient is calculated from the experimental results at M1 by computing the Q-value of the resonance at  $f_0=97.9 \text{ Hz}$ , using  $R=1-\delta_r 8V/cS$  with,  $\delta_r=2\pi f_0/2Q$  the decay constant of the room's resonance.

Both impulse responses from the measurements and simulations were transformed to the frequency domain by using a forward Fourier transform. The end of the time signals is tapered by a single-sided Gaussian window with a length of 500 samples (approximately, 5.6 ms) to avoid the Gibbs effect. Furthermore, the time function of the numerical source is obtained from the following analytical expression:  $p_{s,ana}(t) = [(r_{sr}-ct)/2r_{sr}]e^{(-\ln(2)/b^2)(r_{sr}-ct)^2} + [(r_{sr}+ct)/2r_{sr}]e^{(-\ln(2)/b^2)(r_{sr}+ct)^2}$  (with  $r_{sr}$  the source-receiver distance). This function is transformed to the frequency domain to normalize the calculated impulse responses in DG by the source power spectrum. Likewise, the experimental results have been normalized by the B&K 4295 sound power spectra. The source spectra of an equivalent source B&K 4295 has

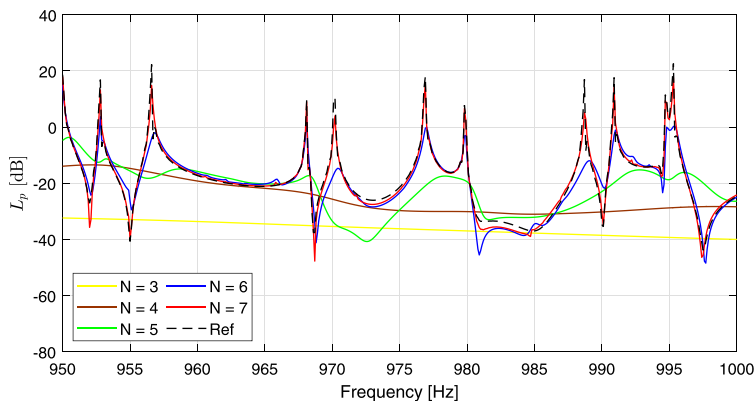


FIG. 4. (Color online) Receiver sound pressure response level between 950 and 1000 Hz.

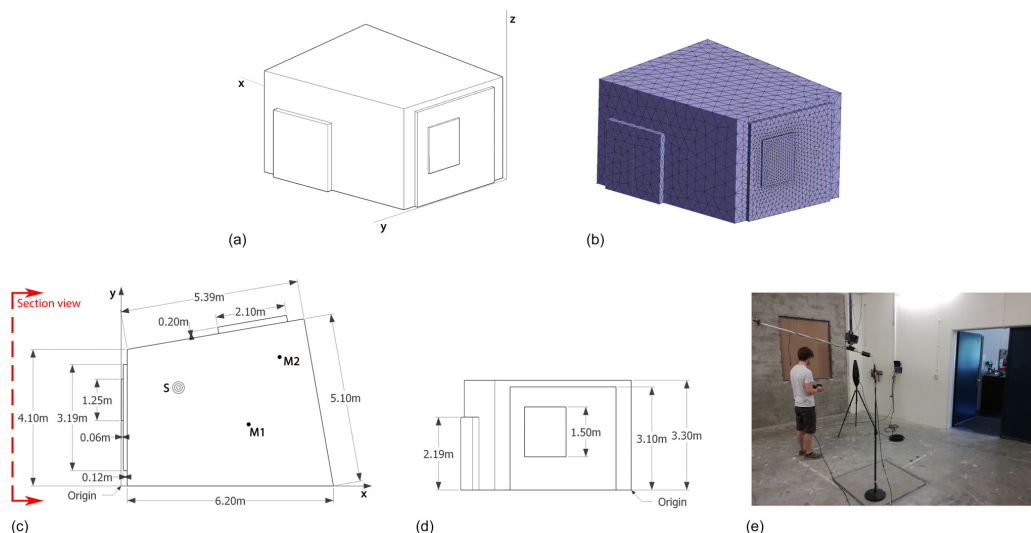


FIG. 5. (Color online) Graphical data of the room under investigation: (a) isometric view; (b) isometric view with surface elements; (c) plan view; (d) section view; (e) picture during the measurements.

been obtained by measurements in the anechoic room of the Department of Medical Physics and Acoustics at Carl von Ossietzky Universität Oldenburg. The corrected results should be taken with care at frequencies below 50 Hz, due to limitations of the anechoic field in the determination of the power spectra of the source. The numerical and experimental results have been normalized at 100 Hz, using the results of position M1.

The comparison between numerical and experimental solutions is shown in Fig. 6 for narrow and 1/3 octave frequency bands. The results are quite satisfactory considering that only one uniform real-valued impedance has been used for the whole frequency range of interest. The biggest deviation, 3.6 dB, is found at position M2 in the 63 Hz 1/3 octave band, while for position M1 the maximum deviation is 2.8 dB in the 250 Hz 1/3 octave band. The average deviation for the 1/3 octave band spectra is 1.2 dB for M1 and 2.3 dB for M2. Overall, the deviations shown in Fig. 6 are within a reasonable range. Factors like the geometrical mismatches between the real room and the model or the uncertainty in the location of the source and microphone positions are influencing the deviations.

## V. CONCLUSIONS

In this paper, the time-domain nodal Discontinuous Galerkin (DG) method has been evaluated as a method to solve the linear acoustic equations for room acoustic purposes. A nodal DG method is used for the evaluation of the spatial derivatives, and for time-integration a low-storage optimized eight-stage explicit Runge-Kutta method is adopted. A new formulation of the impedance boundary condition, which is based on the plane wave reflection coefficient, is proposed to simulate the locally

reacting surfaces with frequency-independent real-valued impedances and its stability is analyzed using the energy method.

The time-domain nodal Discontinuous Galerkin (DG) method is implemented for four configurations. The first test case is a free field propagation, where the dissipation error and the dispersion error are investigated using different polynomial orders. Numerical dissipation exists due to the upwind numerical flux. The benefits of using high-order basis are demonstrated by the significant improvement in accuracy. When DPW is around 9, the dissipation error is  $1.1 \times 10^{-4}$  dB and the phase error is less than  $3 \times 10^{-4}$ ° under propagation of one wavelength. In the second configuration, the validity and convergence of the proposed impedance boundary formulation is demonstrated by investigating the single reflection of a point source over a planar impedance surface. It is found that the accuracy is rather independent on the incidence angle. As a third scenario, a cuboid room with rigid boundaries is used, for which a long-time (10 s) simulation is run. By comparing against the analytical solution, it can be concluded again that with a sufficiently high polynomial order, the dispersion and dissipation error become very small. Finally, the comparison between numerical and experimental solutions shows that DG is a suitable tool for acoustic predictions in rooms. Taking into account that only one uniform real-valued impedance has been used for the whole frequency range of interest, the results are quite satisfactory. In this case, the implementation of frequency dependent boundary conditions will clearly improve the precision of the numerical results.

In this study, the performance of the time-domain nodal DG method is investigated by comparing with analytical solutions and experimental results, without comparing with

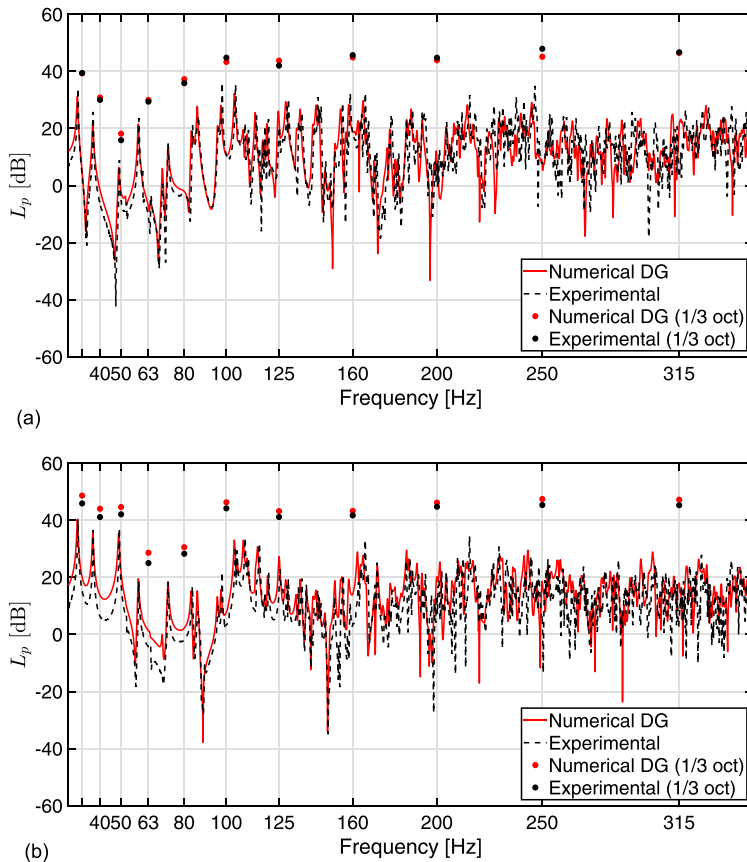


FIG. 6. (Color online) Sound pressure level  $L_p$  in the real room configuration for the experimental and the DG results in narrow frequency bands (black broken line and red solid line, respectively) and 1/3 octave bands (black dot and red dot, respectively) for the microphone positions (a) M1 and (b) M2.

other commonly used room acoustics modelling techniques such as FDTD and FEM. The aim of this work is to demonstrate the viability of the DG method to room acoustics modelling, where high-order accuracy and geometrical flexibility are of key importance. With the opportunity to massively parallelize the DG method, it has great potential as a wave-based method for room acoustic purposes. Whereas the results show that high accuracy can be achieved with DG, some issues remain to be addressed. The improvements in accuracy using high-order schemes come at a cost of smaller time step size for the sake of stability. There is a trade-off between a high-order scheme with a small time step and fewer spatial points and low-order methods, where a larger time step is allowed but a higher number of spatial points are needed to achieve the same accuracy. Further investigations are needed to find out the most cost-efficient combination of the polynomial order and the mesh size under a given accuracy requirement. Also, when the mesh configuration is fixed by the geometry, the local adaptivity of polynomial orders and time step sizes could be a feasible approach to improve the computational efficiency of DG for room acoustics applications. Furthermore, general frequency-dependent impedance boundary conditions as

well as extended reacting boundary conditions are still to be rigorously developed in DG.

## ACKNOWLEDGMENTS

This project has received funding from the European Union's Horizon 2020 research and innovation programme under Grant Agreement No. 721536. The second author is supported by the ministry of finance of the Republic of Indonesia under framework of endowment fund for education (LPDP). Additionally, we would like to thank the Department of Medical Physics and Acoustics at Carl von Ossietzky Universität Oldenburg for their help in the estimation of the sound power spectra of the sound source.

## APPENDIX: DERIVATIONS OF THE TOTAL DISCRETE ACOUSTIC ENERGY OF THE SEMI-DISCRETE SYSTEM

It can be seen that the local energy can be recovered from the product of the element mass matrix  $\mathbf{M}^k$  and the nodal vectors  $\mathbf{u}_h^k$  as follows:

$$\begin{aligned} (u_h^k)^T M^k u_h^k &= \int_{D^k} \sum_{i=1}^{N_p} u_h^k(x_i^k, t) l_i^k(x) \sum_{j=1}^{N_p} u_h^k(x_j^k, t) l_j^k(x) dx \\ &= \|u_h^k\|_{D^k}^2. \end{aligned} \quad (A1)$$

Furthermore, it can be verified that

$$\begin{aligned} (u_h^k)^T S_x^k p_h^k &= \int_{D^k} \sum_{i=1}^{N_p} p_h^k(x_i^k, t) l_i^k(x) \sum_{j=1}^{N_p} u_h^k(x_j^k, t) \frac{\partial l_j^k(x)}{\partial x} dx \\ &= \int_{D^k} p_h^k(x, t) \frac{\partial u_h^k(x, t)}{\partial x} dx = \left( p_h^k, \frac{\partial u_h^k}{\partial x} \right)_{D^k} \end{aligned} \quad (A2)$$

and

$$\begin{aligned} (u_h^k)^T M^{kr} p_h^{kr} &= \int_{\partial D^{kr}} \sum_{i=1}^{N_p} u_h^k(x_i^k, t) l_i^k(x) \sum_{j=1}^{N_{fp}} p_h^{kr}(x_j^{kr}, t) l_j^{kr}(x) dx \\ &= \int_{\partial D^{kr}} \sum_{i=1}^{N_{fp}} u_h^{kr}(x_i^{kr}, t) l_i^{kr}(x) \sum_{j=1}^{N_{fp}} p_h^{kr}(x_j^{kr}, t) l_j^{kr}(x) dx \\ &= \int_{\partial D^{kr}} u_h^{kr}(x, t) p_h^{kr}(x, t) dx = (u_h^{kr}, p_h^{kr})_{\partial D^{kr}}. \end{aligned} \quad (A3)$$

Now, the total discrete acoustic energy  $E_h$  of the semi-discrete formulation Eq. (13) can be calculated. By pre-multiplying Eq. (13a) with  $\rho(u_h^k)^T$ , pre-multiplying Eq. (13b) with  $\rho(v_h^k)^T$ , pre-multiplying Eq. (13c) with  $\rho(w_h^k)^T$ , pre-multiplying Eq. (13d) with  $(1/\rho c^2)(p_h^k)^T$  and sum them together, using the relations mentioned in Eqs. (A1), (A2), yields

$$\begin{aligned} \frac{d}{dt} E_h^k &= - \sum_{r=1}^f \left( n_x^{kr} (u_h^{kr}, p_h^{kr})_{\partial D^{kr}} + n_y^{kr} (v_h^{kr}, p_h^{kr})_{\partial D^{kr}} \right. \\ &\quad + n_z^{kr} (w_h^{kr}, p_h^{kr})_{\partial D^{kr}} \dots + \rho (u_h^k)^T \sum_{r=1}^f M^{kr} \hat{F}_u^{kr} \\ &\quad + \rho (v_h^k)^T \sum_{r=1}^f M^{kr} \hat{F}_v^{kr} + \rho (w_h^k)^T \sum_{r=1}^f M^{kr} \hat{F}_w^{kr} \\ &\quad \left. + \frac{1}{\rho c^2} (p_h^k)^T \sum_{r=1}^f M^{kr} \hat{F}_p^{kr} \right), \end{aligned} \quad (A4)$$

where the divergence theorem is used to obtain the surface integral term, that is

$$\begin{aligned} &\left( u_h^k, \frac{\partial p_h^k}{\partial x} \right)_{D^k} + \left( v_h^k, \frac{\partial p_h^k}{\partial y} \right)_{D^k} + \left( w_h^k, \frac{\partial p_h^k}{\partial z} \right)_{D^k} \\ &\quad + \left( p_h^k, \frac{\partial u_h^k}{\partial x} \right)_{D^k} + \left( p_h^k, \frac{\partial v_h^k}{\partial y} \right)_{D^k} + \left( p_h^k, \frac{\partial w_h^k}{\partial z} \right)_{D^k} \\ &= \sum_{r=1}^f \left( n_x^{kr} (u_h^{kr}, p_h^{kr})_{\partial D^{kr}} + n_y^{kr} (v_h^{kr}, p_h^{kr})_{\partial D^{kr}} \right. \\ &\quad \left. + n_z^{kr} (w_h^{kr}, p_h^{kr})_{\partial D^{kr}} \right). \end{aligned} \quad (A5)$$

Substitute the numerical flux Eqs. (15) into Eq. (A4) and use Eq. (A3), after some simple algebraic manipulations, the semi-discrete acoustic energy balance on element yields

$$\frac{d}{dt} E_h^k = \sum_{r=1}^f \mathcal{R}_h^{kr}, \quad (A6)$$

where

$$\begin{aligned} \mathcal{R}_h^{kr} &= (p_h^{kr}, v_{hn}^{kr})_{\partial D^{kr}} - \frac{1}{2} (\omega_o^{kr}, p_h^{kr} + \rho c v_{hn}^{kr})_{\partial D^{kr}} \\ &\quad + \frac{1}{2} (\omega_i^{kr}, p_h^{kr} - \rho c v_{hn}^{kr})_{\partial D^{kr}} \end{aligned} \quad (A7)$$

is the discrete energy flux through the shared surface  $\partial D^{kr}$  or equivalently  $\partial D^{ls}$  between the neighboring elements  $D^k$  and  $D^l$  in the interior of the computation domain.  $\omega_o$  and  $\omega_i$  are the characteristic waves defined in Eq. (18). By using the condition that the outward normal vector of neighboring elements are opposite, the final form of energy contribution from the coupling across one shared interface reads

$$\begin{aligned} \mathcal{R}_h^{kr} + \mathcal{R}_h^{ls} &= - \left( \frac{1}{2\rho c} \|p_h^{kr}\|_{\partial D^{kr}}^2 + \frac{\rho c}{2} \|n_x^{kr} [u_h^{kr}] \right. \\ &\quad \left. + n_y^{kr} [v_h^{kr}] + n_z^{kr} [w_h^{kr}] \|_{\partial D^{kr}}^2 \right), \end{aligned} \quad (A8)$$

which is non-positive. This ends the discussion for the interior elements. Now, for elements that have at least one surface lying on the real-valued impedance boundary, e.g., element  $D^m$  with surface  $\partial D^{mt} \in \partial\Omega_h$ , the numerical flux is calculated using Eq. (19). After some algebraic operations, the energy flux through the reflective boundary surface becomes

$$\mathcal{R}_h^{mt} = - \left( \frac{1 - R^{mt}}{2\rho c} \|p_h^{mt}\|_{\partial D^{mt}}^2 + \frac{\rho c}{2} (1 + R^{mt}) \|v_{hn}^{mt}\|_{\partial D^{mt}}^2 \right). \quad (A9)$$

Finally, by summing the energy flux through all of the faces of the mesh, we get the total acoustic energy of the whole semi-discrete system as in Eq. (23).

<sup>1</sup>M. R. Schroeder, "Novel uses of digital computers in room acoustics," *J. Acoust. Soc. Am.* **33**(11), 1669–1669 (1961).

<sup>2</sup>M. Vorländer, "Computer simulations in room acoustics: Concepts and uncertainties," *J. Acoust. Soc. Am.* **133**(3), 1203–1213 (2013).

<sup>3</sup>L. Savijs and U. P. Svensson, "Overview of geometrical room acoustic modeling techniques," *J. Acoust. Soc. Am.* **138**(2), 708–730 (2015).

<sup>4</sup>B. Hamilton, "Finite difference and finite volume methods for wave-based modelling of room acoustics," Ph.D. dissertation, The University of Edinburgh, Edinburgh, Scotland, 2016.

<sup>5</sup>V. Valeau, J. Picaut, and M. Hodgson, "On the use of a diffusion equation for room-acoustic prediction," *J. Acoust. Soc. Am.* **119**(3), 1504–1513 (2006).

<sup>6</sup>J. M. Navarro, J. Escolano, and J. J. López, "Implementation and evaluation of a diffusion equation model based on finite difference schemes for sound field prediction in rooms," *Appl. Acoust.* **73**(6-7), 659–665 (2012).

<sup>7</sup>D. Botteldooren, "Finite-difference time-domain simulation of low-frequency room acoustic problems," *J. Acoust. Soc. Am.* **98**(6), 3302–3308 (1995).

- <sup>8</sup>J. Sheaffer, M. van Walstijn, and B. Fazenda, "Physical and numerical constraints in source modeling for finite difference simulation of room acoustics," *J. Acoust. Soc. Am.* **135**(1), 251–261 (2014).
- <sup>9</sup>C. Spa, A. Rey, and E. Hernandez, "A GPU implementation of an explicit compact FDTD algorithm with a digital impedance filter for room acoustics applications," *IEEE/ACM Trans. Audio Speech Lang. Process.* **23**(8), 1368–1380 (2015).
- <sup>10</sup>B. Hamilton and S. Bilbao, "FDTD methods for 3-D room acoustics simulation with high-order accuracy in space and time," *IEEE/ACM Trans. Audio Speech Lang. Process.* **25**(11), 2112–2124 (2017).
- <sup>11</sup>T. Okuzono, T. Yoshida, K. Sakagami, and T. Otsuru, "An explicit time-domain finite element method for room acoustics simulations: Comparison of the performance with implicit methods," *Appl. Acoust.* **104**, 76–84 (2016).
- <sup>12</sup>S. Bilbao, "Modeling of complex geometries and boundary conditions in finite difference/finite volume time domain room acoustics simulation," *IEEE Trans. Audio Speech Lang. Process.* **21**(7), 1524–1533 (2013).
- <sup>13</sup>R. Mehra, N. Raghuvanshi, L. Savioja, M. C. Lin, and D. Manocha, "An efficient GPU-based time domain solver for the acoustic wave equation," *Appl. Acoust.* **73**(2), 83–94 (2012).
- <sup>14</sup>C. Spa, A. Garriga, and J. Escolano, "Impedance boundary conditions for pseudo-spectral time-domain methods in room acoustics," *Appl. Acoust.* **71**(5), 402–410 (2010).
- <sup>15</sup>M. Hornikx, W. De Roeck, and W. Desmet, "A multi-domain Fourier pseudospectral time-domain method for the linearized Euler equations," *J. Comput. Phys.* **231**(14), 4759–4774 (2012).
- <sup>16</sup>M. Hornikx, C. Hak, and R. Wenmaekers, "Acoustic modelling of sports halls, two case studies," *J. Build. Perform. Simul.* **8**(1), 26–38 (2015).
- <sup>17</sup>B. Cockburn and C.-W. Shu, "TVB Runge-Kutta local projection discontinuous Galerkin finite element method for conservation laws II: General framework," *Math. Comput.* **52**(186), 411 (1989).
- <sup>18</sup>Y. Reynen, W. De Roeck, G. Rubio, M. Baelmans, and W. Desmet, "A 3D discontinuous Galerkin method for aeroacoustic propagation," in *Twelfth International Congress on Sound and Vibration*, Lisbon, Portugal (2005).
- <sup>19</sup>J. Nytra, L. Čermák, and M. Jícha, "Applications of the discontinuous Galerkin method to propagating acoustic wave problems," *Adv. Mech. Eng.* **9**(6), 168781401770363 (2017).
- <sup>20</sup>A. Modave, A. St-Cyr, and T. Warburton, "GPU performance analysis of a nodal discontinuous Galerkin method for acoustic and elastic models," *Comput. Geosci.* **91**, 64–76 (2016).
- <sup>21</sup>Y. Reynen, M. Baelmans, and W. Desmet, "Efficient implementation of Tam and Auriault's time-domain impedance boundary condition," *AIAA J.* **46**(9), 2368–2376 (2008).
- <sup>22</sup>K.-Y. Fung and H. Ju, "Broadband time-domain impedance models," *AIAA J.* **39**(8), 1449–1454 (2001).
- <sup>23</sup>V. E. Ostashev, D. K. Wilson, L. Liu, D. F. Aldridge, N. P. Symons, and D. Marlin, "Equations for finite-difference, time-domain simulation of sound propagation in moving inhomogeneous media and numerical implementation," *J. Acoust. Soc. Am.* **117**(2), 503–517 (2005).
- <sup>24</sup>H. L. Atkins and C.-W. Shu, "Quadrature-free implementation of discontinuous Galerkin method for hyperbolic equations," *AIAA J.* **36**(5), 775–782 (1998).
- <sup>25</sup>J. S. Hesthaven and T. Warburton, *Nodal Discontinuous Galerkin Methods: Algorithms, Analysis and Applications* (Springer-Verlag, New York, 2007), Chaps. 2,3,4,6,10.
- <sup>26</sup>J. S. Hesthaven and C.-H. Teng, "Stable spectral methods on tetrahedral elements," *SIAM J. Sci. Comput.* **21**(6), 2352–2380 (2000).
- <sup>27</sup>R. J. LeVeque, *Finite Volume Methods for Hyperbolic Problems* (Cambridge University Press, Cambridge, 2002), Chap. 2.
- <sup>28</sup>P. Lasaint and P.-A. Raviart, "On a finite element method for solving the neutron transport equation," in *Mathematical Aspects of Finite Elements in Partial Differential Equations* (Elsevier, Amsterdam, 1974), pp. 89–123.
- <sup>29</sup>F. Q. Hu and H. Atkins, "Eigensolution analysis of the discontinuous Galerkin method with nonuniform grids: I. One space dimension," *J. Comput. Phys.* **182**(2), 516–545 (2002).
- <sup>30</sup>M. Ainsworth, "Dispersive and dissipative behaviour of high order discontinuous Galerkin finite element methods," *J. Comput. Phys.* **198**(1), 106–130 (2004).
- <sup>31</sup>F. Q. Hu, M. Hussaini, and P. Rasetarinera, "An analysis of the discontinuous Galerkin method for wave propagation problems," *J. Comput. Phys.* **151**(2), 921–946 (1999).
- <sup>32</sup>F. Hu and H. Atkins, "Two-dimensional wave analysis of the discontinuous Galerkin method with non-uniform grids and boundary conditions," in *8th AIAA/CEAS Aeroacoustics Conference & Exhibit* (2002), p. 2514.
- <sup>33</sup>T. Toulorge and W. Desmet, "Optimal Runge-Kutta schemes for discontinuous Galerkin space discretizations applied to wave propagation problems," *J. Comput. Phys.* **231**(4), 2067–2091 (2012).
- <sup>34</sup>H. Atkins, "Continued development of the discontinuous Galerkin method for computational aeroacoustic applications," in *3rd AIAA/CEAS Aeroacoustics Conference* (1997), p. 1581.
- <sup>35</sup>B.-T. Chu and L. S. Kovásznyai, "Non-linear interactions in a viscous heat-conducting compressible gas," *J. Fluid Mech.* **3**(5), 494–514 (1958).
- <sup>36</sup>K. W. Thompson, "Time dependent boundary conditions for hyperbolic systems," *J. Comput. Phys.* **68**(1), 1–24 (1987).
- <sup>37</sup>B. Engquist and A. Majda, "Absorbing boundary conditions for numerical simulation of waves," *Proc. Natl. Acad. Sci.* **74**(5), 1765–1766 (1977).
- <sup>38</sup>B. Gustafsson, *High Order Difference Methods for Time Dependent PDE* (Springer-Verlag, Berlin, 2007), Chap. 2.
- <sup>39</sup>S. Bilbao, B. Hamilton, J. Botts, and L. Savioja, "Finite volume time domain room acoustics simulation under general impedance boundary conditions," *IEEE/ACM Trans. Audio Speech Lang. Process.* **24**(1), 161–173 (2016).
- <sup>40</sup>D. Dragna, K. Attenborough, and P. Blanc-Benon, "On the inadvisability of using single parameter impedance models for representing the acoustical properties of ground surfaces," *J. Acoust. Soc. Am.* **138**(4), 2399–2413 (2015).
- <sup>41</sup>S. C. Reddy and L. N. Trefethen, "Stability of the method of lines," *Numer. Math.* **62**(1), 235–267 (1992).
- <sup>42</sup>H. O. Kreiss and L. Wu, "On the stability definition of difference approximations for the initial boundary value problem," *Appl. Numer. Math.* **12**(1-3), 213–227 (1993).
- <sup>43</sup>C. Bogey and C. Bailly, "A family of low dispersive and low dissipative explicit schemes for flow and noise computations," *J. Comput. Phys.* **194**(1), 194–214 (2004).
- <sup>44</sup>C. Geuzaine and J.-F. Remacle, "GMSH: A 3-D finite element mesh generator with built-in pre- and post-processing facilities," *Int. J. Numer. Meth. Eng.* **79**(11), 1309–1331 (2009).
- <sup>45</sup>X. Di and K. E. Gilbert, "An exact Laplace transform formulation for a point source above a ground surface," *J. Acoust. Soc. Am.* **93**(2), 714–720 (1993).
- <sup>46</sup>H. Kuttruff, *Acoustics: An Introduction* (CRC Press, Boca Raton, FL, 2006), Chap. 9.
- <sup>47</sup>J. Saarela, J. Botts, B. Hamilton, and L. Savioja, "Audibility of dispersion error in room acoustic finite-difference time-domain simulation as a function of simulation distance," *J. Acoust. Soc. Am.* **139**(4), 1822–1832 (2016).

---

## Errata of Paper I

- Eq. (11)

$$\mathbf{L} = \begin{bmatrix} -n_z & n_y & n_x/2 & -n_x/2 \\ n_z & -n_x & n_y/2 & -n_y/2 \\ -n_y & n_x & n_z/2 & -n_z/2 \\ 0 & 0 & \rho_0 c_0/2 & \rho_0 c_0/2 \end{bmatrix}, \quad \mathbf{\Lambda} = \begin{bmatrix} 0 & 0 & 0 & 0 \\ 0 & 0 & 0 & 0 \\ 0 & 0 & c_0 & 0 \\ 0 & 0 & 0 & -c_0 \end{bmatrix}.$$

should be replaced by

$$\mathbf{L} = \begin{bmatrix} -n_y & -n_z & n_x/2 & -n_x/2 \\ n_x & 0 & n_y/2 & -n_y/2 \\ 0 & n_x & n_z/2 & -n_z/2 \\ 0 & 0 & \rho_0 c_0/2 & \rho_0 c_0/2 \end{bmatrix}, \quad \mathbf{\Lambda} = \begin{bmatrix} 0 & 0 & 0 & 0 \\ 0 & 0 & 0 & 0 \\ 0 & 0 & c_0 & 0 \\ 0 & 0 & 0 & -c_0 \end{bmatrix}.$$

---

# Paper II

# Time-domain impedance boundary condition modeling with the discontinuous Galerkin method for room acoustics simulations

Huiqing Wang<sup>a)</sup> and Maarten Hornikx<sup>b)</sup>

*Building Physics and Services, Department of the Built Environment, Eindhoven University of Technology, P.O. Box 513, 5600 MB Eindhoven, The Netherlands*

## ABSTRACT:

The time-domain nodal discontinuous Galerkin (TD-DG) method is emerging as a potential wave-based method for three-dimensional (3D) room acoustics modeling, where high-order accuracy in the low frequency range, geometrical flexibility, and accurate modeling of boundary conditions are of critical importance. This paper presents a formulation of broadband time-domain impedance boundary conditions (TDIBC) of locally-reacting surfaces in the framework of the TD-DG method. The formulation is based on the approximation of the plane-wave reflection coefficient at normal incidence in the frequency domain using a sum of template rational functions, which can be directly transformed to the time-domain. The coupling of the TDIBCs with the discontinuous Galerkin discretization is achieved through the characteristic waves of the upwind flux along the boundary, where a series of first-order auxiliary differential equations is time-integrated in a high-order way. To verify the performance of the formulation, various numerical tests of single reflection scenarios are shown to demonstrate the cost efficiency and memory-efficiency of high-order basis functions, among which a 3D application to an impedance boundary of rigidly backed glass-wool baffle for room acoustic purposes is presented. © 2020 Acoustical Society of America.

<https://doi.org/10.1121/10.0001128>

(Received 31 August 2019; revised 2 April 2020; accepted 3 April 2020; published online 23 April 2020)

[Editor: Lauri Savioja]

Pages: 2534–2546

## I. INTRODUCTION

Sound propagation in a room is a complicated process due to the geometry of the room and the objects inside it. Furthermore, a variety of surface natures and surface impedances, which are typically frequency-dependent, make it extremely hard to achieve analytical representations of the acoustic field. Therefore, computer simulation of the sound field in indoor environments has become a common tool for the analysis of sound in rooms.<sup>1</sup>

In general, room acoustic modeling techniques can be divided into two categories, namely, geometrical acoustics methods and wave-based methods. Thanks to the steady increase in computing power, wave-based methods have become more mature during the past decades.<sup>2</sup> Compared to frequency-domain wave-based methods, time-domain modeling allows single run broadband calculations with moving sources and time-varying domains and generates directly the impulse response of the room. After applications to fields as aeroacoustics,<sup>3</sup> the time-domain discontinuous Galerkin (TD-DG) method has for the first time been evaluated as a potential wave-based method for room acoustics modeling purposes.<sup>4</sup> Its high accuracy and ability to handle complex boundary geometries were demonstrated through verifications by analytical solutions and by comparison against measurement results of a real room. Since the

acoustic wave equation is solved element-wise, highly efficient parallel-computing solvers that exploit modern hardware have been developed.<sup>5,6</sup> The applicability of the discontinuous Galerkin (DG) solver to a large scale room acoustics simulation is demonstrated in Ref. 7, in analogy to the example of a cathedral-like geometry presented in Ref. 8. However, in order to provide physical simulation results that match real materials, a time-domain impedance boundary condition (TDIBC) formulation that handles frequency-dependent acoustic properties is needed.

The acoustic behavior of a locally reactive reflecting surface can be characterized by the surface impedance,<sup>9</sup> the admittance,<sup>10–12</sup> or the plane-wave reflection coefficient.<sup>13–16</sup> Although these quantities are mathematically equivalent, the implementations of their respective TDIBC models differ at a discrete level. Furthermore, for time-domain computations, the impedance models defined in the frequency domain should satisfy the causality, reality, and passivity conditions in order to be physically admissible.<sup>9,17,18</sup> One approach to incorporate the frequency-dependency is to model the impedance boundary based on the mass-spring-damper system.<sup>10,11,19–22</sup> Besides, approaches based on well-chosen basis functions or digital filters in the frequency domain have been developed. Zhong *et al.*<sup>12</sup> proposed to transform the frequency domain transfer function of the impedance model in the form of rational polynomials to an equivalent time-domain representation using the state-space canonical form. Approaches based on digital filter design have been proposed in Refs. 23 and 24. Another popular family of impedance

<sup>a)</sup>Electronic mail: h.wang6@tue.nl, ORCID: 0000-0003-3465-3555.

<sup>b)</sup>ORCID: 0000-0002-8343-6613.

models is the so-called multi-pole model,<sup>10,13,14,16,25–28</sup> which offers great flexibility for fitting impedance values while ensuring physical admissibility conditions.

The aforementioned various TDIBC formulations and the corresponding stability analysis are usually tailored to the specific discretization methods that are used to simulate acoustic wave propagation. For example, a formulation based on the admittance in the framework of the finite volume method and its fully-discrete stability analysis using the trapezoid rule approximation to the time derivative is presented in Ref. 29. For the TD-DG method, an early attempt to implement the impedance boundary condition was made by Reyman *et al.*,<sup>10</sup> where the three-parameter impedance model<sup>20</sup> was reformulated in the form of a complex conjugate pole. The normal velocity on the impedance boundary was updated based on the convolution of the pressure from previous time steps with the impulse response of the admittance and the convolution is calculated in a piecewise-linear recursive way. Recently, two formulations based on the reflection coefficient instead of the impedance or admittance were proposed in Ref. 30 and Ref. 4 at the same time. Compared to the TDIBC formulations based on either the impedance or the admittance, the formulation using the reflection coefficient is computationally desirable as it is capable of handling singular cases of both the hard-wall and pressure-release boundaries without the need for exceptional treatments, where the impedance and the admittance value approaches infinity, respectively. Reference 4 adopts the upwind flux based on the characteristics of the hyperbolic law throughout the whole computational domain while Ref. 30 uses the centered flux along the impedance boundary and the upwind flux on the interior of the domain. From the analysis of dispersive properties,<sup>31,32</sup> the central flux has zero dissipation error. However, it could exhibit unphysical waves. Compared to the upwind flux, it is less accurate in terms of the dispersion error, which is of vital importance for the room acoustic auralization applications as shown by Saarelna *et al.*<sup>34</sup>

The main objective of this work is to develop a robust, efficient and generic TDIBC for locally-reacting materials, aiming at a further step towards a fully-fledged TD-DG solver for realistic room acoustic simulations. The formulation of the numerical flux along the impedance boundary is derived straightforwardly based on the plane-wave reflection coefficient and the characteristic acoustic waves, and its detailed implementations in the DG method are presented. The extension of previous frequency-independent impedance boundary formulation<sup>4</sup> to the frequency-dependent one is achieved through the multi-pole representation of the reflection coefficient in the frequency domain. The fitting of parameters of this representation for an empirical impedance model or measurement data is achieved by solving an optimization problem. Combined with the auxiliary differential equations (ADE) method, the whole computation can be performed in a low-storage and high-order accuracy manner. To validate this formulation, numerical simulations of a single reflection scenario are performed. The convergence rates are verified and the benefits of using the high-order polynomial basis are highlighted. Both the amplitude and the phase

error from the reflection, which are important for room acoustics modeling featuring multiple reflections, are investigated and quantified for both the plane-wave reflection in a one-dimensional (1D) setting and the spherical-wave reflection in a three-dimensional (3D) case. Application to a typical impedance model of a rigid-frame porous material for room acoustic uses is used to demonstrate the feasibility of the proposed approach.

The paper is organized as follows. The formulations of impedance boundary conditions within the TD-DG method are presented in Sec. II. Section III discusses and quantifies the accuracy of the implemented formulation by comparison with analytical solutions. Finally, the conclusions and outlook can be found in Sec. IV.

## II. TDIBC IN DG METHOD

### A. Governing equations and spatial discretization

In this work, the governing equations are the linear acoustic equations for a motionless propagation medium

$$\begin{aligned}\frac{\partial \mathbf{v}}{\partial t} + \frac{1}{\rho} \nabla p &= \mathbf{0}, \\ \frac{\partial p}{\partial t} + \rho c^2 \nabla \cdot \mathbf{v} &= 0,\end{aligned}\quad (1)$$

where  $\mathbf{v} = [u, v, w]^T$  is the particle velocity vector,  $p$  is the sound pressure,  $\rho$  is the constant density of air, and  $c$  is the constant speed of sound. Equivalently, Eq. (1) reads

$$\frac{\partial \mathbf{q}}{\partial t} + \nabla \cdot \mathbf{F}(\mathbf{q}) = \frac{\partial \mathbf{q}}{\partial t} + \mathbf{A}_j \frac{\partial \mathbf{q}}{\partial x_j} = 0, \quad (2)$$

where  $\mathbf{q}(x, t) = [u, v, w, p]^T$  is the acoustic variable vector and  $\mathbf{A}_j$  is the constant flux Jacobian matrix with coordinate index  $j \in [x, y, z]$ . Let  $D^k$  be a set of simplex and geometrically conformal elements that discretize the computational domain  $\Omega_h$ , i.e.,  $\Omega_h = \bigcup_{k=1}^K D^k$ . The local solution  $\mathbf{q}_h^k(x, t)$  in element  $D^k$ , where subscript  $h$  denotes the numerical approximation, is given by

$$\mathbf{q}_h^k(x, t) = \sum_{i=1}^{N_p} \mathbf{q}_h^k(x_i^k, t) l_i^k(x), \quad (3)$$

where  $\mathbf{q}_h^k(x_i^k, t)$  are the unknown nodal values,  $l_i^k(x_i^k)$  is the multi-dimensional Lagrange polynomial basis of order  $N$ , which satisfies  $l_i^k(x_j^k) = \delta_{ij}$ , and indices  $i, j$  denote the ordering of nodes.  $N_p$  is the number of local basis functions (or nodes) inside a single element and equal to  $(N + d)!/(N!d!)$  for simplex elements, where  $d$  is the dimensionality. The basis (shape) function  $l_i^k(x)$  is determined by the nodal distribution  $\mathbf{x}_i^k$ , and in this study, the Legendre-Gauss-Lobatto (LGL) quadrature points are used for 1D problems and the  $\alpha$ -optimized nodes distribution<sup>35</sup> is used for 3D tetrahedron elements due to its low Lebesgue constants. After the Galerkin projection and integration by parts twice, the semi-discrete nodal DG formulation of Eq. (2) reads,

$$\int_{D^k} \left( \frac{\partial \mathbf{q}_h^k}{\partial t} + \nabla \cdot \mathbf{F}_h^k(\mathbf{q}_h^k) \right) \ell_i^k d\mathbf{x} = \int_{\partial D^k} \mathbf{n} \cdot (\mathbf{F}_h^k(\mathbf{q}_h^k) - \mathbf{F}^*) \ell_i^k d\mathbf{x}, \quad (4)$$

where  $\mathbf{n} = [n_x, n_y, n_z]$  is the outward normal vector of the element surface  $\partial D^k$ .  $\mathbf{F}^*$ , the so-called numerical flux across element intersection  $\partial D^k$ , is a function of both the solution value from the interior side of the intersection, i.e.,  $\mathbf{q}_h^-$  and the exterior value  $\mathbf{q}_h^+$ . In this study, the upwind numerical flux is used throughout the whole domain because of its low dispersive and dissipation error.<sup>33,36</sup> It is defined by considering the direction of the characteristic speed, i.e.,

$$\mathbf{n} \cdot \mathbf{F}^*(\mathbf{q}_h^-, \mathbf{q}_h^+) = \mathbf{L}(\mathbf{\Lambda}^+ \mathbf{L}^{-1} \mathbf{q}_h^- + \mathbf{\Lambda}^- \mathbf{L}^{-1} \mathbf{q}_h^+), \quad (5)$$

where  $\mathbf{\Lambda}$  is a diagonal matrix with diagonal entries  $[0, 0, c, -c]$ .  $\mathbf{\Lambda}^+$  and  $\mathbf{\Lambda}^-$  contain the positive and negative entries of  $\mathbf{\Lambda}$ , respectively.  $\mathbf{L}$  is the eigenmatrix of the normally projected flux Jacobian, i.e.,

$$\begin{aligned} \mathbf{A}_n &= (n_x \mathbf{A}_x + n_y \mathbf{A}_y + n_z \mathbf{A}_z) \\ &= \mathbf{L} \mathbf{\Lambda} \mathbf{L}^{-1}. \end{aligned} \quad (6)$$

Physically,  $\mathbf{\Lambda}^+$  ( $\mathbf{\Lambda}^-$ , respectively) corresponds to the characteristic waves propagating along (opposite to respectively) the outward normal direction  $\mathbf{n}$ , which is referred to as outgoing waves out of  $D_k$  (incoming waves into  $D_k$ , respectively). Therefore, the outgoing waves are associated with the interior solution  $\mathbf{q}_h^-$ , whereas the incoming waves are dependent on the exterior (neighboring) solution  $\mathbf{q}_h^+$ . Finally, the semi-discrete formulation is obtained by substituting the nodal basis expansion Eq. (3) and the upwind flux Eq. (5) into the strong formulation Eq. (4). The resulting vector-matrix form of the formulation and more descriptions of implementations can be found in Ref. 4.

It is well known that generally, the rate of convergence of the DG scheme in terms of the global  $L^2$  error is  $h^{N+1/2}$  ( $h$  being the element size).<sup>37</sup> When solving initial value problems such as calculating the room impulse response considered here, the dominant error comes from the spatial representations of the initial conditions, while the additional dispersive and dissipative errors from the wave propagation are relatively small and only visible after a very long time integration.<sup>31</sup> When the upwind flux is used, the dissipation error is of order  $(\kappa h)^{2N+2}$  while the dispersion error is of order  $(\kappa h)^{2N+3}$ ,<sup>33,36</sup> where  $\kappa$  is the wavenumber. It should be noted that the audibility of the numerical error on the perceptual level is important for practical room acoustic simulations. Future studies are needed to investigate the modeling requirements and error constraints of the TD-DG scheme for the auralization purposes.

## B. Numerical flux formulation of TDIBC

Previously, a frequency-independent impedance boundary formulation was proposed to simulate a locally-reacting surface within the DG method and its semi-discrete stability

was proved using the energy method.<sup>4</sup> The essential idea is to reformulate the numerical flux along the normal direction to the impedance boundary surface by utilizing the characteristic waves of the linear acoustic equations and the reflection coefficient  $R$ . The incoming and outgoing characteristic acoustic waves, which are denoted as  $\varpi_n^{in}$  and  $\varpi_n^{out}$ , and oriented in the opposite and the same direction of the outward normal  $\mathbf{n}$  along the boundary surface, respectively, are defined as

$$\varpi_n^{in}(\omega) = \frac{p(\omega)}{\rho c} - v_n(\omega), \quad (7)$$

$$\varpi_n^{out}(\omega) = \frac{p(\omega)}{\rho c} + v_n(\omega), \quad (8)$$

where  $v_n(\omega) = \mathbf{v}(\omega) \cdot \mathbf{n}$  denotes the particle velocity component normal to the surface at a given angular frequency  $\omega$ . Let  $Z_s$  denote the normalized surface impedance, i.e.,

$$Z_s(\omega) = \frac{1}{\rho c} \frac{p(\omega)}{v_n(\omega)}, \quad (9)$$

and the plane-wave reflection coefficient  $R(\omega)$  at normal incidence angle satisfies<sup>1</sup>

$$R(\omega) = \frac{Z_s(\omega) - 1}{Z_s(\omega) + 1}. \quad (10)$$

Inserting Eq. (9) into Eq. (10) directly yields the following condition concerning the reflection coefficient and characteristic waves

$$R(\omega) = \frac{\varpi_n^{in}(\omega)}{\varpi_n^{out}(\omega)}. \quad (11)$$

The time-domain implementation of the impedance boundary condition is realized by coupling the above condition Eq. (11) with the DG discretization through the reformulation of the upwind flux near the boundaries. The use of the plane-wave reflection coefficient at normal incidence is consistent with the fact that the numerical flux from the nodal DG scheme is always normal to the boundary surface. Furthermore, the impedance surface is assumed to be locally reacting, which holds true when the sound speed in the reflecting material is much lower than that of the incident wave, especially for porous materials with a high flow resistivity.<sup>38</sup> However, it should be noted that many common materials used in room acoustics such as solid panels and membranes are extendedly-reacting.

In this work, the real-valued frequency-independent reflection coefficient  $R_\infty$  is extended to the frequency-dependent one  $R(\omega)$  through the use of the multi-pole model. The whole TDIBC formulation consists of three steps. The first step is to transform the impedance values  $Z_s(\omega)$ , which can be obtained from either a continuous semi-empirical impedance model or measured discrete impedance values, within the interested frequency range, to the corresponding normal reflection

coefficient  $R(\omega)$  using Eq. (10). Second, the target reflection coefficient  $R(\omega)$  is approximated with a sum of rational functions<sup>39</sup>

$$\begin{aligned} R(\omega) &\approx R_\infty + \sum_{k=1}^S \frac{A_k}{\zeta_k + i\omega} \\ &\quad + \sum_{l=1}^T \frac{1}{2} \left( \frac{B_l - iC_l}{\alpha_l - i\beta_l + i\omega} + \frac{B_l + iC_l}{\alpha_l + i\beta_l + i\omega} \right) \\ &= R_\infty + \sum_{k=1}^S \frac{A_k}{\zeta_k + i\omega} + \sum_{l=1}^T \frac{B_l i\omega + C_l \beta_l + \alpha_l B_l}{(\alpha_l + i\omega)^2 + \beta_l^2}, \end{aligned} \quad (12)$$

where  $[R_\infty, A_k, B_l, C_l, \zeta_k, \alpha_l, \beta_l] \in \mathbb{R}$  are all real numerical parameters.  $R_\infty$  is the limit value of  $R(\omega)$  as the frequency approaches infinity.  $\zeta_k$  and  $\alpha_l \pm i\beta_l$  are the real poles and complex conjugate pole pairs respectively. To satisfy the causality and reality conditions  $\zeta_k, \alpha_l, \beta_l$  need to be positive, and the passivity condition is fulfilled when  $|R_n(\omega)| \leq 1$ .<sup>16</sup>

By applying the inverse Fourier transform to Eq. (12), the so-called reflection impulse response function in the time-domain is obtained as

$$\begin{aligned} R(t) &\approx R_\infty \delta(t) + \sum_{k=1}^S A_k e^{-\zeta_k t} H(t) \\ &\quad + \sum_{l=1}^T e^{-\alpha_l t} (B_l \cos(\beta_l t) + C_l \sin(\beta_l t)) H(t), \end{aligned} \quad (13)$$

where  $\delta(t)$  and  $H(t)$  are the Dirac delta and Heaviside function, respectively. As shown in Ref. 39, each term in  $R(t)$  can be interpreted as follows. The first term of Eq. (13) stands for the instantaneous response since  $R_\infty$  is the frequency independent value or high-frequency limit of  $R(\omega)$ . The second term is an exponentially decaying relaxation function, which mimics the absorption behavior of porous materials. The last group of terms is the so-called damped multi-oscillators that can be linked to resonator-type absorbers, where the imaginary part of the pole  $\beta_l$  determines the oscillation period and the real part  $\alpha_l$  governs the decaying rate.

The third and last step of the proposed TDIBC formulation is to enforce the multi-pole impedance model into the numerical flux along the impedance boundary surface. The time-domain counterpart of the characteristic acoustic waves as defined in Eqs. (7) and (8) can be obtained by pre-multiplying the acoustic variables  $\mathbf{q}$  with the left eigenmatrix  $\mathbf{L}^{-1}$ , i.e.,

$$\mathbf{L}^{-1} \mathbf{q} = \begin{bmatrix} 0 \\ 0 \\ \varpi_n^{out}(t) \\ \varpi_n^{in}(t) \end{bmatrix} = \begin{bmatrix} 0 \\ 0 \\ \frac{p(t)}{\rho c} + v_n(t) \\ \frac{p(t)}{\rho c} - v_n(t) \end{bmatrix}. \quad (14)$$

It should be noted that the first two characteristic terms in Eq. (14) are numerically irrelevant in the whole boundary formulation since their characteristic speeds (the first two diagonal values in  $\Lambda$ ) are zero. Finally, the numerical flux formulation of the TDIBC reads

$$\mathbf{n} \cdot \mathbf{F}^*(\mathbf{q}_h^-) = \mathbf{L} \Lambda [0, 0, \varpi_n^{out}(t), \varpi_n^{in}(t)]^T, \quad (15)$$

where  $\varpi_n^{out}(t)$  can be first calculated with the interior solution values at each of discrete nodes along the boundary as

$$\varpi_n^{out}(t) = \frac{p^-(t)}{\rho c} + v_n^-(t), \quad (16)$$

and then based on the condition of Eq. (11), the time-domain incoming wave  $\varpi_n^{in}(t)$  is obtained from the convolution of  $\varpi_n^{out}(t)$  with  $R(t)$  of Eq. (13),

$$\varpi_n^{in}(t) = \int_{-\infty}^t \varpi_n^{out}(\tau) R(t - \tau) d\tau. \quad (17)$$

To compute the convolution Eq. (17), the ADE method<sup>39,40</sup> is used. Substitution of the reflection impulse response  $R(t)$  of Eq. (13) into Eq. (17) yields

$$\begin{aligned} \varpi_n^{in}(t) &= R_\infty \varpi_n^{out}(t) + \sum_{k=1}^S A_k \phi_k(t) \\ &\quad + \sum_{l=1}^T [B_l \psi_l^{(1)}(t) + C_l \psi_l^{(2)}(t)], \end{aligned} \quad (18)$$

where the so-called accumulators or auxiliary variables  $\phi_k(t), \psi_l^{(1)}(t), \psi_l^{(2)}(t)$ , are given by

$$\phi_k(t) = \int_0^t \varpi_n^{out}(\tau) e^{-\zeta_k(t-\tau)} d\tau, \quad (19a)$$

$$\psi_l^{(1)}(t) = \int_0^t \varpi_n^{out}(\tau) e^{-\alpha_l(t-\tau)} \cos(\beta_l(t-\tau)) d\tau, \quad (19b)$$

$$\psi_l^{(2)}(t) = \int_0^t \varpi_n^{out}(\tau) e^{-\alpha_l(t-\tau)} \sin(\beta_l(t-\tau)) d\tau. \quad (19c)$$

The first term in Eq. (18) corresponds to the real-valued impedance boundary formulation. The bounds of the integrals in Eq. (19) are reduced to  $[0, t]$  due to the causality constraint indicated in the Heaviside function  $H(t)$ . The accumulators are calculated by solving the following first-order ordinary differential equations (ODEs) with zero initial values, which result from the differentiation of Eqs. (19) with respect to time

$$\frac{\partial \phi_k}{\partial t} + \zeta_k \phi_k(t) = \varpi_n^{out}(t), \quad (20a)$$

$$\frac{\partial \psi_l^{(1)}}{\partial t} + \alpha_l \psi_l^{(1)}(t) + \beta_l \psi_l^{(2)}(t) = \varpi_n^{out}(t), \quad (20b)$$

$$\frac{\partial \psi_l^{(2)}}{\partial t} + \alpha_l \psi_l^{(2)}(t) - \beta_l \psi_l^{(1)}(t) = 0. \quad (20c)$$

As shown by Dragna *et al.*,<sup>39</sup> the ADE method keeps the same order accuracy of a general multi-stage time integration scheme. Furthermore, since these accumulators only exist on the boundary nodes and only one time stage history of their values need to be stored, this approach has the benefit of low memory requirements.

### C. Discussions on time stepping and stability

In this work, the basic idea of method of lines (MOL) is followed. After the spatial discretization with the DG method, a five-stage, fourth-order explicit Runge-Kutta (RK) scheme<sup>41</sup> is used to integrate all the time-derivatives of the discretized system. An explicit time-stepping method comes with the conditional stability, which necessitates an upper bound on the time step size  $\Delta t$ . From the classical stability analysis of the MOL,<sup>42,43</sup> it is required that the time step size  $\Delta t$  is small enough so that the product of  $\Delta t$  with the full eigenvalue spectrum of the spatially-discretized system falls inside the stability region of the time integration scheme.<sup>42,43</sup> However, for the proposed scheme, the spatial discretization with the DG method is no longer completely decoupled from the time integration. To be more specific, the spatially-dependent upwind flux along the impedance boundary involves the time-integrated auxiliary variables, which are in turn stated explicitly in terms of the spatial dependent variables as shown in Eqs. (18) and (20). As a result, the stability analysis for the coupled system as considered here is not as straightforward as the well-established von Neumann analysis, which is typically applied to an initial-valued system of ODEs as in Ref. 29. Instead of providing a solid proof of discrete stability, the preliminary stability analysis for coupled systems from Refs. 39 and 44 are adopted for reference. It was claimed that the maximum allowable time step is determined by two factors: (1) the usual Courant-Friedrichs-Lewy (CFL) condition for the spatial discretization with DG method, which requires that  $\Delta t \leq C_1 / \max |\lambda_N|$ , where  $\lambda_N$  represents the eigenvalues of the spatial discretization by DG method and  $C_1$  is a constant depending on the stability region of the time-stepping method; (2) the stiffness of the ADEs as shown in Eq. (20), which is influenced by the maximum possible value of the parameters  $\zeta, \alpha, \beta$  in the multi-pole approximation. In this work, as will be presented in the following section, the stiffness is restricted so that the stability of the ADEs is automatically satisfied given a time-step size resulting from the first factor. For the first factor, it is known that for the linear system with first order of spatial differentiation, the gradients of the normalized  $N$ th order polynomial basis are of order  $\mathcal{O}(N^2/h)$  near the boundary part of the element,<sup>31</sup> consequently, the magnitude of the maximum eigenvalue  $\lambda_N$  scales with the polynomial order  $N$  as:  $\max(\lambda_N) \propto N^2$ , indicating that  $\Delta t \propto N^{-2}$ . This severe time step size restriction greatly limits the computational efficiency of high polynomial order approximations.<sup>44</sup> The temporal time steps are determined in the following way:<sup>31</sup>

$$\Delta t = C_{CFL} \cdot \min(\Delta x_i) \cdot \frac{1}{c} \cdot \frac{1}{N^2}, \quad (21)$$

where  $\Delta x_i$  is the smallest edge length of mesh elements and  $C_{CFL}$  is a constant of order  $\mathcal{O}(1)$ .

### D. Properties of rational functions and parameters identification

When fitting a generic broadband impedance model with Eq. (12), the fitted solutions are not unique. The three admissibility conditions need to be verified for each set of parameters as, otherwise, unphysical instabilities arise. Also, the additional computational work is proportional to the number of poles used. Furthermore, each term in the reflection impulse response  $R(t)$  may vary drastically even though the corresponding frequency domain model  $R(\omega)$  as a whole approximates the same impedance models or data equally well. Consequently, for the sake of numerical stability and computational efficiency, restrictions on the parameter values and number of poles are needed.

Each rational function with single real pole has two degrees of freedom (DoF). It is a monotonically decreasing function over frequency in terms of magnitude, which resembles a low-pass filter. At zero frequency, the maximum value is  $A/\zeta$  obtained from Eq. (12) and the rate at which the magnitude decreases becomes smaller with increasing value of  $\zeta$ .

The rational function with complex conjugate pole pair has four parameters (DoFs). Recall that the mass-spring-damper three-parameter impedance model is expressed as

$$Z_s(\omega) = R_0 + X_1 i\omega + \frac{X_{-1}}{i\omega}, \quad (22)$$

with the resistance  $R_0$ , the stiffness  $X_{-1}$ , and the mass  $X_1$  being positive. Inserting above Eq. (22) into Eq. (10) yields

$$R(\omega) = 1 - \frac{2i\omega/X_1}{-\omega^2 + \frac{R_0 + 1}{X_1} i\omega + \frac{X_{-1}}{X_1}}. \quad (23)$$

By comparing Eq. (23) with the complex-pole rational function, it can be seen that they differ in the constant term 1, the sign of the complex part in the numerator, and the number of parameters. In an attempt to mimic the physical behavior of a mass-spring-damper system, we define  $C\beta + B\alpha = 0$ , i.e.,  $C = -\alpha B/\beta$ . Consequently, the DoFs are reduced to three and the magnitude of each rational function  $B i\omega / (-\omega^2 + 2\alpha i\omega + \alpha^2 + \beta^2)$  now increases from 0 at zero frequency to the maximum value of  $B/2\alpha$  at the resonance frequency  $\omega_0 = \sqrt{\alpha^2 + \beta^2}$ , and then approaches 0 asymptotically.

To give an example of how to obtain the parameters of the multi-pole approximation for a specific impedance model, we consider a glass-wool baffle mounted on a rigid backing that is typical for room acoustic purposes. The surface impedance is modeled by the Johnson-Champoux-Allard-Lafarge (JCAL) model,<sup>45</sup> which is a phenomenological model considering wave propagation in porous materials

on a microscopic scale. The characteristic impedance  $Z_c$  reads  $Z_c = \sqrt{\rho_{\text{eff}} B_{\text{eff}}}$ , where the effective density  $\rho_{\text{eff}}$  and the effective bulk modulus  $B_{\text{eff}}$  are described by

$$\rho_{\text{eff}} = \frac{\rho_{\infty}}{\varphi} \left[ 1 + \frac{\sigma \varphi}{i \omega \alpha_{\infty} \rho} \left( 1 + \frac{4 i \alpha_{\infty}^2 \eta \rho}{\sigma^2 \Lambda^2 \varphi^2} \right)^{1/2} \right], \quad (24)$$

$$B_{\text{eff}} = \frac{\gamma P_0}{\varphi} \left( \gamma - \frac{\gamma - 1}{1 + \frac{\varphi \eta}{i \omega k_0' \rho P_r} \left( 1 + \frac{4 i \omega k_0'^2 \rho P_r}{\eta \Lambda^2 \varphi^2} \right)^{1/2}} \right)^{-1}. \quad (25)$$

The descriptions of physical parameters and their values for a typical glass wool material measured from experiments<sup>46</sup> are given in Table IV in the Appendix. The surface impedance of rigidly backed porous layer with thickness of  $d$  reads

$$Z_s = -i Z_c \cot(\kappa_{\text{eff}} d), \quad (26)$$

where the wavenumber of the porous material is given as  $\kappa_{\text{eff}} = \omega \sqrt{\rho_{\text{eff}} / B_{\text{eff}}}$ . In this study, the parameters in the multi-pole fit are obtained by the optimization technique first presented by Cotté *et al.*<sup>25</sup> It is shown<sup>25</sup> that the optimization technique is capable of ensuring the positivity of the fitting parameters in order to meet the causality and reality conditions. Furthermore, the number of poles can be pre-defined and the maximum values of parameters can be confined such that the stiffness of ADEs falls below the threshold as determined by the discrete stability condition. However, different from the general impedance boundary formulations using admittance as described in Refs. 11 and 29, where the condition for passivity is framed in terms of the positivity of real-valued fitting coefficients of the impedance model, the passivity condition of the current impedance boundary formulation is fulfilled when  $|R_n(\omega)| \leq 1$ .<sup>16</sup> Consequently, a posterior check  $|R_n(\omega)| \leq 1$  is needed.

For the JCAL model under consideration, it is sufficient to use real poles alone since the absorption coefficient increases monotonously with frequency. Since  $R(\omega)$  is a complex value, both the real parts and the imaginary parts should be fitted simultaneously instead of the amplitude and the phase in order to avoid wrap around ambiguity.<sup>11</sup> The real-pole approximation can be rearranged to

$$R(\omega) \approx \sum_{k=1}^S \frac{A_k}{\zeta_k + i\omega} = \sum_{k=1}^S \frac{A_k \zeta_k}{\zeta_k^2 + \omega^2} - i \sum_{k=1}^S \frac{A_k \omega}{\zeta_k^2 + \omega^2}. \quad (27)$$

Following the approach as in Ref. 25, the optimization is performed considering 100 frequencies logarithmically sampled between 20 and 1000 Hz, and the Euclidean norm of the deviation of real parts are minimized while keeping the difference of imaginary parts at each of the sampled frequency under a tolerance value  $\epsilon$ , i.e.,

TABLE I. Coefficients  $A_k$  and  $\zeta_k$  of the real pole approximation for the rigidly backed layer of JCAL model.

Coefficients	$A_k$	$\zeta_k$
$k=1$	$3.4454 \times 10^2$	$1.2967 \times 10^3$
$k=2$	$1.1999 \times 10^4$	$4.3215 \times 10^4$
$k=3$	$4.9999 \times 10^4$	$2.8108 \times 10^3$
$k=4$	$2.9954 \times 10^3$	$1.4546 \times 10^4$
$k=5$	$-4.9298 \times 10^4$	$2.8111 \times 10^3$

$$\min_{A_k, \zeta_k} \left( \sqrt{\sum_{i=1}^{100} \left| \text{Re}[R(\omega(i))] - \sum_{k=1}^S \frac{A_k \zeta_k}{\zeta_k^2 + \omega(i)^2} \right|^2} \right)$$

such that  $\begin{cases} 0 \leq \zeta_k \leq \zeta_{\text{max}} \\ \forall i, \left| \text{Im}[R(\omega(i))] + \sum_{k=1}^S \frac{A_k \omega(i)}{\zeta_k^2 + \omega(i)^2} \right| \leq \epsilon, \end{cases}$

(28)

where  $\zeta_{\text{max}}$  is the threshold value for  $\zeta$  due to the discrete stability condition and is chosen as  $5 \times 10^4$  in this work considering the CFL condition and the interested frequency range up to 1000 Hz. To solve this minimization problem, the interior-point algorithm<sup>47</sup> of the non-linear minimization function `fmincon` from the MATLAB optimization toolbox<sup>48</sup> is used. A series of optimizations is run to get a good fit. In the first run, the initial values of  $A_k$  and  $\zeta_k$  are chosen randomly between 0 and  $\zeta_{\text{max}}$  and a relatively large value of  $\epsilon$  is used, e.g.,  $\epsilon = 1 \times 10^{-1}$ . Then, the obtained set of coefficients is

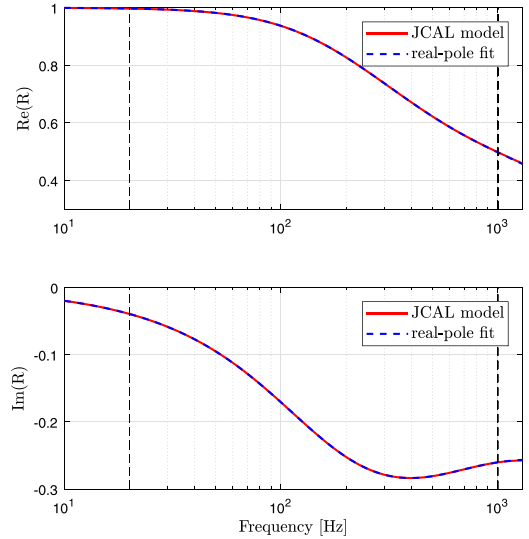


FIG. 1. (Color online) Real and imaginary part of the normal reflection coefficient of rigidly backed layer of JCAL model (red solid line), real pole fitting with the set of coefficients in Table IV (dashed blue line) in frequency band 20–1000 Hz.

used as the initial value for the next optimization with a smaller value of  $\epsilon$ . The process continues until a good approximation is obtained. Numerical experiments show that there is a compromise between the number of poles and the fitting accuracy. One set of coefficients is given in Table I, and the fitted reflection coefficient is plotted in Fig. 1. The maximum absolute value error at the sampled frequencies are  $6.1513 \times 10^{-4}$  and  $3.6357 \times 10^{-5}$  for the real and imaginary parts, respectively.

### III. NUMERICAL VERIFICATIONS

In this work, all the simulations are initiated with the same Gaussian-shaped pressure conditions

$$p(\mathbf{x}, t = 0) = e^{-(\ln 2/b^2)(\mathbf{x}-\mathbf{x}_s)^2}, \quad (29a)$$

$$v(\mathbf{x}, t = 0) = 0, \quad (29b)$$

where  $\mathbf{x}_s$  represents the source coordinates and  $b$  the half-bandwidth of this Gaussian pulse. A smaller value of  $b$  indicates a source spectrum up to a higher frequency.

#### A. Numerical properties and error in 1D

To verify the convergence property of the proposed formulation of the TDIBC and to quantify both the dissipation and dispersion error, a 1D single reflection scenario is considered. Each of the following experiment consists of two simulations. In the first simulation, the direct sound signal, denoted as  $p_d(t)$ , is recorded. In the second simulation, a reflecting surface is present and the measured sound pressure signals contain both the direct sound and the sound reflected from the impedance surface. The reflected sound signal  $p_r(t)$  can be obtained by subtracting  $p_d(t)$ . The spectra of the direct sound and the reflected sound, denoted as  $P_d(f)$  and  $P_r(f)$ , respectively, are obtained by Fourier transforming  $p_d$  and  $p_r$  without windowing. Let  $R_1$  denote the distance between the source and the receiver and  $R_2$  is the distance between the receiver and the image source mirrored by the reflecting impedance surface. The numerical plane-wave reflection coefficient  $R_{num}$  is calculated as follows:

$$R_{num}(f) = \frac{P_r(f) \cdot G(\kappa R_1)}{P_d(f) \cdot G(\kappa R_2)}, \quad (30)$$

where  $G(\kappa R)$  is the 1D Green's function for the free field propagation and  $\kappa$  is the wavenumber. For room acoustic modeling, where multiple reflections happen inside an enclosure, it is important to quantify the error arising from each reflection. The dissipation error  $\epsilon_{amp}$  in dB and the phase error  $\epsilon_\theta$  in % from a single reflection are calculated as follows:

$$\epsilon_{amp}(f) = 20 \log_{10} \left| \frac{R_{ana}(f)}{R_{num}(f)} \right|, \quad (31a)$$

$$\epsilon_\theta(f) = \frac{1}{\pi} |\vartheta(R_{ana}(f)) - \vartheta(R_{num}(f))| \times 100\%, \quad (31b)$$

where  $R_{ana}(f)$  is the analytical plane-wave reflection coefficient and  $\vartheta(\cdot)$  extracts the phase angle of a complex number. For a given broadband incident acoustic wave of arbitrary amplitude, the loss of sound pressure level (SPL) and the distortion of the phase across the frequency range of interest can be quantified.

Consider a 1D test case with an impedance boundary condition on the left ( $x=0$  m) and a non-reflecting boundary condition on the right ( $x=10$  m). The Gaussian pressure pulse is located  $x_s=6$  m while the receiver location is at  $x_r=3$  m.  $b$  is chosen as 0.15 such that the pulse has a significant frequency content up to 1000 Hz. The simulation is run for a non-dimensional time of  $\tilde{t} = t/(l_{ref}/c) = 15$ , where  $t$  is physical time and  $l_{ref} = 1$  m is used as the reference length, to make sure that the rightward-traveling wave has left the domain while the reflected leftward-traveling wave has passed the receiver location to a sufficient extent. The real-valued, single real pole, and single complex conjugate pole cases are considered separately. Without loss of generality, the real-valued specific impedance is chosen as  $Z_s = 19$ , the real pole coefficients are chosen as  $[A, \zeta] = [6.4 \times 10^3, 8 \times 10^3]$ . The complex conjugate pole pair has coefficient  $[B, C, \alpha, \beta] = [1.3195 \times 10^3, -7.6179 \times 10^2, 9.4247 \times 10^2, 1.6324 \times 10^3]$ , which corresponds to a maximum value of reflection coefficient 0.7 at the resonance frequency 300 Hz.

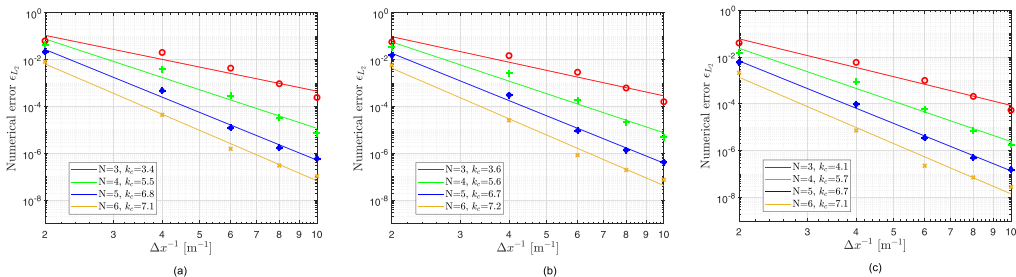


FIG. 2. (Color online) Convergence rate test of  $\epsilon_{L2}$  with  $CFL = 1$  and  $N = 3, 4, 5, 6$ : (a) real-valued impedance, (b) single real pole, (c) single complex conjugate pole.

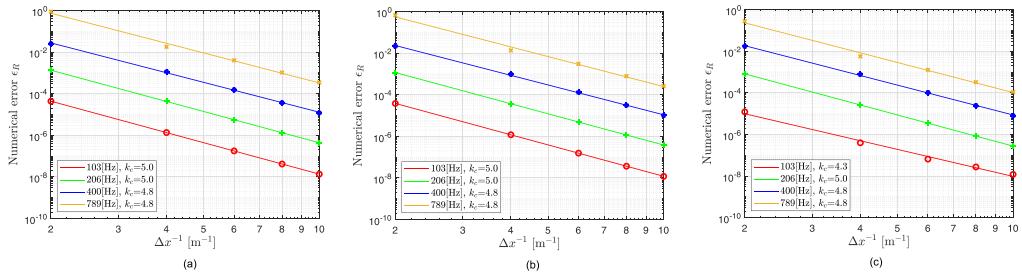


FIG. 3. (Color online) Convergence rate test of  $\epsilon_R(f)$  with  $C_{CFL} = 1$ . (a) Real-valued impedance, (b) single real pole, (c) single complex conjugate pole.

### 1. Convergence rate verification

The numerical errors originate from the spatial and temporal discretization of the interior domain, as well as from the impedance boundary formulation, where an extra recursive convolution error may be involved. Before quantifying the error magnitudes, first, the convergence rate, denoted by  $k_c$  with respect to the mesh sizes, is verified. The physical domain is discretized with  $[20, 40, 60, 80, 100]$  uniform elements ( $\Delta x = [0.5, 0.25, 0.167, 0.125, 0.1]$  m). Two error measures are used. The first one is the standard  $L^2$  error defined as  $\epsilon_{L^2} = \|p_{ana}(\bar{t} = 15) - p_{num}(\bar{t} = 15)\|_{L^2}$ , where  $p_{ana}(\bar{t} = 15)$  and  $p_{num}(\bar{t} = 15)$  denote the analytical solution<sup>49</sup> and the numerical solution at the final time across the whole domain.  $\|\cdot\|_{L^2}$  denotes the  $L^2$  integration, which is carried out numerically and accurately up to the order of polynomial approximation. The second error measure is defined as the absolute-valued deviation of magnitude of the reflection coefficient at discrete sampling frequencies, i.e.,  $\epsilon_R(f) = |R_{ana}(f) - R_{num}(f)|$ .

In practice, it is desirable to set  $C_{CFL}$  very close to the stability limit to save computational time. In order to get insights into the effects of the temporal errors on the convergence rate from both the time derivative approximation and the convolution, all test are performed using relatively large time steps that correspond to  $C_{CFL} = 1$  in Eq. (21) for each set of the polynomial basis order and the mesh size. The

global  $\epsilon_{L^2}$  error is shown in Fig. 2, where a first-order fit is used to calculate the convergence rate. The expected convergence rate  $h^{N+1/2}$  with different polynomial orders is observed for all kinds of boundaries considered. Figure 3 shows the convergence rate  $k_c$  of the reflection coefficient magnitude at some frequencies with a polynomial basis of order  $N = 4$ . It can be seen that for all types of boundaries, the convergence rate lies between 4 and 5 as expected across the frequency range of interest. Furthermore, by comparing the real-valued impedance boundaries with the other two frequency-dependent boundaries in both Figs. 2 and 3, it can be seen that the magnitudes of error of all types of boundaries are almost the same, indicating that the extra time integration error from the coupled ADEs are negligible. Numerical tests with a smaller time step of  $C_{CFL} = 0.1$  have been carried out and it is found that the numerical error remains the same. In other words, the spatial error from the DG discretization dominates over the time integration error arising from the time partial derivative approximation of the wave equation and the coupled ADEs.

### 2. Cost efficiency and memory efficiency of high order basis functions

One benefit of the DG scheme is its low dissipation and dispersion error for a given mesh resolution with the usage

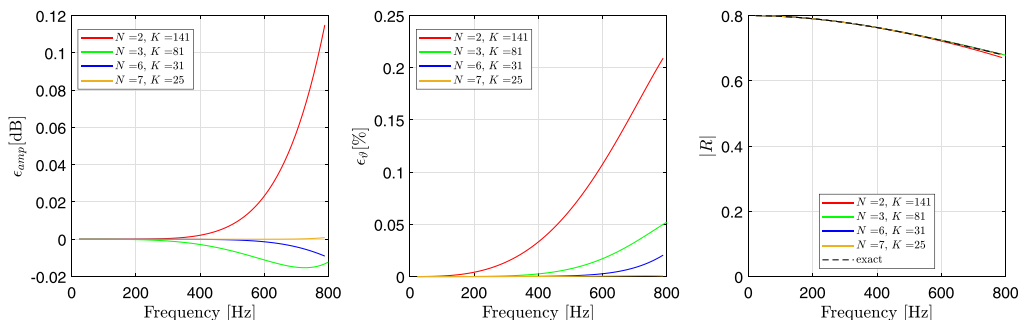


FIG. 4. (Color online) The dissipation error  $\epsilon_{amp}$  in dB, the phase error  $\epsilon_\theta$  in % and the amplitude of the plane-wave reflection coefficient from a single reflection for a single real pole model.

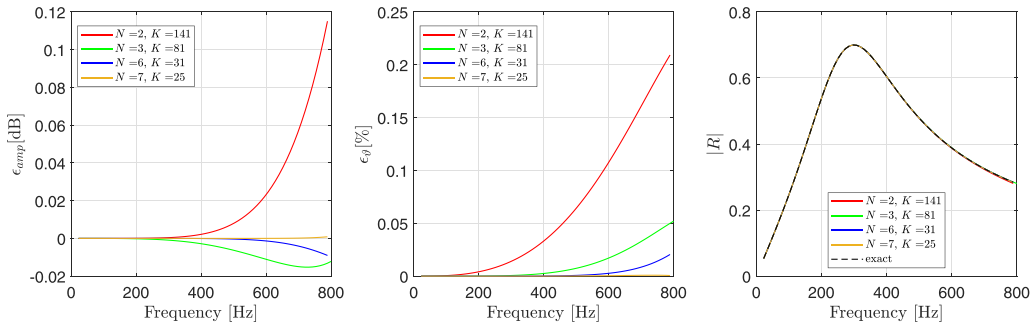


FIG. 5. (Color online) The dissipation error  $\epsilon_{amp}$  in dB, the phase error  $\epsilon_{\theta}$  in % and the amplitude of the plane-wave reflection coefficient from a single reflection for a single complex conjugate pole model.

of high-order polynomial basis function results. However, a small time step size is needed to satisfy the conditional stability of the explicit time-integration scheme. Another concern is related to the computational memory space to store all the acoustic variables and the geometry information of the mesh. For room acoustic simulations, the desired length of the impulse response determines the simulation time, while the highest frequency of interest decides the required memory space under a given mesh resolution.

To investigate whether the high-order basis function is a good choice for modeling frequency-dependent impedance boundary in terms of the cost efficiency the following measure as a function of basis function order  $N$  is used to give a general estimate of the computational cost under a required simulation time<sup>44</sup>

$$W_c(N) = N_{timesteps} \cdot N_{DOF}, \quad (32)$$

where  $N_{timesteps}$  is the number of time steps and  $N_{DOF}$  is the total number of DOF. This simplified computational cost measure assumes serial computations and excludes the effects of advanced parallel computing and matrix operations on the computational time. For 1D problems,  $N_{DOF} = (N + 1) \cdot K$  ( $K$  being the number of elements), and under the explicit time-stepping stability condition as in Eq. (21), the computational cost can be re-written as

$$W_c(N) = C \cdot K \cdot N^2 \cdot (N + 1) \cdot K, \quad (33)$$

where the constant factor  $C$  is determined by the CFL number and the number of acoustic variables. Now, suppose the computational budget is set by restricting  $K \cdot N^2 \cdot (N + 1) \cdot K \approx 2.4 \times 10^5$ , then, for polynomial basis function of order  $N = [2, 3, 6, 7]$ , the number of mesh elements  $K = [141, 81, 31, 25]$ . Simulations with a practically large time step that corresponds to  $C_{CFL} = 1$  in Eq. (21) are performed for each combined set of the polynomial basis order and mesh.

Figure 4 shows the dissipation error  $\epsilon_{amp}$  and the phase error  $\epsilon_{\theta}$  as defined in Eq. (31), as well as the amplitude of the plane-wave reflection coefficient from a single reflection corresponding to a single real pole model, while Fig. 5 presents the results for a single complex conjugate pole model. It can be seen that the numerical errors using high-order polynomial basis functions such as  $N = 6, 7$ , are much smaller than those with low-order basis functions like  $N = 2, 3$ , indicating that high-order basis functions achieve a better accuracy under a given computational complexity. In other words, under a given threshold value for dissipation and dispersion error, high-order basis functions use less computational power. However, it should be noted that the cost efficiency benefits of using high-order basis concluded above are based on the simplified measure of the computational cost as in Eq. (32), while in practice, other factors such as the parallel implementations could affect the computational time as well.

To check the memory efficiency of high-order basis functions, similar numerical experiments as described above are performed with the polynomial basis function of order  $N = [3, 5, 7]$  and the time step size resulting from  $C_{CFL} = 1$

TABLE II. The dissipation error  $\epsilon_{amp}$  in dB as a function of DPW for various polynomial order  $N = [3, 5, 7]$ .

DPW	Single real pole			Single complex conjugate pole		
	$N = 3$	$N = 5$	$N = 7$	$N = 3$	$N = 5$	$N = 7$
8	$1.4786 \times 10^0$	$1.1201 \times 10^{-1}$	$5.4273 \times 10^{-2}$	$1.4789 \times 10^0$	$1.1199 \times 10^{-1}$	$5.4275 \times 10^{-2}$
10	$1.4626 \times 10^{-1}$	$1.5818 \times 10^{-2}$	$6.7342 \times 10^{-3}$	$1.4639 \times 10^{-1}$	$1.5808 \times 10^{-2}$	$6.7357 \times 10^{-3}$
12	$3.1635 \times 10^{-2}$	$1.7270 \times 10^{-3}$	$1.4177 \times 10^{-3}$	$3.1596 \times 10^{-2}$	$1.7212 \times 10^{-3}$	$1.4185 \times 10^{-3}$

TABLE III. The phase error  $\epsilon_\theta$  % as a function of DPW for various polynomial order  $N = [3, 5, 7]$ .

DPW	Single real pole			Single complex conjugate pole		
	$N = 3$	$N = 5$	$N = 7$	$N = 3$	$N = 5$	$N = 7$
8	$1.2155 \times 10^0$	$4.9461 \times 10^{-1}$	$3.5896 \times 10^{-2}$	$1.2113 \times 10^0$	$4.9467 \times 10^{-1}$	$3.5932 \times 10^{-2}$
10	$9.2882 \times 10^{-1}$	$1.6612 \times 10^{-1}$	$1.6333 \times 10^{-2}$	$9.2877 \times 10^{-1}$	$1.6613 \times 10^{-2}$	$1.6323 \times 10^{-2}$
12	$5.4287 \times 10^{-2}$	$7.1990 \times 10^{-2}$	$7.4670 \times 10^{-3}$	$5.4289 \times 10^{-1}$	$7.1992 \times 10^{-2}$	$7.4616 \times 10^{-3}$

in Eq. (21). The corresponding number of mesh elements are chosen as  $K = [60, 40, 30]$  in order to have almost the same number of DOF, i.e.,  $N_{DOF} = 240$ . The dissipation and dispersion error is quantified with respect to the DOF per wavelength (DPW), which is defined as<sup>4</sup>

$$DPW = \frac{c}{f} \cdot \left( \frac{N_p \cdot K}{V} \right)^{1/d}. \quad (34)$$

Here,  $f$  is the frequency of interest,  $N_p = N + 1$  is the number of points inside single 1D element,  $d$  is the physical dimension, and  $V$  is the volume of the whole domain. For the considered 1D test,  $DPW \approx [8, 10, 12]$  when  $f \approx [1000, 800, 680]$  Hz. Table II shows the dissipation error  $\epsilon_{amp}$  for both the single real pole case and the single complex conjugate pole case, while the results of the phase error  $\epsilon_\theta$  are displayed in Table III. Almost the same error magnitudes are obtained for both types of poles. Furthermore, it can be observed that given the same spatial resolution, high-order basis functions achieve better accuracy compared to low-order basis functions.

### B. 3D single reflection from an impedance surface modeled by JCAL

To verify the impedance boundary condition formulation in 3D, a large 3D domain with a reflecting impedance boundary on the bottom is now considered. The impedance of the reflecting boundary is the surface impedance of the rigidly backed glass-wool panel as in Eq. (26). This test case mimics

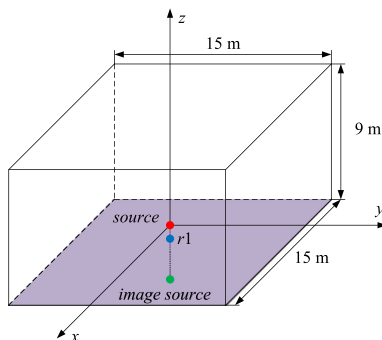


FIG. 6. (Color online) 3D computational domain to obtain reflected sound at normal incidence.

the reflection scenarios that happen multiple times in a real room acoustic simulation. The Gaussian pressure pulse is centered at  $\mathbf{x}_s = [0, 0, 0]$  m, a plane reflecting surface is placed 2 m away from the source at  $z = -2$  m and two receivers are placed at  $\mathbf{x}_{r1} = [0, 0, -1]$  m and  $\mathbf{x}_{r2} = [4, 4, -1]$  m, which corresponds to the normal incidence and the oblique incidence with an incidence angle of  $63^\circ$ , respectively. The value of  $b$  as in Eq. (29) is chosen as 0.17 so that the pulse has a significant frequency content up to 700 Hz. In this work, the hard wall boundary conditions are imposed on exterior boundaries of the whole computational domain, and the simulations are stopped as soon as the pulse has passed the receivers' location to a sufficient extent, but before the reflected waves from the exterior boundaries reach the receivers. For the normal incidence case, Fig. 6 shows the configuration diagram to obtain the reflected sound at the first receiver  $\mathbf{x}_{r1}$  with a reflecting surface on the bottom. For the oblique incidence case, a cubic domain of dimension  $[-5.5, 9.5] \times [-5.5, 9.5] \times [-2, 7.5]$  in meters is used to obtain the reflected sound at  $\mathbf{x}_{r2}$ . The simulations are run for a non-dimensional time of  $\bar{t} = t/(l_{ref}/c) = 10$ . Uniform structured tetrahedra meshes generated with the meshing software GMSH<sup>50</sup> are used for this study. In order to have sufficient spatial resolution at the highest frequency of interest 700 Hz, the mesh size is chosen as 0.5 m and simulations with polynomial basis of order  $N = [7, 9]$  are performed, resulting in DPW of  $[8.8, 10.8]$ . The time step sizes used correspond to  $C_{CFL} = 1$  as in Eq. (21).

The analytical solutions of the total pressure, which includes both the direct sound and the reflected sound, for the considered test case exist in the frequency domain.<sup>51</sup> For the Gaussian pulse as described in Eq. (29), the direct sound reaching the receivers can be calculated analytically as  $p_{d,ana}(t) = [(r_{sr} - ct)/2r_{sr}]e^{(-\ln 2/b^2)(r_{sr} - ct)^2} + [(r_{sr} + ct)/2r_{sr}]e^{(-\ln 2/b^2)(r_{sr} + ct)^2}$  (with  $r_{sr}$  being the source-receiver distance).<sup>4</sup> Figure 7 shows the comparison of the simulated pressure and the analytical solutions for both cases in terms of the amplitude and the phase. A good match between these results is observed, demonstrating the correct implementation and high precision of the proposed boundary scheme.

However, the comparison of the pressure field alone hardly reveals detailed information regarding the error behaviour. To investigate that, the error measures of Eq. (31) defined in the 1D tests are considered. The analytical spherical-wave reflection coefficient  $R_{ana}$ <sup>52</sup> corresponding to the rigidly backed glass-wool as in Eq. (26) and the numerical reflection coefficient  $R_{num}$  is calculated as shown in

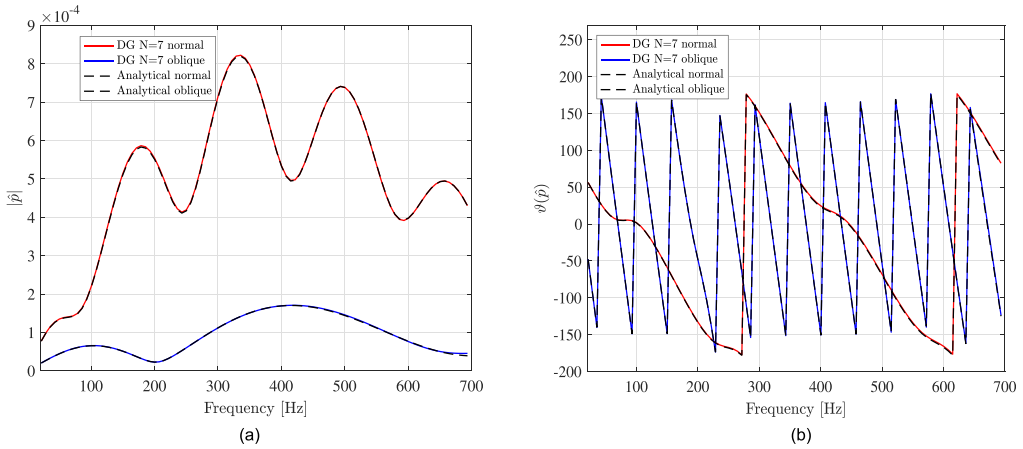


FIG. 7. (Color online) Complex pressure of a single reflection from a locally reacting, frequency dependent impedance boundary, compared with the analytical solution. (a) Amplitude. (b) Phase in degree.

Ref. 4. It should be noted that the observed numerical errors could arise from several potential mechanisms, including the dissipation and dispersion during the wave propagation, the reflection from the impedance boundary. In particular,

early truncation of the recorded time signal has a large effect on the low frequency error. In order to focus on the error arising from the boundary condition alone and to rule out the effects of other mechanisms, the well-established hard

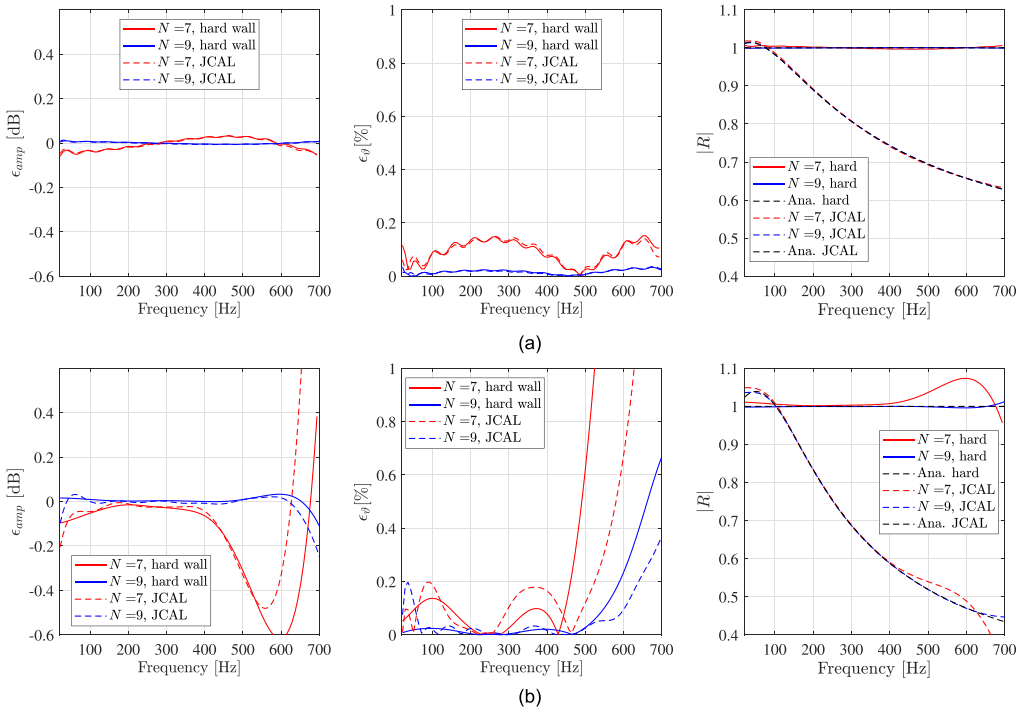


FIG. 8. (Color online) The dissipation error  $\epsilon_{amp}$ , the phase error  $\epsilon_\phi$  in and the amplitude of the spherical-wave reflection coefficient for the rigidly backed JCAL layer and the rigid wall. (a) Normal incidence. (b) Oblique incidence.

wall boundary condition<sup>31,53</sup> and its associated error is used as a reference bound for the reflecting surface. Its implementation has been verified in previous work<sup>4</sup> by comparison against the analytical solution for a 3D cuboid room with rigid walls. Figure 8 shows the results of both the normal incidence and the oblique incidence cases. It is observed that the error behaviour of the proposed impedance boundary condition more or less follows the hard wall case. The small deviation can be partly attributed to the approximation error of the JCAL model using the multi-pole models. Furthermore, reduction of error in the high frequency range with a higher polynomial order illustrates the convergence.

## IV. CONCLUSIONS

In this work, a numerical formulation for the TDIBC implementations in the framework of the TD-DG method is developed for the simulation of broadband sound propagation problems, specially targeting at the room acoustic applications. The essential idea is to model the acoustic reflection behaviour of a locally-reacting surface using the reflection coefficient  $R(\omega)$  in the form of a multi-pole model and then reformulate the corresponding time-domain upwind flux. This work is an extension of previous frequency-independent impedance boundary formulation to a generic broadband one. The properties of the multi-pole model are discussed, followed by a straightforward and effective parameter identification strategy to ensure the fully-discrete stability of the whole formulation. An application example of a typical impedance boundary of a rigidly-backed glass-wool baffle for room acoustic purposes is presented.

To verify the performance of the formulation, the reflection coefficients obtained from numerical tests are compared with the analytical ones. The 1D tests verify the high-order convergence property of the proposed formulation for accurately representing the reflection behavior of the plane wave. Meanwhile, the benefits of using high-order polynomial basis functions are demonstrated through the single reflection scenario, indicating a significant improvement in both cost efficiency and memory efficiency. The 3D tests further demonstrate the capacity of the proposed methodology for representing practical locally-reacting impedance boundary in the multi-dimensional case. To sum up, the proposed method further strengthens the potential of the TD-DG method as a wave-based method for room acoustics modeling.

## ACKNOWLEDGMENTS

This project has received funding from the European Union's Horizon 2020 research and innovation programme under Grant No. 721536. Additionally, we would like to thank Mr. Finnur Pind from the Department of Electrical Engineering at Technical University of Denmark for his kind help with the analytical solution of the 3D reflecting surface test case. Last but not least, the constructive comments and suggestions from the anonymous reviewers are greatly appreciated.

## APPENDIX

TABLE IV. Overview of the JCAL impedance model.

Property	Value
Atmospheric pressure $P_0$ (Pa)	$1.01 \times 10^5$
Speed of sound $c$ (m · s <sup>-1</sup> )	343
Density $\rho$ (kg · m <sup>-3</sup> )	1.2
Airflow resistivity $\sigma$ (Pa · s · m <sup>-2</sup> )	70821
Porosity $\phi$	0.967
Tortuosity $\alpha_\infty$	1.049
Viscous characteristic length $\Lambda$ (m)	$6 \times 10^{-5}$
Thermal characteristic length $\Lambda'$ (m)	$1.4 \times 10^{-4}$
Static thermal permeability $k_0$ (m <sup>2</sup> )	$6.345 \times 10^{-9}$
Dynamic viscosity $\eta$ (N · m <sup>-2</sup> )	$1.82 \times 10^{-5}$
Prandtl number $Pr$	0.71
Layer thickness $d$ (m)	0.04
Specific heat ratio $\gamma$	1.4

<sup>1</sup>H. Kuttruff, *Room Acoustics* (CRC Press, Boca Raton, FL, 2016).

<sup>2</sup>T. Sakuma, S. Sakamoto, and T. Otsuru, *Computational Simulation in Architectural and Environmental Acoustics* (Springer, New York, 2014).

<sup>3</sup>I. Touloupoulos and J. A. Ekaterinaris, "High-order discontinuous galerkin discretizations for computational aeroacoustics in complex domains," *AIAA J.* **44**(3), 502–511 (2006).

<sup>4</sup>H. Wang, I. Sihar, R. Pagán Muñoz, and M. Hornikx, "Room acoustics modelling in the time-domain with the nodal discontinuous galerkin method," *J. Acoust. Soc. Am.* **145**(4), 2650–2663 (2019).

<sup>5</sup>A. Modave, A. St-Cyr, and T. Warburton, "GPU performance analysis of a nodal discontinuous galerkin method for acoustic and elastic models," *Comput. Geosci.* **91**, 64–76 (2016).

<sup>6</sup>S. Schoeder, W. Wall, and M. Kronbichler, "Exwave: A high performance discontinuous galerkin solver for the acoustic wave equation," *SoftwareX* **9**, 49–54 (2019).

<sup>7</sup>S. M. Schoeder, "Efficient discontinuous Galerkin methods for wave propagation and iterative optoacoustic image reconstruction," Ph.D. thesis, Technische Universität München, München, Germany, 2019.

<sup>8</sup>S. Bilbao, "Modeling of complex geometries and boundary conditions in finite difference/finite volume time domain room acoustics simulation," *IEEE Trans. Audio Speech Lang. Process.* **21**(7), 1524–1533 (2013).

<sup>9</sup>S. Rienstra, "Impedance models in time domain, including the extended helmholtz resonator model," in *Proceedings of the 12th AIAA/CEAS Aeroacoustics Conference (27th AIAA Aeroacoustics Conference)*, Cambridge, MA (May 8–10, 2006), p. 2686.

<sup>10</sup>Y. Reymen, M. Baelmans, and W. Desmet, "Efficient implementation of Tam and Aurialt's time-domain impedance boundary condition," *AIAA J.* **46**(9), 2368–2376 (2008).

<sup>11</sup>S. Bilbao, B. Hamilton, J. Botts, and L. Savioja, "Finite volume time domain room acoustics simulation under general impedance boundary conditions," *IEEE/ACM Trans. Audio Speech Lang. Process. (TASLP)* **24**(1), 161–173 (2016).

<sup>12</sup>S. Zhong, X. Zhang, and X. Huang, "A controllable canonical form implementation of time domain impedance boundary conditions for broadband aeroacoustic computation," *J. Comput. Phys.* **313**, 713–725 (2016).

<sup>13</sup>K.-Y. Fung and H. Ju, "Broadband time-domain impedance models," *AIAA J.* **39**(8), 1449–1454 (2001).

<sup>14</sup>H. Ju and K.-Y. Fung, "Time-domain simulation of acoustic sources over an impedance plane," *J. Comput. Acoust.* **10**(03), 311–329 (2002).

<sup>15</sup>K.-Y. Fung and H. Ju, "Time-domain impedance boundary conditions for computational acoustics and aeroacoustics," *Int. J. Comput. Fluid Dyn.* **18**(6), 503–511 (2004).

<sup>16</sup>Q. Douasbin, C. Scalo, L. Selle, and T. Poinot, "Delayed-time domain impedance boundary conditions (d-tidbc)," *J. Comput. Phys.* **371**, 50–66 (2018).

- <sup>17</sup>D. Dragna and P. Blanc-Benon, "Physically admissible impedance models for time-domain computations of outdoor sound propagation," *Acta Acust. united Ac.* **100**(3), 113 (2014).
- <sup>18</sup>D. Dragna, K. Attenborough, and P. Blanc-Benon, "On the inadvisability of using single parameter impedance models for representing the acoustic properties of ground surfaces," *J. Acoust. Soc. Am.* **138**(4), 2399–2413 (2015).
- <sup>19</sup>D. Botteldooren, "Finite-difference time-domain simulation of low-frequency room acoustic problems," *J. Acoust. Soc. Am.* **98**(6), 3302–3308 (1995).
- <sup>20</sup>C. K. Tam and L. Auriault, "Time-domain impedance boundary conditions for computational aeroacoustics," *AIAA J.* **34**(5), 917–923 (1996).
- <sup>21</sup>K. Kowalczyk and M. van Walsstijn, "Formulation of locally reacting surfaces in FDTD/K-DWM modelling of acoustic spaces," *Acta Acust. united Ac.* **94**(6), 891–906 (2008).
- <sup>22</sup>S. Sakamoto, H. Nagatomo, A. Ushiyama, and H. Tachibana, "Calculation of impulse responses and acoustic parameters in a hall by the finite-difference time-domain method," *Acoust. Sci. Technol.* **29**(4), 256–265 (2008).
- <sup>23</sup>K. Kowalczyk and M. V. Walsstijn, "Modeling frequency-dependent boundaries as digital impedance filters in FDTD and K-DWM room acoustics simulations," *J. Audio Eng. Soc.* **56**(7/8), 569–583 (2008).
- <sup>24</sup>J. Escalano, F. Jacobsen, and J. J. López, "An efficient realization of frequency dependent boundary conditions in an acoustic finite-difference time-domain model," *J. Sound Vib.* **316**(1–5), 234–247 (2008).
- <sup>25</sup>B. Cotté, P. Blanc-Benon, C. Bogey, and F. Poisson, "Time-domain impedance boundary conditions for simulations of outdoor sound propagation," *AIAA J.* **47**(10), 2391–2403 (2009).
- <sup>26</sup>D. Dragna, B. Cotté, P. Blanc-Benon, and F. Poisson, "Time-domain simulations of outdoor sound propagation with suitable impedance boundary conditions," *AIAA J.* **49**(7), 1420–1428 (2011).
- <sup>27</sup>D. Dragna, P. Blanc-Benon, and F. Poisson, "Time-domain solver in curvilinear coordinates for outdoor sound propagation over complex terrain," *J. Acoust. Soc. Am.* **133**(6), 3751–3763 (2013).
- <sup>28</sup>R. Troian, D. Dragna, C. Bailly, and M.-A. Galland, "Broadband liner impedance eduction for multimodal acoustic propagation in the presence of a mean flow," *J. Sound Vib.* **392**, 200–216 (2017).
- <sup>29</sup>S. Bilbao and B. Hamilton, "Passive volumetric time domain simulation for room acoustics applications," *J. Acoust. Soc. Am.* **145**(4), 2613–2624 (2019).
- <sup>30</sup>F. Monteghetti, D. Matignon, and E. Piot, "Energy analysis and discretization of nonlinear impedance boundary conditions for the time-domain linearized Euler equations," *J. Comput. Phys.* **375**, 393–426 (2018).
- <sup>31</sup>J. S. Hesthaven and T. Warburton, *Nodal Discontinuous Galerkin Methods: Algorithms, Analysis and Applications* (Springer-Verlag, New York, 2007).
- <sup>32</sup>F. Q. Hu, M. Hussaini, and P. Rasetarinera, "An analysis of the discontinuous Galerkin method for wave propagation problems," *J. Comput. Phys.* **151**(2), 921–946 (1999).
- <sup>33</sup>F. Hu and H. Atkins, "Two-dimensional wave analysis of the discontinuous Galerkin method with non-uniform grids and boundary conditions," in *Proceedings of the 8th AIAA/CEAS Aeroacoustics Conference & Exhibit*, Breckenridge, CO (June 17–20, 2002), p. 2514.
- <sup>34</sup>J. Saarela, J. Botts, B. Hamilton, and L. Savioja, "Audibility of dispersion error in room acoustic finite-difference time-domain simulation as a function of simulation distance," *J. Acoust. Soc. Am.* **139**(4), 1822–1832 (2016).
- <sup>35</sup>J. S. Hesthaven and C.-H. Teng, "Stable spectral methods on tetrahedral elements," *SIAM J. Sci. Comput.* **21**(6), 2352–2380 (2000).
- <sup>36</sup>M. Ainsworth, "Dispersive and dissipative behaviour of high order discontinuous Galerkin finite element methods," *J. Comput. Phys.* **198**(1), 106–130 (2004).
- <sup>37</sup>P. Lasaint and P.-A. Raviart, "On a finite element method for solving the neutron transport equation," in *Mathematical Aspects of Finite Elements in Partial Differential Equations* (Elsevier, Amsterdam, the Netherlands, 1974), pp. 89–123.
- <sup>38</sup>K. Gunnarsdóttir, C.-H. Jeong, and G. Marbjerg, "Acoustic behavior of porous ceiling absorbers based on local and extended reaction," *J. Acoust. Soc. Am.* **137**(1), 509–512 (2015).
- <sup>39</sup>D. Dragna, P. Pineau, and P. Blanc-Benon, "A generalized recursive convolution method for time-domain propagation in porous media," *J. Acoust. Soc. Am.* **138**(2), 1030–1042 (2015).
- <sup>40</sup>R. M. Joseph, S. C. Hagness, and A. Taflov, "Direct time integration of Maxwell's equations in linear dispersive media with absorption for scattering and propagation of femtosecond electromagnetic pulses," *Opt. Lett.* **16**(18), 1412–1414 (1991).
- <sup>41</sup>M. H. Carpenter and C. A. Kennedy, "Fourth-order 2N-storage Runge-Kutta schemes," Report No. NASA-TM-109112 (NASA, Washington, DC, 1994).
- <sup>42</sup>S. C. Reddy and L. N. Trefethen, "Stability of the method of lines," *Numer. Math.* **62**(1), 235–267 (1992).
- <sup>43</sup>B. Gustafsson, *High Order Difference Methods for Time Dependent PDE* (Springer-Verlag, Berlin, Germany, 2007).
- <sup>44</sup>F. Pind, A. P. Engsig-Karup, C.-H. Jeong, J. S. Hesthaven, M. S. Mejlum, and J. Strömman-Andersen, "Time domain room acoustic simulations using the spectral element method," *J. Acoust. Soc. Am.* **145**(6), 3299–3310 (2019).
- <sup>45</sup>D. Lafarge, P. Lemarinier, J. F. Allard, and V. Tarnow, "Dynamic compressibility of air in porous structures at audible frequencies," *J. Acoust. Soc. Am.* **102**(4), 1995–2006 (1997).
- <sup>46</sup>N. Hoekstra, "Sound absorption of periodically spaced baffles," M.S. thesis, Eindhoven University of Technology, Eindhoven, the Netherlands, 2016.
- <sup>47</sup>R. H. Byrd, M. E. Hribar, and J. Nocedal, "An interior point algorithm for large-scale nonlinear programming," *SIAM J. Optim.* **9**(4), 877–900 (1999).
- <sup>48</sup>Mathworks Inc., *MATLAB Optimization Toolbox (R2018b)* (The MathWorks, Inc., Natick, MA 2018).
- <sup>49</sup>Y. Özyörük and L. N. Long, "A time-domain implementation of surface acoustic impedance condition with and without flow," *J. Comput. Acoust.* **5**(03), 277–296 (1997).
- <sup>50</sup>C. Geuzaine and J.-F. Remacle, "Gmsh: A 3-D finite element mesh generator with built-in pre- and post-processing facilities," *Int. J. Numer. Methods Eng.* **79**(11), 1309–1331 (2009).
- <sup>51</sup>K. W. Thompson, "Time dependent boundary conditions for hyperbolic systems," *J. Comput. Phys.* **68**(1), 1–24 (1987).
- <sup>52</sup>X. Di and K. E. Gilbert, "An exact Laplace transform formulation for a point source above a ground surface," *J. Acoust. Soc. Am.* **93**(2), 714–720 (1993).
- <sup>53</sup>H. Atkins, "Continued development of the discontinuous Galerkin method for computational aeroacoustic applications," in *Proceedings of the 3rd AIAA/CEAS Aeroacoustics Conference*, Atlanta, GA (May 12–14, 1997), p. 1581.

---

## Errata of Paper II

- Reference 51. K. W. Thompson, "Time dependent boundary conditions for hyperbolic systems," J. Comput. Phys. 68(1), 1–24 (1987).  
should be replaced by  
S.I. Thomasson, "Reflection of waves from a point source by an impedance boundary." The Journal of the Acoustical Society of America 59(4), 780-785(1976).

---

---

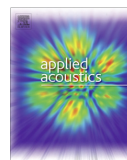
# Paper III



ELSEVIER

Contents lists available at ScienceDirect

## Applied Acoustics

journal homepage: [www.elsevier.com/locate/apacoust](http://www.elsevier.com/locate/apacoust)

## Frequency-dependent transmission boundary condition in the acoustic time-domain nodal discontinuous Galerkin model

Huiqing Wang<sup>\*</sup>, Jieun Yang, Maarten Hornikx

Building Physics and Services, Department of the Built Environment, Eindhoven University of Technology, P.O. Box 513, 5600 MB Eindhoven, The Netherlands

## ARTICLE INFO

## Article history:

Received 14 November 2019

Received in revised form 13 February 2020

Accepted 18 February 2020

## ABSTRACT

Accurate modeling of boundary conditions is of critical importance for acoustic simulations. Recently, the time-domain nodal discontinuous Galerkin (TD-DG) method has emerged as a potential wave-based method for acoustic modeling. Although the acoustic reflection behavior of various time-domain impedance boundaries has been studied extensively, the modeling of the sound transmission across a locally-reacting layer of impedance discontinuity is far less developed. This paper presents a formulation of broadband time-domain transmission boundary conditions for locally-reacting surfaces in the framework of the TD-DG method. The formulation simulates the acoustic wave behavior at each of the boundary nodes using the plane-wave theory. Through the multi-pole model representation of the transmission coefficient, various types of transmission layers can be simulated. One-dimensional numerical examples demonstrate the capability of the proposed formulation to accurately simulate the reflection and transmission characteristics of the limp wall and the porous layer, where quantitative error behavior against analytical results is presented. Furthermore, to demonstrate the applicability, two scenarios of two-dimensional acoustic environment are considered. One is the sound transmission between two rooms partitioned by a limp panel and the other is the sound propagation through a transmissive noise barrier. Comparison of the predicted results from the proposed method against the results from the frequency-domain finite element simulations further verifies the formulation.

© 2020 The Authors. Published by Elsevier Ltd. This is an open access article under the CC BY-NC-ND license (<http://creativecommons.org/licenses/by-nc-nd/4.0/>).

## 1. Introduction

Numerical simulation of sound fields in complex enclosures is a research subject of continuing interest and has been applied in many fields, for example, architecture design [1–3], automotive design [4], virtual reality [5], aircraft cabin noise control [6]. In general, there are mainly two groups of acoustic modeling approaches, namely geometrical acoustic methods [7] and wave-based methods. For the geometrical acoustic methods, simplifying assumptions regarding sound propagation and reflection are being made, which directly deteriorate the simulation accuracy of complex wave phenomena such as interferences, scattering and diffraction, especially in the low-frequency range. Besides that, geometrical acoustic methods often use simplified 3D models, where neglected geometrical details of the configurations are replaced by equivalent scattering coefficients [8]. By contrast, wave-based methods address sound propagation in complex scenarios from a more physical point of view and solve the governing partial differential equations based on numerical methods. The acoustic field over

the whole enclosure is captured completely. Compared to frequency-domain wave-based methods, time-domain modeling allows single run broadband calculations with moving sources and time-varying domains and generates the impulse response of the room. Therefore, they are favored for the purpose of auralisation. There are various methodologies, including finite-difference time-domain method (FDTD) [9], finite-element (FEM) [10], finite-volume (FVM) methods [11] and pseudospectral time-domain method (PSTD) [12]. These methods differ in terms of the fundamental formulation, the implementation complexity, the computational cost, the accuracy in representing realistic and geometrically complicated boundary conditions, and the ability to suppress the dissipation and dispersion error.

After decades of developments in various areas of computational engineering, the time-domain discontinuous Galerkin (DG) method [13–16] has for the first time been evaluated as a potential wave-based method for room acoustic modeling purposes [17]. The DG method is known to be weakly dissipative and dispersive for wave propagation due to its high-order polynomial basis discretization [18] and thus well suitable for cost-efficient simulations over a long time duration. Since it operates on unstructured (curvilinear) mesh and allows for local refinement in terms of

<sup>\*</sup> Corresponding author.

E-mail address: [h.wang6@tue.nl](mailto:h.wang6@tue.nl) (H. Wang).

the polynomial order and the mesh size, the DG method is capable of simulating arbitrary complex geometries without geometrical simplifications. Though computationally intensive, the DG method solves governing equations elementwise and uses the so-called numerical flux at adjacent element interfaces to communicate the information between them, thus it is well suited to parallel computation [19,20], particularly when explicit time-integration methods are used. Recently, it has become possible to apply the DG method to large scale wave propagation problems [21].

A major concern for realistic acoustic simulations is the accurate modeling of boundary interfaces, where more physical mechanisms apart from free propagation come into play, such as diffusion, diffraction, scattering, absorption, transmission, and coupling with another medium [22]. For time-domain simulations, many efforts have been devoted to model the reflection and absorption behavior of materials using the frequency-dependent impedance boundary conditions with various of the above-mentioned methodologies, which can be found in Refs. [23,24]. In the specific framework of the time-domain DG method, the formulations for the locally-reacting impedance boundary condition have been presented in Refs. [25–27]. However, when the propagating acoustic wave experiences a locally-reacting boundary, part of it is reflected while the other part is transmitted, and the distribution depends on the degree of the impedance mismatch [28]. Therefore, in the area of the general linear acoustics, it would be desirable to develop a uniform acoustic boundary condition that could take both the sound reflection and transmission into account. To address this issue, Toyoda and Ishikawa [22] have proposed a locally-reacting boundary condition within the FDTD framework using the mass-damper-spring (MDS) system inserted between propagation media to simulate the frequency-dependent absorption and transmission characteristics. The MDS boundary has in total seven parameters to fit the frequency characteristics of materials in terms of the impedance, including three masses, two damping and two spring constants. To the best of authors' knowledge, no formulation regarding the sound transmission boundary condition has been presented so far for the time-domain DG method.

In this work, a formulation of the transmission boundary condition for locally-reacting materials is derived based on the plane wave theory. The frequency-dependent transmission characteristics are incorporated into the formulation through the multi-pole representation of the plane wave transmission coefficient in the frequency domain. This multi-pole model defined from rational functions has been widely used in time-domain impedance boundary conditions [29,25,30–33]. The fitting of parameters in this representation for a target transmission characteristic is achieved by the optimization technique as firstly presented by Cotté et al. [30]. The time-domain implementation based on the auxiliary differential equations (ADE) method [34,35] is used.

The paper is organized as follows. The formulations of the reflection and transmission boundary conditions within the time-domain DG method are derived in Section 2. The formulation of multi-pole models for three practical cases, i.e., limp wall partition, mass-damper-spring partition, and locally-reacting porous layer, is illustrated in Section 3. Section 4 presents several 1D and 2D numerical examples to demonstrate the validity and accuracy of the implemented formulation. Finally, the conclusions and outlook can be found in Section 5.

## 2. Reflection and transmission boundary condition in the time-domain DG scheme

### 2.1. Spatial discretization of a sound field

In this work, the governing equations are the linear acoustic equations for a motionless propagation medium

$$\begin{aligned} \frac{\partial \mathbf{v}}{\partial t} + \frac{1}{\rho} \nabla p &= \mathbf{0}, \\ \frac{\partial p}{\partial t} + \rho c^2 \nabla \cdot \mathbf{v} &= 0, \end{aligned} \quad (1)$$

where  $\mathbf{v} = [u, v, w]^T$  is the particle velocity vector,  $p$  is the sound pressure,  $\rho$  is the constant density and  $c$  is the constant speed of sound. Also, Eq. (1) can be written as

$$\frac{\partial \mathbf{q}}{\partial t} + \nabla \cdot \mathbf{F}(\mathbf{q}) = \frac{\partial \mathbf{q}}{\partial t} + \mathbf{A}_j \frac{\partial \mathbf{q}}{\partial x_j} = 0, \quad (2)$$

where  $\mathbf{q}(\mathbf{x}, t) = [u, v, w, p]^T$  is the acoustic variable vector and  $\mathbf{A}_j$  is the constant flux Jacobian matrix with coordinate index  $j \in [x, y, z]$ . Let  $D^k$  be a set of simplex and geometrically conformal elements that discretize the computational domain  $\Omega_h$ , i.e.,  $\Omega_h = \bigcup_{k=1}^K D^k$ . The local solution  $\mathbf{q}_h^k(\mathbf{x}, t)$  in element  $D^k$ , where subscript  $h$  denotes the numerical approximation, is given by:

$$\mathbf{q}_h^k(\mathbf{x}, t) = \sum_{i=1}^{N_p} \mathbf{q}_i^k(\mathbf{x}_i, t) l_i^k(\mathbf{x}), \quad (3)$$

where  $\mathbf{q}_i^k(\mathbf{x}_i, t)$  are the unknown nodal values and  $l_i^k(\mathbf{x})$  is the multi-dimensional Lagrange polynomial basis of order  $N$ , which satisfies  $l_i^k(\mathbf{x}_j) = \delta_{ij}$ .  $N_p$  is the number of local basis functions (or nodes) inside a single element and equal to  $(N+d)!/(N!d!)$  for simplex elements, where  $d$  is the dimensionality. In this study, the Legendre-Gauss-Lobatto (LGL) quadrature points are used for the 1D cases and the  $\alpha$ -optimized node distribution [36] is used for the 2D cases due to its low Lebesgue constants. After the Galerkin projection and integration by parts twice, the semi-discrete nodal DG formulation of Eq. (2) reads:

$$\int_{D^k} \left( \frac{\partial \mathbf{q}_h^k}{\partial t} + \nabla \cdot \mathbf{F}_h^k(\mathbf{q}_h^k) \right) l_i^k d\mathbf{x} = \int_{\partial D^k} \mathbf{n} \cdot (\mathbf{F}_h^k(\mathbf{q}_h^k) - \mathbf{F}^*) l_i^k d\mathbf{x}, \quad (4)$$

where  $\mathbf{n} = [n_x, n_y, n_z]$  is the outward normal vector of the element surface  $\partial D^k$ .  $\mathbf{F}^*$ , the so-called numerical flux across element intersection  $\partial D^k$ , is a function of both the solution value from the interior side of the intersection, i.e.,  $\mathbf{q}_h^-$  and the exterior value  $\mathbf{q}_h^+$ . In this study, the upwind numerical flux is used throughout the whole domain because of its low dispersive and dissipation error [18,37]. To derive the upwind flux, we utilize the hyperbolic property of the system and decompose the normal flux on the interface  $\partial D^k$  into outgoing and incoming waves, the so-called characteristic modes. Mathematically, an eigendecomposition conducted to the normally projected flux Jacobian yields:

$$\begin{aligned} \mathbf{A}_n &= (n_x \mathbf{A}_x + n_y \mathbf{A}_y + n_z \mathbf{A}_z) \\ &= \begin{bmatrix} 0 & 0 & 0 & \frac{n_x}{\rho} \\ 0 & 0 & 0 & \frac{n_y}{\rho} \\ 0 & 0 & 0 & \frac{n_z}{\rho} \\ \rho c^2 n_x & \rho c^2 n_y & \rho c^2 n_z & 0 \end{bmatrix} \\ &= \mathbf{L} \mathbf{\Lambda} \mathbf{L}^{-1}, \end{aligned} \quad (5)$$

where

$$\mathbf{L} = \begin{bmatrix} -n_z & n_y & n_x/2 & -n_x/2 \\ n_z & -n_x & n_y/2 & -n_y/2 \\ -n_y & n_x & n_z/2 & -n_z/2 \\ 0 & 0 & \rho c/2 & \rho c/2 \end{bmatrix}, \quad \mathbf{\Lambda} = \begin{bmatrix} 0 & 0 & 0 & 0 \\ 0 & 0 & 0 & 0 \\ 0 & 0 & c & 0 \\ 0 & 0 & 0 & -c \end{bmatrix} \quad (6)$$

The numerical upwind flux is defined by considering the direction of the characteristic speed, i.e.,

$$\mathbf{n} \cdot \mathbf{F}(\mathbf{q}_h^-, \mathbf{q}_h^+) = \mathbf{L}(\Lambda^+ \mathbf{L}^{-1} \mathbf{q}_h^- + \Lambda^- \mathbf{L}^{-1} \mathbf{q}_h^+), \quad (7)$$

where  $\Lambda^+$  and  $\Lambda^-$  contain the positive and negative parts of  $\Lambda$ . Physically,  $\Lambda^+$  ( $\Lambda^-$ , respectively) corresponds to the characteristic waves propagating along (opposite to, respectively) the outward normal direction  $\mathbf{n}$ , which are referred to as outgoing waves out of  $D^k$  (incoming waves into  $D^k$ , respectively). Therefore, the outgoing waves are associated with the interior solution  $\mathbf{q}_h^-$  whereas the incoming waves are dependent on the exterior (neighboring) solution  $\mathbf{q}_h^+$ . Finally, the semi-discrete formulation is obtained by substituting the nodal basis expansion Eq. (3) and the upwind flux Eq. (7) into the strong formulation Eq. (4). The resulting vector-matrix form of the formulation and more details of the implementation can be found in Ref. [17].

## 2.2. Formulation of the reflection and transmission boundary conditions

The prescription of the numerical flux plays a key role in the DG scheme. Apart from linking neighboring interior elements, it serves to impose the boundary condition and to guarantee the stability of the formulation. In the following, we will first present the formulation of frequency-independent reflection and transmission boundary conditions of locally reacting type. Then, the extension of the formulation to the frequency-dependent case will be shown.

For the DG method, boundary conditions are enforced weakly through the numerical flux on the boundary surfaces either by reformulating the flux subject to specific boundary conditions or by providing the exterior values of the solution  $\mathbf{q}_h^+$  [38] needed for the numerical flux. In both cases, the interior values  $\mathbf{q}_h^-$  are needed. In this work, the reflection and transmission boundary conditions are enforced by providing the exterior values of the solution  $\mathbf{q}_h^+$  that conform with the acoustic characteristics of the boundary. As illustrated in Fig. 1, the reflection and transmission boundary that takes the form of a flat surface/layer of an impedance discontinuity separates two propagation media 1 and 3. In the DG modeling framework, this boundary is considered as an internal interface connecting the neighboring interior elements in media 1 and 3, which are denoted as  $D^{k1}$  and  $D^{k3}$ , respectively. To set the correct exterior values of the solution needed for the upwind flux Eq. (7), the classical plane wave theory is used. Without loss of generality, suppose that a plane wave propagates perpendicular to the interface in the positive  $x$ -direction, which intersects the  $x$ -axis at  $x = 0$ . According to the plane wave theory [2], the pressure and the particle velocity of the incident wave in medium 1 satisfy

$$p_{i1}(x, t) = \hat{p}_0 \exp[i(\omega t - kx)] \quad (8a)$$

$$u_{i1}(x, t) = \frac{\hat{p}_0}{\rho c} \exp[i(\omega t - kx)], \quad (8b)$$

where  $\hat{p}_0$  is the amplitude,  $\omega$  is the angular frequency and  $k$  is the wavenumber. The corresponding reflected wave at the interface is

$$p_{r1}(x, t) = R \cdot \hat{p}_0 \exp[i(\omega t + kx)] \quad (9a)$$

$$u_{r1}(x, t) = -R \cdot \frac{\hat{p}_0}{\rho c} \exp[i(\omega t + kx)], \quad (9b)$$

while the transmitted wave from medium 1 to medium 3 reads

$$p_{t13}(x, t) = T \cdot \hat{p}_0 \exp[i(\omega t - kx)] \quad (10a)$$

$$u_{t13}(x, t) = T \cdot \frac{\hat{p}_0}{\rho c} \exp[i(\omega t - kx)], \quad (10b)$$

where  $R$  and  $T$  are the plane wave reflection coefficient and transmission coefficient, respectively. By setting  $x = 0$  in the above Eqs. (8)–(10), the following explicit relations between the incident, the reflected and the transmitted waves on the flat discontinuity surface are obtained

$$p_{r1}(0, t) = R \cdot p_{i1}(0, t) \quad (11a)$$

$$u_{r1}(0, t) = -R \cdot u_{i1}(0, t) \quad (11b)$$

$$p_{t13}(0, t) = T \cdot p_{i1}(0, t) \quad (11c)$$

$$u_{t13}(0, t) = T \cdot u_{i1}(0, t). \quad (11d)$$

Similarly, for the plane wave traveling in the negative  $x$ -direction perpendicular to the interface from medium 3 towards medium 1, we yield the following relations

$$p_{r3}(0, t) = R' \cdot p_{i3}(0, t) \quad (12a)$$

$$u_{r3}(0, t) = -R' \cdot u_{i3}(0, t) \quad (12b)$$

$$p_{t31}(0, t) = T' \cdot p_{i3}(0, t) \quad (12c)$$

$$u_{t31}(0, t) = T' \cdot u_{i3}(0, t). \quad (12d)$$

Here,  $R'$  and  $T'$  are the plane wave reflection coefficient and transmission coefficient for the wave propagating from medium 3 towards medium 1, which can be different values from  $R$  and  $T$  in Eq. (11). For more general cases where the discontinuity surface is in arbitrary direction, the same relations as shown in Eqs. (11) and (12) hold for the incident, reflected and transmitted pressure, as well as the corresponding acoustic particle velocity vector component in each direction, i.e.,  $\mathbf{v} = [u, v, w]$  due to Eq. (1).

To impose the upwind flux as stated in Eq. (7), we regard the local reflected wave and transmitted wave as the exterior information coming from neighboring element and let the local incident wave govern the interior value. Therefore, for the boundary nodes lying on the medium 1 side, which are denoted with superscript 1, we set  $p^{1-} = p_{i1}$ ,  $u^{1-} = u_{i1}$ ,  $v^{1-} = v_{i1}$ ,  $w^{1-} = w_{i1}$  and  $p^{1+} = p_{r1} + p_{t31}$ ,  $u^{1+} = u_{r1} + u_{t31}$ ,  $v^{1+} = v_{r1} + v_{t31}$ ,  $w^{1+} = w_{r1} + w_{t31}$ . Due to the relations prescribed in Eqs. (11) and (12), the exterior values as a function of interior values are determined in the following way:

$$p^{1+} = R \cdot p^{1-} + T \cdot p^{3-} \quad (13a)$$

$$u^{1+} = -R \cdot u^{1-} + T \cdot u^{3-} \quad (13b)$$

$$v^{1+} = -R \cdot v^{1-} + T \cdot v^{3-} \quad (13c)$$

$$w^{1+} = -R \cdot w^{1-} + T \cdot w^{3-}. \quad (13d)$$

Substitute above exterior values into Eq. (7), the upwind flux for the boundary element  $D^{k1}$  in medium 1 is

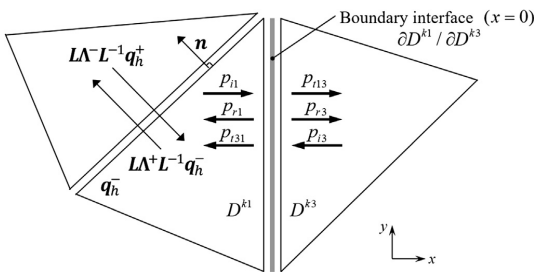


Fig. 1. Upwind numerical flux for interior triangular elements and plane wave behavior across the transmission boundary.

$$\mathbf{n} \cdot \mathbf{F}^*(\mathbf{q}_h^{1-}, \mathbf{q}_h^{1+}) = \mathbf{L}(\mathbf{A}^+ \mathbf{L}^{-1} \mathbf{q}_h^{1-} + \mathbf{A}^- \mathbf{L}^{-1} \mathbf{q}_h^{1+})$$

$$= \begin{bmatrix} \frac{n_x c}{2} \left( \frac{1+R}{\rho c} p^{1-} + (1+R) v_{n1}^{1-} + T \cdot \frac{p^{3-}}{\rho c} - T \cdot v_{n1}^{3-} \right) \\ \frac{n_y c}{2} \left( \frac{1+R}{\rho c} p^{1-} + (1+R) v_{n1}^{1-} + T \cdot \frac{p^{3-}}{\rho c} - T \cdot v_{n1}^{3-} \right) \\ \frac{n_z c}{2} \left( \frac{1+R}{\rho c} p^{1-} + (1+R) v_{n1}^{1-} + T \cdot \frac{p^{3-}}{\rho c} - T \cdot v_{n1}^{3-} \right) \\ \xi \left( p^{1-} - R \cdot p^{1-} - T \cdot p^{3-} + \rho c (v_{n1}^{1-} - R \cdot v_{n1}^{1-} + T \cdot v_{n1}^{3-}) \right) \end{bmatrix}, \quad (14)$$

where  $v_{n1}^{1-} = \mathbf{v}^{1-} \cdot \mathbf{n}_1$ ,  $v_{n1}^{3-} = \mathbf{v}^{3-} \cdot \mathbf{n}_1$  and  $\mathbf{n}_1$  is the outward normal vector of the surface element  $D^{k1}$ .

For the purpose of computational efficiency and compact implementation for the frequency-dependent case, the above upwind flux expression can be simplified by grouping terms in the form of the characteristic acoustic waves. The incoming and outgoing characteristic acoustic waves across a surface with outward normal vector  $\mathbf{n}$  are defined as

$$\varpi_n^{\text{in}} = \frac{p}{\rho c} - \mathbf{v} \cdot \mathbf{n} \quad (15)$$

$$\varpi_n^{\text{out}} = \frac{p}{\rho c} + \mathbf{v} \cdot \mathbf{n}. \quad (16)$$

Through algebraic manipulations, upwind flux in Eq. (14) can be reformulated as

$$\mathbf{n} \cdot \mathbf{F}^*(\mathbf{q}_h^{1-}, \mathbf{q}_h^{1+}) = \mathbf{L}(\mathbf{A}^+ \mathbf{L}^{-1} \mathbf{q}_h^{1-} + \mathbf{A}^- \mathbf{L}^{-1} \mathbf{q}_h^{1+})$$

$$= \mathbf{L} \mathbf{A} \begin{bmatrix} 0 \\ 0 \\ \varpi_{n1}^{\text{out}1-} \\ R \cdot \varpi_{n1}^{\text{out}1-} + T \cdot \varpi_{n3}^{\text{out}3-} \end{bmatrix}, \quad (17)$$

with  $\varpi_{n1}^{\text{out}1-} = p^{1-}/\rho c + \mathbf{v}^{1-} \cdot \mathbf{n}_1$  and  $\varpi_{n3}^{\text{out}3-} = p^{3-}/\rho c + \mathbf{v}^{3-} \cdot \mathbf{n}_3$ , where  $\mathbf{n}_3$  is the outward normal vector of the surface element  $D^{k3}$  and the normal vector  $\mathbf{n}_1$  and  $\mathbf{n}_3$  are in opposite direction, i.e.,  $\mathbf{n}_1 = -\mathbf{n}_3$ . Therefore, in the current reflection and transmission boundary flux formulation, the incoming characteristic waves include both the reflected characteristic waves  $R \cdot \varpi_{n1}^{\text{out}1-}$  and the transmitted characteristic waves  $T \cdot \varpi_{n3}^{\text{out}3-}$  across the partitioning interface from the other medium.

It should be noted that the local plane wave behavior happening exactly on the boundary surface is due to the locally-reacting assumption of the medium on the boundary. In other words, acoustic waves on each of the boundary nodes in 3D physical space behave locally in a 1D manner along the normal direction of the boundary surface. However, it should be kept in mind that the locally high-order polynomial basis function of the DG scheme is able to well represent a local physical wavefront of non-planar shape approaching the boundary surface. What's more, since the numerical flux from the nodal DG scheme is always normal to the boundary surface, the reflection coefficient  $R$  and the transmission coefficient  $T$  should be the ones at normal incidence. Practical examples of the reflection and transmission coefficients across a flat locally-reacting layer will be discussed in Section 3.

Although the formulation for the frequency-independent reflection and transmission boundary condition presented above is derived at a given single frequency  $\omega$ , it in principle also holds true for a frequency-dependent complex-valued reflection and transmission boundary, where a phase delay can be taken into account as well. In the following, key steps to calculate the transmitted characteristic waves are presented, and the reflected characteristic waves can be obtained in the same manner as shown in Ref. [27]. Firstly, the frequency-dependent target plane wave transmission

coefficient  $T(\omega)$  is approximated in the frequency domain with a sum of rational functions as

$$T(\omega) \approx T_\infty + \sum_{k=1}^S \frac{A_k}{\zeta_k + i\omega} + \sum_{l=1}^T \frac{1}{2} \left( \frac{B_l - iC_l}{\alpha_l - i\beta_l + i\omega} + \frac{B_l + iC_l}{\alpha_l + i\beta_l + i\omega} \right)$$

$$= T_\infty + \sum_{k=1}^S \frac{A_k}{\zeta_k + i\omega} + \sum_{l=1}^T \frac{B_l i\omega + C_l \beta_l + \alpha_l B_l}{(\alpha_l + i\omega)^2 + \beta_l^2}, \quad (18)$$

where  $[T_\infty, A_k, B_l, C_l, \zeta_k, \alpha_l, \beta_l] \in \mathbb{R}$  are all real numerical parameters that fit the plane wave reflection coefficient for normally incident sound waves. To be more specific,  $T_\infty$  is the frequency independent value of  $T(\omega)$  as the frequency approaches infinity.  $\zeta_k$  and  $\alpha_l \pm i\beta_l$  are the real poles and complex conjugate pole pairs, respectively. In the time-domain, the so-called impulse response function of the transmission is obtained from the inverse Fourier transform of  $T(\omega)$

$$T(t) \approx T_\infty \delta(t) + \sum_{k=1}^S A_k e^{-\zeta_k t} H(t) + \sum_{l=1}^T e^{-\alpha_l t} (B_l \cos(\beta_l t) + C_l \sin(\beta_l t)) H(t), \quad (19)$$

where  $\delta(t)$  and  $H(t)$  are the Dirac delta and Heaviside function, respectively. As shown in Ref. [35], each term in  $T(t)$  has a physical interpretation. The first term of Eq. (19) stands for the instantaneous response. The second term is an exponentially decaying relaxation function. The last group of terms are the so-called damped multi-oscillators, where the imaginary part of the pole  $\beta_l$  determines the oscillation period and the real part  $\alpha_l$  governs the decaying rate.

The final step of the proposed formulation is to obtain the equivalent time-domain expression of the incoming transmitted (reflected, respectively) characteristic waves similar to the frequency-independent one  $T \cdot \varpi_{n3}^{\text{out}3-}$  ( $R \cdot \varpi_{n1}^{\text{out}1-}$ , respectively) as in Eq. (17). To be specific, it involves the convolution of the time-domain outgoing wave  $\varpi_{n3}^{\text{out}3-}(t)$  ( $\varpi_{n1}^{\text{out}1-}(t)$ , respectively) and the transmission impulse response function  $T(t)$  (reflection impulse response function  $R(t)$ , respectively). The outgoing wave  $\varpi_{n1}^{\text{out}1-}(t)$  in element  $D^{k1}$  can be firstly calculated with the interior solution values at each of discrete nodes along the boundary as

$$\varpi_{n1}^{\text{out}1-}(t) = \frac{p^{1-}(t)}{\rho c} + v_{n1}^{1-}(t). \quad (20)$$

Similarly, outgoing wave  $\varpi_{n3}^{\text{out}3-}(t)$  in element  $D^{k3}$  is

$$\varpi_{n3}^{\text{out}3-}(t) = \frac{p^{3-}(t)}{\rho c} + v_{n3}^{3-}(t). \quad (21)$$

The final form of the frequency-dependent upwind flux is expressed as

$$\mathbf{n} \cdot \mathbf{F}^*(\mathbf{q}_h^{1-}, \mathbf{q}_h^{1+}) = \mathbf{L}(\mathbf{A}^+ \mathbf{L}^{-1} \mathbf{q}_h^{1-} + \mathbf{A}^- \mathbf{L}^{-1} \mathbf{q}_h^{1+})$$

$$= \mathbf{L} \mathbf{A} \begin{bmatrix} 0 \\ 0 \\ \varpi_{n1}^{\text{out}1-} \\ \int_{-\infty}^t \varpi_{n1}^{\text{out}1-}(\tau) R(t-\tau) d\tau + \int_{-\infty}^t \varpi_{n3}^{\text{out}3-}(\tau) T(t-\tau) d\tau \end{bmatrix}. \quad (22)$$

To compute the convolution in Eq. (22) in a time efficient and low-storage manner, the auxiliary differential equations (ADE) method, originally developed by Joseph et al. [34] for electromagnetic applications, is employed in this study. For example, the incoming transmitted characteristic waves are calculated as

$$\int_{-\infty}^t \varpi_{n3}^{\text{out}3-}(\tau) T(t-\tau) d\tau = T_\infty \varpi_{n3}^{\text{out}3-}(t) + \sum_{k=1}^S A_k \phi_k(t)$$

$$+ \sum_{l=1}^T [B_l \psi_l^1(t) + C_l \psi_l^2(t)], \quad (23)$$

where the new terms  $\phi_k(t)$ ,  $\psi_1^1(t)$ ,  $\psi_2^2(t)$ , referred to as accumulators or auxiliary variables, are given by:

$$\phi_k(t) = \int_0^t \varpi_{n3}^{out3-}(\tau) e^{-\zeta_k(t-\tau)} d\tau, \quad (24a)$$

$$\psi_1^1(t) = \int_0^t \varpi_{n3}^{out3-}(\tau) e^{-\alpha_1(t-\tau)} \cos(\beta_1(t-\tau)) d\tau, \quad (24b)$$

$$\psi_2^2(t) = \int_0^t \varpi_{n3}^{out3-}(\tau) e^{-\alpha_2(t-\tau)} \sin(\beta_2(t-\tau)) d\tau. \quad (24c)$$

The first term in Eq. (23) corresponds to the frequency-independent reflected wave as presented in Eq. (17). The bounds of the integrals in above Eq. (24) are reduced to  $[0, t]$  due to the causality constraint indicated in the Heaviside function  $H(t)$ . Instead of computing accumulators based on the integral of Eq. (24), the accumulators are calculated by solving the following first-order ordinary differential equations, which result from the differentiation of Eq. (24) with respect to time,

$$\frac{\partial \phi_k}{\partial t} + \zeta_k \phi_k(t) = \varpi_{n3}^{out3-}(t), \quad (25)$$

$$\frac{\partial \psi_1^1}{\partial t} + \alpha_1 \psi_1^1(t) + \beta_1 \psi_2^2(t) = \varpi_{n3}^{out3-}(t), \quad (26)$$

$$\frac{\partial \psi_2^2}{\partial t} + \alpha_2 \psi_2^2(t) - \beta_2 \psi_1^1(t) = 0. \quad (27)$$

The above system is numerically integrated from zero initial values using the same time-integration scheme as for the semi-discrete DG formulation in Eq. (4), which will be shown in the following. Therefore, as shown by Dragna et al. [35], the ADE method keeps the same order of accuracy of a general multi-stage time integration scheme. It should be noted that these accumulators only exist on the boundary nodes.

### 2.3. Time stepping and stability

After the spatial discretization by the nodal DG method, the semi-discrete system can be expressed in a general form of ordinary differential equations (ODE) as:

$$\frac{d\mathbf{q}_h}{dt} = \mathcal{L}(\mathbf{q}_h(t), t), \quad (28)$$

where  $\mathbf{q}_h$  is the vector of all discrete nodal solutions and  $\mathcal{L}$  the spatial discretization operator of the DG method. A five-stage, fourth-order explicit Runge–Kutta (RK) scheme [39] is used to integrate Eq. (28), i.e.,

$$\begin{cases} \mathbf{q}_h^{(0)} = \mathbf{q}_h^n, \\ \mathbf{k}^{(i)} = \mathbf{a}_i \mathbf{k}^{(i-1)} + \Delta t \mathcal{L}(\mathbf{t}^n + c_i \Delta t, \mathbf{q}_h^{(i-1)}), \\ \mathbf{q}_h^{(i)} = \mathbf{q}_h^{(i-1)} + b_i \mathbf{k}^{(i)}, \\ \mathbf{q}_h^{n+1} = \mathbf{q}_h^{(5)}, \end{cases} \quad \text{for } i = 1, \dots, 5 \quad (29)$$

where  $\Delta t = t^{n+1} - t^n$  is the time step,  $\mathbf{q}_h^{n+1}$  and  $\mathbf{q}_h^n$  are the solution vectors at time  $t^{n+1}$  and  $t^n$ , respectively. The coefficients  $a_i, b_i$ , and  $c_i$  of the Runge–Kutta method can be found in Ref. [39].

The explicit time-stepping method comes with the conditional stability, which requires that the time step size  $\Delta t$  is small enough so that the product of  $\Delta t$  with the full eigenvalue spectrum of ODE system falls inside the stability region of the time integration scheme [40,41]. The whole ODE system under consideration includes both the spatially-discretized linear acoustic equations and the ADEs, which are coupled together along the impedance boundary. Therefore, as shown in Refs. [35,42], the maximum allowable time step is determined by two factors: (1) the usual

Courant–Friedrichs–Lewy (CFL) condition for the spatial discretization with the DG scheme, which requires that  $\Delta t \leq C_1 / \max|\lambda_N|$ , where  $\lambda_N$  represents the eigenvalues of the spatial discretization by the DG scheme and  $C_1$  is a constant depending on the stability region of the time-stepping method; (2) the stiffness of the ADEs. As shown in Eqs. (25)–(27), the stiffness of the ADEs is influenced by the maximum possible value of the parameters  $\zeta, \alpha$  and  $\beta$  in the multi-pole approximation. In this work, the stiffness is restricted so that the stability of the ADEs is automatically satisfied given a time-step size resulting from the first factor. The measures for restrictions will be presented in Section 3.4. For the first factor, it is known that for the linear system with the first order of spatial differentiation, the gradients of the normalized  $N$ -th order polynomial basis are of order  $\mathcal{O}(N^2/h)$  near the boundary part of the element [16], consequently, the magnitude of the maximum eigenvalue  $\lambda_N$  scales with the polynomial order  $N$  as:  $\max(\lambda_N) \propto N^2$ , indicating that  $\Delta t \propto N^{-2}$ . The temporal time steps are determined in the following way [16]:

$$\Delta t = C_{CFL} \cdot \min(\Delta x_i) \cdot \frac{1}{c} \cdot \frac{1}{N^2},$$

where  $\Delta x_i$  is the smallest edge length of mesh elements and  $C_{CFL}$  is a constant of order  $\mathcal{O}(1)$ .

### 3. Multi-pole modeling of practical locally-reacting boundaries

The presented formulation of the reflection and transmission boundary condition needs the plane wave reflection and transmission coefficients at normal incidence conforming to the reflection and transmission characteristics of the boundary considered. As shown in Eqs. (11) and (12), the formulation also applies to cases where the simulated boundary has asymmetrical reflection and transmission properties. The purpose of this section is to present a few practical scenarios where sound reflection and transmission happen over a flat surface of the impedance discontinuity, and to illustrate how the multi-pole modeling approach can be applied in practice to simulate the sound reflection and transmission on the boundaries of locally-reacting media. The locally-reacting assumption, which indicates that reactions (velocity, displacement, acceleration, etc.) at a certain point on the surface are related to the sound pressure of only that point, holds true for: (a) isotropic porous absorptive materials with a high flow resistivity or large losses, especially when the speed of longitudinal wave in such materials is much lower than that of the adjacent propagation media [43]; (b) anisotropic solids, such as plates with low stiffness, perforated structure or honeycomb core structure, where the lateral wave is rapidly attenuated or blocked.

#### 3.1. Transmission through a limp wall (mass law)

A simple case of the impedance discontinuity that has practical importance in architectural acoustics is a limp wall, where only the mass effect is considered and the interior stiffness or damping is ignored. It can be seen as a simplified model of a thin partition between two enclosures, whose thickness is much smaller than the wavelength in the frequency range of interest [44]. Due to the continuum assumption, the wall vibrates with the same frequency and magnitude of the fluid particle that it is in direct contact with, and the normal component of velocity is continuous. Different from the classical elastic plate theory [45], the flexural rigidity of the wall is ignored, and therefore the wall acts in a locally-reacting way and the corresponding reflection coefficient  $R(\omega)$  and the transmission coefficient  $T(\omega)$  are derived based on the Newton's second law and the continuity assumption of the nor-

mal velocity, as shown in Ref. [28]. They can be further re-written in the following multi-pole model form

$$R(\omega) = 1 - \frac{2Z_c/m}{i\omega + 2Z_c/m}, \quad (31)$$

$$T(\omega) = \frac{2Z_c/m}{i\omega + 2Z_c/m}, \quad (32)$$

where  $Z_c$  is the characteristic impedance of the propagation media and  $m$  (kg/m<sup>2</sup>) is the surface density of the wall.

### 3.2. Transmission through a mass-damper-spring (MDS) partition

A more general case of locally-reacting partition is to incorporate the damper and the spring effects into the surface partition between two media, which results in a mass-damper-spring (MDS) system as illustrated in Fig. 2. The flexible partition of mass per unit area  $m$  is mounted upon a viscously damped, elastic suspension, with the linear damping constant  $r_d$  per unit area and the spring constant  $s$  per unit area, respectively. This simplified model could approximate the fundamental mode of a large vibrating panel [46]. Unlike the FDTD approach presented in Ref. [22], where the governing motion equations of the MDS system are discretized explicitly by the central difference scheme, in this study, the MDS partition is treated as a whole system of the impedance discontinuity, and the transmission and reflection coefficients required for the upwind flux formulation are derived. As shown in Ref. [28], the wall impedance becomes  $i\omega m + r_d - is/\omega$ . Applying the same Newton's second law and the continuity assumption of the normal velocity as for the limp wall case, the corresponding reflection coefficient  $R(\omega)$  and the transmission coefficient  $T(\omega)$  are obtained as

$$R(\omega) = 1 - \frac{2Z_c}{i(\omega m - s/\omega) + 2Z_c + r_d}, \quad (33)$$

$$T(\omega) = \frac{2Z_c}{i(\omega m - s/\omega) + 2Z_c + r_d}. \quad (34)$$

However, compared to the limp wall case, there is an extra frequency-dependent term  $s/\omega$  in the denominators of above two Eqs. (33) and (34) due to spring effect. Consequently, both the reflection coefficient  $R(\omega)$  and the transmission coefficient  $T(\omega)$  cannot be re-written in the multi-pole model form as shown in Eq. (18). Consequently, a further approximation is needed to express  $R(\omega)$  and  $T(\omega)$  using the rational functions as basis functions. The approximation procedure will be discussed in Section 3.4.

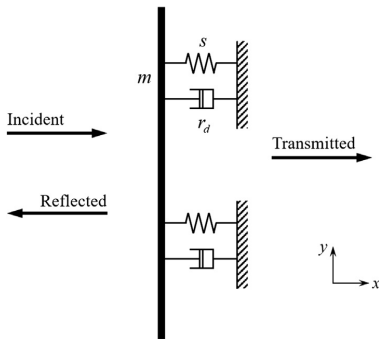


Fig. 2. Simplified model of reflection and transmission through a single-leaf partition under normal incidence sound waves.

### 3.3. Transmission through of a locally-reacting porous layer

Another practical scenario where the sound transmission matters would be the noise barriers that are made of porous materials. As illustrated in Fig. 3, suppose that the locally-reacting porous layer has a thickness of  $d$ , the transmission and reflection behavior occurring in three different regions with respective characteristic impedance values  $Z_1$ ,  $Z_2$ , and  $Z_3$  are governed by the continuity condition of both the pressure and the normal velocity on the discontinuity interfaces. The corresponding plane wave reflection coefficient  $R(\omega)$  and the transmission coefficient  $T(\omega)$  are derived as [47]

$$R(\omega) = \frac{(Z_2 + Z_3)(Z_2 - Z_1)e^{i2k_2d} + (Z_3 - Z_2)(Z_2 + Z_1)}{(Z_2 + Z_3)(Z_2 + Z_1)e^{i2k_2d} + (Z_3 - Z_2)(Z_2 - Z_1)}, \quad (35)$$

$$T(\omega) = \frac{4Z_2Z_3}{(Z_3 - Z_2)(Z_2 - Z_1)e^{-ik_2d} + (Z_2 + Z_3)(Z_2 + Z_1)e^{ik_2d}}, \quad (36)$$

where  $k_2$  is the wavenumber and  $Z_2$  is the characteristic impedance of the locally-reacting layer. In this study,  $Z_1$  and  $Z_3$  are chosen as the characteristic impedance of air, i.e.,  $Z_1 = Z_3 = \rho c$ . Like the case of the MDS system, a parameter fitting procedure is needed to approximate  $R(\omega)$  and  $T(\omega)$  with the multi-pole model.

### 3.4. Parameter fitting of the multi-pole model

In order to fit the multi-pole representation of the target reflection coefficient and the target transmission coefficient, denoted by  $R_{tar}(\omega)$  and  $T_{tar}(\omega)$ , respectively, there are several parameter identification methods available, e.g., the vector fitting technique [48] and the optimization technique [30]. A comparative study by Cotté et al. [30] shows that the optimization technique is preferred over the vector fitting technique since it is straightforward to confine the values of parameters and the number of poles to satisfy admissibility and stability conditions. Therefore, in this study, the optimization technique as in Ref. [30] is used. Since  $R_{tar}(\omega)$  and  $T_{tar}(\omega)$  can be complex values, both the real parts and the imaginary parts should be fitted simultaneously, instead of the amplitude and the phase, in order to avoid wraparound ambiguity [49]. In the following, the fitting procedure for the target transmission coefficient  $T_{tar}(\omega)$  is presented and the same procedure can be applied to the target reflection coefficient  $R_{tar}(\omega)$ . Let  $T_{fit}(\omega)$  denote the fitting multi-pole approximation as in Eq. (18) of  $T_{tar}(\omega)$ , the optimization is performed considering  $f_s$  discrete frequencies sampled within the interested frequency range in a certain manner, e.g., logarithmically or linearly spaced. Then, the Euclidean norm of the deviation of real parts are minimized while keeping the difference of imaginary parts at each of the sampled frequency under a tolerance value  $\epsilon$ , i.e.,

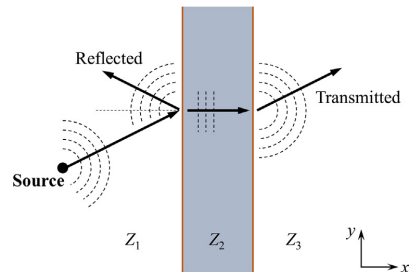


Fig. 3. Reflection and transmission through of a locally-reacting porous layer.

$$\min_{A_k, \zeta_k, \alpha_i, \beta_i, B_i, C_i} \left( \sqrt{\sum_{i=1}^{f_s} |\text{Re}[T_{\text{tar}}(\omega_i) - T_{\text{fit}}(\omega_i)]|} \right) \quad (37)$$

$$\text{such that} \begin{cases} 0 \leq \zeta_k \leq \zeta_{\max} \\ 0 \leq \alpha_i \leq \alpha_{\max} \\ 0 \leq \beta_i \leq \beta_{\max} \\ \forall i, \quad |\text{Im}[T_{\text{tar}}(\omega_i) - T_{\text{fit}}(\omega_i)]| \leq \epsilon. \end{cases}$$

where  $\zeta_{\max}$ ,  $\alpha_{\max}$ , and  $\beta_{\max}$  are the threshold values for  $\zeta$ ,  $\alpha$ , and  $\beta$  for the sake of the time-stepping stability. To solve this minimization problem, the interior-point algorithm [50] of the non-linear minimization function `fmincon` from the MATLAB optimization toolbox [51] is used. A series of optimizations are run to get a good fit. In the first run, the initial values of  $(A_k, \zeta_k, \alpha_i, \beta_i, B_i, C_i)$  are chosen randomly between 0 and  $\zeta_{\max}$ ,  $\alpha_{\max}$ ,  $\beta_{\max}$ , respectively, and a relatively large value of  $\epsilon$  is used, e.g.,  $\epsilon = 1 \times 10^{-1}$ . Then, the obtained set of coefficients are used as the initial values for the next optimization with a smaller value of  $\epsilon$ . The process continues until the threshold value of  $\epsilon$  meets the accuracy requirement. An example of parameter fitting will be shown in the following numerical test.

#### 4. Numerical examples and discussions

This section presents both one-dimensional and two-dimensional numerical examples to verify the proposed formulation of the time-domain reflection and transmission boundary condition. Depending on whether a multi-pole approximation is needed, two types of locally-reacting boundaries are considered in this study. One is the limp wall boundary, the reflection and transmission coefficients of which can be represented exactly with the real pole model as shown in Eqs. (31) and (32). The other one is the locally-reacting porous layer, which needs a further level of approximation of the reflection and transmission coefficients using the multi-pole model in Eq. (18). It should be noted that the mass-damper-spring (MDS) partition could be tackled with the same methodology as the porous layer. All of the following numerical experiments are initiated with the Gaussian-shaped pressure conditions as

$$p(\mathbf{x}, t = 0) = e^{-\frac{\ln 2}{b^2}(\mathbf{x} - \mathbf{x}_s)^2}, \quad (38a)$$

$$v(\mathbf{x}, t = 0) = 0, \quad (38b)$$

with  $\mathbf{x}_s$  being the source coordinates and  $b$  being the half-bandwidth of this Gaussian pulse.

##### 4.1. One-dimensional cases

As illustrated in Fig. 4, the sound field has a single monopole source at  $x_s = -3$  m and two receivers at  $x_{r1} = -0.5$  m and  $x_{r2} = 1.5$  m, respectively. The transmissive boundary is placed at  $x = 0$  m. The computational domain are terminated at both ends  $x = \pm 5$  m with the perfectly absorbing boundary condition, which

is achieved by discarding the incoming wave component in the numerical upwind flux [38].  $b$  is chosen as 0.15 such that the initial Gaussian pulse has a significant frequency content up to 1000 Hz.

For the one-dimensional test case, the analytical values of the frequency-dependent plane wave reflection and transmission coefficients are available. In order to obtain the numerical reflection coefficient  $R_{\text{num}}$  and the transmission coefficient  $T_{\text{num}}$ , two simulations are conducted. In the first simulation, the transmissive boundary is removed and the direct sound signal, denoted as  $p_d(t)$ , at each of two receivers is recorded. In the second simulation, the transmissive boundary is present, the measured sound pressure signal at first receiver  $x_{r1}$  contains both the direct sound and the sound reflected from the transmissive boundary while the signal at second receiver  $x_{r2}$  contains the transmitted signal alone  $p_t(t)$ . The reflected sound signal  $p_r(t)$  can be obtained by subtracting  $p_d(t)$ . The spectra of the direct sound, the reflected sound, and the transmitted sound, denoted as  $P_d(f)$ ,  $P_r(f)$ , and  $P_t(f)$ , respectively, are obtained by Fourier transformation of  $p_d$ ,  $p_r$ , and  $p_t$  without windowing. Let  $R_1$  denote the distance between the source and the receiver and  $R_2$  be the distance between the receiver and the image source mirrored by the reflecting surface. The numerical reflection coefficient  $R_{\text{num}}$  is calculated as follows:

$$R_{\text{num}}(f) = \frac{P_r(f) \cdot G(kR_1)}{P_d(f) \cdot G(kR_2)}, \quad (39)$$

where  $G(kR) = -e^{-ikR}/(2ik)$  is the 1D Green's function for the sound propagation in free field. Similarly, the numerical transmission coefficient  $T_{\text{num}}$  results from the ratio of the transmitted sound and the direct sound. As shown in Ref. [17], it is desirable to have around 10 points per wavelength (PPW) to achieve a satisfactory accuracy. Therefore, we discretize the computational domain with  $K = 30$  elements, corresponding to  $\Delta x = 1/3$  m, and inside each element, a polynomial basis of order  $N = 8$  is used, resulting into a PPW value of 9.2 at the frequency of 1000 Hz. According to Eq. (30), the time step size used is  $\Delta t = 4.871 \times 10^{-5}$  s, corresponding to  $C_{\text{FL}} = 1$ . The simulations are run for  $t = 0.5$  s so that the pulse has passed the receiver locations to a sufficient extent.

To quantify the error arising from each reflection and transmission, the dissipation error  $\epsilon_{\text{amp}}$  in dB and the phase error  $\epsilon_{\vartheta}$  in % from a single transmission are calculated as follows

$$\epsilon_{\text{amp}}(f) = 20 \log_{10} \left| \frac{T_{\text{ana}}(f)}{T_{\text{num}}(f)} \right|, \quad (40a)$$

$$\epsilon_{\vartheta}(f) = \frac{1}{\pi} |\vartheta(T_{\text{ana}}(f)) - \vartheta(T_{\text{num}}(f))| \times 100\%, \quad (40b)$$

where  $\vartheta(\cdot)$  extracts the phase angle of a complex number. Similarly, the error from a single reflection can be calculated by replacing  $T$  with  $R$  in above two equations. Therefore, for a given broadband incident acoustic wave of arbitrary amplitude, the loss of SPL and the distortion of the phase across the frequency range of interest can be quantified.

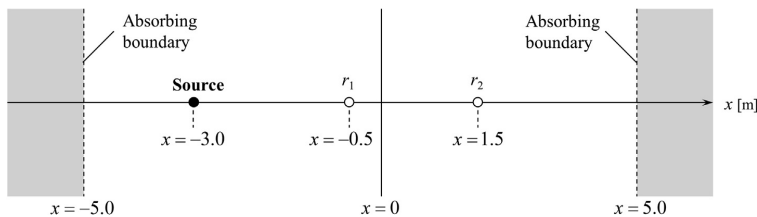


Fig. 4. 1D computational configuration with a transmissive boundary.

The first type of the transmissive boundary to be investigated is the limp wall case that is governed by the mass law. As discussed in Section 3.1, the surface mass density  $m$  of the thin partition material is the only parameter that affects the reflection and transmission characteristics. Here, two values of  $m = 10 \text{ kg/m}^2$  and  $m = 20 \text{ kg/m}^2$  are considered, corresponding to 3 cm thick materials of typical wood panels and light concrete, respectively. The analytical reflection coefficient  $R_{ana}$  and the transmission coefficient  $T_{ana}$  are calculated as shown in Eqs. (31) and (32). Fig. 5 presents the comparison of the results obtained by the numerical simulations and by the analytical solution. Both of the amplitudes of the reflection and the transmission coefficients match quite well with the analytical ones. As expected, all error increases gradually with increasing frequency due to the decreased PPW. Concretely, the dissipation error falls onto the order of magnitude  $\mathcal{O}(10^{-4})$  and the phase error is below 0.02%.

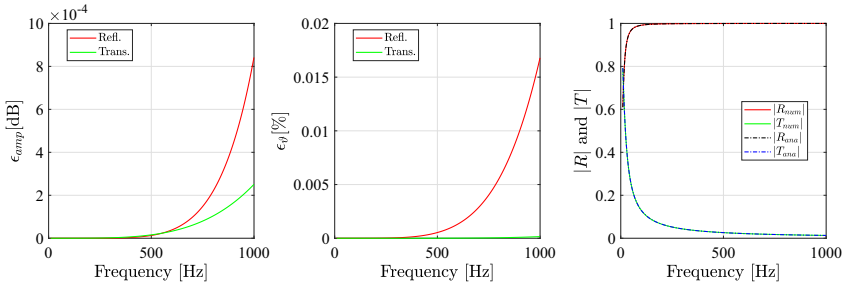
As for the locally-reacting porous layer, we consider a glass wool that is typically used as baffles for room acoustic purposes. Supposed its characteristic impedance  $Z_c$  is governed by the Johnson-Champoux-Allard-Lafarge (JCAL) model [52], which is a phenomenological model describing wave propagation in porous materials on a macroscopic scale and is expressed as  $Z_c = \sqrt{\rho_{eff} B_{eff}}$ . The effective density  $\rho_{eff}$  and the effective bulk modulus  $B_{eff}$  are described by

$$\rho_{eff} = \frac{\rho \alpha_\infty}{\phi} \left[ 1 + \frac{\sigma \phi}{i \omega \alpha_\infty \rho} \left( 1 + \frac{4i \alpha_\infty^2 \eta \rho}{\sigma^2 \Lambda^2 \phi^2} \right)^{1/2} \right], \quad (41)$$

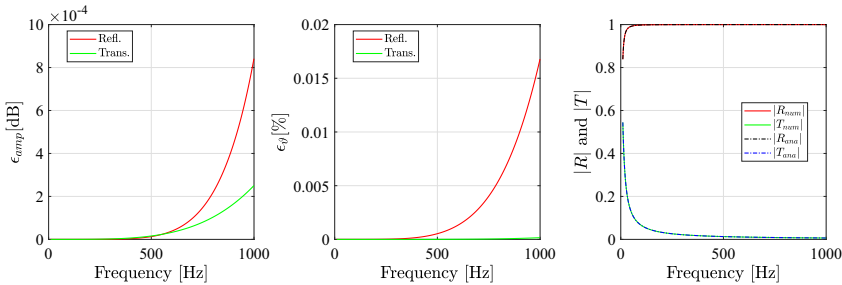
$$B_{eff} = \frac{\gamma P_0}{\phi} \left( \gamma - \frac{\gamma - 1}{1 + \frac{\phi \eta}{i \omega k_0 \rho P_r} \left( 1 + \frac{4i \omega k_0^2 \rho P_r}{\eta \Lambda^2 \phi^2} \right)^{1/2}} \right)^{-1}. \quad (42)$$

The wavenumber of the porous material is given as  $k_{eff} = \omega \sqrt{\rho_{eff}/B_{eff}}$ . The descriptions of physical parameters are given in Table A.3 in Appendix A and their values for the considered glass wool were measured by experiments [53]. In order to model the reflection and transmission properties of the porous layer, firstly, the characteristic impedance  $Z_c$  is inserted into the plane wave reflection coefficient  $R(\omega)$  as in Eq. (35) and the transmission coefficient  $T(\omega)$  as in Eq. (36). Then, the resulting target  $R_{tar}(\omega)$  and  $T_{tar}(\omega)$  are approximated with rational functions in the multi-pole form using the optimization techniques presented in Section 3.4. For the considered JCAL model, it is easy to verify that the magnitude of both  $R_{tar}(\omega)$  and  $T_{tar}(\omega)$  are monotonic decreasing function of frequency, which allows us to use real-poles alone for the approximation. The optimization is performed considering 100 frequencies logarithmically sampled between 20 and 1000 Hz, and the tolerance value  $\epsilon$  for the deviation of the imaginary part is chosen as  $1 \times 10^{-4}$ . Numerical tests show that there is a compromise between the number of poles and the fitting accuracy. Sets of fitting parameters for  $R(\omega)$  and  $T(\omega)$  are given in Table 1 and Table 2, respectively. The maximum absolute value error at the sampled frequencies are  $2.362 \times 10^{-3}$  and  $6.118 \times 10^{-5}$  for the real and imaginary part of the reflection coefficient, respectively, and the error for the transmission coefficient are  $2.636 \times 10^{-3}$  and  $5.418 \times 10^{-5}$ . The dissipation error  $\epsilon_{amp}$ , the phase error  $\epsilon_\phi$  as defined in Eq. (40) of the fitted coefficients are shown in Fig. 6, including the magnitude of both target and fitted coefficients as well.

The numerically simulated frequency-dependent characteristics of the porous layer are compared against the analytical ones in Fig. 7. Similar to the limp wall test case, the amplitudes of both the reflection and the transmission coefficients agree well with the analytical ones. However, the amplitudes and the frequency-



(a) Case 1: surface mass density  $m = 10 \text{ kg/m}^2$



(b) Case 2: surface mass density  $m = 20 \text{ kg/m}^2$

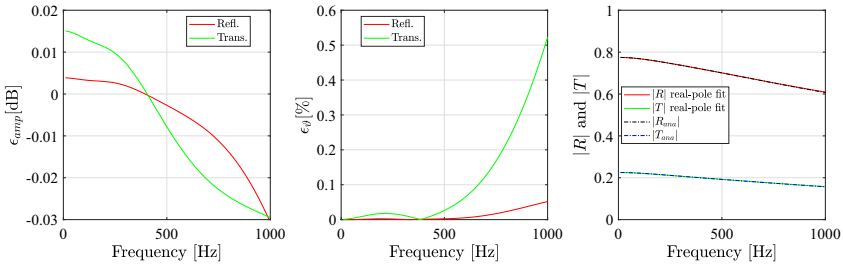
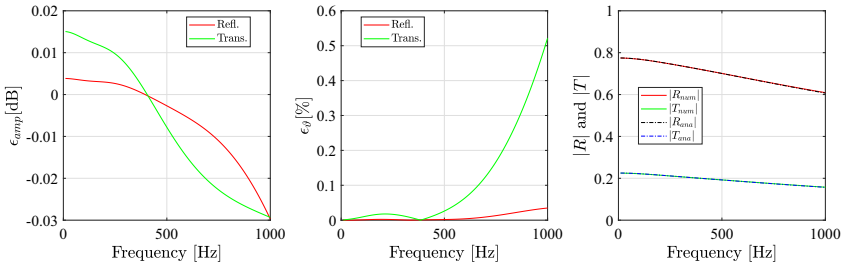
Fig. 5. The dissipation error  $\epsilon_{amp}$ , the phase error  $\epsilon_\phi$  and the magnitude of transmission and reflection coefficients for the 1D limp wall.

**Table 1**Fitting parameters  $A_k$  and  $\zeta_k$  of the real pole approximation for the reflection coefficient  $R(\omega)$  of the glass wool.

Coefficients	$k = 1$	$k = 2$	$k = 3$	$k = 4$
$A_k$	$3.124 \times 10^3$	$6.956 \times 10^1$	$8.175 \times 10^3$	$2.459 \times 10^3$
$\zeta_k$	$4.771 \times 10^4$	$1.747 \times 10^3$	$2.735 \times 10^4$	$6.641 \times 10^3$

**Table 2**Fitting parameters  $A_k$  and  $\zeta_k$  of the real pole approximation for the transmission coefficient  $T(\omega)$  of the glass wool.

Coefficients	$k = 1$	$k = 2$	$k = 3$	$k = 4$	$k = 5$
$A_k$	$-9.751 \times 10^3$	$1.087 \times 10^3$	$1.703 \times 10^3$	$6.401 \times 10^3$	$5.397 \times 10^1$
$\zeta_k$	$3.117 \times 10^4$	$6.121 \times 10^3$	$7.807 \times 10^3$	$5.773 \times 10^4$	$1.738 \times 10^3$

**Fig. 6.** The dissipation error  $\epsilon_{amp}$ , the phase error  $\epsilon_\phi$  and the magnitude of the fitted transmission and reflection coefficients for the 1D porous layer.**Fig. 7.** The dissipation error  $\epsilon_{amp}$ , the phase error  $\epsilon_\phi$  and the magnitude of the numerically simulated transmission and reflection coefficient for the 1D porous layer.

dependency of the quantified errors, especially the dissipation error, are quite different from the limp wall case. Through comparison of Figs. 6 and 7, it can be observed that the approximation error of  $R$  and  $T$  using the multi-pole model dominates over the DG discretization error for the overall error. This implies that the fitting quality of the multi-pole model plays a crucial role in the overall accuracy.

#### 4.2. Two-dimensional cases

This section is devoted to the verification of the transmission boundary condition in a two-dimensional sound field. Different from the one-dimensional test case, where the analytical values of the reflection and transmission coefficients are available, here, the numerical results obtained from the time-domain DG simulations are firstly transformed into the frequency-domain and then compared against the results obtained by the frequency-domain finite element (FE) analysis with the commercial software COMSOL Multiphysics<sup>®</sup> [54]. For each of the following numerical tests, the

free field responses at receivers are calculated firstly for both time-domain DG and frequency-domain FE simulations, in order to normalize the difference of the source power spectra between the DG simulations and frequency-domain FE simulations.

The first test case involves a rectangular domain evenly separated by a limp panel in the middle as shown in Fig. 8, which mimics a typical building acoustic scenario of sound transmission between two rooms partitioned by a thin structure. Here, the reflection and transmission characteristics of the limp panel are governed by the mass law as discussed in Section 3.1. Without loss of generality, two values of surface mass density  $m = 30 \text{ kg/m}^2$  and  $m = 65 \text{ kg/m}^2$  are used for the limp panel, representing light and moderately heavy room partitions, respectively. All the other boundaries are assigned as a uniform real-valued absorption coefficient of 0.36, which corresponds to the reflection coefficient of  $R = 0.8$ . The locations of the sound source and receivers are illustrated in Fig. 8. The half-bandwidth of Gaussian pulse is chosen as  $b = 0.25$  such that the source has a sufficient power up to 600 Hz. The computational domain for the DG simulation is

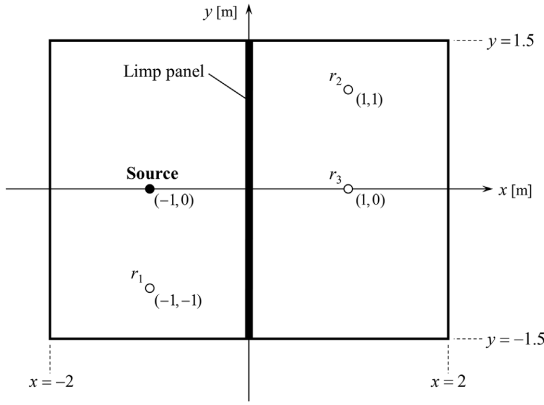
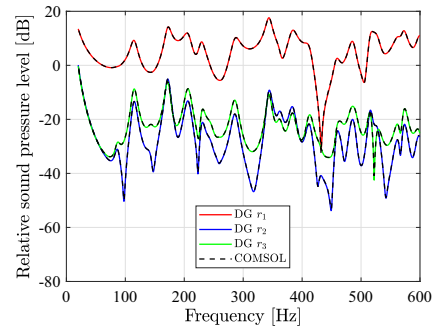


Fig. 8. Computational configuration of a two-dimensional sound field with a limp wall partition.

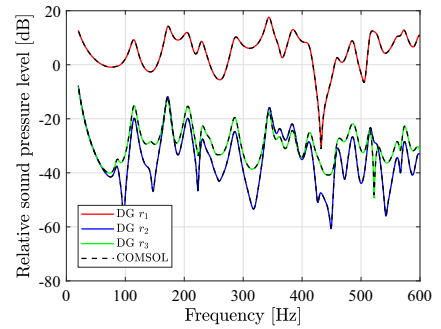
discretized with right angled isosceles triangles of equal leg length of 0.5 m, resulting into  $K = 96$  triangle elements. A local polynomial basis of order  $N = 8$  is used in order to have  $PPW = 10.8$  up-to frequency of 600 Hz. The time step size is  $\Delta t = 2.278 \times 10^{-5}$  s, corresponding to  $C_{FL} = 1$  as described in Eq. (30). The simulations are run for  $t = 0.45$  s and the time signal at each of the receiver locations approaches zero eventually due to the wall absorptions. For the frequency-domain FE analysis, the model was built in pressure acoustic module of the COMSOL Multiphysics® [54]. The monopole point source with a volume flow rate per unit length  $1 \text{ m}^2/\text{s}$  is applied at the source position. On the boundary corresponding to the limp panel, an interior impedance boundary condition with a frequency dependent impedance value  $i\omega m$  is imposed. On all the other boundaries, impedance boundary conditions with the surface impedance of  $Z_s = (1 + R)/(1 - R)$  are imposed. The meshes are discretized so that there are at least 6 elements per the shortest wavelength in the frequency range of interest, which is the wavelength of the time-harmonic acoustic waves at 600 Hz in this case, in order to ensure accuracy of the analysis.

The relative sound pressure level, which is obtained by calculating the amplitude of ratio of the pressure spectra with respect to the free field, is used for the comparison between the time-domain DG method and the frequency-domain FEM. As shown in Fig. 9, both numerical results agree well with each other at three receiver locations for two different surface mass density values. To demonstrate the comparison in terms of the phase shift, the phase angles of the ratio of the pressure spectra with respect to the free field spectra are compared in Fig. 10. For the sake of clarity, the phase angles at different receivers are shifted by a constant in the plot. A very good match between the time-domain simulations and the frequency-domain simulations can be observed.

The second test case considered is the sound propagation across a finite-height noise barrier made of the same porous glass-wool material as used in the one-dimensional test case. The schematic diagrams for both the DG and FE simulations are shown in Fig. 11. The source is located at  $(x_s, y_s) = (-2, 0)$  m and four receivers at  $(x_{r1}, y_{r1}) = (-1, 0)$ ,  $(x_{r2}, y_{r2}) = (-1, 3)$ ,  $(x_{r3}, y_{r3}) = (1, 0)$ , and  $(x_{r4}, y_{r4}) = (1, 3)$  m are distributed symmetrically with respect to the barrier, which is attached to the hard ground and has a height of  $H = 4$  m and width of  $W = 4$  cm. To mimic a real noise barrier mounted on a hard ground surface, the top edge of the barrier is a rigid boundary, whereas both side edges are treated as a transmissive porous layer. The other boundaries are assumed to be rigid.



(a)  $m = 30 \text{ kg/m}^2$



(b)  $m = 65 \text{ kg/m}^2$

Fig. 9. Comparison of the relative sound pressure level between the DG simulation and the FE simulation for the limp wall case with two different surface mass density  $m$ .

In order to capture the diffraction effects from the top edge of the barrier, the full geometry details of the barrier are meshed and modeled. For this test case, unstructured triangle meshes are generated with the meshing software GMSH [55]. As illustrated in Fig. 12, the mesh is locally refined near the top edge of the sound barrier and mesh elements far away from the sound barrier have an edge length of approximately 0.5 m. A local polynomial basis of order  $N = 8$  is adopted. The global uniform time step size is  $\Delta t = 1.391 \times 10^{-6}$  s, corresponding to  $C_{FL} = 1$  as described in Eq. (30). The impulse response from the DG simulation is recorded until the reflected waves from the exterior boundaries reach the receivers while ensuring that the pulse has passed the receivers' location to a sufficient extent.

In FE simulation, the barrier is modelled as an anisotropic medium with different acoustic densities in  $x$  and  $y$  directions to imitate the locally reacting wave behavior inside the porous layer, as it is described in Section 3.3. Therefore, the acoustic density in the  $x$  direction of the medium is represented as same as the effective density of the porous material in Eq. (41) but an infinite value is imposed for the acoustic density in the  $y$  direction to prohibit the wave propagation along the  $y$  direction. In addition, to truncate computational regions of an infinitely open space, perfectly matched layers (PMLs) are added on the top as well as at the left and right ends of the domain as shown in Fig. 11(b). Again, there are at least 6 elements per wavelength corresponding to the time-harmonic acoustic waves at 600 Hz, in order to ensure accuracy of the analysis.

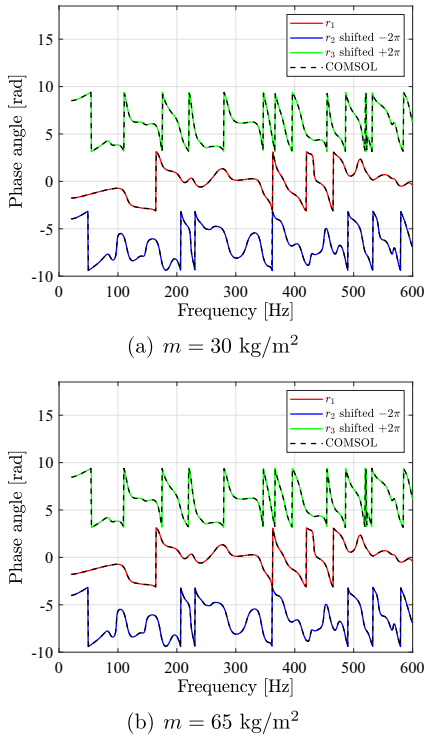


**Fig. 10.** Comparison of the phase angle of ratio between the DG simulation and the FE simulation for the limp wall case with two different surface mass density  $m$ .

Similar to the previous test case, the comparison of the relative sound pressure level and the phase angles of the pressure spectra ratio at different receiver locations are shown in Figs. 13 and 14, respectively. Again, a good match between the time-domain DG simulations and the frequency-domain FE simulations is found. It should be noted that the pressure waves arriving at the receivers across the barrier include not only the transmission components, but also the components diffracted over the hard barrier top, since the geometry details are fully resolved by both simulations. However, the discrepancies between two simulations in terms of the high order diffraction components, which should have existed due to the early truncated DG simulation, are mitigated due to the absorption effect of the noise barrier.

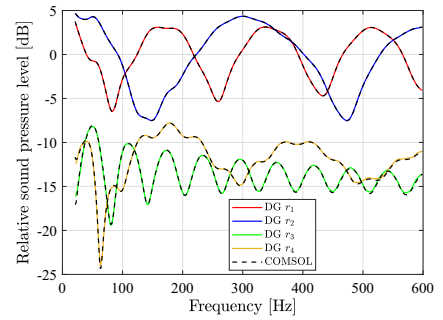


**Fig. 13.** Comparison of the relative sound pressure level between the DG simulation and the FE simulation for the noise barrier case.

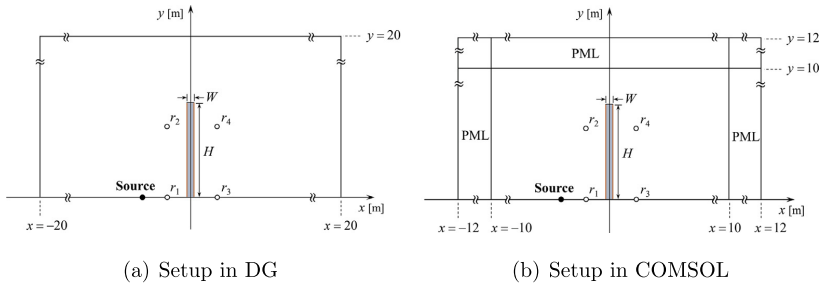


**Fig. 11.** Schematic diagram of a two-dimensional configuration with a noise barrier.

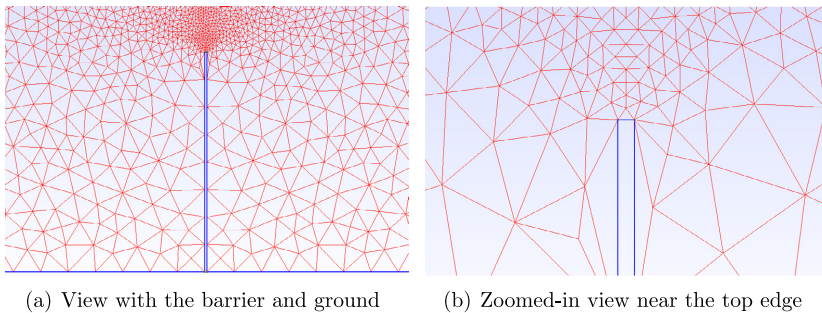


**Fig. 12.** 2D mesh around the noise barrier for the DG simulation.

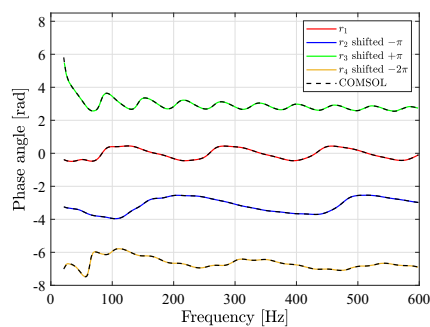


Fig. 14. Comparison of the phase angle of ratio between the DG simulation and the FE simulation for the noise barrier case.

5. Conclusion

In this study, a general time-domain transmission boundary condition in the framework of the time-domain DG method is developed for the broadband simulations of general linear acoustics, with potential applications to the areas of room acoustics, building acoustics, urban acoustics to name a few. The proposed numerical formulation is able to simulate frequency-dependent reflection and transmission characteristics of a locally-reacting boundary. The essential idea is to model the acoustic characteristics of a locally-reacting surface using the plane wave reflection coefficient and transmission coefficients in the form of a multi-pole model and then reformulate the corresponding time-domain upwind flux. Practical examples of the boundary modeling with the multi-pole model approach are presented.

To verify the performance of the formulation, one-dimensional numerical tests are performed and convergence of the numerical results to the analytical ones are demonstrated. Furthermore, it has been shown that the both dissipation and dispersion errors depend largely on the accuracy of parameters fitting of the multi-pole models. In this work, an optimization-based method is employed to obtain the fitting parameters. Although it is sufficient to verify the formulation for the locally-reacting boundaries with one-dimensional examples, two-dimensional numerical tests are conducted to further demonstrate the general practicability of the boundary formulation within the time-domain DG framework. Excellent agreement of numerical results obtained by the proposed time-domain method and the frequency-domain FEM are observed. However, for acoustic boundaries where non-negligible interactions happen, the locally-reacting assumption may lead to inaccurate representation of the acoustic behavior. Therefore, further developments of modeling extendedly-reacting boundaries will be undertaken in future works.

Declaration of Competing Interest

The authors declare that they have no known competing financial interests or personal relationships that could have appeared to influence the work reported in this paper.

Acknowledgements

This project has received funding from the European Union's Horizon 2020 research and innovation programme under grant agreement No. 721536.

Appendix A

Table A.3  
Overview of the JCAL impedance model parameters for the glass wool.

Property	Value
Atmospheric pressure $P_0$ [Pa]	$1.01 \times 10^5$
Speed of sound $c$ [m·s <sup>-1</sup> ]	343
Density $\rho$ [kg·m <sup>-3</sup> ]	1.2
Airflow resistivity $\sigma$ [Pa·s·m <sup>-2</sup> ]	70821
Porosity $\phi$	0.967
Tortuosity $\alpha_\infty$	1.049
Viscous characteristic length $\Lambda$ [m]	$6 \times 10^{-5}$
Thermal characteristic length $\Lambda'$ [m]	$1.4 \times 10^{-4}$
Static thermal permeability $k'_0$ [m <sup>2</sup> ]	$6.345 \times 10^{-9}$
Dynamic viscosity $\eta$ [N·m <sup>-2</sup> ]	$1.82 \times 10^{-5}$
Prandtl number $Pr$	0.71
Layer thickness $d$ [m]	0.04
Specific heat ratio $\gamma$	1.4

References

[1] Pelzer S, Aspöck L, Schröder D, Vorländer M. Integrating real-time room acoustics simulation into a cad modeling software to enhance the architectural design process. *Buildings* 2014;4(2):113–38.

[2] Kuttruff H. *Room acoustics*. New York: CRC Press; 2016.

[3] Sakuma T, Sakamoto S, Otsuru T. *Computational simulation in architectural and environmental acoustics*. Springer; 2014.

[4] Aretz M, Vorländer M. Combined wave and ray based room acoustic simulations of audio systems in car passenger compartments, part i: Boundary and source data. *Appl Acoust* 2014;76:82–99.

[5] Mehra R, Rungta A, Golas A, Lin M, Manocha D. Wave: Interactive wave-based sound propagation for virtual environments. *IEEE Trans Visualization Comput Graphics* 2015;21(4):434–42.

[6] Mallardo V, Aliabadi M, Brancati A, Marant V. An accelerated bem for simulation of noise control in the aircraft cabin. *Aerospace Sci Technol* 2012;23(1):418–28.

[7] Savioja L, Svensson UP. Overview of geometrical room acoustic modeling techniques. *J Acoust Soc Am* 2015;138(2):708–30.

[8] Cox T, D'Antonio P. *Acoustic absorbers and diffusers: theory, design and application*. CRC Press; 2016.

[9] Botteldooren D. Finite-difference time-domain simulation of low-frequency room acoustic problems. *J Acoust Soc Am* 1995;98(6):3302–8.

[10] Okuzono T, Yoshida T, Sakagami K, Otsuru T. An explicit time-domain finite element method for room acoustics simulations: Comparison of the performance with implicit methods. *Appl Acoust* 2016;76:84.

[11] Bilbao S. Modeling of complex geometries and boundary conditions in finite difference/finite volume time domain room acoustics simulation. *IEEE Trans Audio, Speech, Language Process* 2013;21(7):1524–33.

[12] Hornikx M, Krijnen T, van Harten L. openPSTD: The open source pseudospectral time-domain method for acoustic propagation. *Comput Phys Commun* 2016;203:298–308.

[13] Atkins HL, Shu C-W. Quadrature-free implementation of discontinuous Galerkin method for hyperbolic equations. *AIAA J* 1998;36(5):775–82.

[14] Delorme P, Mazet P, Peyret C, Ventribout Y. Computational aeroacoustics applications based on a discontinuous galerkin method. *Comptes Rendus Mécanique* 2005;333(9):676–82.

[15] Cockburn B, Karniadakis GE, Shu C-W. *Discontinuous Galerkin methods: theory, computation and applications*, vol. 11. Springer Science & Business Media; 2012.

[16] Hesthaven JS, Warburton T. *Nodal discontinuous Galerkin methods: Algorithms Analysis and Applications*. New York: Springer-Verlag; 2007.

[17] Wang H, Sihar I, Pagán Muñoz R, Hornikx M. Room acoustics modelling in the time-domain with the nodal discontinuous galerkin method. *J Acoust Soc Am* 2019;145(4):2650–63.

[18] Hu F, Atkins H. Two-dimensional wave analysis of the discontinuous Galerkin method with non-uniform grids and boundary conditions. In: *8th AIAA/CEAS Aeroacoustics Conference & Exhibit*. p. 2514.

[19] Modave A, St-Cyr A, Warburton T. GPU performance analysis of a nodal discontinuous galerkin method for acoustic and elastic models. *Comput Geosci* 2016;91:64–76.

[20] Schoeder S, Wall W, Kronbichler M. Exwave: A high performance discontinuous galerkin solver for the acoustic wave equation. *SoftwareX* 2019;9:49–54.

[21] Schoeder SM. *Efficient Discontinuous Galerkin Methods for Wave Propagation and Iterative Optoacoustic Image Reconstruction*. Ph.D. dissertation. Technische Universität München; 2019.

[22] Toyoda M, Ishikawa S. Frequency-dependent absorption and transmission boundary for the finite-difference time-domain method. *Appl Acoust* 2019;145:159–66.

- [23] Richter C, Hay JA, Schönwald N, Busse S, Thiele F. A review of time-domain impedance modelling and applications. *J Sound Vib* 2011;330(16):3859–73.
- [24] Fung K-Y, Ju H. Time-domain impedance boundary conditions for computational acoustics and aeroacoustics. *Int J Comput Fluid Dyn* 2004;18(6):503–11.
- [25] Reyman Y, Baelmans M, Desmet W. Efficient implementation of Tam and Auriault's time-domain impedance boundary condition. *AIAA J* 2008;46(9):2368–76.
- [26] Monteghetti F, Matignon D, Piot E. Energy analysis and discretization of nonlinear impedance boundary conditions for the time-domain linearized euler equations. *J Comput Phys* 2018;375:393–426.
- [27] Wang H, Hornikx M. Broadband time-domain impedance boundary modeling with the discontinuous galerkin method for room acoustics simulations. In: 23rd International Congress on Acoustics, p. 779–86.
- [28] Kim Y-H. Sound propagation: an impedance based approach. John Wiley & Sons; 2010.
- [29] Fung K-Y, Ju H. Broadband time-domain impedance models. *AIAA J* 2001;39(8):1449–54.
- [30] Cotté B, Blanc-Benon P, Bogey C, Poisson F. Time-domain impedance boundary conditions for simulations of outdoor sound propagation. *AIAA J* 2009;47(10):2391–403.
- [31] Dragna D, Cotté B, Blanc-Benon P, Poisson F. Time-domain simulations of outdoor sound propagation with suitable impedance boundary conditions. *AIAA J* 2011;49(7):1420–8.
- [32] Troian R, Dragna D, Bailly C, Galland M-A. Broadband liner impedance eduction for multimodal acoustic propagation in the presence of a mean flow. *J Sound Vib* 2017;392:200–16.
- [33] Douasbin Q, Scalo C, Selle L, Poinsot T. Delayed-time domain impedance boundary conditions (d-tdibc). *J Comput Phys* 2018;371:50–66.
- [34] Joseph RM, Hagness SC, Taflov A. Direct time integration of maxwell's equations in linear dispersive media with absorption for scattering and propagation of femtosecond electromagnetic pulses. *Opt Lett* 1991;16(18):1412–4.
- [35] Dragna D, Pineau P, Blanc-Benon P. A generalized recursive convolution method for time-domain propagation in porous media. *J Acoust Soc Am* 2015;138(2):1030–42.
- [36] Hesthaven JS, Teng C-H. Stable spectral methods on tetrahedral elements. *SIAM J Sci Comput* 2000;21(6):2352–80.
- [37] Ainsworth M. Dispersive and dissipative behaviour of high order discontinuous Galerkin finite element methods. *J Comput Phys* 2004;198(1):106–30.
- [38] Atkins H. Continued development of the discontinuous Galerkin method for computational aeroacoustic applications. In: 3rd AIAA/CEAS Aeroacoustics Conference, p. 1581.
- [39] M.H. Carpenter, C.A. Kennedy, Fourth-order 2n-storage runge-kutta schemes, in: NASA-TM-109112, 1994.
- [40] Reddy SC, Trefethen LN. Stability of the method of lines. *Numer Math* 1992;62(1):235–67.
- [41] Gustafsson B. High order difference methods for time dependent PDE. Berlin: Springer-Verlag; 2007.
- [42] Pind F, Engsig-Karup AP, Jeong C-H, Hesthaven JS, Mejling MS, Strømman-Andersen J. Time domain room acoustic simulations using the spectral element method. *J Acoust Soc Am* 2019;145(6):3299–310.
- [43] Gunnarsdóttir K, Jeong C-H, Marbjerg G. Acoustic behavior of porous ceiling absorbers based on local and extended reaction. *J Acoust Soc Am* 2015;137(1):509–12.
- [44] Kinsler LE, Frey AR, Coppens AB, Sanders JV. Fundamentals of acoustics, Fundamentals of Acoustics, 4th Edition, by Lawrence E. Kinsler, Austin R. Frey, Alan B. Coppens, James V. Sanders, pp. 560. ISBN 0-471-84789-5. Wiley-VCH, December 1999. (1999) 560.
- [45] Reddy JN. Theory and analysis of elastic plates and shells. CRC Press; 2006.
- [46] Fahy F, Gardonio P. Sound and structural vibration – radiation, transmission and response. Elsevier; 2007.
- [47] Brekhovskikh LM, Godin OA. Acoustics of layered media I: Plane and quasi-plane waves, vol. 5. Springer Science & Business Media; 2012.
- [48] Gustavsen B, Semlyen A. Rational approximation of frequency domain responses by vector fitting. *IEEE Trans Power Delivery* 1999;14(3):1052–61.
- [49] Bilbao S, Hamilton B, Botts J, Savioja L. Finite volume time domain room acoustics simulation under general impedance boundary conditions. *IEEE/ACM Trans Audio Speech Language Processing (TASLP)* 2016;24(1):161–73.
- [50] Byrd RH, Hribar ME, Nocedal J. An interior point algorithm for large-scale nonlinear programming. *SIAM J Optim* 1999;9(4):877–900.
- [51] MATLAB Optimization Toolbox (R2018b), The MathWorks, Inc., Natick, Massachusetts, USA, 2018.
- [52] Lafarge D, Lemarinier P, Allard JF, Tarnow V. Dynamic compressibility of air in porous structures at audible frequencies. *J Acoust Soc Am* 1997;102(4):1995–2006.
- [53] Hoekstra N. Sound absorption of periodically spaced baffles Master thesis. Eindhoven University of Technology; 2016.
- [54] COMSOL AB, Stockholm, Sweden, COMSOL Multiphysics v. 5.4.
- [55] Geuzaine C, Remacle J-F. Gmsh: A 3-D finite element mesh generator with built-in pre- and post-processing facilities. *Int J Numer Meth Eng* 2009;79(11):1309–31.

---

## Errata of Paper III

It should be noted that the statement following Eqs. (33) and (34) in section 3.2, which is “*However, compared to the limp wall case, there is an extra frequency-dependent term  $s/\omega$  in the denominators of above two equations (33) and (34) due to spring effect. Consequently both the reflection coefficient  $R(\omega)$  and the transmission coefficient  $T(\omega)$  cannot be re-written in the multi-pole model form as shown in Eq. (18). Consequently, a further approximation is needed to express  $R(\omega)$  and  $T(\omega)$  using the rational functions as basis functions. The approximation procedure will be discussed in Sec. 3.4.*”, is incorrect.

As shown in the following, both the plane wave reflection coefficient  $R(\omega)$  and transmission coefficient  $T(\omega)$  can be re-cast in a multi-pole form with complex poles and therefore, no further approximation is needed for  $R(\omega)$  and  $T(\omega)$ . Recall that the multi-pole model approximation is (taking  $T(\omega)$  for example),

$$\begin{aligned} T(\omega) &\approx T_\infty + \sum_{k=1}^S \frac{A_k}{\zeta_k + i\omega} + \sum_{l=1}^K \frac{1}{2} \left( \frac{B_l - iC_l}{\alpha_l - i\beta_l + i\omega} + \frac{B_l + iC_l}{\alpha_l + i\beta_l + i\omega} \right) \\ &= T_\infty + \sum_{k=1}^S \frac{A_k}{\zeta_k + i\omega} + \sum_{l=1}^K \frac{B_l i\omega + C_l \beta_l + \alpha_l B_l}{\alpha_l^2 + \beta_l^2 + 2\alpha_l i\omega - \omega^2}. \end{aligned}$$

As shown in Eq. (34) of **Paper III**, the transmission coefficient  $T(\omega)$  for the mass-damper-spring (MDS) partition is

$$\begin{aligned} T(\omega) &= \frac{2Z_c}{i(\omega m - s/\omega) + 2Z_c + r_d} \\ &= \frac{2Z_c i\omega/m}{s/m + i\omega(2Z_c + r_d)/m - \omega^2}. \end{aligned}$$

By comparing above two equations, it is straightforward to obtain the relations between the multi-pole model parameters and the MDS parameters as  $B = 2Z_c/m$ ,  $\alpha = (2Z_c + r_d)/(2m)$ ,  $\beta = \sqrt{s/m - \alpha^2}$ ,  $C = -\alpha B/\beta$ .

Therefore, the texts following Eqs. (33) and (34) in section 3.2 should be corrected to: “*Through derivations, it is straightforward to express the transmission coefficient  $T(\omega)$  in terms of the multi-pole model parameters with  $B = 2Z_c/m$ ,  $\alpha = (2Z_c + r_d)/(2m)$ ,  $\beta = \sqrt{s/m - \alpha^2}$ ,  $C = -\alpha B/\beta$ , whereas the reflection coefficient  $R(\omega)$  only differs by the constant 1 and the sign of  $B$ .*”

---

---

## Paper IV

# An arbitrary high-order discontinuous Galerkin method with local time-stepping for linear acoustic wave propagation

Huiqing Wang,<sup>a)</sup> Matthias Cosnefroy, and Maarten Hornikx<sup>b)</sup>

*Building Physics and Services, Department of the Built Environment, Eindhoven University of Technology, P.O. Box 513, Eindhoven, 5600 MB, The Netherlands*

## ABSTRACT:

This paper presents a numerical scheme of arbitrary order of accuracy in both space and time, based on the arbitrary high-order derivatives methodology, for transient acoustic simulations. The scheme combines the nodal discontinuous Galerkin method for the spatial discretization and the Taylor series integrator (TSI) for the time integration. The main idea of the TSI is a temporal Taylor series expansion of all unknown acoustic variables in which the time derivatives are replaced by spatial derivatives via the Cauchy-Kovalewski procedure. The computational cost for the time integration is linearly proportional to the order of accuracy. To increase the computational efficiency for simulations involving strongly varying mesh sizes or material properties, a local time-stepping (LTS) algorithm accompanying the arbitrary high-order derivatives discontinuous Galerkin (ADER-DG) scheme, which ensures correct communications between domains with different time step sizes, is proposed. A numerical stability analysis in terms of the maximum allowable time step sizes is performed. Based on numerical convergence analysis, we demonstrate that for nonuniform meshes, a consistent high-order accuracy in space and time is achieved using ADER-DG with LTS. An application to the sound propagation across a transmissive noise barrier validates the potential of the proposed method for practical problems demanding high accuracy. © 2021 Acoustical Society of America.

<https://doi.org/10.1121/10.0003340>

(Received 2 October 2020; revised 3 December 2020; accepted 21 December 2020; published online 25 January 2021)

[Editor: Nickolas Vlahopoulos]

Pages: 569–580

## I. INTRODUCTION

Recent years have witnessed rapid developments and applications of the time-domain discontinuous Galerkin (TD-DG) method for modeling wave propagation phenomena,<sup>1–8</sup> which possesses many favorable properties, such as high-order accuracy, geometric flexibility, and its capability of handling inhomogeneous media and physically absorbing media.<sup>9–11</sup> It first discretizes the volumetric space into non-overlapping mesh elements that can be locally refined to meet the geometrical constraints. Then, solutions of governing acoustic equations are approximated spatially with a polynomial basis. Because the locally defined basis functions can be discontinuous across element interfaces, the resulting mass matrix is block diagonal, which favors a fully explicit time-marching scheme with intrinsic parallel computations.<sup>12,13</sup> Last, following the numerical methodology of the method of lines, the resulting semi-discrete formulations in the form of coupled ordinary differential equations (ODEs) are integrated in time by an ODE solver. Explicit Runge-Kutta (RK) methods, which involve only a linear combination of the right-hand-side evaluations of the semi-discrete formulation, are usually used because they are easy to implement, and each unknown solution only needs one extra memory unit to store its intermediate stage values with low-storage RK methods.<sup>14–20</sup>

However, despite the abovementioned advantages, industrial applications of the TD-DG method for computational acoustics remain hindered by the high computational cost for longtime simulations, and advancements to improve the computational efficiency are needed. One major criticism arises from the severely restrictive maximum allowable time step imposed by the well-known Courant-Friedrichs-Lewy (CFL) conditional stability condition accompanying explicit time integration schemes. As far as practical acoustic simulations are concerned, local mesh refinement is usually needed to capture complex geometry features, such as abruptly varying surfaces, resulting in stiff terms in ODEs that necessitate a much smaller time step. When global time-stepping (GTS) is used, as is often the practice with the method of lines, the uniformly defined time step is constrained by the smallest element in the mesh, excessively slowing down the time-marching over the whole domain. Apart from the mesh-induced stiffness, the modeling of physically absorbing media<sup>9,10</sup> is a potential source of stiffness as well. A natural solution to the restrictive time steps required for stability of explicit GTS methods is to switch to unconditionally stable implicit methods. However, for three-dimensional problems with a large number of unknowns, the computational efficiency of such an approach is debatable because solving a large linear system at every time step is time consuming.<sup>21</sup> An alternative is to use implicit-explicit (IMEX) schemes,<sup>22–24</sup> which applies an explicit integrator to the non-stiff/coarse part and an implicit

<sup>a)</sup>Electronic mail: h.wang6@tue.nl, ORCID: 0000-0003-3465-3555.

<sup>b)</sup>ORCID: 0000-0002-8343-6613.

integrator to the stiff/refined part such that the same time step is used everywhere. Additionally, exponential-based time integrators<sup>25,26</sup> alleviate the stability restrictions by removing the stiffness on the explicit time integration through transforming the differential equations. However, pitfalls, such as lower-order coupling errors, coupling stability problems, ill-conditioning issues for highly disparate meshes, and cumbersome implementations, may occur. An alternative approach to mitigate the time step restriction is to use explicit local time-stepping (LTS) methods, also called multiple or multi-rate time-stepping (MTS) in the literature, which use smaller time steps where necessary while remaining fully explicit in the entire mesh. This increases the efficiency drastically as larger elements can be advanced with large local time steps. Over the past decades, various LTS methods have been developed in the scientific computing community targeting either general ODEs<sup>27–29</sup> or specific spatial discretization methods.<sup>30</sup> As far as the DG method is concerned, LTS schemes based on the second-order leap-frog (LF2) method,<sup>31–34</sup>  $p$ th-order Runge-Kutta (RK $p$ ,  $p \leq 4$ ) methods,<sup>35–40</sup>  $p$ th-order Adams-Bashforth multistep schemes (AB $p$ ,  $p \leq 4$ ),<sup>41</sup> and the causal-path concept, combining LF2 and RK4 (Ref. 42), have been proposed for wave propagation problems. Recently, the arbitrary high-order derivatives discontinuous Galerkin (ADER-DG) method with the LTS scheme was used to model transient electromagnetic,<sup>43</sup> elastic,<sup>44,45</sup> and acoustic<sup>46</sup> wave propagation. The arbitrary high-order derivatives (ADER) time integration approach follows the Taylor series method and expands the unknown solutions directly into a temporal Taylor series in which all of the time derivatives are converted into spatial derivatives by repeatedly using the governing partial differential equations (the so-called Cauchy-Kovalevski procedure). The high-order spatial derivatives are approximated with the DG method. The ADER approach is a one-step explicit scheme that does not require intermediate stages while maintaining the same approximation order in space and time. Despite such attractive properties, it has a drawback that the high-order spatial derivatives of the polynomial basis are rather tedious to derive and implement, especially when non-affine (curved) elements with varying Jacobians are involved.

This work aims to further develop the TD-DG method to be more robust and efficient in simulating transient acoustic wave propagation from the following two aspects. First, inspired by a new class of high-order scheme recently introduced for seismic<sup>47</sup> and electromagnetic<sup>48,49</sup> wave modeling, we present a variant of the ADER-DG approach to solve the time-dependent linear acoustic equations with an arbitrary order of accuracy in time and space and incorporate necessary formulations of time-domain impedance and transmission boundary conditions for indoor-outdoor acoustic simulation purposes. The governing acoustic equations are first spatially discretized with the DG method by projection onto the space-dependent polynomial basis functions to obtain the semi-discrete formulation in terms

of time-dependent expansion coefficients. Then, these coefficients are time integrated by the Taylor series integrator (TSI). The needed time derivatives are replaced with the numerically approximated spatial derivatives by recursively using the semi-discrete formulation. These constitute a discrete version of the Cauchy-Kovalevski procedure. Second, we propose a new LTS algorithm to accompany the ADER-DG scheme to overcome the inefficiency and stability issues occurring in stiff systems. Without any overlapping subdomains or extrapolation involved, the proposed coupling procedure between domains with different time steps maintains the same high-order accuracy as that of the GTS scheme by using the underlying TSI in a straightforward and efficient manner and is valid for arbitrary ratios of time steps. Furthermore, the computational cost grows linearly with respect to temporal orders of accuracy. The CFL stability conditions are investigated numerically with the aim of providing guidance on time step sizes in practical simulations. An application to the sound propagation across a transmissive noise barrier exhibits the computational benefits of the proposed LTS schemes.

The paper is organized as follows. In Sec. II, spatial discretization of linear acoustic equations with impedance and transmission boundary conditions by the DG method is briefly reviewed. A detailed description of the proposed time-stepping scheme follows in Sec. III. Numerical stability analysis and convergence rate tests are presented in Sec. IV. Application to the sound propagation across a transmissive noise barrier is shown in Sec. V. Finally, concluding remarks can be found in Sec. VI.

## II. SPATIAL DISCRETIZATION OF LINEAR ACOUSTIC EQUATIONS WITH THE NODAL DG METHOD

To avoid redundant repetitions with previous works<sup>50</sup> while introducing necessary notations for the convenience of discussion, first, we briefly review the main ingredients of the nodal DG method, which is used for the spatial discretization. Acoustic wave propagation can be described by the following coupled system of linear acoustic equations:

$$\begin{aligned} \frac{\partial \mathbf{v}}{\partial t} + \frac{1}{\rho} \nabla p &= 0, \\ \frac{\partial p}{\partial t} + \rho c^2 \nabla \cdot \mathbf{v} &= 0, \quad \text{in } \Omega \times [0, t], \end{aligned} \quad (1)$$

where  $\mathbf{v}(\mathbf{x}, t) = [u, v, w]^T$  is the particle velocity vector,  $p(\mathbf{x}, t)$  is the sound pressure,  $\mathbf{x}$  is the position in the spatial domain of interest  $\Omega$ ,  $\rho$  is the constant density of air, and  $c$  is the constant speed of sound ( $c = 343$  m/s and  $\rho = 1.2$  kg/m<sup>3</sup> in this work). Equivalently, Eq. (1) reads

$$\frac{\partial \mathbf{q}}{\partial t} + \nabla \cdot \mathbf{F}(\mathbf{q}) = \frac{\partial \mathbf{q}}{\partial t} + \mathbf{A}_j \frac{\partial \mathbf{q}}{\partial x_j} = 0, \quad (2)$$

where  $\mathbf{q}(\mathbf{x}, t) = [u, v, w, p]^T$  is the unknown acoustic variable vector and  $\mathbf{A}_j$  is the constant flux Jacobian matrix with spatial coordinate index  $j \in \{1, 2, 3\}$  and  $x_1 = x$ ,  $x_2 = y$ ,  $x_3 = z$ . The computational domain  $\Omega$  is divided into non-overlapping simplex elements  $D^k$ , i.e.,  $\Omega = \cup_{k=1}^K D^k$ . In this work, the quadrature-free approach<sup>1</sup> is adopted and the nodal discontinuous Galerkin algorithm as presented in Ref. 4 is followed. The local solution  $\mathbf{q}_h^k(\mathbf{x}, t)$  in element  $D^k$ , where subscript  $h$  denotes the numerically approximated variable, is given by

$$\mathbf{q}_h^k(\mathbf{x}, t) = \sum_{i=1}^{N_p} \mathbf{q}_h^k(\mathbf{x}_i^k, t) l_i^k(\mathbf{x}), \quad (3)$$

where  $\mathbf{q}_h^k(\mathbf{x}_i^k, t)$  are the unknown nodal values,  $l_i^k(\mathbf{x}_i^k)$  is the multidimensional Lagrange polynomial basis of order  $N$ , which satisfies  $l_i^k(\mathbf{x}_j^k) = \delta_{ij}$ , and indices  $i, j$  denote the ordering of the nodes.  $N_p$  is the number of local basis functions (or nodes) inside a single element and is equal to  $(N+d)!/(N!d!)$  for simplex elements, where  $d$  is the dimensionality. The basis (shape) function  $l_i^k(\mathbf{x})$  is determined by the nodal distribution  $\mathbf{x}_i^k$ , and in this study, the Legendre-Gauss-Lobatto (LGL) quadrature points are used for one-dimensional (1D) problems and the  $\alpha$ -optimized nodal distribution<sup>51</sup> is used for multidimensional elements due to its low Lebesgue constants. Also, the test function space is spanned by the same basis polynomials  $l_i^k(\mathbf{x})$ . After the Galerkin projection of Eq. (2) and twice integrations by parts, the strong formulation reads

$$\int_{D^k} \left( \frac{\partial \mathbf{q}_h^k}{\partial t} + \nabla \cdot \mathbf{F}_h^k(\mathbf{q}_h^k) \right) l_i^k d\mathbf{x} = \int_{\partial D^k} \mathbf{n} \cdot (\mathbf{F}_h^k(\mathbf{q}_h^k) - \mathbf{F}^*(\mathbf{q}_h^-, \mathbf{q}_h^+)) l_i^k d\mathbf{x}, \quad (4)$$

where  $\mathbf{n} = [n_x, n_y, n_z]$  is the outward normal vector of the element surface  $\partial D^k$ .  $\mathbf{F}^*(\mathbf{q}_h^-, \mathbf{q}_h^+)$ , the so-called numerical flux across element intersection  $\partial D^k$ , is a function of both the solution value from the interior side of the intersection, i.e.,  $\mathbf{q}_h^-$  and the neighboring exterior value  $\mathbf{q}_h^+$ . In this study, the upwind numerical flux is used throughout the whole domain because of its low dispersion and dissipation errors.<sup>52,53</sup> It is defined by considering the direction of propagating characteristic waves, i.e.,

$$\mathbf{n} \cdot \mathbf{F}^*(\mathbf{q}_h^-, \mathbf{q}_h^+) = \mathbf{L}(\Lambda^+ \mathbf{L}^{-1} \mathbf{q}_h^- + \Lambda^- \mathbf{L}^{-1} \mathbf{q}_h^+), \quad (5)$$

where  $\Lambda$  is a diagonal matrix with diagonal entries  $[0, 0, c, -c]$ , corresponding to the speed of each characteristic wave.  $\Lambda^+$  and  $\Lambda^-$  contain the positive and negative entries of  $\Lambda$  respectively.  $\mathbf{L}$  is the eigenmatrix of the normally projected flux Jacobian, i.e.,

$$\mathbf{A}_n = (n_x \mathbf{A}_x + n_y \mathbf{A}_y + n_z \mathbf{A}_z) = \mathbf{L} \Lambda \mathbf{L}^{-1}, \quad (6)$$

where

$$\mathbf{L} = \begin{bmatrix} -n_y & -n_z & n_x/2 & -n_x/2 \\ n_x & 0 & n_y/2 & -n_y/2 \\ 0 & n_x & n_z/2 & -n_z/2 \\ 0 & 0 & \rho c/2 & \rho c/2 \end{bmatrix}, \quad \mathbf{A} = \begin{bmatrix} 0 & 0 & 0 & 0 \\ 0 & 0 & 0 & 0 \\ 0 & 0 & c & 0 \\ 0 & 0 & 0 & -c \end{bmatrix}. \quad (7)$$

Physically,  $\Lambda^+$  ( $\Lambda^-$ , respectively) corresponds to the characteristic waves propagating along (opposite to) the outward normal direction  $\mathbf{n}$ , which are referred to as outgoing waves out of  $D_k$  (incoming waves into  $D_k$ ). Therefore, the outgoing waves are associated with the interior solution  $\mathbf{q}_h^-$ , whereas the incoming waves are dependent on the exterior (neighboring) solution  $\mathbf{q}_h^+$ . Finally, the semi-discrete formulation is obtained by substituting the nodal basis expansion [Eq. (3)] and the upwind flux [Eq. (5)] into the strong formulation [Eq. (4)]. The resulting vector-matrix form of the formulation and additional descriptions of implementations can be found in Ref. 50.

Besides the spatial discretization inside the computational domain, proper formulations of the boundary conditions are of critical importance because boundaries of various shapes introduce a considerable amount of complexities into the wave patterns over a long time, such as absorption, transmission, and coupling with structural vibrations.<sup>9–11,54,55</sup> For the DG method, boundary conditions are enforced weakly through the numerical flux. In this work, the formulations of broadband time-domain impedance and transmission boundary conditions for locally reacting surfaces are considered.<sup>10,11</sup> The essential idea is to reformulate the numerical flux based on the characteristic waves of the linear acoustic equations, together with the plane wave reflection coefficient  $R$  and transmission coefficient  $T$  at normal incidence. The use of coefficients at normal incidence is consistent with the fact that only the normal component of the numerical flux to the boundary surface contributes to the surface integral in Eq. (4). As shown in Refs. 10 and 11, the inputs required for the boundary formulation are the complex-valued plane wave reflection coefficient  $R(\omega)$  and transmission coefficient  $T(\omega)$  as a function of the angular frequency  $\omega$  in the frequency domain, which may be obtained from (semi-) analytical impedance models or measured discrete impedance values. Then, both coefficients are approximated within the frequency range of interest using multipole models.<sup>56–58</sup> For example,  $R(\omega)$  is approximated as

$$R(\omega) \approx R_\infty + \sum_{k=1}^S \frac{A_k}{\zeta_k + i\omega} + \sum_{l=1}^T \frac{1}{2} \left( \frac{B_l - iC_l}{\alpha_l - i\beta_l + i\omega} + \frac{B_l + iC_l}{\alpha_l + i\beta_l + i\omega} \right) = R_\infty + \sum_{k=1}^S \frac{A_k}{\zeta_k + i\omega} + \sum_{l=1}^T \frac{B_l i\omega + C_l \beta_l + \alpha_l B_l}{(\alpha_l + i\omega)^2 + \beta_l^2}, \quad (8)$$

where  $[R_\infty, A_k, B_l, C_l, \zeta_k, \alpha_l, \beta_l] \in \mathbb{R}$  are all real numerical fitting parameters.  $R_\infty$  is the frequency-independent value, e.g.,  $R_\infty = 1$  for the hard wall boundary.  $\zeta_k$  and  $\alpha_l \pm i\beta_l$  are the real poles and complex conjugate pole pairs,  $S$  and  $T$  are their numbers, respectively. The numerical properties of the multipole model and parameter fitting procedures can be found in Ref. 10 while a few examples of practical locally reacting boundaries are discussed in Ref. 11. By applying the inverse Fourier transform to Eq. (8), the so-called reflection impulse response function in the time-domain is obtained as

$$R(t) \approx R_\infty \delta(t) + \sum_{k=1}^S A_k e^{-\zeta_k t} H(t) + \sum_{l=1}^T e^{-\alpha_l t} (B_l \cos(\beta_l t) + C_l \sin(\beta_l t)) H(t), \quad (9)$$

where  $\delta(t)$  and  $H(t)$  are the Dirac delta and Heaviside functions, respectively. The transmission impulse response function  $T(t)$  can be calculated similarly. As derived in Ref. 11, the general form of upwind flux along the boundary is expressed as

$$\mathbf{n} \cdot \mathbf{F}^*(\mathbf{q}_h^-, \mathbf{q}_h^+) = \mathbf{L} \mathbf{A} \begin{bmatrix} 0 \\ 0 \\ \varpi_n^{\text{out}} \\ \int_{-\infty}^t \varpi_n^{\text{out}}(\tau) R(t-\tau) d\tau + \int_{-\infty}^t \varpi_n^{\text{out}*}(\tau) T(t-\tau) d\tau \end{bmatrix}. \quad (10)$$

Here,  $\varpi_n^{\text{out}}(t)$  is the outgoing characteristic wave that is calculated with the interior solution values  $\mathbf{q}_h^-$  at each of the discrete nodes along the boundary as

$$\varpi_n^{\text{out}}(t) = \frac{p^-(t)}{\rho c} + \mathbf{v}^-(t) \cdot \mathbf{n}, \quad (11)$$

where  $\mathbf{n}$  is the outward normal vector of the boundary element surface. Similarly,  $\varpi_n^{\text{out}*}$  is the outgoing wave coming from the neighboring element that lies on the other side of the transmissive boundary surface and is calculated using exterior solution values as  $\varpi_n^{\text{out}*} = p^+(t)/\rho c - \mathbf{v}^+(t) \cdot \mathbf{n}$ . It should be noted that when transmission is not considered,  $T(t)$  becomes zero and Eq. (10) reduces to the flux for the general impedance boundary.

To compute the convolution terms in Eq. (10), the auxiliary differential equations (ADEs) method<sup>59,60</sup> is used. For example, substitution of the reflection impulse response  $R(t)$  [Eq. (9)] into  $\int_{-\infty}^t \varpi_n^{\text{out}}(\tau) R(t-\tau) d\tau$  yields

$$\varpi_n^{\text{in}}(t) = R_\infty \varpi_n^{\text{out}}(t) + \sum_{k=1}^S A_k \phi_k(t) + \sum_{l=1}^T [B_l \psi_l^{(1)}(t) + C_l \psi_l^{(2)}(t)], \quad (12)$$

where  $\phi_k(t), \psi_l^{(1)}(t), \psi_l^{(2)}(t)$  are the so-called accumulators or auxiliary variables and are given, respectively, by the following ODEs:

$$\frac{d\phi_k}{dt} + \zeta_k \phi_k(t) = \varpi_n^{\text{out}}(t), \quad (13a)$$

$$\frac{d\psi_l^{(1)}}{dt} + \alpha_l \psi_l^{(1)}(t) + \beta_l \psi_l^{(2)}(t) = \varpi_n^{\text{out}}(t), \quad (13b)$$

$$\frac{d\psi_l^{(2)}}{dt} + \alpha_l \psi_l^{(2)}(t) - \beta_l \psi_l^{(1)}(t) = 0. \quad (13c)$$

The above system is numerically integrated from zero initial values using the same time integration scheme as for the semi-discrete DG formulation in Eq. (4), which will be shown in the following.

### III. THE ADER-DG SCHEME AND LTS

#### A. The ADER Taylor Series time integrator

After the spatial discretization by the nodal DG method, the total semi-discrete system can be expressed in a general form of ODEs as

$$\frac{\partial \tilde{\mathbf{q}}_h}{\partial t} = \mathcal{L}(\tilde{\mathbf{q}}_h(t), t), \quad (14)$$

where  $\tilde{\mathbf{q}}_h$  denotes the union of all unknown solutions, including acoustic variables  $\mathbf{q}_h$  as in Eq. (4) and auxiliary variables from the boundary conditions. Here,  $\mathcal{L}$  considers both the spatial discretization operator of DG in Eq. (4) and the ADEs of Eqs. (13a)–(13c). To introduce the Taylor Series time integrator scheme, we expand  $\tilde{\mathbf{q}}_h$  into a truncated Taylor series with respect to time and omit the time derivative terms of order higher than  $N_t$ , obtaining

$$\tilde{\mathbf{q}}_h(t + \Delta t) = \tilde{\mathbf{q}}_h(t) + \sum_{i=1}^{N_t} \frac{\Delta t^i}{i!} \frac{\partial^i \tilde{\mathbf{q}}_h(t)}{\partial t^i}. \quad (15)$$

Then, the discrete Cauchy-Kovalewski procedure is used to replace the time derivatives in the above Taylor series by spatial derivatives through the repeated use of Eq. (14), i.e.,

$$\frac{\partial^i \tilde{\mathbf{q}}_h}{\partial t^i} = \frac{\partial}{\partial t} \frac{\partial^{i-1} \tilde{\mathbf{q}}_h}{\partial t^{i-1}} = \mathcal{L} \left( \frac{\partial^{i-1} \tilde{\mathbf{q}}_h}{\partial t^{i-1}} \right) = \mathcal{L}^i \tilde{\mathbf{q}}_h. \quad (16)$$

This yields the final time-discrete formulation

$$\tilde{\mathbf{q}}_h(t + \Delta t) = \tilde{\mathbf{q}}_h(t) + \sum_{i=1}^{N_t} \gamma_i \Delta t^i \mathcal{L}^i \tilde{\mathbf{q}}_h(t), \quad (17)$$

where  $\gamma_i = 1/i!$  are coefficients of the Taylor series. For this conceptually simple scheme, the order of accuracy  $N_t$  becomes merely a numerical parameter that can be flexibly fixed. Thanks to the iterative nature of the high-order derivative construction, the computational cost is linearly proportional to the order  $N_t$ , i.e., an  $N_t$ th-order approximation needs only  $N_t$  times the right-hand-side evaluations of Eq. (14). Furthermore, the algorithm can be implemented efficiently in the  $2N$ -storage format, which means that for each variable, only one additional storage is needed to store the derivative value besides its solution value at the same time. Within each time step, the solutions are updated iteratively by adding one specific Taylor series term, which is updated from a lower-order derivative to the next higher-order derivative by evaluating the right-hand-side of Eq. (14). It should be noted that the closed-form solution to any explicit RK method<sup>14-20</sup> can be written in a form similar to that of Eq. (17). The TSI method can, therefore, be readily generalized to an arbitrary set of optimized coefficients and is not limited to the standard coefficients of the Taylor series.

The TSI scheme, as an explicit time-stepping method, features the CFL conditional stability that sets an upper bound on the time step size. The stability and accuracy of an explicit scheme is characterized by applying it to the model equation,

$$\frac{\partial u}{\partial t} = \lambda u, \quad \lambda \in \mathbb{C}, \quad (18)$$

with a time step  $\Delta t = t^{n+1} - t^n$ . This yields the relation  $u^{n+1} = R(z)u^n$ , where  $z = \lambda \Delta t$ .  $R$  is the complex amplification polynomial<sup>61</sup> given by

$$R(z) = \sum_{i=0}^{N_t} \gamma_i z^i. \quad (19)$$

Besides accuracy, the amplification polynomial  $R(z)$  also determines the absolute stability region  $S$  of the scheme as

$$S = \{z : |R(z)| \leq 1\}. \quad (20)$$

To evaluate the fully discrete stability of the ADER-DG scheme with a given time step  $\Delta t$ , the eigenvalues  $\lambda_N(\mathcal{L})$  of the semi-discrete operator  $\mathcal{L}$  are substituted into Eq. (18). Then, the stability condition becomes

$$\lambda \Delta t \in S, \quad \forall \lambda \in \lambda_N(\mathcal{L}). \quad (21)$$

Equation (21) is a necessary condition for the absolute stability in a general sense.<sup>62,63</sup> It can also serve as an excellent guideline for the time step choice.<sup>4</sup> In this work, we follow this guideline and determine the time step in the following way:<sup>4</sup>

$$\Delta t = C_{\text{CFL}} \frac{1}{N^2} \min(\Delta x_i) \frac{1}{c}, \quad (22)$$

where  $\Delta x_i$  is a measure of the element size and  $C_{\text{CFL}}$  is a constant of order  $\mathcal{O}(1)$ . Recall that  $N$  is the spatial approximation order. Here, we split the conventionally defined CFL number, which is, in practice, set to  $1/(2N+1)$  for a discretization combination of the  $N$ th-order DG method and an  $(N+1)$ th-order explicit RK method,<sup>2</sup> as a product of  $C_{\text{CFL}}$  and  $1/N^2$ . The factor  $1/N^2$  is attributed to the fact<sup>4,64</sup> that the eigenvalue spectrum of the spatial operator of DG grows at a rate slightly slower than does  $\mathcal{O}(N^2)$ , whereas  $C_{\text{CFL}}$  accounts for the effect of the size of the absolute stability region of time integration schemes of various orders. Because both the eigenvalue spectrum of the DG operator and the absolute stability region of the TSI schemes are defined implicitly, the exact values of  $C_{\text{CFL}}$  will be determined numerically in Sec. IV A.

## B. LTS strategy

Practical simulations typically use meshes of different sizes for regions of various dimensions to capture the necessary geometrical details while maintaining the computational efficiency. In addition, spatial variations in the sound speed  $c$  across elements influence the stiffness or the eigenvalue spectrum of the semi-discrete system (14). Furthermore, the fitting parameters of the multipole model for the impedance boundary condition as in Eq. (8) may introduce extra stiffness. To satisfy the CFL stability condition (21), the global time step is dictated by the most demanding factor, e.g., the smallest element. To overcome this inefficiency, an explicit LTS strategy accompanying the TSI scheme is introduced.

For a convenient demonstration but without loss of generality, consider a 1D computational domain with two subdomains that are composed of coarse and fine meshes and denoted as  $\Omega_c$  and  $\Omega_f$ , respectively, with their local time steps  $\Delta t_c$  and  $\Delta t_f$ , as illustrated in Fig. 1. Suppose the local time steps follow the relation  $\Delta t_c = \sigma \Delta t_f$ , where the ratio of time step sizes  $\sigma$  is determined based on mesh partitioning and efficiency considerations. As we will see, the proposed LTS strategy can be extended to a ratio of an arbitrary value. However, for ease of explanation, the case with an integer  $\sigma$

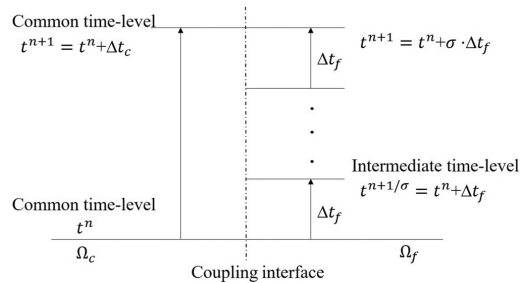


FIG. 1. Illustration of the LTS algorithm in the 1D space.

TABLE I. Stability limits  $C_{\text{CFLmax}}$  for ADER-DG with upwind fluxes and a uniform mesh.

	$N = 3$	$N = 4$	$N = 5$	$N = 6$	$N = 7$	$N = 8$
$N_t = 3$	1.171	1.434	1.653	1.835	1.994	2.134
$N_t = 4$	1.308	1.600	1.841	2.043	2.217	2.372
$N_t = 5$	1.511	1.848	2.126	2.359	2.562	2.739
$N_t = 6$	1.669	2.042	2.348	2.605	2.832	3.028
$N_t = 7$	1.858	2.272	2.612	2.901	3.150	3.368
$N_t = 8$	2.026	2.478	2.849	3.164	3.437	3.677
LS - RK5	1.980	2.437	2.815	3.135	3.412	3.656

is presented in detail as follows. First, starting from a certain synchronized time  $t^n = t_0 + n\Delta t_c$  (as it happens at the initial time  $t = t_0$ ), the global solutions step forward simultaneously using their local time steps. To be specific, the solutions inside the coarse region  $\tilde{\mathbf{q}}_c^n$  are advanced to the next *synchronous time level*  $t^{n+1} = t^n + \Delta t_c$  by the TSI formula

$$\tilde{\mathbf{q}}_c^{n+1} = \tilde{\mathbf{q}}_c^n + \sum_{i=1}^{N_t} \gamma_i \Delta t_c^i \frac{\partial^i \tilde{\mathbf{q}}_c^n}{\partial t^i}, \quad (23)$$

whereas the solutions inside the fine region  $\tilde{\mathbf{q}}_f^n$  are advanced to its next *intermediate time level*  $t^{n+1/\sigma} = t^n + \Delta t_f$  by the TSI formula

$$\tilde{\mathbf{q}}_f^{n+1/\sigma} = \tilde{\mathbf{q}}_f^n + \sum_{i=1}^{N_t} \gamma_i \Delta t_f^i \frac{\partial^i \tilde{\mathbf{q}}_f^n}{\partial t^i}. \quad (24)$$

The time derivatives needed for the local TSI advancements in Eqs. (23) and (24) can be calculated using the known solutions  $\tilde{\mathbf{q}}^n$  at the synchronous time level  $t^n$  in the same iterative way as for a GTS scheme as shown in Eq. (16). The next step is to advance the newly obtained solutions  $\tilde{\mathbf{q}}_f^{n+1/\sigma}$  inside the fine region to its next intermediate time level  $t^{n+2/\sigma} = t^n + 2\Delta t_f$  in a manner similar to that of Eq. (24). However, in this case, the time derivatives  $\partial^i \tilde{\mathbf{q}}_f^{n+1/\sigma} / \partial t^i$ ,  $i \in \{1, \dots, N_t\}$  cannot be calculated directly using Eq. (16). Recall that the spatial discretization operator  $\mathcal{L}$  for the discrete Cauchy-Kovalevski procedure involves the numerical flux approximation, which depends on the solution values along the interface belonging to neighboring elements.

Therefore, to calculate the spatial discretization operator of fine elements that lie next to the interface between the coarse and fine meshes, the solution values along the interface on the coarse mesh are required. Specifically, along the dividing interface, solution values  $\tilde{\mathbf{q}}_c^{n+1/\sigma}$  are needed to get  $\partial \tilde{\mathbf{q}}_f^{n+1/\sigma} / \partial t$ ,  $\partial \tilde{\mathbf{q}}_c^{n+1/\sigma} / \partial t$  are needed to get  $\partial^2 \tilde{\mathbf{q}}_f^{n+1/\sigma} / \partial t^2$ , ..., and so on. These desired solution/derivative values on the coarse mesh at different intermediate time levels ( $t^{n+j/\sigma} = t^n + j\Delta t_f$ ,  $j \in \{1, \dots, \sigma\}$ ), are obtained by using their own Taylor series expansions around the synchronous time level, which is supposed to be valid throughout  $[t^n, t^{n+1}]$ , i.e.,

$$\tilde{\mathbf{q}}_c^{n+j/\sigma} = \tilde{\mathbf{q}}_c^n + \sum_{i=1}^{N_t} \gamma_i (j\Delta t_f)^i \frac{\partial^i \tilde{\mathbf{q}}_c^n}{\partial t^i}, \quad j \in \{1, \dots, \sigma\}, \quad (25a)$$

$$\frac{\partial^k \tilde{\mathbf{q}}_c^{n+j/\sigma}}{\partial t^k} = \frac{\partial^k \tilde{\mathbf{q}}_c^n}{\partial t^k} + \sum_{i=k+1}^{N_t} \gamma_{i-k} (j\Delta t_f)^{i-k} \frac{\partial^i \tilde{\mathbf{q}}_c^n}{\partial t^i}, \quad k \in \{1, \dots, N_t - 1\}, \quad (25b)$$

where the derivative terms  $\partial^i \tilde{\mathbf{q}}_c^n / \partial t^i$  are pre-saved while advancing the coarse elements using Eq. (23). The presented coupling procedure provides an accurate evolution of solutions by exploiting the nature of the Taylor series expansion and ensures the correct communication between the coarse and fine regions. Because only the solution/derivative values at the nodes along the interface are needed for flux computations during the coupling procedure, the incurred memory and computation costs are negligible for the entire system. As will be seen later, the same order of accuracy as that of the GTS scheme is maintained, and the stability is ensured locally without a huge compromise on time steps.

To theoretically appreciate the potential speedup that can be achieved by such a LTS scheme, we assume that the fine domain  $\Omega_f$  takes up  $\chi$  fraction of the whole domain, whereas the proportion of the remaining coarse domain  $\Omega_c$  is  $1 - \chi$ . If GTS is used, all elements are advanced with the small time step  $\Delta t_f$ , and the computational cost (or, equivalently, the total number of element-wise right-hand-side evaluations) is proportional to

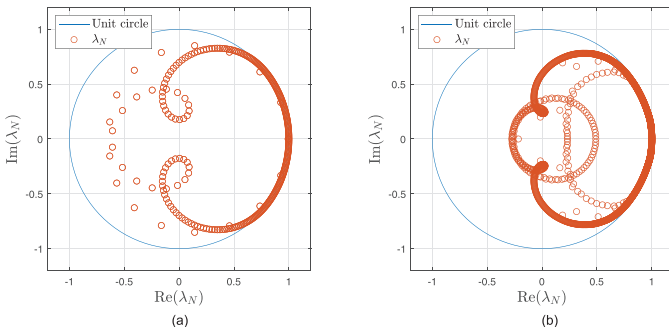


FIG. 2. (Color online) Distribution of eigenvalues of the amplification matrix  $\mathbf{R}$  for a uniform time step with  $N = N_t = 6$ ,  $C_{\text{CFL}} = C_{\text{CFLmax}}$ . (a)  $\sigma = 1$  and (b)  $\sigma = 5$ .

TABLE II. The ratio of stability limits  $C_{\text{CFL}_{\text{max}}}$  of a nonuniform mesh with  $\sigma = 5$  and LTS to the  $C_{\text{CFL}_{\text{max}}}$  with a uniform mesh with GTS as in Table I.

	$N = 3$	$N = 4$	$N = 5$	$N = 6$	$N = 7$	$N = 8$
$N_t = 3$	1.000	1.000	1.000	1.000	1.000	1.000
$N_t = 4$	0.999	0.999	0.997	0.998	0.999	0.999
$N_t = 5$	0.994	0.993	0.996	0.995	0.994	0.996
$N_t = 6$	0.990	0.990	0.990	0.992	0.991	0.991
$N_t = 7$	0.985	0.988	0.986	0.987	0.990	0.988
$N_t = 8$	0.982	0.981	0.983	0.984	0.983	0.983

$$N^{\text{GTS}} = \frac{1}{\Delta t_f}.$$

In contrast, if LTS is used, the computational cost scales as

$$N^{\text{LTS}} = \frac{\chi}{\Delta t_f} + \frac{1 - \chi}{\Delta t_c}.$$

Therefore, the theoretical speedup  $\nu$  is obtained as the ratio

$$\nu = \frac{N^{\text{GTS}}}{N^{\text{LTS}}} = \frac{\sigma}{1 - \chi + \sigma\chi} \geq 1. \quad (26)$$

Two extreme cases are noteworthy to understand Eq. (26). One case is that the two time steps are extremely disparate, i.e.,  $\sigma \gg 1$ , then we obtain

$$\lim_{\sigma \rightarrow \infty} \nu = \frac{1}{\chi},$$

indicating that a dramatic speedup is achieved if a small fraction of elements need a very small time step. The other case is when there are a small number of fine elements, i.e.,  $\chi \rightarrow 0$ , and then the speedup is determined by the ratio of time steps as

$$\lim_{\chi \rightarrow 0} \nu = \sigma.$$

The above two-level formulation with integer-valued ratios can be extended to general real-valued time step ratios of arbitrarily many levels of local time steps to accommodate

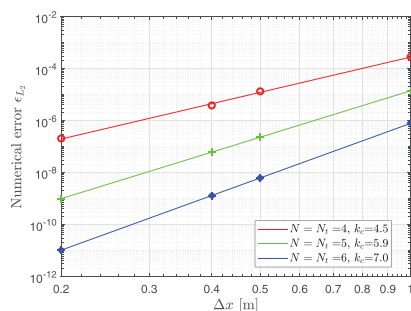


FIG. 4. (Color online) Convergence rate test with periodic boundary conditions,  $C_{\text{CFL}} = C_{\text{CFL}_{\text{max}}}$  and  $N = N_t = 4, 5, 6$ .

the needs arising from practical simulations, e.g., mesh partitioning. It should be mentioned that the cost of the coupling procedure [Eqs. (25a) and (25b)], which can be performed efficiently with matrix-vector multiplication, together with accompanying storage needs, is negligible compared to the overall computational work. A common approach to save the memory cost is to group elements with similar maximum allowable time steps together and, then, to adopt one uniform time step for each group.

## IV. NUMERICAL STUDIES OF THE ADER-DG SCHEME WITH LTS

In this section, numerical experiments are performed to investigate the numerical properties of the ADER-DG scheme with both GTS and LTS.

### A. Numerical stability analysis

The stability properties are studied by applying the ADER-DG scheme to the 1D linear acoustic equation (1) with periodic boundary conditions. Consider a computational domain of size  $x \in [0, 4]$  m, where  $[0, 2]$  m is discretized with an equidistant mesh of size  $\Delta x_c$ , whereas  $[2, 4]$  m is discretized with an equidistant mesh of size  $\Delta x_f = \Delta x_c / \sigma$ . First, the stability with a uniform time step is evaluated. To that end, we assemble the DG spatial discretization operator

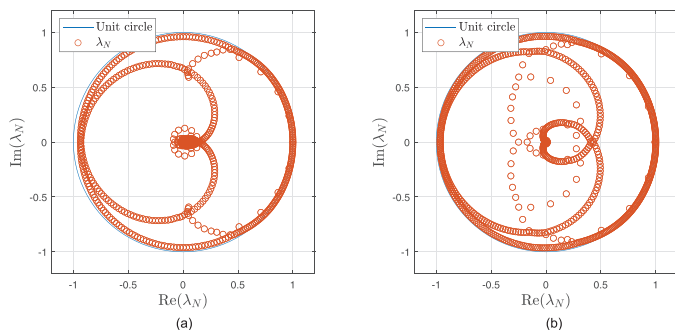


FIG. 3. (Color online) Distribution of eigenvalues of the amplification matrix  $\mathbf{R}$  for a nonuniform time step  $\sigma = 5$ ,  $C_{\text{CFL}} = C_{\text{CFL}_{\text{max}}}$ . (a)  $N = N_t = 4$  and (b)  $N = N_t = 6$ .

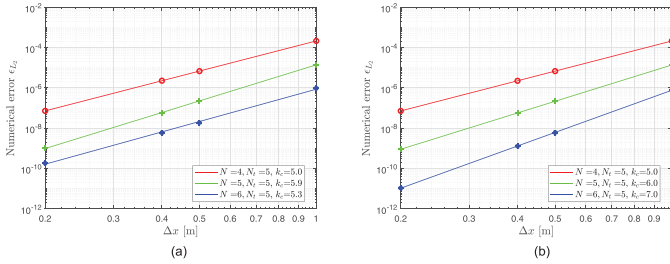


FIG. 5. (Color online) Convergence rate test of ADER-DG with  $N_t = 5$  and periodic boundary conditions. (a)  $C_{CFL} = C_{CFL_{max}} > 1$  and (b)  $C_{CFL} = 1$ .

$\mathcal{L}$  and insert it into an  $N_t$ th-order TSI time integration [Eq. (17)]. Then, it is straightforward to obtain the amplification matrix  $\mathbf{R}$  that relates the solutions between two time levels as  $\mathbf{q}_n^{n+1} = \mathbf{R}\mathbf{q}_n^n$ , where

$$\mathbf{R} = \mathbf{I} + \sum_{i=1}^{N_t} \gamma_i \Delta t^i \mathcal{L}^i, \quad (27)$$

and  $\mathbf{I}$  is the identity matrix. The fully discrete formulation is stable if all eigenvalues of matrix  $\mathbf{R}$ , denoted as  $\lambda_N(\mathbf{R})$ , have a modulus less or equal to unity, i.e.,

$$\max(|\lambda_N(\mathbf{R})|) \leq 1. \quad (28)$$

For the uniform time step case, eigenvalues of matrix  $\mathbf{R}$  are related to the product of eigenvalues of the spatial operator  $\mathcal{L}$  and the time step as  $\lambda_N(\mathbf{R}) = R(\lambda_N(\mathcal{L})\Delta t)$ , and the condition of Eq. (28) is equivalent to the stability condition of Eq. (21). The eigenvalues based on a uniform mesh with  $\Delta x_c = \Delta x_f = 0.1$  m are calculated, and a simple bisection method is used to find the maximum allowable time step by iteratively reducing the time step subject to the stability condition of Eq. (28). Table I presents the maximum allowable  $C_{CFL}$  values as in Eq. (22) for different combinations of time and space discretization orders, which match exactly the corresponding CFL number limit for the standard RK method as reported in Ref. 2. For each fixed spatial order  $N$ ,  $C_{CFL_{max}}$  increases with the time integration order  $N_t$  as the absolute stability region grows. Furthermore, since the eigenvalue spectrum of the DG discretization operator grows at a rate slightly slower than  $\mathcal{O}(N^2)$ , a slight increase in  $C_{CFL_{max}}$  with respect to  $N$  is observed as well. As a comparison, the low-storage five-stage fourth-order RK (LS-RK5) scheme,<sup>15</sup> which is devised and optimized to enhance stability, has a much larger stability region than the fifth-order TSI scheme at the cost of a compromising accuracy.

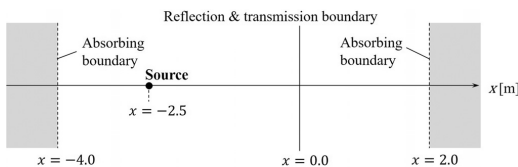


FIG. 6. A 1D configuration with impedance and transmissive boundaries.

The stability limit also applies to the nonuniform mesh case, where  $C_{CFL}$  is determined by the finer mesh. Figure 2 displays the distribution of eigenvalues of the amplification matrix  $\mathbf{R}$  for a uniform mesh with  $\Delta x_c = \Delta x_f = 0.1$  m as well as a nonuniform mesh with  $\Delta x_c = 5\Delta x_f = 0.1$  m.

Next, the stability of the proposed LTS scheme is evaluated, and we now consider the domain with a nonuniform mesh of ratio  $\sigma = 5$ . To obtain the amplification matrix  $\mathbf{R}$ , the TSI for both the coarse and fine regions [Eqs. (23) and (24), respectively], together with the coupling procedure [Eqs. (25a) and (25b)], are applied to the semi-discrete formulation [Eq. (14)]. Clearly, the eigenvalues of  $\mathbf{R}(\Delta t_c, \Delta t_f)$ , arising from the LTS scheme, are different from those for a GTS scheme. Ideally, the LTS scheme would introduce no further constraint on the time step size and, therefore, the same CFL condition as in the GTS case would be obtained. However, it is found that the maximum allowable CFL-like constants  $C_{CFL_{max}}^*$  for the LTS scheme are slightly smaller than the maximum allowable CFL-like constants for the GTS case, which is typical for a spatially nonoverlapping coupling procedure.<sup>33,36</sup> Their ratios are shown in Table II. Figure 3 shows two examples of distributions of the eigenvalues. Similar numerical experiments with different values of  $\sigma$  have been performed to test the CFL stability conditions for the LTS scheme. It is found that a ratio value of 0.95 would yield a stable scheme in all of the tests, indicating that the developed coupling procedure does not have a significant negative impact on the stability limit of the TSI, in general.

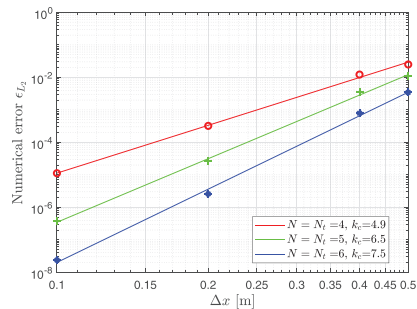


FIG. 7. (Color online) Convergence rate test with impedance and transmission boundaries,  $C_{CFL} = C_{CFL_{max}}$  and  $N = N_t = 4, 5, 6$ .

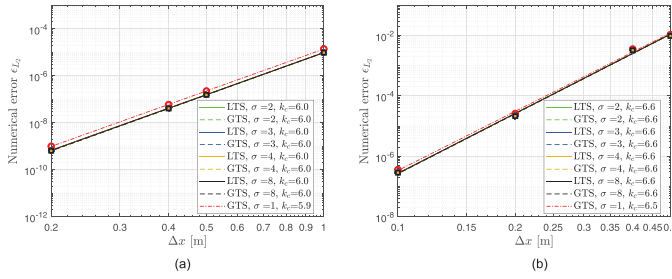


FIG. 8. (Color online) Convergence rate of LTS and its comparison with GTS with  $C_{\text{CFL}} = 0.95C_{\text{CFLmax}}$ ,  $N = N_t = 5$  and  $\sigma = 1, 2, 3, 4, 8$ . (a) Periodic and (b) impedance and transmission boundaries.

## B. Convergence rate of ADER-DG

### 1. Periodic boundary with GTS

To investigate the convergence rate of the proposed ADER-DG method for free field propagation, the 1D linear acoustic equation [Eq. (1)] on the interval  $x \in [0, 4]$  m with uniform meshes are solved. Periodic boundary conditions are prescribed on both ends, and the initial condition is a sine wave of wavelength  $\lambda_w = 4$  m,

$$p(x, t = 0) = \sin(-0.5\pi x), \quad (29a)$$

$$u(x, t = 0) = \frac{1}{\rho c} \sin(-0.5\pi x). \quad (29b)$$

First, numerical tests are conducted for various orders of accuracy in space and time with a uniform maximum allowable CFL number on a sequence of mesh sizes  $\Delta x$ . The  $L^2$  space-time error defined as  $\epsilon_{L^2} = \|p_{\text{ana}}(T_f) - p_{\text{num}}(T_f)\|_{L^2}$  is used to evaluate the accuracy, where  $p_{\text{ana}}(T_f)$  and  $p_{\text{num}}(T_f)$  denote the analytical solution and the numerical solution, respectively, at the final time  $T_f = (16 \text{ m})/c$  across the whole domain.  $\|\cdot\|_{L^2}$  denotes the  $L^2$  norm, which is carried out numerically and accurately up to the order of the polynomial approximation. As shown in Fig. 4, the observed convergence rates  $k_c$ , which are calculated by linear fitting with the least square method, are as expected.

Next, to investigate the effects of temporal error on the spatial convergence rate, we repeat previous tests with a fixed time integration order of  $N_t = 5$  and different time step sizes. Figure 5(a) displays the results obtained using the maximum allowable time step for ADER-DG as prescribed from Table I. It can be seen that above a certain spatial resolution, the time integration error becomes dominant over the spatial error, and the spatial convergence rate is deteriorated. As shown in Fig. 5(b), a smaller time step reduces the temporal error and the expected spatial convergence rate of ADER-DG scheme is recovered.

### 2. Impedance and transmission boundary with GTS

Now, convergence rates of the ADER-DG scheme for wave propagation involving time-domain impedance and transmission boundary conditions are verified, where the ADEs [Eqs. (13a)–(13c)] are integrated using the same time integration scheme. As illustrated in Fig. 6, the transmission

and impedance boundary is located at  $x = 0$  m, and the source at  $x_s = -2.5$  m initiates the simulation with the Gaussian-shaped pressure conditions

$$p(x, t = 0) = e^{(-\ln 2/b^2)(x-x_s)^2}, \quad (30a)$$

$$v(x, t = 0) = 0, \quad (30b)$$

where  $b = 0.15$  m is the half-bandwidth of the Gaussian pulse. Convergence tests similar to those in the periodic boundary case are performed. The numerical solutions at the final time  $T_f = 4/c$  s, when both the reflected and transmitted waves are present in the domain, are compared against the analytical solutions.<sup>65</sup> Without loss of generality, one single real pole  $[A, \zeta]_R = [6.4 \times 10^3, 8 \times 10^3]$  is used for fitting the reflection coefficient  $R$  as in Eq. (8) while the transmission coefficient  $T$  is defined by  $[A, \zeta]_T = [5 \times 10^3, 9 \times 10^3]$ . The  $L^2$  error with conforming spatial and temporal approximation order is plotted in Fig. 7. The expected convergence rates are yielded.

## C. Convergence of ADER-DG with LTS and comparison against GTS

To verify the convergence rate of ADER-DG with the proposed LTS scheme, we repeat the above numerical tests using nonuniform meshes. For the periodic boundary case, the original computational domain  $x \in [0, 4]$  m is split into two parts with different mesh sizes. The coarse part  $x \in [0, 2]$  m is discretized with an equidistant mesh of size  $\Delta x_c$ , whereas the fine part  $x \in [2, 4]$  m has a mesh of size  $\Delta x_f = \Delta x_c/\sigma$ . For the impedance and transmission boundary case, the interface between the coarse region  $x \in [-4, 0]$  m and the fine region  $x \in [0, 2]$  m coincides with the reflective and transmissive boundary. With a uniform CFL value, the time step sizes are different between the two regions. The  $\epsilon_{L^2}$  error for different values of mesh size ratio  $\sigma$  and a fixed order of accuracy is presented in Fig. 8 for both boundary cases. As a comparison, the results obtained from the GTS scheme are shown as well. It can be seen that for all of the tested time step ratios  $\sigma$ , the expected convergence rates  $k_c$  are observed for LTS, and the scheme introduces no extra error compared to the GTS scheme.

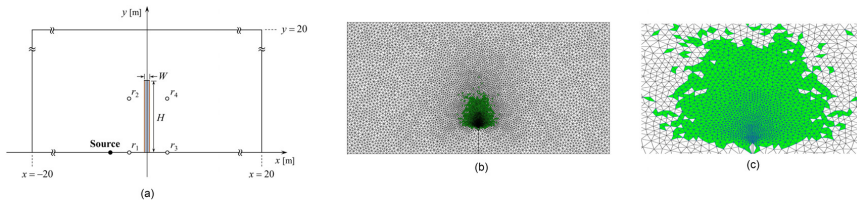


FIG. 9. (Color online) Geometry and mesh of the noise barrier. (a) Schematic diagram, (b) overall mesh, and (c) zoomed-in view of the fine mesh near the top edge.

## V. APPLICATION

To demonstrate the functionality and speedup potential of the proposed ADER-DG scheme with LTS for practical applications, wave propagation across a finite-height noise barrier made of porous glass-wool material is simulated, which is a configuration pertaining to outdoor sound propagation. The schematic diagram is shown in Fig. 9(a) with the outer boundaries far away from the barrier to prevent spurious reflected waves from influencing the pressure response. The source is located at  $(x_s, y_s) = (-2, 0)$  and four receivers are located at  $(-1, 0)$ ,  $(-1, 3)$ ,  $(1, 0)$ , and  $(1, 3)$  are distributed symmetrically with respect to the barrier, which has a height of  $H=4$  m and a width of  $W=0.04$  m. To mimic a real noise barrier mounted on a hard ground surface, the rigid boundary condition is imposed on the top edge of the barrier, whereas both side edges are modeled with the reflective and transmissive boundary conditions. The characteristic impedance of the locally reacting glass-wool layer is assumed to follow the phenomenological Johnson-Champoux-Allard-Lafarge (JCAL) model<sup>66</sup> with its physical parameters measured experimentally.<sup>11</sup> To model the reflection and transmission properties of the layer, four and five real poles are used to fit the reflection and transmission coefficients from the time-domain boundary conditions, respectively, as shown in Ref. 11. The other boundaries are assumed to be rigid.

The two-dimensional domain is discretized with 13 427 unstructured triangles.<sup>67</sup> As illustrated in Fig. 9(b), the mesh is locally refined near the top edge of the sound barrier in order to capture the geometry features and diffraction effects. A relatively simple mesh size measure, which is the shortest edge length  $h$ , is chosen for determining the time step size based on the CFL condition (22). In-depth discussions on appropriate triangular mesh measures can be found in Refs. 68 and 69. Mesh elements far away from the sound barrier have an edge length of approximately 0.5 m. Here, suppose the shortest edge length is denoted by  $h_{\min}$ , we treat all of the elements with the shortest length that satisfies  $h \leq 6h_{\min}$  as the fine mesh elements, i.e., the green triangles in Fig. 9(c). There are, in total, 2729 fine triangles scattered around the barrier, which suggests a speedup ratio of  $\nu \approx 3$  with the LTS scheme according to Eq. (26).

To evaluate the accuracy of the LTS scheme, we use the numerical solutions obtained by the RK-DG method with the GTS scheme and the same mesh, which have been

verified against the finite element solutions in the frequency domain,<sup>11</sup> as the reference solutions. Following the same numerical setup of the reference solution, a uniform CFL-like constant  $C_{\text{CFL}} = 1$  is used, as well as a spatial polynomial basis of order  $N=8$ , together with a fifth-order TSI, which shares the same computational cost as the LS-RK5 scheme, are used. The time steps in two regions follow the relation  $\Delta t_c = 6\Delta t_f$ . The Gaussian distribution with  $b=0.25$  m as in Eqs. (30a) and (30b) acts as the source and initiates the simulation. The comparison of pressure signals at two receiver locations obtained from both the GTS scheme and LTS scheme are shown in Fig. 10, where a high level of agreement is observed. For receiver 2, the main components are the direct sound and the reflected sound from the barrier, whereas receiver 4 experiences the pressure signal diffracted over the hard barrier top as well as the faint pressure signal transmitted through the barrier. Besides the time-domain comparisons, the relative sound pressure level, which is obtained by normalizing the total spectrum against the spectrum of the free field solution, and its phase angle at different receiver locations are shown in Figs. 11(a) and 11(b), respectively. Again, a perfect match of the frequency-domain results between the GTS scheme and the LTS scheme is found.

## VI. CONCLUSION

In this work, we present an ADER-DG approach with the LTS scheme to solve the time-dependent linear acoustic equations with an arbitrary order of accuracy in time and

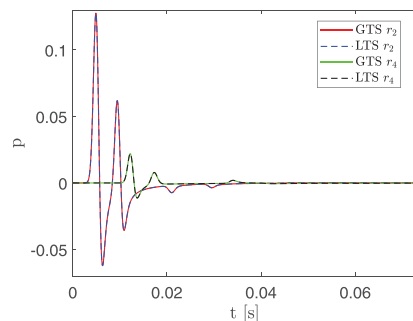


FIG. 10. (Color online) Time history of the pressure signal at receivers  $r_2$  and  $r_4$ .

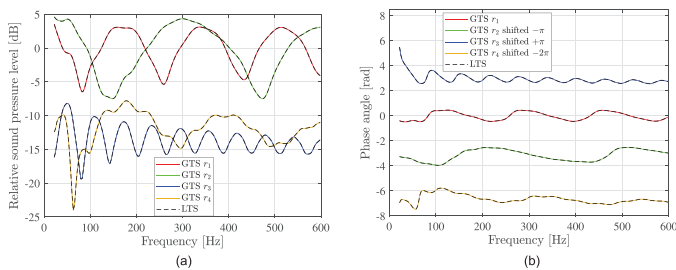


FIG. 11. (Color online) Comparison between the GTS and LTS for the noise barrier case. (a) Relative sound pressure level and (b) phase angle.

space. Built upon the well-known nodal DG method for the spatial discretization, it performs the time integration using TSI in an efficient and accurate manner. Necessary formulations of time-domain acoustic boundary conditions are included for indoor-outdoor acoustic simulation purposes. Numerical experiments and applications are performed to validate the stability and convergence properties. It is shown that the proposed LTS scheme enables a significant reduction in computational cost while maintaining the desired high-order accuracy. Applications to more practical sound propagation problems involving complex geometries and material properties will be addressed in future work.

- <sup>1</sup>H. L. Atkins and C.-W. Shu, "Quadrature-free implementation of discontinuous Galerkin method for hyperbolic equations," *AIAA J.* **36**(5), 775–782 (1998).
- <sup>2</sup>B. Cockburn and C.-W. Shu, "Runge-Kutta discontinuous Galerkin methods for convection-dominated problems," *J. Sci. Comput.* **16**(3), 173–261 (2001).
- <sup>3</sup>B. Cockburn, G. E. Karniadakis, and C.-W. Shu, *Discontinuous Galerkin Methods: Theory, Computation and Applications* (Springer-Verlag, Berlin Heidelberg, 2000), Vol. 11.
- <sup>4</sup>J. S. Hesthaven and T. Warburton, *Nodal Discontinuous Galerkin Methods: Algorithms, Analysis and Applications* (Springer, New York, 2007).
- <sup>5</sup>T. Lähivaara and T. Huttunen, "A non-uniform basis order for the discontinuous Galerkin method of the 3D dissipative wave equation with perfectly matched layer," *J. Comput. Phys.* **229**(13), 5144–5160 (2010).
- <sup>6</sup>L. C. Wilcox, G. Stadler, C. Burstedde, and O. Ghattas, "A high-order discontinuous Galerkin method for wave propagation through coupled elastic-acoustic media," *J. Comput. Phys.* **229**(24), 9373–9396 (2010).
- <sup>7</sup>M. Kronbichler, S. Schoeder, C. Müller, and W. A. Wall, "Comparison of implicit and explicit hybridizable discontinuous Galerkin methods for the acoustic wave equation," *Int. J. Numer. Methods Eng.* **106**(9), 712–739 (2016).
- <sup>8</sup>N. C. Nguyen, J. Peraire, and B. Cockburn, "High-order implicit hybridizable discontinuous Galerkin methods for acoustics and elastodynamics," *J. Comput. Phys.* **230**(10), 3695–3718 (2011).
- <sup>9</sup>F. Monteghetti, D. Matignon, and E. Piot, "Energy analysis and discretization of nonlinear impedance boundary conditions for the time-domain linearized Euler equations," *J. Comput. Phys.* **375**, 393–426 (2018).
- <sup>10</sup>H. Wang and M. Hornikx, "Time-domain impedance boundary condition modeling with the discontinuous Galerkin method for room acoustics simulations," *J. Acoust. Soc. Am.* **147**(4), 2534–2546 (2020).
- <sup>11</sup>H. Wang, J. Yang, and M. Hornikx, "Frequency-dependent transmission boundary condition in the acoustic time-domain nodal discontinuous Galerkin model," *Appl. Acoust.* **164**, 107280 (2020).
- <sup>12</sup>A. Modave, A. St-Cyr, and T. Warburton, "GPU performance analysis of a nodal discontinuous Galerkin method for acoustic and elastic models," *Comput. Geosci.* **91**, 64–76 (2016).
- <sup>13</sup>S. Schoeder, W. Wall, and M. Kronbichler, "ExWave: A high performance discontinuous Galerkin solver for the acoustic wave equation," *SoftwareX* **9**, 49–54 (2019).

- <sup>14</sup>J. Williamson, "Low-storage Runge-Kutta schemes," *J. Comput. Phys.* **35**(1), 48–56 (1980).
- <sup>15</sup>M. H. Carpenter and C. A. Kennedy, "Fourth-order 2N-storage Runge-Kutta schemes," in NASA-TM-109112 (1994).
- <sup>16</sup>F. Hu, M. Y. Hussaini, and J. Manthey, "Low-dissipation and low-dispersion Runge-Kutta schemes for computational acoustics," *J. Comput. Phys.* **124**(1), 177–191 (1996).
- <sup>17</sup>D. Stanescu and W. Habashi, "2N-storage low dissipation and dispersion Runge-Kutta schemes for computational acoustics," *J. Comput. Phys.* **143**(2), 674–681 (1998).
- <sup>18</sup>C. Bogey and C. Bailly, "A family of low dispersive and low dissipative explicit schemes for flow and noise computations," *J. Comput. Phys.* **194**(1), 194–214 (2004).
- <sup>19</sup>J. Berland, C. Bogey, and C. Bailly, "Low-dissipation and low-dispersion fourth-order Runge-Kutta algorithm," *Comput. Fluids* **35**(10), 1459–1463 (2006).
- <sup>20</sup>T. Toulorge and W. Desmet, "Optimal Runge-Kutta schemes for discontinuous Galerkin space discretizations applied to wave propagation problems," *J. Comput. Phys.* **231**(4), 2067–2091 (2012).
- <sup>21</sup>D. A. Kopriva and E. Jimenez, "An assessment of the efficiency of nodal discontinuous Galerkin spectral element methods," in *Recent Developments in the Numerics of Nonlinear Hyperbolic Conservation Laws* (Springer, Berlin, Heidelberg, 2013), pp. 223–235.
- <sup>22</sup>A. Kanevsky, M. H. Carpenter, D. Gottlieb, and J. S. Hesthaven, "Application of implicit-explicit high order Runge-Kutta methods to discontinuous-Galerkin schemes," *J. Comput. Phys.* **225**(2), 1753–1781 (2007).
- <sup>23</sup>V. Dolean, H. Fahs, L. Fezoui, and S. Lanteri, "Locally implicit discontinuous Galerkin method for time domain electromagnetics," *J. Comput. Phys.* **229**(2), 512–526 (2010).
- <sup>24</sup>S. Descombes, S. Lanteri, and L. Moya, "Locally implicit time integration strategies in a discontinuous Galerkin method for Maxwell's equations," *J. Sci. Comput.* **56**(1), 190–218 (2013).
- <sup>25</sup>M. Hochbruck and A. Ostermann, "Exponential multistep methods of Adams-type," *BIT Numer. Math.* **51**(4), 889–908 (2011).
- <sup>26</sup>H. Wang, L. Xu, B. Li, S. Descombes, and S. Lanteri, "A new family of exponential-based high-order DGT methods for modeling 3-D transient multiscale electromagnetic problems," *IEEE Trans. Antennas Propag.* **65**(11), 5960–5974 (2017).
- <sup>27</sup>C. W. Gear and D. Wells, "Multirate linear multistep methods," *BIT Numer. Math.* **24**(4), 484–502 (1984).
- <sup>28</sup>M. Günther, A. Kvaerno, and P. Rentrop, "Multirate partitioned Runge-Kutta methods," *BIT Numer. Math.* **41**(3), 504–514 (2001).
- <sup>29</sup>V. Savcenco, W. Hundsdorfer, and J. Verwer, "A multirate time stepping strategy for stiff ordinary differential equations," *BIT Numer. Math.* **47**(1), 137–155 (2007).
- <sup>30</sup>M. J. Berger and J. Olinger, "Adaptive mesh refinement for hyperbolic partial differential equations," *J. Comput. Phys.* **53**(3), 484–512 (1984).
- <sup>31</sup>S. Piperno, "Symplectic local time-stepping in non-dissipative DGT methods applied to wave propagation problems," *ESAIM: Math. Modell. Numer. Anal.* **40**(5), 815–841 (2006).
- <sup>32</sup>E. Montseny, S. Pernet, X. Ferrière, and G. Cohen, "Dissipative terms and local time-stepping improvements in a spatial high order discontinuous Galerkin scheme for the time-domain Maxwell's equations," *J. Comput. Phys.* **227**(14), 6795–6820 (2008).
- <sup>33</sup>J. Diaz and M. J. Grote, "Energy conserving explicit local time stepping for second-order wave equations," *SIAM J. Sci. Comput.* **31**(3), 1985–2014 (2009).

- <sup>34</sup>J. Diaz and M. J. Grote, "Multi-level explicit local time-stepping methods for second-order wave equations," *Comput. Methods Appl. Mech. Eng.* **291**, 240–265 (2015).
- <sup>35</sup>M. J. Grote, M. Mehlin, and T. Mitkova, "Runge-Kutta-based explicit local time-stepping methods for wave propagation," *SIAM J. Sci. Comput.* **37**(2), A747–A775 (2015).
- <sup>36</sup>M. Almquist and M. Mehlin, "Multilevel local time-stepping methods of Runge-Kutta-type for wave equations," *SIAM J. Sci. Comput.* **39**(5), A2020–A2048 (2017).
- <sup>37</sup>C. J. Trahan and C. Dawson, "Local time-stepping in Runge-Kutta discontinuous Galerkin finite element methods applied to the shallow-water equations," *Comput. Methods Appl. Mech. Eng.* **217–220**, 139–152 (2012).
- <sup>38</sup>L. Liu, X. Li, and F. Q. Hu, "Nonuniform time-step Runge-Kutta discontinuous Galerkin method for computational aeroacoustics," *J. Comput. Phys.* **229**(19), 6874–6897 (2010).
- <sup>39</sup>C. Dawson, C. J. Trahan, E. J. Kubatko, and J. J. Westerink, "A parallel local timestepping Runge-Kutta discontinuous Galerkin method with applications to coastal ocean modeling," *Comput. Methods Appl. Mech. Eng.* **259**, 154–165 (2013).
- <sup>40</sup>L. Krivodonova, "An efficient local time-stepping scheme for solution of nonlinear conservation laws," *J. Comput. Phys.* **229**(22), 8537–8551 (2010).
- <sup>41</sup>M. J. Grote and T. Mitkova, "High-order explicit local time-stepping methods for damped wave equations," *J. Comput. Appl. Math.* **239**, 270–289 (2013).
- <sup>42</sup>L. Angulo, J. Alvarez, F. L. Teixeira, M. F. Pantoja, and S. G. Garcia, "Causal-path local time-stepping in the discontinuous Galerkin method for Maxwell's equations," *J. Comput. Phys.* **256**, 678–695 (2014).
- <sup>43</sup>A. Taube, M. Dumbser, C.-D. Munz, and R. Schneider, "A high-order discontinuous Galerkin method with time-accurate local time stepping for the Maxwell equations," *Int. J. Numer. Modell.: Electron. Networks, Devices Fields* **22**(1), 77–103 (2009).
- <sup>44</sup>M. Käser and M. Dumbser, "An arbitrary high-order discontinuous Galerkin method for elastic waves on unstructured meshes—I. The two-dimensional isotropic case with external source terms," *Geophys. J. Int.* **166**(2), 855–877 (2006).
- <sup>45</sup>M. Dumbser, M. Käser, and E. F. Toro, "An arbitrary high-order discontinuous Galerkin method for elastic waves on unstructured meshes—V. Local time stepping and  $p$ -adaptivity," *Geophys. J. Int.* **171**(2), 695–717 (2007).
- <sup>46</sup>S. Schoeder, M. Kronbichler, and W. A. Wall, "Arbitrary high-order explicit hybridizable discontinuous Galerkin methods for the acoustic wave equation," *J. Sci. Comput.* **76**(2), 969–1006 (2018).
- <sup>47</sup>M. Käser, M. Dumbser, J. De La Puente, and H. Igel, "An arbitrary high-order discontinuous Galerkin method for elastic waves on unstructured meshes—III. Viscoelastic attenuation," *Geophys. J. Int.* **168**(1), 224–242 (2007).
- <sup>48</sup>S. Schomann, N. Godel, T. Warburton, and M. Clemens, "Local timestepping techniques using Taylor expansion for modeling electromagnetic wave propagation with discontinuous Galerkin-FEM," *IEEE Trans. Magn.* **46**(8), 3504–3507 (2010).
- <sup>49</sup>H. Qi, X. Wang, J. Zhang, and J. Wang, "An ADER discontinuous Galerkin method with local time-stepping for transient electromagnetics," *Comput. Phys. Commun.* **229**, 106–115 (2018).
- <sup>50</sup>H. Wang, I. Sihar, R. P. Muñoz, and M. Hornikx, "Room acoustics modelling in the time-domain with the nodal discontinuous Galerkin method," *J. Acoust. Soc. Am.* **145**(4), 2650–2663 (2019).
- <sup>51</sup>J. S. Hesthaven and C.-H. Teng, "Stable spectral methods on tetrahedral elements," *SIAM J. Sci. Comput.* **21**(6), 2352–2380 (2000).
- <sup>52</sup>F. Hu and H. Atkins, "Two-dimensional wave analysis of the discontinuous Galerkin method with non-uniform grids and boundary conditions," in *8th AIAA/CEAS Aeroacoustics Conference and Exhibit* (2002), p. 2514.
- <sup>53</sup>M. Ainsworth, "Dispersive and dissipative behaviour of high order discontinuous Galerkin finite element methods," *J. Comput. Phys.* **198**(1), 106–130 (2004).
- <sup>54</sup>M. Toyoda and J. Motooka, "Prediction of permeable thin absorbers using the finite-difference time-domain method," *J. Acoust. Soc. Am.* **143**(5), 2870–2877 (2018).
- <sup>55</sup>M. Toyoda and S. Ishikawa, "Frequency-dependent absorption and transmission boundary for the finite-difference time-domain method," *Appl. Acoust.* **145**, 159–166 (2019).
- <sup>56</sup>H. Ju and K.-Y. Fung, "Time-domain simulation of acoustic sources over an impedance plane," *J. Comput. Acoust.* **10**(03), 311–329 (2002).
- <sup>57</sup>B. Cotté, P. Blanc-Benon, C. Bogey, and F. Poisson, "Time-domain impedance boundary conditions for simulations of outdoor sound propagation," *AIAA J.* **47**(10), 2391–2403 (2009).
- <sup>58</sup>D. Dragna, P. Blanc-Benon, and F. Poisson, "Time-domain solver in curvilinear coordinates for outdoor sound propagation over complex terrain," *J. Acoust. Soc. Am.* **133**(6), 3751–3763 (2013).
- <sup>59</sup>R. M. Joseph, S. C. Hagness, and A. Taflov, "Direct time integration of Maxwell's equations in linear dispersive media with absorption for scattering and propagation of femtosecond electromagnetic pulses," *Opt. Lett.* **16**(18), 1412–1414 (1991).
- <sup>60</sup>D. Dragna, P. Pineau, and P. Blanc-Benon, "A generalized recursive convolution method for time-domain propagation in porous media," *J. Acoust. Soc. Am.* **138**(2), 1030–1042 (2015).
- <sup>61</sup>J. C. Butcher, *The Numerical Analysis of Ordinary Differential Equations: Runge-Kutta and General Linear Methods* (Wiley-Interscience, New York, 1987).
- <sup>62</sup>S. C. Reddy and L. N. Trefethen, "Stability of the method of lines," *Numerische Mathematik* **62**(1), 235–267 (1992).
- <sup>63</sup>H. O. Kreiss and L. Wu, "On the stability definition of difference approximations for the initial boundary value problem," *Appl. Numer. Math.* **12**(1–3), 213–227 (1993).
- <sup>64</sup>L. Krivodonova and R. Qin, "An analysis of the spectrum of the discontinuous Galerkin method," *Appl. Numer. Math.* **64**, 1–18 (2013).
- <sup>65</sup>Y. Özyörük and L. N. Long, "A time-domain implementation of surface acoustic impedance condition with and without flow," *J. Comput. Acoust.* **05**(03), 277–296 (1997).
- <sup>66</sup>D. Lafarge, P. Lemariniere, J. F. Allard, and V. Tarnow, "Dynamic compressibility of air in porous structures at audible frequencies," *J. Acoust. Soc. Am.* **102**(4), 1995–2006 (1997).
- <sup>67</sup>C. Geuzaine and J.-F. Remacle, "Gmsh: A 3-D finite element mesh generator with built-in pre-and post-processing facilities," *Int. J. Numer. Methods Eng.* **79**(11), 1309–1331 (2009).
- <sup>68</sup>N. Chalmers and L. Krivodonova, "A robust CFL condition for the discontinuous Galerkin method on triangular meshes," *J. Comput. Phys.* **403**, 109095 (2020).
- <sup>69</sup>T. Toulorge and W. Desmet, "CFL conditions for Runge-Kutta discontinuous Galerkin methods on triangular grids," *J. Comput. Phys.* **230**(12), 4657–4678 (2011).

---

---

# Paper V

# Wave-based room acoustic simulations of an open plan office

Huiqing Wang<sup>1,\*</sup>, Wouter Wittebol<sup>1</sup>, Matthias Cosnefroy<sup>1</sup>, Maarten Hornikx<sup>1</sup>, Remy Wenmaekers<sup>2</sup>

<sup>1</sup>Building Physics and Services, Department of the Built Environment, Eindhoven University of Technology,  
P.O. Box 513, 5600 MB Eindhoven, The Netherlands

<sup>2</sup>Level Acoustics & Vibration, De Rondom 10, 5612 AP Eindhoven, The Netherlands

\*{[h.wang6@tue.nl](mailto:h.wang6@tue.nl)}

## Abstract

In this study, room acoustic simulations of a real open plan office using the time-domain discontinuous Galerkin (TD-DG) method are performed, as a preliminary attempt to assess the accuracy and applicability of this wave-based method for realistic sound field analysis in the low-frequency range. This TD-DG simulation involves the developed techniques of locally-reacting frequency-dependent impedance boundary conditions and the local-time stepping scheme. The required input for the boundary modeling of relevant absorption materials is obtained from the absorption coefficients measured in a reverberation room based on the international standard ISO 354. Observed discrepancies, in terms of the room acoustic parameters, between the measurements and simulation results indicate the limitation of the detailed wave-based modeling in the absence of a precise boundary characterization.

**Keywords:** wave-based simulation, time-domain discontinuous Galerkin method, open-plan office.

## 1 Introduction

Wave-based room acoustic simulation methods simulate sound propagation by directly solving the wave equation based on numerical approximation techniques. Compared to the well-established geometrical acoustic (GA) simulation techniques [1], which are built upon the assumption that sound acts as rays, wave-based methods are able to accurately capture inherent complex wave-phenomena such as scattering, diffraction and phase effects. Despite their superior accuracy, wave-based methods suffer from a heavy computational cost. Therefore, GA simulation methods have been the prevailing approach for acoustic practitioners and researchers for simulating the acoustic fields of large rooms like concert halls and theaters; while it is generally acknowledged that wave-based methods serve as preferred alternatives to GA models for rooms with small volumes below the Schroeder frequency, where the modal overlap is low. Recently, the time-domain discontinuous Galerkin (TD-DG) wave-based method has been investigated for room acoustic modeling purposes [2, 3] and efforts have been made to enhance its performance in terms of acoustic boundary modeling [2, 4, 5], efficiency [6] and high-performance computing [2].

A comprehensive evaluation of the accuracy of room acoustic simulations typically involves a comparison with measurements. For state-of-the-art of room acoustic modeling software that are based on GA models, round robin experiments have been performed using acoustic scenes of different levels of complexity [7] and benchmark databases have been established [8]. Audible deviations are observed, and it proves to be a challenging task to guarantee an exact match of model input parameters between simulations and measurements. Sources of input data uncertainties include room geometries, absorption and scattering properties of room surfaces and the source and receiver characteristics [9].

For wave-based methods, there have been on-going research activities trying to close the gap between real-world measurements and simulations as well. Experimental validation of room acoustic simulations inside a reverberation room with a time-domain finite element method (FEM) is reported by Okuzono *et al.*

[10], and a decent agreement of band-limited room impulse responses is observed in three separate octave bands. Comparisons of different boundary representations of porous absorbers in small rooms are performed respectively within the framework of the frequency-domain FEM model [11] and the TD-DG model [12], highlighting the effects of extended reaction of boundary materials for room acoustics. For the TD-DG method, previous validation work [3] has been done inside an empty reverberation room, where the walls are modeled with a uniform real-valued impedance. Later on, benchmark tests with various furniture inside were conducted [13] and the good match with measurements indicate the strong potential for more challenging and larger room scenarios. Another recent study compares measurements with simulation results from the TD-DG method in a small rectangular room with porous absorbers, with a focus on establishing a comprehensive validation and uncertainty quantification framework in wave-based room acoustic simulations [14]. It was found that the input uncertainties associated with the absorption properties makes it intractable to predict common room acoustic parameters within just noticeable difference (JND) thresholds.

In this study, the TD-DG method is applied to simulate the acoustics of a large real open plan office in the low-to-middle frequency range (125 Hz to 500 Hz octave bands), with the aim of assessing the accuracy and applicability of this wave-based method for realistic sound field analysis. The ground truth references to be compared with are measurement results, which were previously published in a study on how room acoustic parameters are affected with varying configurations of furniture and sound absorbing barriers [15]. The acoustic properties of involved boundary surfaces are characterized based on standardized reverberation room measurements [16]. The required specifications of complex-valued reflection coefficients for the wave-based calculations are obtained by transforming the measured Sabine absorption coefficients. The comparison between the simulation and measurement results are conducted in terms of six room acoustic parameters that are derived from the room impulse response.

The paper is organized as follows. The description of the reference room measurements is presented in Sec. 2. Sec. 3 describes the setup of the wave-based simulation model and the approach used for retrieving complex-valued impedance boundary data. Section 4 presents the comparison of simulation results with measurements, as well as discussions on the potential limitations of the current wave-based model.

## 2 Reference measurement

### 2.1. Measurement room and procedures

As shown in Fig. 1, the open plan office under study has a long and narrow floor plan with windows along the walls. Small closed rooms indicated by the blue areas are present to subdivide the long space. The room has a volume of 962 m<sup>3</sup> and the ceiling is 2.9 m tall. During the measurements, the room was completely empty except for the 5 workstation islands. Within each group of 4 workstations, two variations of the setup are considered:

- V1: only tables in the room,
- V2: tables with dividing panels and side panels.

The source location and the 9 receiver locations are denoted by the red and yellow circles respectively, with the exact position of the source and of one receiver ( $R_9$ ) provided. The table depth for each sitting position is 0.8 m and the source and microphones are positioned 0.3 m away from the tables. More geometrical details can be found in Ref. [15]. The measurements have been performed following ISO 3382-3 [17]. An omnidirectional sound source (B&K 4292) and omnidirectional microphones were connected to a laptop with measurement software Dirac 6 (B&K 7841) via a triton USB device (AE) and an amplifier (B&K 2734).

### 2.2. Acoustic properties of room materials

The room has a sound absorbing suspended ceiling of 20 mm thick Rockfon panels with an air cavity of at least 200 mm. The floor is covered with carpet. Dividing and side panels, which are made of 25 mm chipboard,

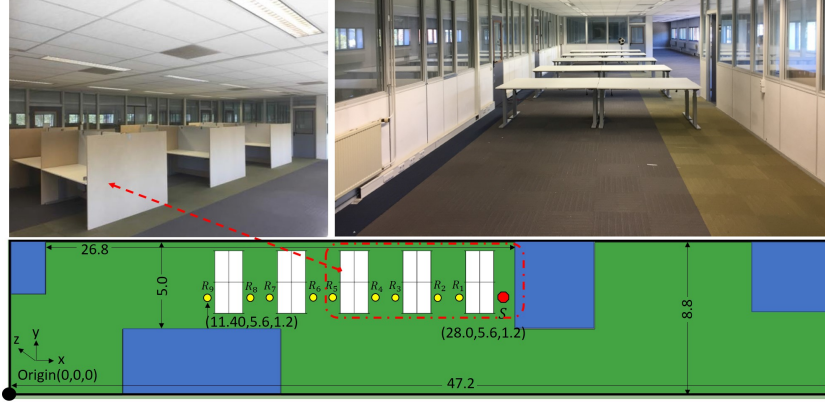


Figure 1: Pictures of the measured open plan office and its floor plan in top view.

stand on the floor and have a height of 1.5 m. To increase sound absorption, 30 mm thick melamine foam is applied to both sides of the upper 1.3 m part of the dividing panels that are along the y-direction.

The acoustic properties of the room surface materials, which are represented with the Sabine absorption coefficients in this work, are measured in a reverberation chamber according to ISO354 [16] and are available in octave bands as shown in Table 1. The Sabine absorption coefficients are measured by the reverberation chamber method as follows:

$$\alpha_{Sab} = \frac{55.3V}{Sc_0} \left( \frac{1}{T_2} - \frac{1}{T_1} \right), \quad (1)$$

where  $V$  is the volume of the reverberation chamber,  $S$  is the area of the material sample,  $T_1$  is the reverberation

Table 1: Measured Sabine absorption coefficients  $\alpha_{Sab}$  of materials in octave bands. The values in parentheses are the estimated size-corrected ones used in simulations, as described in Sec. 3

Frequency [Hz]/Materials	Ceiling	Foam	Carpet
125	0.45 (0.45)	0.10 (0.11)	0.02 (0.01)
250	0.70 (0.72)	0.35 (0.33)	0.03 (0.03)
500	0.90 (0.87)	0.60 (0.62)	0.07 (0.08)

time for an empty condition, and  $T_2$  is the reverberation time with the test sample. It should be mentioned that due to the limited volume of the reverberation chamber, the measurements for the suspended ceiling are performed with the mounting type E-200 of ISO 354 [16], *i.e.*, placing the test sample with a 200 mm cavity behind it.

### 3 Wave-based modeling

#### 3.1. Brief description of the time-domain DG method

The simulations are performed using an in-house simulation tool based on the TD-DG method. This section presents the main formulations whereas additional details can be found in Refs. [3, 4, 6]. Under the assumption of lossless propagation medium, the sound propagation is governed by the following partial differential equations

$$\frac{\partial q}{\partial t} + \nabla \cdot \mathbf{F}(q) = \frac{\partial q}{\partial t} + \mathbf{A}_j \frac{\partial q}{\partial x_j} = 0, \quad (2)$$

where  $\mathbf{q}(\mathbf{x}, t) = [u, v, w, p]^T$  is the acoustic variable vector, containing the particle velocity component  $[u, v, w]$  and the sound pressure  $p$ .  $\rho$  is the constant air density and  $c$  is the constant speed of sound. The constant flux Jacobian matrix  $A_j$  reads

$$A_j = \begin{bmatrix} 0 & 0 & 0 & \frac{\delta_{xj}}{\rho} \\ 0 & 0 & 0 & \frac{\delta_{yj}}{\rho} \\ 0 & 0 & 0 & \frac{\delta_{zj}}{\rho} \\ \rho c^2 \delta_{xj} & \rho c^2 \delta_{yj} & \rho c^2 \delta_{zj} & 0 \end{bmatrix}, \quad (3)$$

with coordinate index  $j \in [x, y, z]$ . Let  $D^k$  be a set of simplex and geometrically conformal elements that discretize the computational domain  $\Omega_h$ , i.e.,  $\Omega_h = \bigcup_{k=1}^K D^k$ . The local solution  $\mathbf{q}_h^k(\mathbf{x}, t)$  in element  $D^k$ , where subscript  $h$  denotes the numerical approximation, is given by:

$$\mathbf{q}_h^k(\mathbf{x}, t) = \sum_{i=1}^{N_p} \mathbf{q}_h^k(\mathbf{x}_i^k, t) l_i^k(\mathbf{x}), \quad (4)$$

where  $\mathbf{q}_h^k(\mathbf{x}_i^k, t)$  are the unknown nodal values and  $l_i^k(\mathbf{x})$  is the multi-dimensional Lagrange polynomial basis of order  $N$ , which satisfies  $l_i^k(\mathbf{x}_j^k) = \delta_{ij}$ .  $N_p$  is the number of local basis functions (or nodes) inside a single element and is equal to  $(N+d)!/(N!d!)$  for simplex elements, where  $d$  is the dimensionality. After the Galerkin projection and integrating by parts twice, the semi-discrete nodal DG formulation of Eq. (2) reads:

$$\int_{D^k} \left( \frac{\partial \mathbf{q}_h^k}{\partial t} + \nabla \cdot \mathbf{F}_h^k(\mathbf{q}_h^k) \right) l_i^k d\mathbf{x} = \int_{\partial D^k} \mathbf{n} \cdot \left( \mathbf{F}_h^k(\mathbf{q}_h^k) - \mathbf{F}^* \right) l_i^k d\mathbf{x}, \quad (5)$$

where  $\mathbf{n} = [n_x, n_y, n_z]$  is the outward normal vector of the element surface  $\partial D^k$ .  $\mathbf{F}^*$  is the numerical flux across element intersection  $\partial D^k$  and in this study, the upwind numerical flux is used throughout the whole domain because of its low dispersive and dissipation error. The semi-discrete formulation is obtained by substituting the nodal basis expansion Eq. (4) into the strong formulation Eq. (5). The resulting vector-matrix form of the formulation and more details of the implementation can be found in Ref. [3].

Locally reacting time-domain impedance boundary conditions (TDIBC) are weakly enforced through the numerical flux terms, where the reflected characteristic wave is expressed as the convolution between the reflection coefficient at normal incidence and the incident characteristic wave. The method of auxiliary differential equations is used to calculate the convolution. The reflection coefficient is represented by the multi-pole model as described in Ref. [4].

The semi-discrete system with a 6th order spatial approximation is integrated in time using a 5th order explicit Taylor series integrator based on the arbitrary high-order derivatives (ADER) methodology, with a local time-stepping scheme incorporated as presented in [6].

### 3.2. Mesh generation

The model geometry is imported into the meshing software Gmsh [18] to generate the unstructured tetrahedral mesh, as shown in Fig. 2 for the V2 setup. The geometrical model contains all details whose dimensions are comparable to the shortest wavelength resolved, which is around 0.5 m. The absorbing foam, dividing panels and desks are modeled as “floating” surfaces with their thicknesses neglected.

It is known that the mesh quality has a pivotal influence on the maximum allowable time step size and the numerical error. In Gmsh, mesh element sizes are usually prescribed by adjusting the so-called characteristic lengths (denoted as  $L_c$ ), which are more or less equal to the length of the element edges. Here, the radius of the largest inscribed sphere  $r_{in}$  is used as the element size measure. The chosen quality measure  $r_q$  is triple of the ratio between  $r_{in}$  and the radius of the smallest circumscribed sphere  $r_{cir}$ , i.e.  $r_q = 3r_{in}/r_{cir}$ . As a reference, a regular tetrahedron has  $r_q = 1$  (optimal mesh quality), and a degenerate tetrahedron (zero volume) has  $r_q = 0$ . Considering the maximum frequency of interest of 500 Hz, meshes with five different

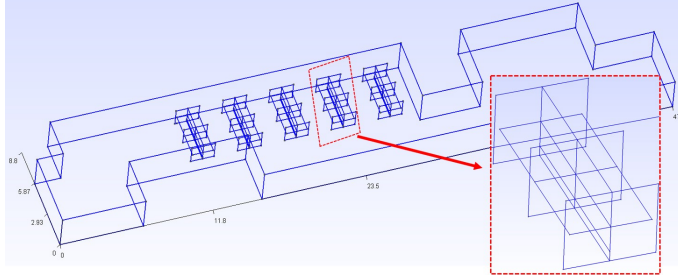


Figure 2: Geometry model in Gmsh.

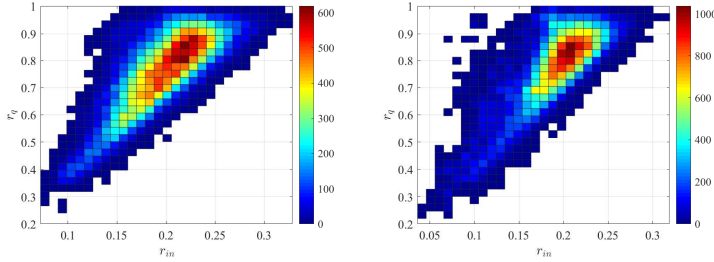


Figure 3: Distribution of the mesh quality measure  $r_q$  and the mesh size measure  $r_{in}$ . V1 and V2 are displayed in the left and right plot respectively. The color indicates the number of elements in each bin.

$L_c = [0.3, 0.35, 0.4, 0.45, 0.5]$  m values are generated for both setups. It is found that decreasing the mesh element size (increasing the number of elements) does not necessarily yield larger values of  $r_q$  (better mesh quality). By comparing the distributions of the mesh quality measure  $r_q$  and the element size measure  $r_{in}$ , the meshes with  $L_c = 0.45$  m are chosen for both setups, with their distributions of  $r_q$  and  $r_{in}$  are shown in Fig. 3. The number of elements are 50379 and 57489 for V1 and V2, respectively. The points per wavelength is 11.2 (11.8) at the center frequency and 7.9 (8.3) at the upper limit of 500 Hz octave band for the V1 (V2) mesh.

In this work, considering the CFL stability condition of the explicit time integration scheme, the time step size is determined by

$$\Delta t = C_{CFL} \cdot \min(r_{in}) \cdot \frac{1}{c} \cdot \frac{1}{(2N + 1)}. \quad (6)$$

In this study,  $C_{CFL}$  is set to 0.9, and  $\min(r_{in}) = 0.074$  m for V1 and  $\min(r_{in}) = 0.042$  m for V2. To accelerate the simulation for the V2 setup, where small elements exist around the corner of table dividers due to the geometry constraint, a local time-stepping scheme [6] is used and all elements are divided into two groups. All elements that have  $r_{in} \leq 3 \min(r_{in})$  are marked as fine elements, accounting for 8.4% of total elements, and are time integrated with  $\Delta t$  of Eq. (6). The rest are considered as coarse elements and have a time step size of  $3\Delta t$ .

### 3.3. Acoustic boundary modeling

The measured Sabine absorption coefficients  $\alpha_{Sab}$  are energy parameters that do not carry phase information. They approximately represent the theoretical random incidence absorption coefficient  $\alpha_{rand}$  for plane wave incidence on an infinitely large surface. However, for wave-based room acoustic simulations, such as the TD-DG method herein, the complex-valued surface impedances or equivalent reflection coefficients are needed for the boundary modeling. In general, it is considered intractable to retrieve the correct complex-valued surface impedance from a real-valued absorption coefficient when there is no more information on the material

available, because there are an infinite number of surface impedance values that yield the same absorption coefficient. To address this issue, a common strategy is to add some assumptions and constraints [19, 20]. First of all, local reaction is assumed, meaning that the surface impedance  $Z_s(\theta)$  is independent of the angle of incidence  $\theta$  (and thus the surface impedance for normal incidence is assumed representative of all incidence angles). Secondly, as proposed in Refs. [21, 20], we assume that the measured Sabine absorption coefficient corresponds to the size-corrected absorption coefficient for the low frequency range of interest, which is proposed by Thomasson [22] as follows:

$$\alpha_{size}(\theta) = 8 \int_0^{\pi/2} \frac{\text{Re}(Z_s(\theta)) \sin \theta}{|Z_s(\theta) + \bar{Z}_r(\theta)|^2} d\theta, \quad (7)$$

where  $\bar{Z}_r$  is the averaged radiation impedance over azimuthal angles  $\phi$  and expressed as  $\bar{Z}_r = \int_0^{2\pi} Z_r d\phi / 2\pi$ . The average radiation impedance can be calculated with numerical integrations in an accurate way, based on tabulated values provided in Table I of Ref. [21].

From the rudimentary assessment of the limited absorption coefficients data, the rigidly-backed foam and carpet correspond to the cases “soft porous” and “hard porous” as discussed in Ref. [20]. It has been shown therein that the surface impedance of rigidly-backing porous materials, which exhibits a monotonic behavior, can be well captured by approximations with fractional derivatives, similar to the multi-pole model representation as used in the TDIBC here. By contrast, the suspended ceiling with a large air cavity is quite difficult to simulate in practice [20], because the cotangent term in the surface impedance produces oscillating behavior. Therefore, the resulting narrow-band frequency variations are impossible to be reasonably captured from the coarse frequency-averaged octave band data. In this work, restricted by the availability of input data, we preliminarily assume that strong oscillations are not present in the current frequency range of interest. The multi-pole parameters needed for the TDIBC are determined by solving an optimization problem. The idea is to optimize the parameters in the multi-pole approximations of the reflection coefficient at normal incidence (denoted as  $R_{nor}$ ), which can be linearly transformed into the surface impedance in Eq. (7), that produces the best match between the measured and the estimated size-corrected absorption coefficient. The magnitude and the phase angle of fitted reflection coefficients  $R_{nor}$  are shown in Fig. 4. The corresponding size-corrected absorption coefficients are the values inside the parenthesis of Table 1.

Besides the considered ceiling, foam and carpet, there are other materials in the room absorbing sound in

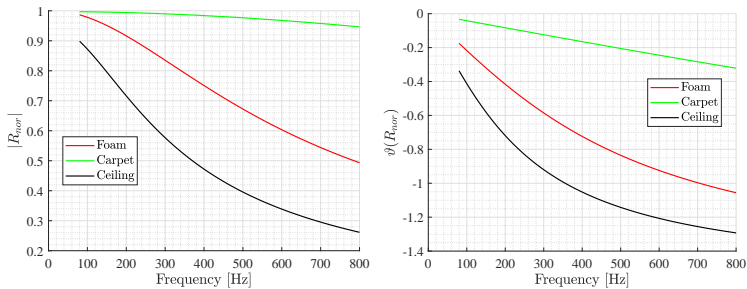


Figure 4: Estimated reflection coefficient at normal incidence.  $\theta(\cdot)$  extracts the phase angle of a complex number.

the considered frequency range, for example the window glass and gypsum board. However, the detailed information on their sizes and acoustic properties are missing. Here, real-valued impedances in octave bands are assigned to all other surfaces in the room guided by the typical values of absorption coefficients provided in Ref. [23], *i.e.*, 0.15, 0.15 and 0.1 for the octave bands 125 Hz, 250 Hz and 500 Hz respectively.

Table 2: Spatial average of the considered room acoustic parameters and their standard deviation for both setups. The values before the slash are the measured ones and after the slash are the simulated ones.

Para.	Oct.	Space aver. V1	Std. V1	Space aver. V2	Std. V2
$T_{30}$ [s]	125	0.83/0.70	0.06/0.08	0.78/0.61	0.09/0.08
	250	0.80/1.14	0.07/0.20	0.76/0.82	0.14/0.12
	500	0.64/1.13	0.07/0.26	0.61/0.79	0.10/0.08
$EDT$ [s]	125	0.70/0.79	0.26/0.31	0.94/0.92	0.33/0.33
	250	0.57/0.78	0.18/0.21	0.77/0.68	0.22/0.25
	500	0.55/0.83	0.20/0.29	0.61/0.69	0.21/0.28
$C_{50}$ [dB]	125	4.70/3.0	3.10/4.94	-0.47/0.34	5.24/2.98
	250	6.50/4.75	2.54/1.66	2.02/5.65	2.89/4.71
	500	6.80/3.31	3.26/3.00	6.25/4.23	3.32/2.71
$T_S$ [ms]	125	77.5/79.0	25.9/33.7	100.9/99.1	35.4/33.7
	250	66.2/77.8	23.6/28.2	88.7/75.5	28.5/29.0
	500	59.2/80.6	25.3/32.8	70.9/76.0	24.7/28.3

## 4 Results

The results from the measurements and the simulations are first evaluated in terms of standard room acoustic parameters as stated in ISO 3382-1 [24], including reverberation time ( $T_{30}$ ), early decay time ( $EDT$ ), clarity ( $C_{50}$ ) and center of gravity ( $T_S$ ). In the DG simulation, the dodecahedron source is modeled by a point source that has a Gaussian shaped time signal with a non-flat spectrum. Therefore, the simulated responses are deconvolved by the spectral division approach with the water level regularization technique [25] applied in order to get the room impulse responses.

In order to evaluate room acoustic parameters that are representative of the whole room, the spatial averaging values, which are obtained from the arithmetic average for all nine receiver locations, are presented in Table 2. The standard deviations provide insights into the spatial variance of the parameters across various locations. The first impression of the comparison results is that none of the simulation results match the measured ones very well, except for the center time  $T_S$  at 125 Hz, which is the center of gravity of the squared impulse response and indicates the balance between clarity and reverberance. Larger deviations are observed for spatial mean values of both  $T_{30}$  and  $EDT$ , which are directly calculated from the energy decay curve. For  $T_{30}$ , lower values are predicted compared to the measurements for both setups in the 125 Hz octave band, whereas higher values are found in the simulations for the 250 Hz and 500 Hz octave bands. For the clarity  $C_{50}$ , the simulated values are lower than the measured ones, except for setup V2 at 125 Hz, implying that the simulated sound field is more perceptually blurred.

The reverberation time of a room is usually regarded as the predominant indicator of its acoustical properties. However, for the open plan office, good speech privacy between workstations is of primary concern. Therefore, the spatial decay rate of speech  $D_{2,S}$  (level reduction when doubling the distance) and A-weighted sound pressure level (SPL) of speech at a distance of 4 m from the sound source ( $L_{p,A,S,4m}$ ) as described in ISO 3382-3 [17] are investigated. The sound power level of the loud speaker and simulation impulse source are normalized based on the SPL at a distance of 1 m in the free-field condition. Due to the limited frequency range of the wave-based simulations, the logarithm summation of the A-weighted SPL is calculated only up to the 500 Hz octave band instead of 8000 Hz for both simulation and measurements. It should be noted that due to the SPL spectrum of normal speech and the A-weighting, the A-weighted SPL of speech almost fully depends on the 500 Hz octave band.

The comparisons for the V1 setup (with empty tables alone) and the V2 setup (with table dividers and side panels) are shown in Fig. 5, where the linear regression is performed to determine  $D_{2,S}$  according to ISO 3382-3 [17]. It can be seen that the simulations have a lower predicted SPL of normal speech for all receiver locations except the eighth receiver. The discrepancies get smaller at further distance. Furthermore, the simulated spatial decay rates of speech  $D_{2,S}$  are smaller than the measured ones in both cases. For the V1 setup, the monotonic decrease of  $L_{p,A,S}$  is well predicted, while a fairly good agreement of the zigzag shape in terms of  $L_{p,A,S}$  is observed for the V2 setup, implying the effects of the table dividers and side panels are taken into account in the simulations.

The considered comparison has proven to be quite challenging. While it is intractable to pin down the exact

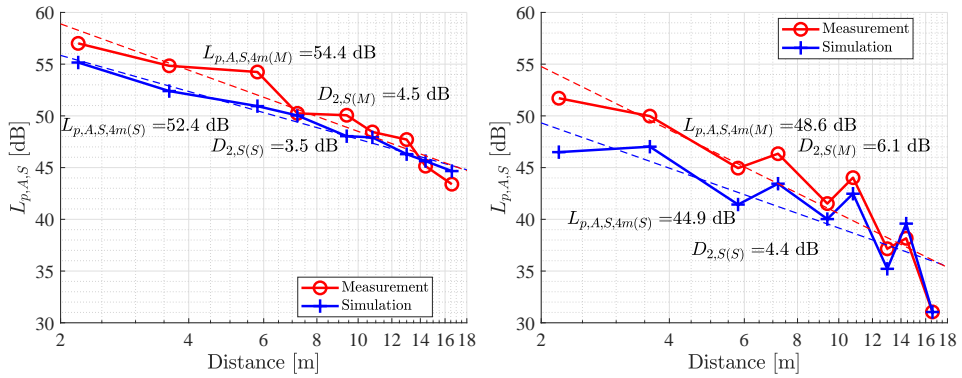


Figure 5: Comparison of  $D_{2,S}$  and  $L_{p,A,S,4m}$ . V1 and V2 are displayed in the left and right plot respectively.

deficiency of the numerical model, the discrepancies between the simulation and measurement results can be elucidated mainly from the following three aspects. First of all, there are inevitable uncertainties and inherent randomness in both the measurements and the simulation inputs, including boundary material properties, geometry and the source/receiver locations. In this study, the lack of knowledge about the exact size of the windows and their acoustic properties could also affects the accuracy of simulated  $T_{30}$  and  $EDT$ .

Secondly, the measured absorption coefficients of three major absorbing materials according to ISO 354 [16] may not truly represent the acoustic properties of the materials due to the limitation of the standard [26, 27]. Furthermore, octave band data does not provide a sufficient frequency resolution for simulation purposes. The acoustic properties of the considered materials might not be monotonic in the interested frequency range, as assumed. Also, the accurate phase information about the surface impedance is missing, which has been shown quite influential in capturing the frequency shift [28] and the reverberation time [29]. This argument is supported by the fact that the standard deviation of  $EDT$  is slightly larger than that of  $T_{30}$ , since  $EDT$  is more sensitive to the relatively sparse early reflections.

Last but not least, the current wave-based simulation models all surfaces as locally reacting. In many applications, this assumption has prevailed due to its simplicity. However, previous studies showed that for grazing incidence waves, considerable discrepancies between locally and extendedly reacting absorbers exist [30]. For the studied office, the distance between the floor and the absorbing ceiling is rather low. As a consequence, grazing incidence might be more pronounced in the early reflections for certain source-receiver positions, resulting in a serious degradation of the accuracy in  $EDT$ . Furthermore, extended reaction most likely arises in the suspended ceiling treatment, which has an air gap larger than 200 mm. It has been shown that absorbers with an air gap exhibit strong extendedly reacting behavior and that a better agreement at larger incidence angles at lower frequencies is observed for extended reaction models [31].

## 5 Conclusion

Wave-based room simulation of a real open plan office in the low-frequency range has been performed with the time-domain discontinuous Galerkin method. The acoustic properties of materials are represented with the energy-based absorption coefficients in octave bands measured with the reverberation chamber method. From this input data, the needed complex-valued surface impedance data is retrieved by fitting the size-corrected Sabine absorption coefficients, assuming monotonic absorption behavior within the interested frequency range. To assess the validity of the whole framework, the simulation results are compared with the measurements in terms of room acoustic parameters.

Noticeable discrepancies between the simulation and measurement results are observed, especially for the reverberation time and early decay time. While it is generally difficult to determine which influencing factors contribute the most to the overall simulation deviations, the potential limitations of the current numerical model are summarized. It should be noted that this work is a preliminary attempt to investigate the applicability for challenging practical cases, where a high level of complexity and uncertainty in model inputs is involved. As future work, experimental validations with increasing level of complexity of room scenarios will be performed. Furthermore, the formulation of extendedly reacting boundary conditions should help to achieve satisfactory improvements in the simulation accuracy.

## References

- [1] Lauri Savioja and U. Peter Svensson. Overview of geometrical room acoustic modeling techniques. *The Journal of the Acoustical Society of America*, 138(2):708–730, aug 2015.
- [2] Finnur Pind. *Wave-Based Virtual Acoustics*. PhD thesis, Technical University of Denmark, 2020.
- [3] Huiqing Wang, Indra Sihar, Raúl Pagán Muñoz, and Maarten Hornikx. Room acoustics modelling in the time-domain with the nodal discontinuous Galerkin method. *The Journal of the Acoustical Society of America*, 145(4):2650–2663, 2019.
- [4] Huiqing Wang and Maarten Hornikx. Time-domain impedance boundary condition modeling with the discontinuous Galerkin method for room acoustics simulations. *The Journal of the Acoustical Society of America*, 147(4):2534–2546, 2020.
- [5] Huiqing Wang, Jieun Yang, and Maarten Hornikx. Frequency-dependent transmission boundary condition in the acoustic time-domain nodal discontinuous Galerkin model. *Applied Acoustics*, 164:107280, 2020.
- [6] Huiqing Wang, Matthias Cosnefroy, and Maarten Hornikx. An arbitrary high-order discontinuous Galerkin method with local time-stepping for linear acoustic wave propagation. *The Journal of the Acoustical Society of America*, 149(1):569–580, 2021.
- [7] Fabian Brinkmann, Lukas Aspöck, David Ackermann, Steffen Lepa, Michael Vorländer, and Stefan Weinzierl. A round robin on room acoustical simulation and auralization. *The Journal of the Acoustical Society of America*, 145(4):2746–2760, 2019.
- [8] Fabian Brinkmann, Lukas Aspöck, David Ackermann, Rob Opdam, Michael Vorländer, and Stefan Weinzierl. A benchmark for room acoustical simulation. concept and database. *Applied Acoustics*, 176:107867, 2021.
- [9] Michael Vorländer. Computer simulations in room acoustics: Concepts and uncertainties. *The Journal of the Acoustical Society of America*, 133(3):1203–1213, mar 2013.
- [10] Takeshi Okuzono, Toru Otsuru, Reiji Tomiku, and Noriko Okamoto. Fundamental accuracy of time domain finite element method for sound-field analysis of rooms. *Applied Acoustics*, 71(10):940–946, 2010.
- [11] Marc Aretz and Michael Vorländer. Efficient modelling of absorbing boundaries in room acoustic FE simulations. *Acta Acustica united with Acustica*, 96(6):1042–1050, 2010.

- [12] Finnur Pind, Cheol-Ho Jeong, Allan P Engsig-Karup, Jan S Hesthaven, and Jakob Strømman-Andersen. Time-domain room acoustic simulations with extended-reacting porous absorbers using the discontinuous Galerkin method. *The Journal of the Acoustical Society of America*, 148(5):2851–2863, 2020.
- [13] Fotis Georgiou, Baltazar Briere de la Hosserraye, Maarten Hornikx, and Philip W Robinson. Design and simulation of a benchmark room for room acoustic auralizations. In *23rd International Congress on Acoustics*, pages 723–730, 2019.
- [14] Tobias Thydal, Finnur Pind, Cheol-Ho Jeong, and Allan P Engsig-Karup. Experimental validation and uncertainty quantification in wave-based computational room acoustics. *Applied Acoustics*, 178:107939, 2021.
- [15] Remy Wenmaekers and Nicole van Hout. How ISO 3382-3 acoustic parameter values are affected by furniture, barriers and sound absorption in a typical open plan office. In *23rd International Congress on Acoustics*, pages 2437–2444, 2019.
- [16] ISO354: 2003. Acoustics - Measurement of sound absorption in a reverberation room. Standard, International Organization for Standardization, Geneva, CH, 2003.
- [17] ISO 3382-3. Acoustics - Measurement of room acoustic parameters - Part 3: Open plan offices. Standard, International Organization for Standardization, Geneva, CH, 2017.
- [18] Christophe Geuzaine and Jean-François Remacle. Gmsh: A 3-D finite element mesh generator with built-in pre-and post-processing facilities. *International Journal for Numerical Methods in Engineering*, 79(11):1309–1331, 2009.
- [19] Jens Holger Rindel. An impedance model for estimating the complex pressure reflection factor. In *Forum Acusticum*, volume 2011, 2011.
- [20] Boris Mondet, Jonas Brunskog, Cheol-Ho Jeong, and Jens Holger Rindel. From absorption to impedance: Enhancing boundary conditions in room acoustic simulations. *Applied Acoustics*, 157:106884, 2020.
- [21] Cheol-Ho Jeong. Converting sabine absorption coefficients to random incidence absorption coefficients. *The Journal of the Acoustical Society of America*, 133(6):3951–3962, 2013.
- [22] Sven-Ingvar Thomasson. On the absorption coefficient. *Acta Acustica united with Acustica*, 44(4):265–273, 1980.
- [23] H. Kuttruff. *Acoustics: An Introduction*. CRC Press, New York, 2006.
- [24] ISO 3382-1. Acoustics - Measurement of room acoustic parameters - Part 1: Performance spaces. Standard, International Organization for Standardization, Geneva, CH, March 2015.
- [25] *Deconvolution, a glimpse ahead*, pages 103–107. Springer Berlin Heidelberg, Berlin, Heidelberg, 1994.
- [26] Martijn Vercammen. On the revision of ISO 354, measurement of the sound absorption in the reverberation room. In *23rd International Congress on Acoustics*, pages 3991–3997, 2019.
- [27] Cheol-Ho Jeong and Ji-Ho Chang. Reproducibility of the random incidence absorption coefficient converted from the sabine absorption coefficient. *Acta Acustica united with Acustica*, 101(1):99–112, 2015.
- [28] Diego M Murillo, Filippo M Fazi, and Jeremy Astley. Room acoustic simulations using the finite element method and diffuse absorption coefficients. *Acta Acustica united with Acustica*, 105(1):231–239, 2019.
- [29] Cheol-Ho Jeong, Doheon Lee, Sébastien Santurette, and Jeong-Guon Ih. Influence of impedance phase angle on sound pressures and reverberation times in a rectangular room. *The Journal of the Acoustical Society of America*, 135(2):712–723, 2014.
- [30] Behrooz Yousefzadeh and Murray Hodgson. Energy-and wave-based beam-tracing prediction of room-acoustical parameters using different boundary conditions. *The Journal of the Acoustical Society of America*, 132(3):1450–1461, 2012.
- [31] Krístrún Gunnarsdóttir, Cheol-Ho Jeong, and Gerd Marbjerg. Acoustic behavior of porous ceiling absorbers based on local and extended reaction. *The Journal of the Acoustical Society of America*, 137(1):509–512, 2015.

---

---

## Acknowledgements

Recollecting my past four-year adventure as a PhD candidate, I feel very lucky to get motivated and inspired by many kind people directly or indirectly. Without their support and help, the work presented in this thesis could not be achieved.

First and foremost, my sincere gratitude goes to my supervisor Prof. Maarten Hornikx. It has been such a rewarding PhD study experience with him. I appreciate him offering this project on room acoustics to me, who even had no idea of what reverberation time is in the beginning. I am grateful for his consistent trust, endless support, profound guidance, in addition to encouraging me to explore my path following my own passion. Many thanks to his time and patience on reading my manuscripts. His scrupulous attitude, critical questions and insightful feedbacks help me to stay on track towards a scientific researcher. More than that, his professionalism and diligence have significantly motivated me, and will continuously motivate me to move on.

I would like to express my gratitude to my co-promotor Dr. Matthias Cosnefroy for supporting the final year of my PhD with his dedicated efforts. All those constructive comments and intelligent suggestions to my thesis are greatly appreciated.

I am also grateful to my supervisory committee members, Prof. Harald van Brummelen, Prof. Stefan Bilbao, Dr. Cheol-Ho Jeong, Dr. Hèrm Hofmeyer, for their interest in my research and time on reviewing my thesis. I appreciate their instructive remarks and positive feedbacks towards my work.

I appreciate all the collaborations from co-authors, Indra, Raúl, Baltazar, Fotis, Jieun, Wouter, Matthias, Dr. Remy Wenmaekers, Felix and Georgios. Thanks for all your intelligible input, stimulating debates and critical reviews.

Great thanks to the funding support of the ACOUTECT project, through which I had the honor to get to know many nice (future) acousticians. All those enjoyable activities will always be precious memories to me. Also, I appreciate all the efforts from the consortium in organizing those wonderful training schools that considerably broaden my knowledge and horizons. Special thanks go to Dr. Onur Atak and Dr. Jacques Cuenca from Siemens Industry Software for their warm welcome and support to our demonstrator secondment.

I would like to thank my friends and colleagues in the building acoustics group for creating a cheerful working morale. Fotis, Raúl, Indra, Chang, Qin, Sai, Jikke, Ella, Fanyu, Antonio, Baltazar, Jieun, JinJack, Wouter, Tanmayee, Maud, Lingge, Matthias, Alessia and Michalis, thank you all for the fruitful conversations, countless discussions, sharing your knowledge, and above all, those occasional relaxing drinkings. I wish to thank the HR personnel/secretary of the department for their

timely support and help whenever I am in need. Furthermore, I would like to thank Indra and Raúl for offering patient assistance, and sharing valuable experience and advice (not only in research), especially during the first few months of my PhD when Maarten was on sabbatical leave. Many thanks go to Wouter and Jieun for all those joyful moments during the pandemic lockdown.

I am blessed with indispensable distractions and care from all my friends that carry me through stressful and difficult times. Thank you! Particularly, a debt of gratitude is owed to Dr. Feng for all your kind support. Special thanks go to Jessie for your warm-hearted help and all delightful moments together. Also thanks to my old friend Dr. Teng Zhou for all those great and cherished time in Delft, Hong Kong, *etc.*.

Lastly, my deepest gratitude to my dear parents and family. Thanks for your unconditional love, solid support throughout my education and firm belief in me. To my mother for teaching me patience and kindness. To my father for your encouragement and standing by my side as always.

---

## Curriculum Vitae

Huiqing Wang was born in August 1989 in Yantai, which is a charming city south to the Bohai Strait along the east coast of mainland China. He finished his pre-college education at Yantai No. 2 High school in 2008. In 2012, he obtained his bachelor degree in *Aircraft Design and Engineering* from Nanjing University of Aeronautics and Astronautics, with specialization in helicopter design. In 2013, he came to the Netherlands for his master study and obtained his MSc degree in *Aerospace Engineering* with a track on aerodynamics from Delft University of Technology. His master thesis topic is *Stochastic Collocation with CFD robustness concepts for multi-dimensional stochastic space*. From 2015 to 2016, he worked as a research engineer on the topic of reduced order modeling at Multibody & Mechatronic Systems Lab at University of Liège, Belgium. From 2016 to 2017, he worked as a research and teaching assistant at Advanced Aircraft Noise Technology Center of Hong Kong University of Science and Technology, Hong Kong SAR. Since November of 2017, Huiqing joined the Building Acoustics group chaired by prof.dr.ir. Maarten Hornikx at the Department of the Built Environment at Eindhoven University of Technology, and started his PhD project within the ITN Marie Skłodowska-Curie Action project ACOUTECT under the 7<sup>th</sup> Framework Programme of the European Union.

**Bouwstenen** is een publicatiereeks van de Faculteit Bouwkunde, Technische Universiteit Eindhoven. Zij presenteert resultaten van onderzoek en andere activiteiten op het vakgebied der Bouwkunde, uitgevoerd in het kader van deze Faculteit.

**Bouwstenen** en andere proefschriften van de TU/e zijn online beschikbaar via:  
<https://research.tue.nl/>

Reeds verschenen in de serie

## **Bouwstenen**

nr 1

### **Elan: A Computer Model for Building Energy Design: Theory and Validation**

Martin H. de Wit

H.H. Driessen

R.M.M. van der Velden

nr 2

### **Kwaliteit, Keuzevrijheid en Kosten: Evaluatie van Experiment Klarendal, Arnhem**

J. Smeets

C. le Nobel

M. Broos

J. Frenken

A. v.d. Sanden

nr 3

### **Crooswijk: Van 'Bijzonder' naar 'Gewoon'**

Vincent Smit

Kees Noort

nr 4

### **Staal in de Woningbouw**

Edwin J.F. Delsing

nr 5

### **Mathematical Theory of Stressed Skin Action in Profiled Sheeting with Various Edge Conditions**

Andre W.A.M.J. van den Bogaard

nr 6

### **Hoe Berekenbaar en Betrouwbaar is de Coëfficiënt $k$ in $x$ -ksigma en $x$ -ks?**

K.B. Lub

A.J. Bosch

nr 7

### **Het Typologisch Gereedschap: Een Verkennende Studie Omtrent Typologie en Omtrent de Aanpak van Typologisch Onderzoek**

J.H. Luiten

nr 8

### **Informatievoorziening en Beheerprocessen**

A. Nauta

Jos Smeets (red.)

Helga Fassbinder (projectleider)

Adrie Proveniers

J. v.d. Moosdijk

nr 9

### **Strukturering en Verwerking van Tijdgegevens voor de Uitvoering van Bouwwerken**

ir. W.F. Schaefer

P.A. Erkelens

nr 10

### **Stedebouw en de Vorming van een Speciale Wetenschap**

K. Doevendans

nr 11

### **Informatica en Ondersteuning van Ruimtelijke Besluitvorming**

G.G. van der Meulen

nr 12

### **Staal in de Woningbouw, Korrosie-Bescherming van de Begane Grondvloer**

Edwin J.F. Delsing

nr 13

### **Een Thermisch Model voor de Berekening van Staalplaatbetonvloeren onder Brandomstandigheden**

A.F. Hamerlinck

nr 14

### **De Wijkgedachte in Nederland: Gemeenschapsstreven in een Stedebouwkundige Context**

K. Doevendans

R. Stolzenburg

nr 15

### **Diaphragm Effect of Trapezoidally Profiled Steel Sheets:**

### **Experimental Research into the Influence of Force Application**

Andre W.A.M.J. van den Bogaard

nr 16

### **Versterken met Smit-Ferrocement: Het Mechanische Gedrag van met Smit-Ferrocement Versterkte Gewapend Betonbalken**

K.B. Lubir

M.C.G. van Wanroy

nr 17

**De Tractaten van  
Jean Nicolas Louis Durand**  
G. van Zeyl

nr 18

**Wonen onder een Plat Dak:  
Drie Opstellen over Enkele  
Vooronderstellingen van de  
Stedebouw**  
K. Doevendans

nr 19

**Supporting Decision Making Processes:  
A Graphical and Interactive Analysis of  
Multivariate Data**  
W. Adams

nr 20

**Self-Help Building Productivity:  
A Method for Improving House Building  
by Low-Income Groups Applied to Kenya  
1990-2000**  
P. A. Erkelens

nr 21

**De Verdeling van Woningen:  
Een Kwestie van Onderhandelen**  
Vincent Smit

nr 22

**Flexibiliteit en Kosten in het Ontwerpproces:  
Een Besluitvormingondersteunend Model**  
M. Prins

nr 23

**Spontane Nederzettingen Begeleid:  
Voorwaarden en Criteria in Sri Lanka**  
Po Hin Thung

nr 24

**Fundamentals of the Design of  
Bamboo Structures**  
Oscar Arce-Villalobos

nr 25

**Concepten van de Bouwkunde**  
M.F.Th. Bax (red.)  
H.M.G.J. Trum (red.)

nr 26

**Meaning of the Site**  
Xiaodong Li

nr 27

**Het Woonmilieu op Begrip Gebracht:  
Een Speurtocht naar de Betekenis van het  
Begrip 'Woonmilieu'**  
Jaap Ketelaar

nr 28

**Urban Environment in Developing Countries**  
editors: Peter A. Erkelens  
George G. van der Meulen (red.)

nr 29

**Statistische Plannen voor de Stad:  
Onderzoek en Planning in Drie Steden**  
prof.dr. H. Fassbinder (red.)  
H. Rikhof (red.)

nr 30

**Stedebouwkunde en Stadsbestuur**  
Piet Beekman

nr 31

**De Architectuur van Djenné:  
Een Onderzoek naar de Historische Stad**  
P.C.M. Maas

nr 32

**Conjoint Experiments and Retail Planning**  
Harmen Oppewal

nr 33

**Strukturformen Indonesischer Bautechnik:  
Entwicklung Methodischer Grundlagen  
für eine 'Konstruktive Pattern Language'  
in Indonesien**

Heinz Frick arch. SIA

nr 34

**Styles of Architectural Designing:  
Empirical Research on Working Styles  
and Personality Dispositions**  
Anton P.M. van Bakel

nr 35

**Conjoint Choice Models for Urban  
Tourism Planning and Marketing**  
Benedict Dellaert

nr 36

**Stedelijke Planvorming als Co-Productie**  
Helga Fassbinder (red.)

nr 37

**Design Research in the Netherlands**

editors: R.M. Oxman

M.F.Th. Bax

H.H. Achten

nr 38

**Communication in the Building Industry**

Bauke de Vries

nr 39

**Optimaal Dimensioneren van  
Gelaste Plaatliggers**

J.B.W. Stark

F. van Pelt

L.F.M. van Gorp

B.W.E.M. van Hove

nr 40

**Huisvesting en Overwinning van Armoede**

P.H. Thung

P. Beekman (red.)

nr 41

**Urban Habitat:  
The Environment of Tomorrow**

George G. van der Meulen

Peter A. Erkelens

nr 42

**A Typology of Joints**

John C.M. Olie

nr 43

**Modeling Constraints-Based Choices  
for Leisure Mobility Planning**

Marcus P. Stemerding

nr 44

**Activity-Based Travel Demand Modeling**

Dick Ettema

nr 45

**Wind-Induced Pressure Fluctuations  
on Building Facades**

Chris Geurts

nr 46

**Generic Representations**

Henri Achten

nr 47

**Johann Santini Aichel:  
Architectuur en Ambiguiteit**

Dirk De Meyer

nr 48

**Concrete Behaviour in Multiaxial  
Compression**

Erik van Geel

nr 49

**Modelling Site Selection**

Frank Witlox

nr 50

**Ecolemma Model**

Ferdinand Beetstra

nr 51

**Conjoint Approaches to Developing  
Activity-Based Models**

Donggen Wang

nr 52

**On the Effectiveness of Ventilation**

Ad Roos

nr 53

**Conjoint Modeling Approaches for  
Residential Group preferences**

Eric Molin

nr 54

**Modelling Architectural Design  
Information by Features**

Jos van Leeuwen

nr 55

**A Spatial Decision Support System for  
the Planning of Retail and Service Facilities**

Theo Arentze

nr 56

**Integrated Lighting System Assistant**

Ellie de Groot

nr 57

**Ontwerpend Leren, Leren Ontwerpen**

J.T. Boekholt

nr 58

**Temporal Aspects of Theme Park Choice  
Behavior**

Astrid Kemperman

nr 59

**Ontwerp van een Geïndustrialiseerde  
Funderingswijze**

Faas Moonen

nr 60

**Merlin: A Decision Support System  
for Outdoor Leisure Planning**

Manon van Middelkoop

nr 61

**The Aura of Modernity**

Jos Bosman

nr 62

**Urban Form and Activity-Travel Patterns**

Daniëlle Snellen

nr 63

**Design Research in the Netherlands 2000**

Henri Achten

nr 64

**Computer Aided Dimensional Control in  
Building Construction**

Rui Wu

nr 65

**Beyond Sustainable Building**

editors: Peter A. Erkelens  
Sander de Jonge  
August A.M. van Vliet

co-editor: Ruth J.G. Verhagen

nr 66

**Das Globalrecyclingfähige Haus**

Hans Löfflad

nr 67

**Cool Schools for Hot Suburbs**

René J. Dierkx

nr 68

**A Bamboo Building Design Decision  
Support Tool**

Fitri Mardjono

nr 69

**Driving Rain on Building Envelopes**

Fabien van Mook

nr 70

**Heating Monumental Churches**

Henk Schellen

nr 71

**Van Woningverhuurder naar  
Aanbieder van Woongenot**

Patrick Dogge

nr 72

**Moisture Transfer Properties of  
Coated Gypsum**

Emile Goossens

nr 73

**Plybamboo Wall-Panels for Housing**

Guillermo E. González-Beltrán

nr 74

**The Future Site-Proceedings**

Ger Maas

Frans van Gassel

nr 75

**Radon transport in  
Autoclaved Aerated Concrete**

Michel van der Pal

nr 76

**The Reliability and Validity of Interactive  
Virtual Reality Computer Experiments**

Amy Tan

nr 77

**Measuring Housing Preferences Using  
Virtual Reality and Belief Networks**

Maciej A. Orzechowski

nr 78

**Computational Representations of Words  
and Associations in Architectural Design**

Nicole Segers

nr 79

**Measuring and Predicting Adaptation in  
Multidimensional Activity-Travel Patterns**

Chang-Hyeon Joh

nr 80

**Strategic Briefing**

Fayez Al Hassan

nr 81

**Well Being in Hospitals**

Simona Di Cicco

nr 82

**Solares Bauen:  
Implementierungs- und Umsetzungs-  
Aspekte in der Hochschulausbildung  
in Österreich**

Gerhard Schuster

nr 83

**Supporting Strategic Design of  
Workplace Environments with  
Case-Based Reasoning**

Shauna Mallory-Hill

nr 84

**ACCEL: A Tool for Supporting Concept  
Generation in the Early Design Phase**

Maxim Ivashkov

nr 85

**Brick-Mortar Interaction in Masonry  
under Compression**

Ad Vermeltfoort

nr 86

**Zelfredzaam Wonen**

Guus van Vliet

nr 87

**Een Ensemble met Grootstedelijke Allure**

Jos Bosman

Hans Schippers

nr 88

**On the Computation of Well-Structured  
Graphic Representations in Architectural  
Design**

Henri Achten

nr 89

**De Evolutie van een West-Afrikaanse  
Vernaculaire Architectuur**

Wolf Schijns

nr 90

**ROMBO Tactiek**

Christoph Maria Ravesloot

nr 91

**External Coupling between Building  
Energy Simulation and Computational  
Fluid Dynamics**

Ery Djunaedy

nr 92

**Design Research in the Netherlands 2005**

editors: Henri Achten

Kees Dorst

Pieter Jan Stappers

Bauke de Vries

nr 93

**Ein Modell zur Baulichen Transformation**

Jalil H. Saber Zaimian

nr 94

**Human Lighting Demands:  
Healthy Lighting in an Office Environment**

Myriam Aries

nr 95

**A Spatial Decision Support System for  
the Provision and Monitoring of Urban  
Greenspace**

Claudia Pelizaro

nr 96

**Leren Creëren**

Adri Proveniers

nr 97

**Simlandscape**

Rob de Waard

nr 98

**Design Team Communication**

Ad den Otter

nr 99

**Humaan-Ecologisch  
Georiënteerde Woningbouw**

Juri Czabanowski

nr 100

**Hambase**

Martin de Wit

nr 101

**Sound Transmission through Pipe  
Systems and into Building Structures**

Susanne Bron-van der Jagt

nr 102

**Het Bouwkundig Contrapunt**

Jan Francis Boelen

nr 103

**A Framework for a Multi-Agent  
Planning Support System**

Dick Saarloos

nr 104

**Bracing Steel Frames with Calcium  
Silicate Element Walls**

Bright Mweene Ng'andu

nr 105

**Naar een Nieuwe Houtskeletbouw**

F.N.G. De Medts

nr 106 and 107  
*Niet gepubliceerd*

nr 108  
**Geborgenheid**  
T.E.L. van Pinxteren

nr 109  
**Modelling Strategic Behaviour in Anticipation of Congestion**  
Qi Han

nr 110  
**Reflecties op het Woondomein**  
Fred Sanders

nr 111  
**On Assessment of Wind Comfort by Sand Erosion**  
Gábor Dezső

nr 112  
**Bench Heating in Monumental Churches**  
Dionne Limpens-Neilen

nr 113  
**RE. Architecture**  
Ana Pereira Roders

nr 114  
**Toward Applicable Green Architecture**  
Usama El Fiky

nr 115  
**Knowledge Representation under Inherent Uncertainty in a Multi-Agent System for Land Use Planning**  
Liyang Ma

nr 116  
**Integrated Heat Air and Moisture Modeling and Simulation**  
Jos van Schijndel

nr 117  
**Concrete Behaviour in Multiaxial Compression**  
J.P.W. Bongers

nr 118  
**The Image of the Urban Landscape**  
Ana Moya Pellitero

nr 119  
**The Self-Organizing City in Vietnam**  
Stephanie Geertman

nr 120  
**A Multi-Agent Planning Support System for Assessing Externalities of Urban Form Scenarios**  
Rachel Katoshevski-Cavari

nr 121  
**Den Schulbau Neu Denken, Fühlen und Wollen**  
Urs Christian Maurer-Dietrich

nr 122  
**Peter Eisenman Theories and Practices**  
Bernhard Kormoss

nr 123  
**User Simulation of Space Utilisation**  
Vincent Tabak

nr 125  
**In Search of a Complex System Model**  
Oswald Devisch

nr 126  
**Lighting at Work: Environmental Study of Direct Effects of Lighting Level and Spectrum on Psycho-Physiological Variables**  
Grazyna Górnicka

nr 127  
**Flanking Sound Transmission through Lightweight Framed Double Leaf Walls**  
Stefan Schoenwald

nr 128  
**Bounded Rationality and Spatio-Temporal Pedestrian Shopping Behavior**  
Wei Zhu

nr 129  
**Travel Information: Impact on Activity Travel Pattern**  
Zhongwei Sun

nr 130  
**Co-Simulation for Performance Prediction of Innovative Integrated Mechanical Energy Systems in Buildings**  
Marija Trčka

nr 131  
*Niet gepubliceerd*

nr 132

**Architectural Cue Model in Evacuation  
Simulation for Underground Space Design**  
Chengyu Sun

nr 133

**Uncertainty and Sensitivity Analysis in  
Building Performance Simulation for  
Decision Support and Design Optimization**  
Christina Hopfe

nr 134

**Facilitating Distributed Collaboration  
in the AEC/FM Sector Using Semantic  
Web Technologies**  
Jacob Beetz

nr 135

**Circumferentially Adhesive Bonded Glass  
Panels for Bracing Steel Frame in Façades**  
Edwin Huveners

nr 136

**Influence of Temperature on Concrete  
Beams Strengthened in Flexure  
with CFRP**  
Ernst-Lucas Klamer

nr 137

**Sturen op Klantwaarde**  
Jos Smeets

nr 139

**Lateral Behavior of Steel Frames  
with Discretely Connected Precast Concrete  
Infill Panels**  
Paul Teewen

nr 140

**Integral Design Method in the Context  
of Sustainable Building Design**  
Perica Savanović

nr 141

**Household Activity-Travel Behavior:  
Implementation of Within-Household  
Interactions**  
Renni Anggraini

nr 142

**Design Research in the Netherlands 2010**  
Henri Achten

nr 143

**Modelling Life Trajectories and Transport  
Mode Choice Using Bayesian Belief Networks**  
Marloes Verhoeven

nr 144

**Assessing Construction Project  
Performance in Ghana**  
William Gyadu-Asiedu

nr 145

**Empowering Seniors through  
Domotic Homes**  
Masi Mohammadi

nr 146

**An Integral Design Concept for  
Ecological Self-Compacting Concrete**  
Martin Hunger

nr 147

**Governing Multi-Actor Decision Processes  
in Dutch Industrial Area Redevelopment**  
Erik Blokhuis

nr 148

**A Multifunctional Design Approach  
for Sustainable Concrete**  
Götz Hüsken

nr 149

**Quality Monitoring in Infrastructural  
Design-Build Projects**  
Ruben Favié

nr 150

**Assessment Matrix for Conservation of  
Valuable Timber Structures**  
Michael Abels

nr 151

**Co-simulation of Building Energy Simulation  
and Computational Fluid Dynamics for  
Whole-Building Heat, Air and Moisture  
Engineering**  
Mohammad Mirsadeghi

nr 152

**External Coupling of Building Energy  
Simulation and Building Element Heat,  
Air and Moisture Simulation**  
Daniel Cóstola

nr 153

**Adaptive Decision Making In  
Multi-Stakeholder Retail Planning**

Ingrid Janssen

nr 154

**Landscape Generator**

Kymo Slager

nr 155

**Constraint Specification in Architecture**

Remco Niemeijer

nr 156

**A Need-Based Approach to  
Dynamic Activity Generation**

Linda Nijland

nr 157

**Modeling Office Firm Dynamics in an  
Agent-Based Micro Simulation Framework**

Gustavo Garcia Manzano

nr 158

**Lightweight Floor System for  
Vibration Comfort**

Sander Zegers

nr 159

**Aanpasbaarheid van de Draagstructuur**

Roel Gijssbers

nr 160

**'Village in the City' in Guangzhou, China**

Yanliu Lin

nr 161

**Climate Risk Assessment in Museums**

Marco Martens

nr 162

**Social Activity-Travel Patterns**

Pauline van den Berg

nr 163

**Sound Concentration Caused by  
Curved Surfaces**

Martijn Vercammen

nr 164

**Design of Environmentally Friendly  
Calcium Sulfate-Based Building Materials:  
Towards an Improved Indoor Air Quality**

Qingliang Yu

nr 165

**Beyond Uniform Thermal Comfort  
on the Effects of Non-Uniformity and  
Individual Physiology**

Lisje Schellen

nr 166

**Sustainable Residential Districts**

Gaby Abdalla

nr 167

**Towards a Performance Assessment  
Methodology using Computational  
Simulation for Air Distribution System  
Designs in Operating Rooms**

Mônica do Amaral Melhado

nr 168

**Strategic Decision Modeling in  
Brownfield Redevelopment**

Brano Glumac

nr 169

**Pamela: A Parking Analysis Model  
for Predicting Effects in Local Areas**

Peter van der Waerden

nr 170

**A Vision Driven Wayfinding Simulation-System  
Based on the Architectural Features Perceived  
in the Office Environment**

Qunli Chen

nr 171

**Measuring Mental Representations  
Underlying Activity-Travel Choices**

Oliver Horeni

nr 172

**Modelling the Effects of Social Networks  
on Activity and Travel Behaviour**

Nicole Ronald

nr 173

**Uncertainty Propagation and Sensitivity  
Analysis Techniques in Building Performance  
Simulation to Support Conceptual Building  
and System Design**

Christian Struck

nr 174

**Numerical Modeling of Micro-Scale  
Wind-Induced Pollutant Dispersion  
in the Built Environment**

Pierre Gousseau

nr 175

**Modeling Recreation Choices  
over the Family Lifecycle**

Anna Beatriz Grigolon

nr 176

**Experimental and Numerical Analysis of  
Mixing Ventilation at Laminar, Transitional  
and Turbulent Slot Reynolds Numbers**

Twan van Hooff

nr 177

**Collaborative Design Support:  
Workshops to Stimulate Interaction and  
Knowledge Exchange Between Practitioners**

Emile M.C.J. Quanjel

nr 178

**Future-Proof Platforms for Aging-in-Place**

Michiel Brink

nr 179

**Motivate:  
A Context-Aware Mobile Application for  
Physical Activity Promotion**

Yuzhong Lin

nr 180

**Experience the City:  
Analysis of Space-Time Behaviour and  
Spatial Learning**

Anastasia Moiseeva

nr 181

**Unbonded Post-Tensioned Shear Walls of  
Calcium Silicate Element Masonry**

Lex van der Meer

nr 182

**Construction and Demolition Waste  
Recycling into Innovative Building Materials  
for Sustainable Construction in Tanzania**

Mwita M. Sabai

nr 183

**Durability of Concrete  
with Emphasis on Chloride Migration**

Przemysław Spiesz

nr 184

**Computational Modeling of Urban  
Wind Flow and Natural Ventilation Potential  
of Buildings**

Rubina Ramponi

nr 185

**A Distributed Dynamic Simulation  
Mechanism for Buildings Automation  
and Control Systems**

Azzedine Yahiaoui

nr 186

**Modeling Cognitive Learning of Urban  
Networks in Daily Activity-Travel Behavior**

Şehnaz Cenani Durmazoğlu

nr 187

**Functionality and Adaptability of Design  
Solutions for Public Apartment Buildings  
in Ghana**

Stephen Agyefi-Mensah

nr 188

**A Construction Waste Generation Model  
for Developing Countries**

Lilliana Abarca-Guerrero

nr 189

**Synchronizing Networks:  
The Modeling of Supernetworks for  
Activity-Travel Behavior**

Feixiong Liao

nr 190

**Time and Money Allocation Decisions  
in Out-of-Home Leisure Activity Choices**

Gamze Zeynep Dane

nr 191

**How to Measure Added Value of CRE and  
Building Design**

Rianne Appel-Meulenbroek

nr 192

**Secondary Materials in Cement-Based  
Products:  
Treatment, Modeling and Environmental  
Interaction**

Miruna Florea

nr 193

**Concepts for the Robustness Improvement  
of Self-Compacting Concrete:  
Effects of Admixtures and Mixture  
Components on the Rheology and Early  
Hydration at Varying Temperatures**

Wolfram Schmidt

nr 194

**Modelling and Simulation of Virtual Natural Lighting Solutions in Buildings**

Rizki A. Mangkuto

nr 195

**Nano-Silica Production at Low Temperatures from the Dissolution of Olivine - Synthesis, Tailoring and Modelling**

Alberto Lazaro Garcia

nr 196

**Building Energy Simulation Based Assessment of Industrial Halls for Design Support**

Bruno Lee

nr 197

**Computational Performance Prediction of the Potential of Hybrid Adaptable Thermal Storage Concepts for Lightweight Low-Energy Houses**

Pieter-Jan Hoes

nr 198

**Application of Nano-Silica in Concrete**

George Quercia Bianchi

nr 199

**Dynamics of Social Networks and Activity Travel Behaviour**

Fariya Sharmeen

nr 200

**Building Structural Design Generation and Optimisation including Spatial Modification**

Juan Manuel Davila Delgado

nr 201

**Hydration and Thermal Decomposition of Cement/Calcium-Sulphate Based Materials**

Ariën de Korte

nr 202

**Republiek van Beelden: De Politieke Werkingen van het Ontwerp in Regionale Planvorming**

Bart de Zwart

nr 203

**Effects of Energy Price Increases on Individual Activity-Travel Repertoires and Energy Consumption**

Dujuan Yang

nr 204

**Geometry and Ventilation: Evaluation of the Leeward Sawtooth Roof Potential in the Natural Ventilation of Buildings**

Jorge Isaac Perén Montero

nr 205

**Computational Modelling of Evaporative Cooling as a Climate Change Adaptation Measure at the Spatial Scale of Buildings and Streets**

Hamid Montazeri

nr 206

**Local Buckling of Aluminium Beams in Fire Conditions**

Ronald van der Meulen

nr 207

**Historic Urban Landscapes: Framing the Integration of Urban and Heritage Planning in Multilevel Governance**

Loes Veldpaus

nr 208

**Sustainable Transformation of the Cities: Urban Design Pragmatics to Achieve a Sustainable City**

Ernesto Antonio Zumelzu Scheel

nr 209

**Development of Sustainable Protective Ultra-High Performance Fibre Reinforced Concrete (UHPFRC): Design, Assessment and Modeling**

Rui Yu

nr 210

**Uncertainty in Modeling Activity-Travel Demand in Complex Urban Systems**

Soora Rasouli

nr 211

**Simulation-based Performance Assessment of Climate Adaptive Greenhouse Shells**

Chul-sung Lee

nr 212

**Green Cities: Modelling the Spatial Transformation of the Urban Environment using Renewable Energy Technologies**

Saleh Mohammadi

nr 213

**A Bounded Rationality Model of Short and Long-Term Dynamics of Activity-Travel Behavior**

Ifigeneia Psarra

nr 214

**Effects of Pricing Strategies on Dynamic Repertoires of Activity-Travel Behaviour**

Elaheh Khademi

nr 215

**Handstorm Principles for Creative and Collaborative Working**

Frans van Gassel

nr 216

**Light Conditions in Nursing Homes: Visual Comfort and Visual Functioning of Residents**

Marianne M. Sinoo

nr 217

**Woonsporen:**

**De Sociale en Ruimtelijke Biografie van een Stedelijk Bouwblok in de Amsterdamse Transvaalbuurt**

Hüseyin Hüsnü Yegenoglu

nr 218

**Studies on User Control in Ambient Intelligent Systems**

Berent Willem Meerbeek

nr 219

**Daily Livings in a Smart Home: Users' Living Preference Modeling of Smart Homes**

Erfaneh Allameh

nr 220

**Smart Home Design: Spatial Preference Modeling of Smart Homes**

Mohammadali Heidari Jozam

nr 221

**Wonen:**

**Discoursen, Praktijken, Perspectieven**

Jos Smeets

nr 222

**Personal Control over Indoor Climate in Offices: Impact on Comfort, Health and Productivity**

Atze Christiaan Boerstra

nr 223

**Personalized Route Finding in Multimodal Transportation Networks**

Jianwe Zhang

nr 224

**The Design of an Adaptive Healing Room for Stroke Patients**

Elke Daemen

nr 225

**Experimental and Numerical Analysis of Climate Change Induced Risks to Historic Buildings and Collections**

Zara Huijbregts

nr 226

**Wind Flow Modeling in Urban Areas Through Experimental and Numerical Techniques**

Alessio Ricci

nr 227

**Clever Climate Control for Culture: Energy Efficient Indoor Climate Control Strategies for Museums Respecting Collection Preservation and Thermal Comfort of Visitors**

Rick Kramer

nr 228

**Fatigue Life Estimation of Metal Structures Based on Damage Modeling**

Sarmediran Silitonga

nr 229

**A multi-agents and occupancy based strategy for energy management and process control on the room-level**

Timilehin Moses Labeodan

nr 230

**Environmental assessment of Building Integrated Photovoltaics: Numerical and Experimental Carrying Capacity Based Approach**

Michiel Ritzen

nr 231

**Performance of Admixture and Secondary Minerals in Alkali Activated Concrete: Sustaining a Concrete Future**

Arno Keulen

nr 232

**World Heritage Cities and Sustainable Urban Development: Bridging Global and Local Levels in Monitoring the Sustainable Urban Development of World Heritage Cities**

Paloma C. Guzman Molina

nr 233

**Stage Acoustics and Sound Exposure in Performance and Rehearsal Spaces for Orchestras: Methods for Physical Measurements**

Remy Wenmaekers

nr 234

**Municipal Solid Waste Incineration (MSWI) Bottom Ash: From Waste to Value Characterization, Treatments and Application**

Pei Tang

nr 235

**Large Eddy Simulations Applied to Wind Loading and Pollutant Dispersion**

Mattia Ricci

nr 236

**Alkali Activated Slag-Fly Ash Binders: Design, Modeling and Application**

Xu Gao

nr 237

**Sodium Carbonate Activated Slag: Reaction Analysis, Microstructural Modification & Engineering Application**

Bo Yuan

nr 238

**Shopping Behavior in Malls**

Widiyani

nr 239

**Smart Grid-Building Energy Interactions: Demand Side Power Flexibility in Office Buildings**

Kennedy Otieno Aduda

nr 240

**Modeling Taxis Dynamic Behavior in Uncertain Urban Environments**

Zheng Zhong

nr 241

**Gap-Theoretical Analyses of Residential Satisfaction and Intention to Move**

Wen Jiang

nr 242

**Travel Satisfaction and Subjective Well-Being: A Behavioral Modeling Perspective**

Yanan Gao

nr 243

**Building Energy Modelling to Support the Commissioning of Holistic Data Centre Operation**

Vojtech Zavrel

nr 244

**Regret-Based Travel Behavior Modeling: An Extended Framework**

Sunghoon Jang

nr 245

**Towards Robust Low-Energy Houses: A Computational Approach for Performance Robustness Assessment using Scenario Analysis**

Rajesh Reddy Kotireddy

nr 246

**Development of sustainable and functionalized inorganic binder-biofiber composites**

Guillaume Doudart de la Grée

nr 247

**A Multiscale Analysis of the Urban Heat Island Effect: From City Averaged Temperatures to the Energy Demand of Individual Buildings**

Yasin Toparlar

nr 248

**Design Method for Adaptive Daylight Systems for buildings covered by large (span) roofs**

Florian Heinzelmann

nr 249

**Hardening, high-temperature resistance and acid resistance of one-part geopolymers**

Patrick Sturm

nr 250

**Effects of the built environment on dynamic repertoires of activity-travel behaviour**

Aida Pontes de Aquino

nr 251

**Modeling for auralization of urban environments: Incorporation of directivity in sound propagation and analysis of a framework for auralizing a car pass-by**

Fotis Georgiou

nr 252

**Wind Loads on Heliostats and Photovoltaic Trackers**

Andreas Pfahl

nr 253

**Approaches for computational performance optimization of innovative adaptive façade concepts**

Roel Loonen

nr 254

**Multi-scale FEM-DEM Model for Granular Materials: Micro-scale boundary conditions, Statics, and Dynamics**

Jiadun Liu

nr 255

**Bending Moment - Shear Force Interaction of Rolled I-Shaped Steel Sections**

Rianne Willie Adriana Dekker

nr 256

**Paralympic tandem cycling and hand-cycling: Computational and wind tunnel analysis of aerodynamic performance**

Paul Fionn Mannion

nr 257

**Experimental characterization and numerical modelling of 3D printed concrete: Controlling structural behaviour in the fresh and hardened state**

Robert Johannes Maria Wolfs

nr 258

**Requirement checking in the building industry: Enabling modularized and extensible requirement checking systems based on semantic web technologies**

Chi Zhang

nr 259

**A Sustainable Industrial Site Redevelopment Planning Support System**

Tong Wang

nr 260

**Efficient storage and retrieval of detailed building models: Multi-disciplinary and long-term use of geometric and semantic construction information**

Thomas Ferdinand Krijnen

nr 261

**The users' value of business center concepts for knowledge sharing and networking behavior within and between organizations**

Minou Weijs-Perrée

nr 262

**Characterization and improvement of aerodynamic performance of vertical axis wind turbines using computational fluid dynamics (CFD)**

Abdolrahim Rezaeiha

nr 263

**In-situ characterization of the acoustic impedance of vegetated roofs**

Chang Liu

nr 264

**Occupancy-based lighting control: Developing an energy saving strategy that ensures office workers' comfort**

Christel de Bakker

nr 265

**Stakeholders-Oriented Spatial Decision Support System**

Cahyono Susetyo

nr 266

**Climate-induced damage in oak museum objects**

Rianne Aleida Luimes

nr 267

**Towards individual thermal comfort: Model predictive personalized control of heating systems**

Katarina Katic

nr 268

**Modelling and Measuring Quality of Urban Life: Housing, Neighborhood, Transport and Job**

Lida Aminian

nr 269

**Optimization of an aquifer thermal energy storage system through integrated modeling of aquifer, HVAC systems and building**

Basar Bozkaya

nr 270

**Numerical modeling for urban sound propagation: developments in wave-based and energy-based methods**

Raúl Pagán Muñoz

nr 271

**Lighting in multi-user office environments: improving employee wellbeing through personal control**

Sanae van der Vleuten-Chraibi

nr 272

**A strategy for fit-for-purpose occupant behavior modelling in building energy and comfort performance simulation**

Isabella I. Gaetani dell'Aquila d'Aragona

nr 273

**Een architectuurhistorische waardestelling van naoorlogse woonwijken in Nederland: Het voorbeeld van de Westelijke Tuinsteden in Amsterdam**

Eleonore Henriette Marie Mens

nr 274

**Job-Housing Co-Dependent Mobility Decisions in Life Trajectories**

Jia Guo

nr 275

**A user-oriented focus to create healthcare facilities: decision making on strategic values**

Emilia Rosalia Catharina Maria Huisman

nr 276

**Dynamics of plane impinging jets at moderate Reynolds numbers – with applications to air curtains**

Adelya Khayrullina

nr 277

**Valorization of Municipal Solid Waste Incineration Bottom Ash - Chemical Nature, Leachability and Treatments of Hazardous Elements**

Qadeer Alam

nr 278

**Treatments and valorization of MSWI bottom ash - application in cement-based materials**

Veronica Caprai

nr 279

**Personal lighting conditions of office workers - input for intelligent systems to optimize subjective alertness**

Juliëtte van Duijnhoven

nr 280

**Social influence effects in tourism travel: air trip itinerary and destination choices**

Xiaofeng Pan

nr 281

**Advancing Post-War Housing: Integrating Heritage Impact, Environmental Impact, Hygrothermal Risk and Costs in Renovation Design Decisions**

Lisanne Claartje Havinga

nr 282

**Impact resistant ultra-high performance fibre reinforced concrete: materials, components and properties**

Peipeng Li

nr 283

**Demand-driven Science Parks: The Perceived Benefits and Trade-offs of Tenant Firms with regard to Science Park Attributes**

Wei Keat Benny Ng

nr 284

**Raise the lantern; how light can help to maintain a healthy and safe hospital environment focusing on nurses**

Maria Petronella Johanna Aarts

nr 285

**Modelling Learning and Dynamic Route and Parking Choice Behaviour under Uncertainty**

Elaine Cristina Schneider de Carvalho

nr 286

**Identifying indoor local microclimates for safekeeping of cultural heritage**

Karin Kompatscher

nr 287

**Probabilistic modeling of fatigue resistance for welded and riveted bridge details. Resistance models and estimation of uncertainty.**

Davide Leonetti

nr 288

**Performance of Layered UHPFRC under Static and Dynamic Loads: Effects of steel fibers, coarse aggregates and layered structures**

Yangyueye Cao

nr 289

**Photocatalytic abatement of the nitrogen oxide pollution: synthesis, application and long-term evaluation of titania-silica composites**

Yuri Hendrix

nr 290

**Assessing knowledge adoption in post-disaster reconstruction: Understanding the impact of hazard-resistant construction knowledge on reconstruction processes of self-recovering communities in Nepal and the Philippines**

Eefje Hendriks

nr 291

**Locating electric vehicle charging stations: A multi-agent based dynamic simulation**

Seheon Kim

nr 292

**De invloed van Lean Management op de beheersing van het bouwproces**

Wim van den Bouwhuisen

nr 293

**Neighborhood Environment and Physical Activity of Older Adults**

Zhengying Liu

nr 294

**Practical and continuous luminance distribution measurements for lighting quality**

Thijs Willem Kruisselbrink

nr 295

**Auditory Distraction in Open-Plan Study Environments in Higher Education**

Pietermella Elizabeth Braat-Eggen

nr 296

**Exploring the effect of the sound environment on nurses' task performance: an applied approach focusing on prospective memory**

Jikke Reinten

nr 297

**Design and performance of water resistant cementitious materials– Mechanisms, evaluation and applications**

Zhengyao Qu

nr 298

**Design Optimization of Seasonal Thermal Energy Storage Integrated District Heating and Cooling System: A Modeling and Simulation Approach**

Luyi Xu

nr 299

**Land use and transport: Integrated approaches for planning and management**

Zhongqi Wang

nr 300

**Multi-disciplinary optimization of building spatial designs: co-evolutionary design process simulations, evolutionary algorithms, hybrid approaches**

Sjonnie Boonstra

nr 301

**Modeling the spatial and temporal relation between urban land use, temperature, and energy demand**

Hung-Chu Chen

nr 302

**Seismic retrofitting of masonry walls with flexible deep mounted CFRP strips**

Ömer Serhat Türkmen

nr 303

**Coupled Aerostructural Shape and Topology Optimization of Horizontal-Axis Wind Turbine Rotor Blades**

Zhijun Wang

nr 304

**Valorization of Recycled Waste Glass and Converter Steel Slag as Ingredients for Building Materials: Hydration and Carbonation Studies**

Gang Liu

nr 305

**Low-Carbon City Development based on Land Use Planning**

Gengzhe Wang

nr 306

**Sustainable energy transition scenario analysis for buildings and neighborhoods - Data driven optimization**

Shalika Saubhagya Wickramarachchi Walker

nr 307

**In-between living and manufactured: an exploratory study on biobuilding components for building design**

Berrak Kirbas Akyurek

nr 308

**Development of alternative cementitious binders and functionalized materials: design, performance and durability**

Anna Monika Kaja

nr 309

**Development a morphological approach for interactive kinetic façade design: Improving multiple occupants' visual comfort**

Seyed Morteza Hosseini

nr 310

**PV in urban context: modeling and simulation strategies for analyzing the performance of shaded PV systems**

Ádám Bognár

nr 311

**Life Trajectory, Household Car Ownership Dynamics and Home Renewable Energy Equipment Adoption**

Gaofeng Gu

nr 312

**Impact of Street-Scale Built Environment on Walking/Cycling around Metro Stations**

Yanan Liu

nr 313

**Advances in Urban Traffic Network Equilibrium Models and Algorithms**

Dong Wang

nr 314

**Development of an uncertainty analysis framework for model-based consequential life cycle assessment: application to activity-based modelling and life cycle assessment of multimodal mobility**

Paul Martin Baustert

nr 315

**Variable stiffness and damping structural joints for semi-active vibration control**

Qinyu Wang

nr 316

**Understanding Carsharing-Facilitating Neighborhood Preferences**

Juan Wang

nr 317

**Dynamic alignment of Corporate Real Estate to business strategies: An empirical analysis using historical data and in-depth modelling of decision making**

Howard Cooke

nr 318

**Local People Matter: Towards participatory governance of cultural heritage in China**

Ji Li

nr 319

**Walkability and Walkable Healthy Neighborhoods**

Bojing Liao

nr 320

**On the role of light directionality in design of healthy offices**

Parisa Khademagha

The acoustic properties of indoor spaces significantly impact our comfort, well-being and productivity. Room acoustic simulations have been a practical tool for acoustic consultants in the design phase of buildings to ensure pleasant and functional acoustic environments. More recently, advancements of modern computing hardware make room acoustic modeling applicable to more computationally intensive real-time systems such as virtual reality applications.

This PhD project aims at contributing to the room acoustic modeling community via the development and validation of an efficient, robust and accurate wave-based method. Reflecting on the state of the art numerical modeling techniques, the time-domain discontinuous Galerkin method is chosen as the focus of this thesis, due to its inherent favorable properties of high-order accuracy, geometric flexibility, and potential for massive parallel computing. The positioning of the method is addressed first, which involves a presentation of its mathematical formulation for solving the linear wave equations, a formulation of real-valued impedance boundary conditions, a semi-discrete stability analysis and numerical verifications. To simulate the locally reacting behavior of sound wave reflection and transmission in the vicinity of boundaries, a time-domain frequency-dependent boundary condition formulation is proposed. Furthermore, a local time-stepping strategy based on the arbitrary high-order derivatives methodology is proposed and numerically verified. A preliminary application to the acoustic field analysis of an open plan office examines the reliability and limitations of the developed scheme for real-world problems.

DEPARTMENT OF THE BUILT ENVIRONMENT